Study of the fatigue behaviour of some Fe-based metallic glass wires

Jorge A. Verduzco Martínez

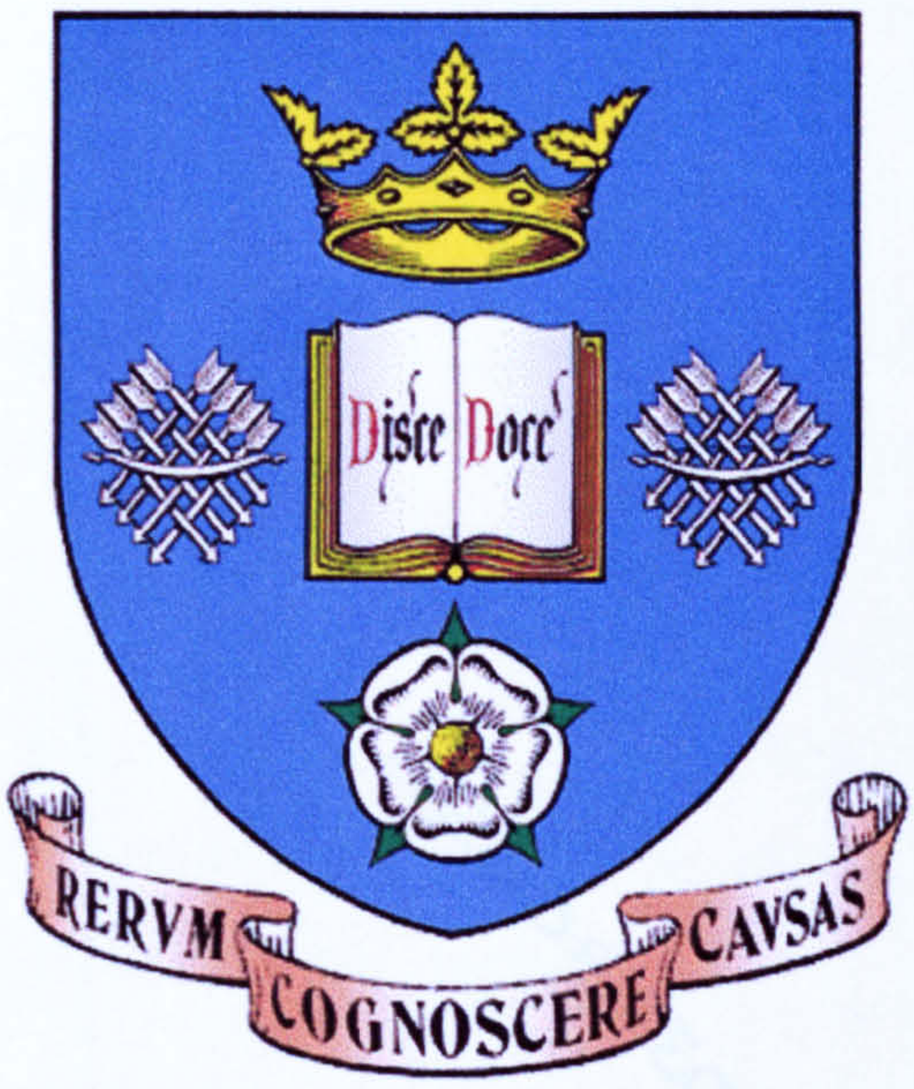

University of Sheffield

Department of Engineering Materials

Submitted for the degree of PhD

October 2000

To Mayra and Janaina

Mamá and Papá

Acknowledgements

Throughout these lines, I would like to express my truthfully acknowledge all the people whom from one or another manner helped me to carry out this work.

Firstly, I sincerely wish to thank my supervisors Prof. Hywel A. Davies and Dr. Russell J. Hand, who, thanks to their wisdom and experience guided me to the realisation of this work. I also wish to thank to the departmental staff, particularly the technicians working in the machine shop and Sorby centre, and more especially to Mr. Ian Lomas and Karen Burton for their gentleness during my stay in this department.

Secondly, I like to express my thankfulness to the members of the Mexican society, who made of my stay in Sheffield more peaceful, it is worth to mention only some of them: Arturo, Beto, Carlos, Edgar, Guillermo, Israel, Jesus, Jorge, José (Solis and Chitty), Oscar and Salvador. More especially to my "compadre" Arnoldo for his support and advise in that difficult moment of my life in Sheffield. I want to take this opportunity to thank my colleagues on M floor for sharing enjoyable moments, specially Cathy, Ibrahim, Phill, Siriporn and Surasit.

My deepest acknowledgements are for my wife Mayra for her support, sacrifice and encouragement during our life in Sheffield, to Janaina for her graciousness that has transformed my life one hundred degrees. For Mamá and Papá who thanks to their advice and, more meaningfully to their example of discipline, respect and work through my life, have guided me in the right direction. I also thank my brothers and sisters for their support and encouragement for the completion of my studies.

Finally, I want to express my gratitude to CONACyT México, for the financial support received for the realisation of this work.

Summary

$Fe_{78-x}Cr_xSi_{10}B_{12}$ and *$Fe_{77.5-x}Cr_xSi_{7.5}B_{15}$* (with *x* values ranging from 0 to 8) glassy metallic alloys have been produced in the form of both wires and ribbons using the *rotating water bath melt spinning process* and *chill block melt spinning process*, respectively. It was found that the $Fe_{77.5-x}Cr_xSi_{7.5}B_{15}$ series had better amorphous wire forming ability than the $Fe_{78-x}Cr_xSi_{10}B_{12}$ series. However, in ribbon form, both series showed good castability as amorphous alloys. Selected mechanical properties of the glassy samples have been compared with those of high tensile steel wire.

Both thermal and mechanical properties were found to be composition-dependent, especially on the Cr content, with the $Fe_{77.5-x}Cr_xSi_{7.5}B_{15}$ series wires being thermally more stable and stronger than their $Fe_{78-x}Cr_xSi_{10}B_{12}$ counterparts.

A new bend type fatigue testing machine that uses two pulleys (DP) has been developed to perform tests on the basis of tension-compression loading cycles. The results have been compared with those obtained by using an existing single pulley (SP) machine that performs only tensile-tensile loading cycles. Although the DP machine can impose compressive to tensile bend stresses at different constant mean stress, it was observed that, for low stress ranges and large constant mean stresses the machine performed equivalent bend tests to those using the SP machine. The fatigue performance of amorphous wires was improved on substituting Fe by Cr and on decreasing the constant mean stress. The high tensile (HT) steel wire apparently had better fatigue performance than amorphous wires in terms of stress range; however, when the results were expressed in terms of strain range, the fatigue performance of amorphous wires was slightly better than HT steel wires, as had been demonstrated in previous studies.

It was observed that, when the DP machine performed compressive to tensile bending stress cycles, the fracture surfaces differed from those observed in the SP machine. Under tensile to tensile conditions, the fracture surfaces observed for samples tested in the DP machine were similar to those tested in the SP machine. Fracture mechanics analysis of the results suggests that embrittlement is occurring ahead of growing fatigue cracks in these amorphous wires.

Contents

Acknowledgements iii

Summary iv

I Introduction 1

II Literature Survey 3

2.1 Metallic glasses 3

2.2 Metallic glass formation 4

2.2.1 Undercooling of the melt and glass formation 4

2.2.2 Glass forming ability in metallic materials 6

2.2.3 Theories of metallic glass formation 9

2.3 Processes for obtaining metallic glass filaments 20

2.3.1 Ribbon filaments 20

2.3.2 Wires 23

2.3.3. Obtaining Fe-based metallic glasses 27

2.4 Mechanical properties of metallic glasses 30

2.4.1 Tensile strength 30

2.4.2 Flow 33

2.4.3 Fracture 44

2.4.4 Fatigue strength 55

2.5 Corrosion resistance 66

2.5.1 Passive film 67

2.5.2 Rapid film formation 69

2.5.3 Effects of metalloids 69

2.5.4 Homogeneity of the film 70

2.5.5 High resistance to localised corrosion 71

2.5.6 Stress corrosion attack and hydrogen embrittlement 72

III Experimental 74

3.1 Ingot preparation 74

3.2 Wire casting 76

3.3 Ribbon casting 78

3.4 Structure 80

3.4.1 X-ray diffraction 80

3.4.2 Differential scanning calorimeter 81
3.5 Mechanical properties 82
3.5.1 Tensile 83
3.5.2 Fracture toughness 83
3.5.3 Fatigue 84
3.5.4 Microhardness 92
3.5.5 Scanning electron microscopy 93
IV Results 94
4.1 Wire casting 94
4.1.1 Process parameters for casting amorphous wires of good quality 95
4.2 Ribbon casting 98
4.3 Structure and thermal properties 101
4.4 Mechanical properties 106
4.4.1 Microhardness 106
4.4.2 Tensile 107
4.4.3 Fracture toughness 107
4.4.4 Fatigue 108
4.5 Fracture morphology 120
4.5.1 Tensile fracture morphology 120
4.5.2 Fatigue fracture morphology 127
V Discussion 137
5.1 Wire casting 137
5.1.1 Jet stability 137
5.1.2 Jet incidence angle 139
5.1.3 Superheat 140
5.1.4 Melt jet velocity/rotating water velocity ratio 141
5.1.5 Melt stabilisers and effect of alloy composition 142
5.2 Ribbon casting 144
5.3 Structure and thermal stability 147
5.4 Mechanical properties 150
5.4.1 Microhardness 150
5.4.2 Tensile 152
5.4.3 Fatigue 155

VI Conclusions 173

VII Suggestions for further work 176

References 177

Chapter I: INTRODUCTION

Amorphous alloys, which are produced by rapid solidification, exhibit excellent physical, and chemical properties and mechanical strengths [1]. Therefore, considerable attention has been devoted to characterising these materials to study their suitability for a variety of applications.

Empirically, a good glass forming alloy is a multicomponent system consisting of more than three elements, which should be of significantly different atomic sizes, preferably more than 12% different from each other in order to help stabilise the liquid and glass phases [2]. These large atomic size differences also lead to large negative heats of mixing which promote low eutectic temperatures and therefore retardation of the crystal nucleation and growth processes.

Among several methods used to obtain amorphous filaments in ribbon and wire forms, it has been proved that the chill melt spinning (CBMS) [3] process for producing ribbons and the so-called "in rotating water bath melt spinning" process (INROWASP) [4] for producing wires are the most convenient techniques for obtaining glassy alloy products in these forms. But not all the good glass forming alloys can easily be produced in wire form especially and the production of wire is restricted to fewer alloy compositions than is the case for CBMS.

The static and dynamic mechanical strengths of some amorphous wires are higher than some of the best commercial high tensile (HT) steel wires [5]. Therefore from an engineering point of view, amorphous wires have potential application where high static and dynamic strengths are required with special attention being paid for use of them as tyre reinforcement [4].

In general, it is difficult to measure the mechanical properties of very fine amorphous wires by conventional methods and thus specialised techniques have been developed to study and analyse them. It has been reported that the fatigue performance of Fe-Si-B-based glassy alloys improves on replacing Fe by Cr, reaching a maximum at 10 at% Cr [5-7].

Beyond this Cr content however, the as-cast wires are brittle rather than ductile with corresponding detriment to the fracture and fatigue resistance. These enhancements in fatigue properties have been observed using tension/tension bending stress tests only [5-7]. Therefore, there is need to investigate the behaviour of the Fe-based alloy wires subjected to compressive/tensile bending stresses as a function of Cr content and to compare their performance with those of HT steel wire. This forms the basis of the present study.

Chapter II: LITERATURE SURVEY

2.1 Metallic Glasses

Metals and metallic alloys having no long-range atomic order are known variously as amorphous alloys, glassy alloys or non-crystalline alloys. They can be prepared by a variety of techniques, which involve rapid solidification of the alloys from the gaseous or liquid state. The atoms are retained in their liquid configuration because solidification occurs extremely rapidly.

The amorphous alloys are characterised by exceptionally high mechanical hardness, tensile and dynamic strengths. Moreover, alloys based on Fe, Co and Fe-Ni are very soft magnetic materials, and alloy glasses based on Co:Fe ratios of 95:5 have zero magnetostriction. Their electrical resistivities are a factor of 3-4 higher than those of crystalline iron or iron-nickel alloy, because the disordered structure scatters electrons more readily. Another important property of some amorphous alloys containing ≥ 8 at % Cr is that they have exceptionally high corrosion resistance.

Amorphous alloys are being commercially exploited in distribution transformers because of their superior intrinsic magnetic properties and importantly because they are cast in very thin sections which reduces eddy current losses. The combination of their magnetic and mechanical properties has also led to their application in magnetic recording heads. They are also widely used for high frequency applications such as chokes and transformers in electronic devices and various types of sensors such as anti-theft tags in stores and libraries. In addition to applications utilising their electrical and magnetic properties, the high static and dynamic strengths of some ferrous glassy alloy wires makes them potentially applicable as tyre reinforcements, and in high strength cables.

2.2 Metallic Glass Formation

2.2.1 Undercooling of the melt and glass formation

Metallic liquids have high fluidity because of the non-directional nature of the *metallic bond* while, in contrast, molten silicates, borates and similar substances, which have strongly covalent atomic bonding, are characterised by very low fluidity or, conversely, high viscosity.

On cooling, a liquid must undercool below the equilibrium crystallisation temperature before crystallisation can begin because of the existence of an energy barrier to the formation of crystal nuclei. The degree of undercooling that occurs depends on several factors, including the initial viscosity of the liquid, the rate at which the viscosity increases with decreasing temperature, the temperature dependence of the free energy difference between the undercooling liquid and the crystal phase, the interfacial energy between the melt and crystal, the volume density and the efficacy of heterogeneous nucleating particles and the imposed cooling rate [8]. The growth rates for crystals in metallic melts are very rapid, once nucleated, and if the rate of heat removal to the surroundings is small, rapid recalescence occurs. On the other hand, the recalescence is decreased and the undercooling is enhanced if the liquid is cooled rapidly by heat removal to a sink and the influence of heterogeneous nucleants is increasingly delayed for kinetic reasons. If the cooling rate is sufficiently high, crystallisation is suppressed because of insufficient time for significant growth or, in the extreme, for nucleation, so that the shear viscosity of the melt increases continuously as shown in figure 2.1. In this case, the atomic configuration of the liquid departs substantially from equilibrium and then becomes homogeneously frozen at the glass transition temperature, T_g. By convention, this structural freezing occurs when the viscosity, η, is about 10^{13} poise.

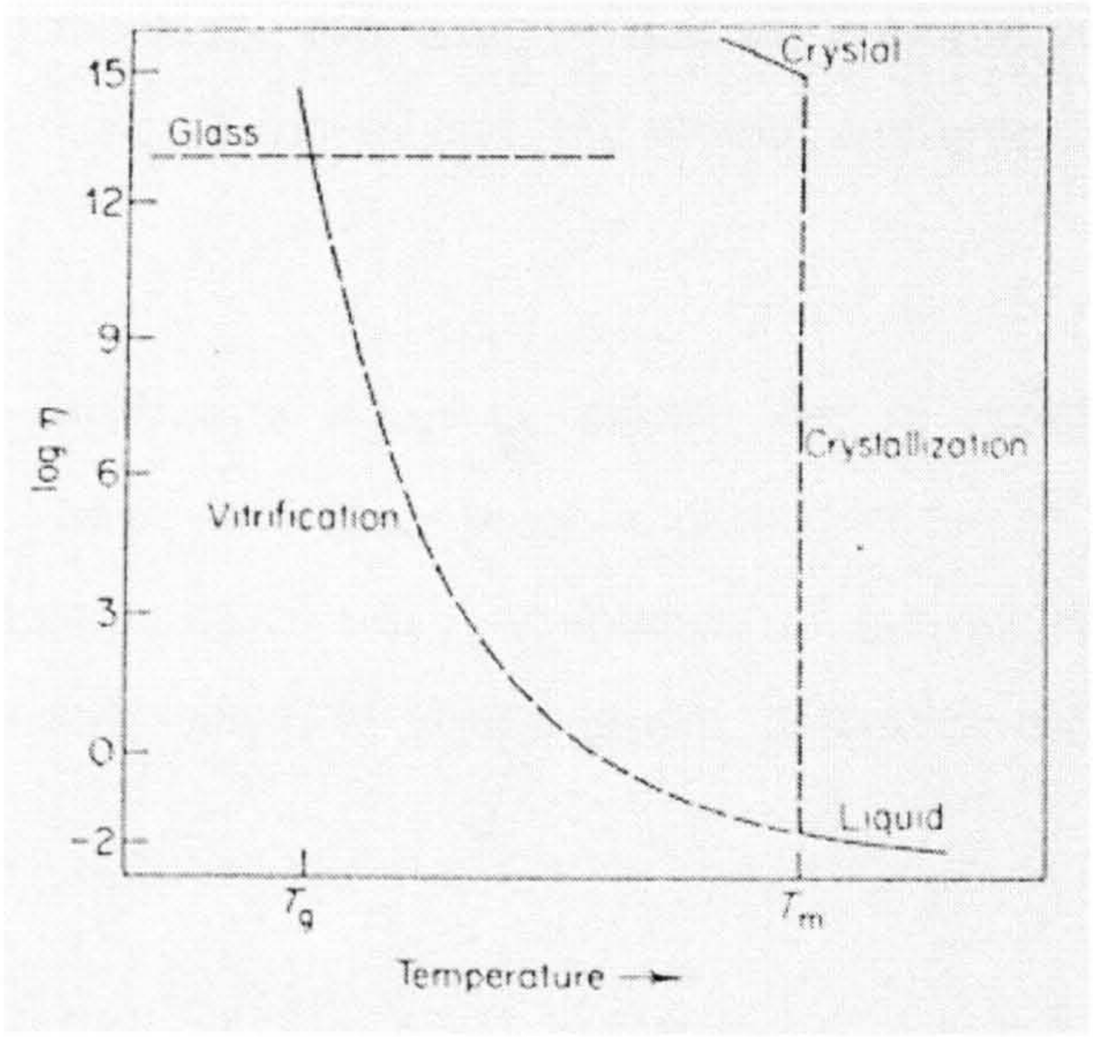

Figure 2.1. Viscosity (η) - Temperature (T) behaviour corresponding to crystallisation and vitrification of a metallic melt [8].

However, T_g and the glass structure are both cooling-rate dependent; during subsequent annealing the different glass structures are manifest by different structural relaxation characteristics. At T_g, the difference in specific heat between liquid and crystal states ΔC_p decreases discontinuously, reflecting the fewer degrees of freedom resulting from the freezing of the structure (see figure 2.2). Once vitrification has taken place, the difference in the specific heat, ΔC_p, of the glass and crystalline states become very small.

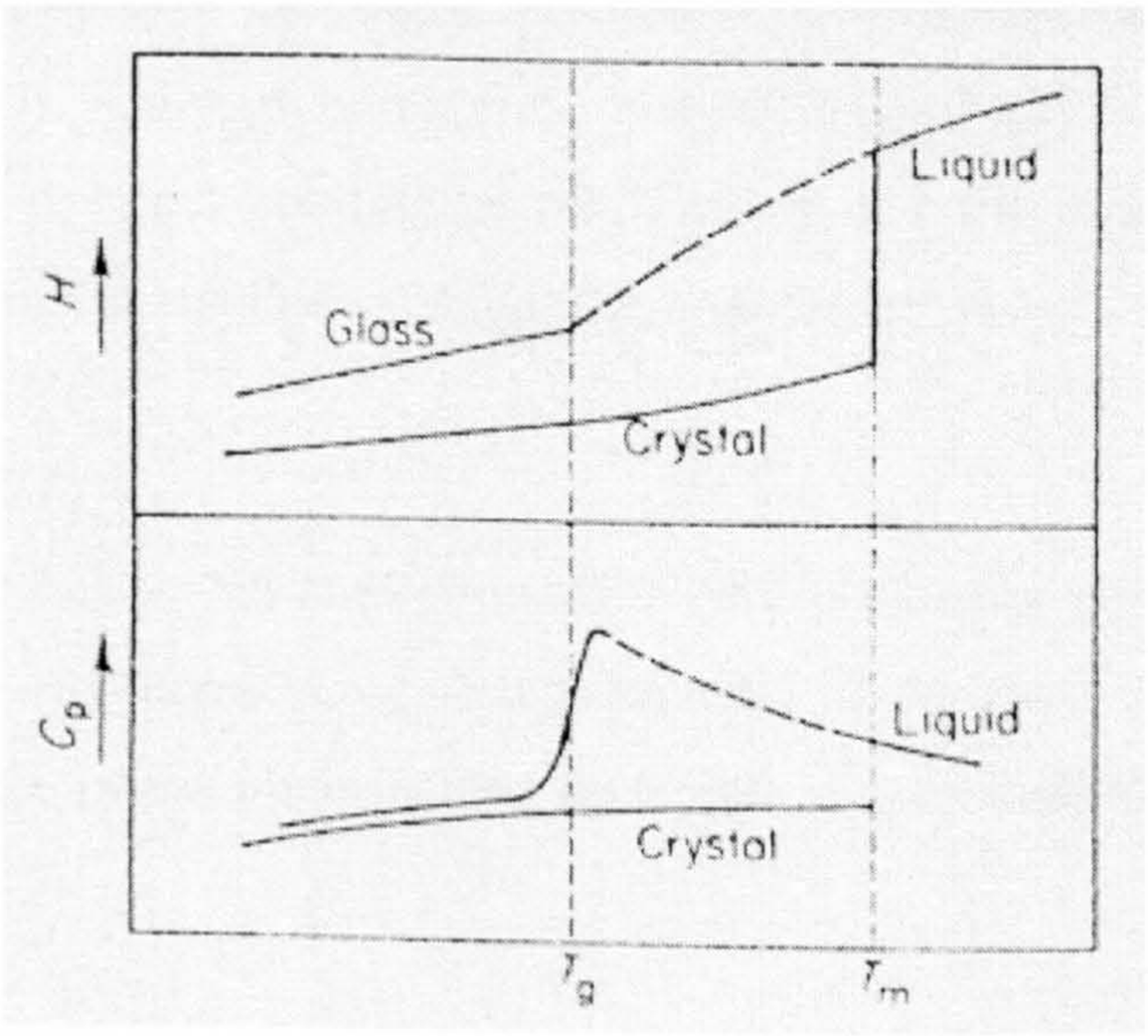

Figure 2.2. Temperature dependence of the enthalpy H and specific heat C_p corresponding to crystallisation and vitrification of a metallic melt [8].

For alloys where the solute atoms are sufficiently concentrated and are sufficiently different in size from those of the solvent, the atomic configurations are stable against crystallisation.

The process of vitrifying a liquid is, strictly, one of avoiding the nucleation of crystals during cooling; however, a more practical definition can be taken as the avoidance of a just detectable fraction of crystal. The kinetics of the nucleation process and, for practical purposes, the early stages of crystal growth determine the glass forming ability, GFA, of a material.

2.2.2 Glass forming ability in metallic materials

Nominally pure metals

From a kinetic point of view, any metallic alloy containing more than, at most, a few atomic per cent of solute, and, possibly as little as a fraction of a percent, could be quenched to a glass, given a sufficiently high cooling rate and, importantly, given that this is cooled to a temperature sufficiently low to avoid spontaneous crystallisation. However, the situation of pure metals and very dilute alloys is less clear since there is little or no barrier to nucleation and growth of crystals.

For instance, pure germanium was found to vitrify at a cooling rate of the order of 10^9 to 10^{10} Ks^{-1}, both by splat quenching in argon [9] and by dispersion of melt as 30 nm particles in argon [10]. Although germanium is metallically bonded in the liquid state, it assumes tetrahedral, covalent bonding on vitrification and the structural rearrangement required for crystallisation stabilises the glass to high temperatures, even in the absence of impurity atoms.

It is suggested that for an amorphous film of a nominally pure metal, a minimum concentration of impurity atoms is required to promote its vitrification, which may depend on the chemical nature of the impurity and its atomic size relative to the host atoms [11-13].

Influence of alloying

The effect of adding solute atoms to a pure metal, especially if they are of different size and chemical character from the host atoms, is to require that significant diffusive rearrangements occur during crystallisation of the glass phase and hence they tend to stabilise the glass. On alloying, as the solute concentration increases, both T_g and T_x, the crystallisation temperature, generally increase. On the other hand, the liquidus temperature, T_l, at which freezing begins under equilibrium conditions, often decreases. Thus, the interval between T_l and T_g generally decreases and in this case, the probability of being able to cool through the interval without inducing crystallisation is enhanced, i.e. the GFA is increased. (The GFA is measured by the magnitude of the critical cooling rate, R_c, and thus of the critical thickness, x_c, of material that can be cooled sufficiently rapidly).

Thus, GFA tends to vary inversely with the ratio T_g/T_l, which is referred to as the reduced glass temperature T_{rg}. The higher is T_g and the lower is T_l, then the higher tends to be the GFA [8]. In addition, the alloy systems having the highest GFA, are those that manifest either one or more deep eutectics, or a steep and substantial decrease in T_l with increasing percentage of solute, to a "plateau" over which T_l is low in comparison with the melting point T_m of the solvent metal.

Classification of readily glass forming alloy systems

By convention, "readily glass forming", RGF, has been taken to indicate alloys that are completely glass forming either when splat-quenched as foils about 10-20 μm thick, when continuously cast as ribbon or strip 10-20 μm thick, or when continuously cast as wire 80 μm diameter. Thus, the glass forming range, GFR, for an alloy system will depend on the value of x_c chosen, the smaller is x_c the wider being the GFR [8].

There are a number of distinct categories of alloy system within which glass formation from the melt occurs readily.

The first class to be discovered and investigated were the late transition metal-metalloid (TL-M) type; the TL elements include Group 7 to 11 elements (IUPAC proposal since 1985). They remain the most important, technologically, especially in the case of glasses based on iron, cobalt and nickel for soft ferromagnetic applications. At one stage in

the past it was thought that GFR was rather narrow and centred around deep eutectics in the range 13-25 at % metalloid. This is the case for many binary systems, e.g. Pd-Si [14] and Fe-B [15], however, there are some exceptions, e.g. Ni-B_{31-41} in addition to Ni-$B_{17-18.5}$ [16] and Co-B_{17-41} [17].

The glass forming tendency may be considerably enhanced by substituting either one or more metalloids or early transition metals (TE, group 4 to 6). In these cases the GFR may broaden or change considerably. For instance, $Pd_{78}Cu_6Si_{16}$ [18] and $Pd_{40}Ni_{40}Pd_{20}$ [19] form glasses much more readily than $Pd_{84}Si_{16}$ and $Pd_{80}P_{20}$, respectively. Similarly $Ni_{92-x}Si_8B_x$ ($10 < x < 39$) alloys are readily glass forming [20]; as are Fe-Si-B alloys, where Si + B content lies between 13 and 35 at % [3].

A number of TE-M alloys, close to primary eutectic compositions which lie mostly in the range 15-30 at % metalloid, are also RGF. The eutectic temperature for binary alloys of this type is generally much higher than those for the TL-M system, reflecting the higher T_m for the TE elements.

The second group consists of alloys of the type TE-TL. Addition of a TL (or a group 12 metal) to TE which have high T_m, generally leads to very rapid decrease in T_l, down to a eutectic. T_l also remains relatively low across one or more intermetallic phases of relatively low stability, and other eutectic reactions, so that the GFR is usually quite wide, even for binary systems. Included in this group are alloys where the TL is a platinum group metal; in this case, the eutectic temperatures are generally very high (above 1500 °C) and their crystallisation temperatures are also very high.

Binary and multicomponent alloys of the group 2 alkaline earth (AE) metals with certain sub-group metals, such as group 4 TE or with TL and group 11 noble metals, represent another class of RGF. The AE metals must be vitrified in a controlled atmosphere because they have extremely high affinities for oxygen, and the resulting glasses are also generally reactive in air.

Finally, another class of RGF alloys are those based on the actinide metals thorium, uranium, neptunium and plutonium as alloys based on these elements have substantially depressed eutectic temperatures (figure 2.3).

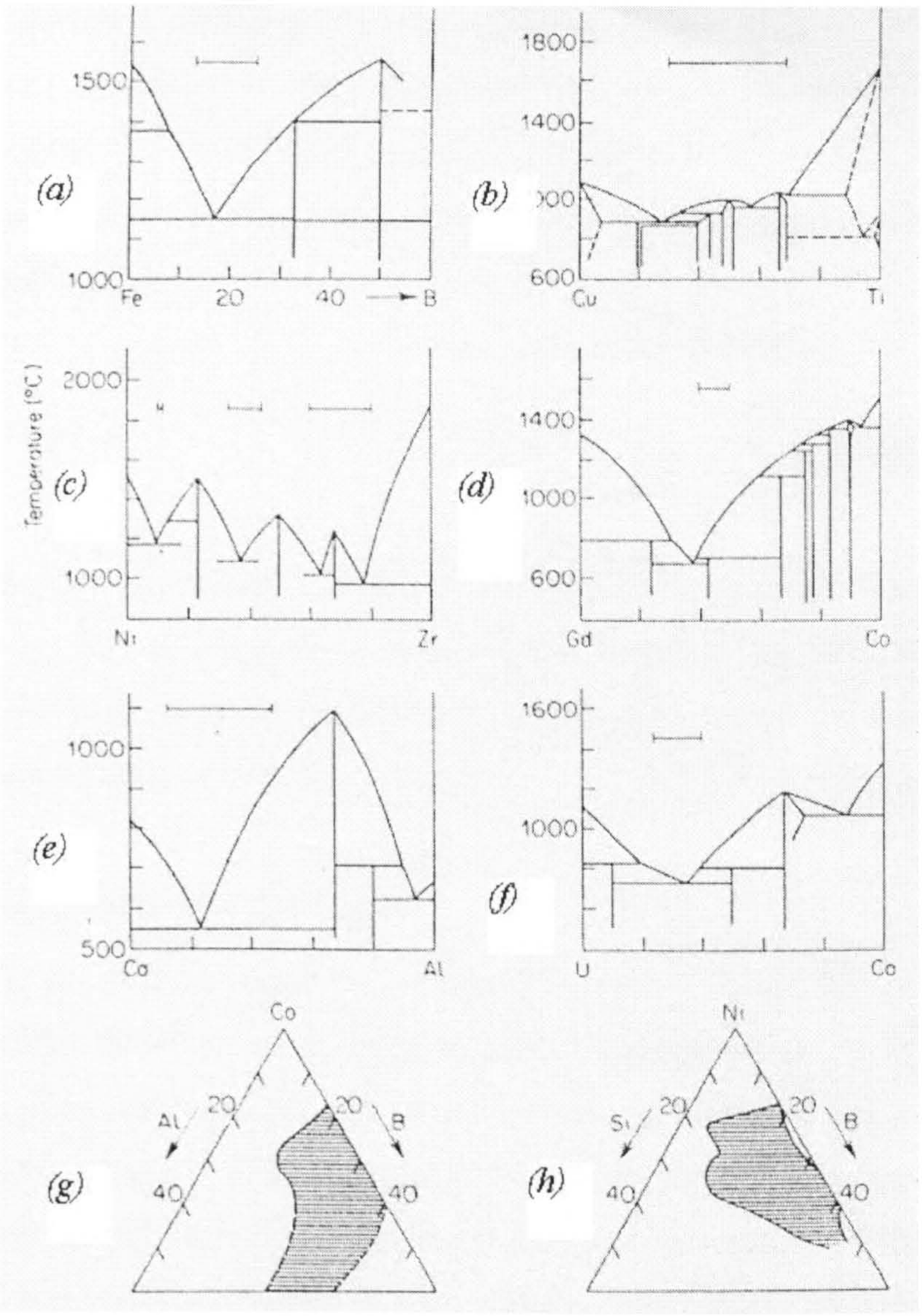

Figure 2.3. Some binary and ternary alloy systems showing the composition dependence of the liquidus temperature and the glass forming ranges to a cooling rate of about 10^6 Ks^{-1} [8].

2.2.3 Theories of Metallic Glass Formation

Since the first formation of an amorphous metallic alloy, several theoretical models of glass formation have been proposed; in this section some of them are briefly summarised.

Cohen and Turnbull

After the report of the formation of a metallic glass, in an Au-Si alloy [21], Cohen and Turnbull [22] noted that the eutectic temperature of the composition $Au_{75}Si_{25}$ alloy

was relatively low and located near the eutectic concentrations. They considered that these factors would be conducive to glass formation in a metallic system. Thus, the glass formation tendency was enhanced by the reduction in reduced melting temperature τ_m caused by adding silicon; the lower was τ_m the greater was the glass forming tendency. τ_m may be estimated using

$$\tau_m = \frac{kT_m}{h_v} \tag{2.1}$$

where h_v is the heat of vaporisation and k is Boltzmann's constant. The undercooling caused by the very high cooling rate of about 10^6 Ks^{-1} facilitated the glass formation in the alloy. They noted that the crystallisation temperature ~290 K was comparable with that expected for pure amorphous metals.

Bennett, Polk and Turnbull

Bennett *et al.* [23] discussed the role of composition in metallic glass formation. They proposed that the alloys most prone to glass formation would be those having the hardest atoms, where the repulsive part of the interatomic potential was steepest, i.e. the noble and transition metals. They also proposed that the alloys based on the noble and transition metals, *A*, with metalloid *B*, with the compositions mostly in the range A_5B to A_3B, were the most stable and easiest to form glasses. They considered that the host atoms form a Bernal dense random packed (DRP) structure [24], with the effectively smaller and softer *B* atoms filling the skeletal interstices and stabilising the random configuration. In many alloy systems, the size distribution of these interstices occurs in the range 15-25 at % *B*, which agrees experimentally with the range for easiest glass formation. This model however, is particularly applied to the formation of the TL-M metallic glasses. In some systems based on transition metals, the region of easiest glass formation falls well outside the range 15-25 at % *B* and, in some cases, the amount of *A* atoms is smaller than *B*.

Chen and Park

In contrast to the model of Bennett *et al.*, discussed above, Chen and Park [25] showed experimentally that the partial molar volumes of Si and Cu in Pd-Si-Cu glassy alloys were independent of composition in the easy glass forming range. They concluded

that the stabilities and formation of glassy alloys are dominated by chemical bonding considerations rather than by the hole filling of the DRP structure. Chen [26] later suggested that adding a second metallic component of different atomic size and strong atomic interaction enhanced the stability and formation of the glassy phase. However, although the melting temperature is often substantially reduced by the third element and the glass formation is improved, it is not clear that the stability of the glassy phase is increased, since T_g in many cases changes rather little.

Nagel and Tauc

Nagel and Tauc [27] considered the role played by the electron gas in influencing glass formation and stability in alloys. They proposed that the back scattering limit, $2k_f$, of the momentum transfer for the free electrons tends to coincide with q_p, the position in momentum space of the first peak of the structure factor, $s(q)$, the Fourier transform of the radial distribution function in glassy alloys. Correspondingly, the Fermi energy of the free electrons would also coincide with a dip in the density of states curve, so that the isotropic liquid state would have a lower energy than the incipient long range ordered state, in a single phase crystal. This approach would help to explain the deep eutectics that occur in the region of 20 at % metalloid in the transition metal-metalloid systems.

The theories of Polk, Chen and Park, and Nagel and Tauc are largely qualitative in approach and do not clearly explain the relative ease of glass formation and its dependence upon composition in alloy systems in general. The tendency to match high glass stability with easy glass formation leads to some confusion about the roles of various factors.

Davies, Aucote and Hull

In order to ensure that the behaviour of metallic glasses was clearly understood, Davies *et al.* [28] proposed that the formation and stability should be considered separately. The glass transition temperature, was taken as a measure of the thermal stability of the glassy phase. In most metallic systems, T_g has a relatively weak dependence upon composition, whereas in the case of transition metal-metalloid systems the minimum cooling rate to form the glassy phase in a given thickness is extremely sensitive to composition. The liquidus temperature for these systems has a high dependence on composition around the deep eutectics. Davies and co-workers proposed that the reduced

glass temperature, defined by T_g/T_m, would, in metallic systems, determine largely the glass forming ability, measured by the critical cooling rate for glass formation, R_c.

Structural or thermodynamic theories generally attempted to consider only whether a given material was or was not a glass former without regard for the imposed cooling rate. The R_c is the natural result of a kinetic approach to metallic glass formation by continuous cooling from the liquid state.

Sarjeant and Roy

Sarjeant and Roy [29] were the first to attempt to estimate theoretically the magnitude of R_c for various inorganic materials including a pure metal, Pb. R_c was assumed to be proportional to T_m and to the relaxation frequency of the structural units; the proportionality constant was determined using the estimated R_c for NaCl. Thus, it was shown that, in Ks^{-1}

$$R_c = 2.0 \, x \, 10^{-6} (T_m)^2 \frac{k}{v' \eta} \qquad (2.2)$$

where v' is the molecular volume (mol/m^3), η the dynamic melt viscosity ($Nm^{-2}s$) at T_m and k is Boltzmann's constant (1.3805×10^{-23} JK^{-1}). For most of the chosen materials, minimum values of R_c were in order of magnitude agreement with experimental observations. However, the predicted R_c for Pb of 10^8 Ks^{-1} is probably 2-3 orders of magnitude too low, even if it were possible to prevent spontaneous crystallisation in the glassy phase. However, with respect to the kinetics of avoiding crystallisation the temperature range just below T_m is relatively unimportant. This theory also has the disadvantage that no account was taken of T_g or the change in viscosity with decreasing temperature.

Turnbull

Turnbull [30] estimated quantitatively the conditions for glass formation by adopting simple nucleation theory and using the criterion for glass formation as being the avoidance of a single homogeneous nucleus. He proposed that the magnitude and temperature dependence of the steady state nucleation frequency, I_v, is determined by the melt viscosity

and its temperature dependence (determined by T_g/T_m) and by the magnitude of $(\alpha\beta)^{1/3}$ where α and β are dimensionless parameters given by:

$$\alpha = \left(Nv^2\right)^{1/3} \cdot \sigma / \Delta H_f \tag{2.3}$$

$$\beta = \Delta S_f / R \tag{2.4}$$

where N is the Avogadro's number, v is the molar volume of the crystal, ΔS_f is the molar entropy of fusion and σ is the liquid/crystal interfacial energy. $(\alpha\beta)^{1/3}$ was found to be ~1/2 for simple monatomic substances such as metals and their alloys. For such a melt the temperature dependence of I_v for various values of T_g/T_m was determined (with η at T_m equal to 10^{-2} Poise). Hence, only liquid droplets containing less than 1,000 atoms could be quenched to a glass for $T_g/T_m = 0$, whereas glass formation was easy for $T_g/T_m = 2/3$. For $T_g/T_m = 1/2$ at an imposed cooling rate of 10^6 Ks^{-1}, droplets less than 60 μm diameter could be chilled to a glass.

Uhlmann

Uhlmann [31], adopting the classical treatment of solid state transformation kinetics [32], related the fraction of transformed phases (crystal in this case) to the homogeneous nucleation frequency, the growth rate and the time. Time-Temperature-Transformation curves were constructed for a barely detectable fraction of crystal (10^{-6}) by using accepted theories of homogeneous nucleation and crystal growth and measured or estimated data for the liquid viscosity between T_m and T_g. The parameter R_c was given by the cooling rate required just bypassing the nose of this curve. For a wide range of substances the cooling rate experimentally obtained was in satisfactory agreement with the curves. Davies and co-workers [11, 28, 33] showed later that this kinetic approach gave satisfactory predictions of R_c for a number of metallic glasses. All the metallic systems were subsequently generalised with this treatment with satisfactory results taking into account the assumptions and uncertainties involved.

Vreeswijk

Nucleation transient times and an adopted criterion for glass formation (the avoidance of a single critical homogeneous nucleus per cm^3) were used by Vreeswijk *et. al.* [34] and thus not requiring consideration of crystal growth. For three of the four metals chosen, the estimates of R_c (Au 10^8, Cu 10^9 and Pb 10^{10} Ks^{-1}) were similar, in view of the uncertainties, to those derived for Ag and Ni by Uhlmann [31] and Davies [28] respectively. For Sn (10^2 Ks^{-1}) the predicted value was, however, inexplicably very low. They assumed an Arrhenius behaviour of the viscosity below T_m for most of the materials; although this would not introduce a substantial error for pure metals, where T_g/T_m is low, it is not a correct assumption in the general case. Since T_g/T_m determines the rate at which the viscosity rises with decreasing temperature below T_m, account should be taken of its magnitude, which in turn influences the nucleation frequency.

Shingu and Ozaki

Shingu and Ozaki [35] attempted to estimate the condition required to form glassy pure Al from the liquid state considering the solidification rate in rapid conduction cooling. They determined the heat flow condition for olid-liquid interface motion by comparing its transfer rate calculated from a heat flow balance, with the kinetically determined crystal growth rate, finding that the latter was exceeded by the former. Subsequently [36] R_c was estimated to be 10^{12} Ks^{-1}. The crystal growth rate was, substantially overestimated because they assumed that the liquid viscosity followed an Arrhenius relation to 800 K undercooling below T_m and, moreover nucleation kinetics were not considered. Since the heat flow calculations did not involve the removal of latent heat of solidification, this theory would seem to be of limited value in predicting glass formation.

Zielinski and Matyja

The effects of clustering in the liquid state on the glass forming tendency for tellurium based alloys, through its influence on the interdiffusion constant and on the concentration of critical nuclei, were estimated by Zielinski and Matyja [37]. It was concluded that clusters promote glass formation and that the theoretical glass forming tendency was in agreement with the experimentally observed glass forming regions for a number of Te based systems. However, glass forming tendency, or the experimental criterion of glass formation, were not given clear quantitative definitions in this work.

Donald and Davies

The prediction of glass forming ability for metallic systems proposed by Donald and Davies [38] is based on:

$$\Delta T^* = \frac{T_l^{mix} - T_l}{T_l^{mix}} \tag{2.5}$$

where T_l^{mix} is a simple rule of mixture liquidus temperature, being $T_l^{mix}=T_m^A x_A+T_m^B x_A$, where T_m^A and T_m^B are the melting points of the pure elements, in a simple eutectic binary $A_{xA}\,B_{xB}$, in their normal isolated state. Hence

$$\frac{\Delta T}{T_l^{mix}} = \frac{T_l^{mix} - T_l}{T_l^{mix}} = \Delta T^* \tag{2.6}$$

This equation can also be used for multicomponent alloys, assuming

$$T_l^{mix} = \sum x_i T_m^i \tag{2.7}$$

where x_i and T_m^i are the mole fraction and melting point respectively of the ith component of an n-component alloy.

By using equation 2.6 a rapid (but approximate) assessment of the GFA of novel alloys may in general be obtained simply from a knowledge of the melting points of the pure components and the liquidus temperature of the alloys. For instance, at $\Delta T^* \sim 0.2$ lies the boundary between glass formers and non-glass formers (at a cooling rate $< 10^7$ Ks^{-1}) – see table 1a of reference 38-. The large majority of the glass formers have values < 0.2. However, from a quantitative viewpoint, if it is considered that as ΔT^* increases the GFA should improve, a few notable contradictions exist, markedly binary and ternary alloys based on Au and Pt which calculations predicted to be very readily glass forming, while experimental results suggested otherwise.

Davies

In order to obtain a more general kinetic model for glass forming, Davies [8, 11] adopted the Johnson-Mehl and Avrami treatment of transformation kinetics for homogeneous nucleation. In this case, assuming that the crystal volume fraction, X, is small the volume fraction formed at time t, is:

$$X \cong \frac{\pi}{3} I_v \cdot u_c^3 \cdot t^4 \tag{2.8}$$

where I_v is the volume nucleation frequency and u_c the crystal growth rate. Assuming the Hoffman free energy model, I_v can be expressed as:

$$I_v = \frac{D_n \cdot \overline{N}_v}{a_o^2} \exp\left(-\frac{1.07}{\Delta T_r^2 \cdot T_r^3}\right) \tag{2.9}$$

where D_n is the atomic diffusion coefficient across the liquid and nucleus interface, a_o is the mean atomic diameter, $\overline{N}_v$ is the average volume concentration of atoms, ΔT_r is the reduced undercooling $(T_l - T)/T_l$, and T_r is the reduced temperature T/T_l and T_l is the equilibrium melting or liquidus temperature. The crystal growth velocity is given by:

$$u_c = \frac{f \cdot D_g}{a_o}\left[1 - \exp\left(-\frac{\Delta T_r \cdot \Delta H_f}{RT}\right)\right] \tag{2.10}$$

where f is the fraction of sites at the crystal-liquid interface where growth can occur (= 1 for close packed crystals and 0.2 ΔT_r for faceted crystals) and D_g is the diffusion coefficient at the crystal-liquid interface.

It was assumed for this purpose that transformation is to a single phase; then, $D_n = D_g = D$, where $D = kT/(3\pi a_o \eta)$.

Thus, substituting equations 2.10 and 2.9 in equation 2.8, the time, t, to achieve a small fraction of crystals, X, is given by:

$$t \sim \frac{9.3\eta}{KT}\left[\frac{\frac{a_o^9 X}{f^3 \cdot \overline{N}_v}\left\{\exp\left(\frac{1.07}{T_r^3 \cdot \Delta T_r^2}\right)\right\}}{\left\{1-\exp\left(-\frac{\Delta T_r \cdot \Delta H_f}{RT}\right)\right\}^3}\right]^{1/4} \tag{2.11}$$

If the temperature dependence of η can be estimated below T_m, then using equation 2.11, a time-temperature-transformation (T-T-T) curve can be constructed expressing the time to form a very small, barely detectable fraction of crystal (X=10^{-6}) as a function of temperature, (figure 2.4). The shape of this curve results from the competition between the driving force for crystallisation, that increases as the undercooling increases, and the atomic mobility which decreases with increasing undercooling. Thus, at temperatures just below T_m and at low temperatures, approaching T_g the times to achieve X are very long while at the nose of the curve, I_v and u_c are both relatively high, resulting in relatively short times. The basis for formation of a glass is the avoidance of this 10^{-6} fraction of crystal, uniformly distributed in an amorphous matrix.

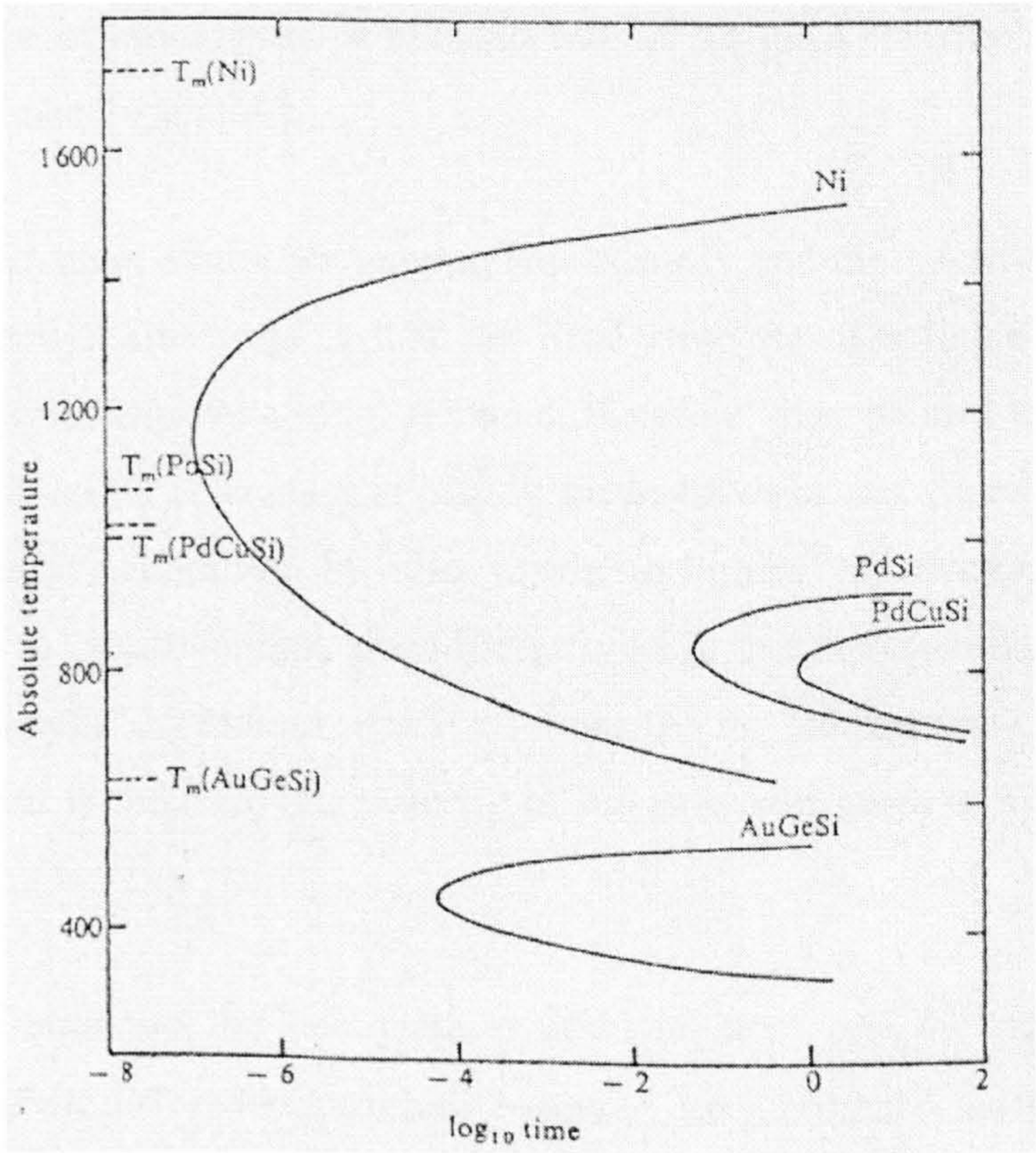

Figure 2.4. Time-temperature-transformation curves corresponding to a fraction crystal of 10^{-6} [11].

R_c can now be approximated by the linear cooling curve required just to avoid the nose of this T-T-T curve and is given by

$$R_c \sim \frac{T_m - T_n}{t_n} \tag{2.12}$$

where T_n and t_n are the temperature and time corresponding to the nose of the curve, respectively.

Egami

More recently, Egami [39] reported that the interactions between atoms are sufficiently simple to allow widely applicable common descriptions of the phenomena, since the metallic bonding is essentially a central force isotropic bonding described, to a large extent, by a relatively simple model.

While both glasses and liquids of metallic alloys are basically described by the dense random packing (DRP) model, the structure of a liquid is more random. As a liquid is cooled, the degree of randomness is reduced and, at the glass transition, the topological randomness becomes frozen [39].

In the liquid state, atoms are moving continuously and the microscopic structure is changing incessantly. This implies that the local structure of a liquid is topologically unstable and continuously collapsing. A liquid, therefore, may be said to be in a state of self-organised criticality. A contact is readily made between this situation and the local topological instability condition. In other words, in liquids, the fluctuation in the local density, and thus the local volume, are sufficiently large that the instability condition must be met at a majority of the atomic sites at all times. As the temperature is reduced and the volume fluctuation is reduced, the majority of the sites will become subcritical, and the structure freezes.

In the DRP structure, the local pressure at the *ith* atom, $p(i)$, the local volume strain, $\varepsilon_v(i) = p(i)/B(i)$ where $B(i)$ is the local bulk modulus, has a normal (Gaussian) distribution. When the root mean square (rms) value of the local volume strain:

$$e_v = \left\langle \varepsilon_v^{\,2}(i) \right\rangle^2 \tag{2.13}$$

is equal to ε_v^{crit}, the change in the volume assigned to each atom at the critical condition (~6.4% = 0.064). Because of the nature of the Gaussian distribution, 15% of the sites have the local ε_v value exceeding ε_v^{crit}. Now this fraction, 15%, happens to correspond to the percolation concentration for the close-packed structure [40]. If the concentration of the sites with free volume is less than the percolation concentration, they will be locally contained, but if it is above the percolation concentration, macroscopic flow of matter will take place, and the system will behave as a liquid. The glass transition therefore takes place when $e_v = \varepsilon_v^{crit}$ and, in the glassy state at $T = 0$ K, this condition is maintained. Indeed the value of e_v calculated for the DRP model is 0.065 [41].

The temperature dependence of e_v can be calculated as

$$e_v = \frac{k \cdot T}{2\langle \Omega \rangle \langle B \rangle} \tag{2.14}$$

where $\langle \Omega \rangle$ is the average local volume. From this the following expression for the glass transition temperature, is obtained:

$$T_g = \frac{2\langle \Omega \rangle \langle B \rangle}{k} \left(\varepsilon_v^{\,crit} \right)^2 = 6.14 x 10^{-3} \frac{\langle \Omega \rangle \langle B \rangle}{k} \tag{2.15}$$

This yields T_g values that agree well with those found experimentally for metallic glasses, for example $Fe_{40}Ni_{40}P_{14}B_6$ [42, 43].

During the quenching of a melt, what determines the glass formation is the stability of the nucleus. If the nucleus can be readily formed, as in the case of a monatomic solid, crystallisation would take place unless the quenching rate is of atomic scale, i.e. 10^{12} K s^{-1} [39]. When the nuclei are difficult to form, crystallisation would take place only after segregation into phases in which nuclei are easily formed. The ease of nucleation must be determined by the transformation strain, $\varepsilon_v^{\,T}$, being subcritical, since otherwise the nearest

neighbour arrangement consistent with the crystalline order, such as 13 atom cluster to form an f.c.c. structure, would not be stable. This leads to the condition:

$$c_A^{crit} \frac{|\Delta\Omega|}{\Omega_B} = 2\varepsilon_v^{crit} = 0.1 \tag{2.16}$$

where c_A^{crit} is the critical concentration of element A for amorphization; $\Delta\Omega = \Omega_A - \Omega_B$; Ω_A and Ω_B are the local volume of elements A and B (matrix), respectively.

2.3 Processes for obtaining metallic glass filaments

The main processes for producing amorphous alloys employed today are those used for casting ribbon and wire forms.

2.3.1 Ribbon filaments

Among the methods to obtain ribbons are the solid chill block processes which are subdivided into *a*) the melt extraction processes (MEP), that include crucible melt extraction and pendant drop melt extraction [44], and *b*) the chill block melt spinning processes (CBMS), which include free jet spinning and planar flow casting (PFC). Both MEP and CBMS have the characteristic of extracting melt from a stagnant or effectively stagnant source by a chill wheel moving at a very high velocity, typically ~20 ms^{-1}.

For MEP, when the molten metal is contained in a crucible, the process is known as crucible melt extraction, (figure 2.5) [44], and when the source of the molten metal is introduced under the action of surface tension/gravity, the process is referred to as pendant drop melt extraction, (figure 2.6). Both processes were originally intended for production of steel fibres, but they have the advantage that a variety of alloys can be produced. The magnitude of the cooling rate can vary from 10^3 to 10^6 Ks^{-1}, depending on product thickness and the velocity of the disk.

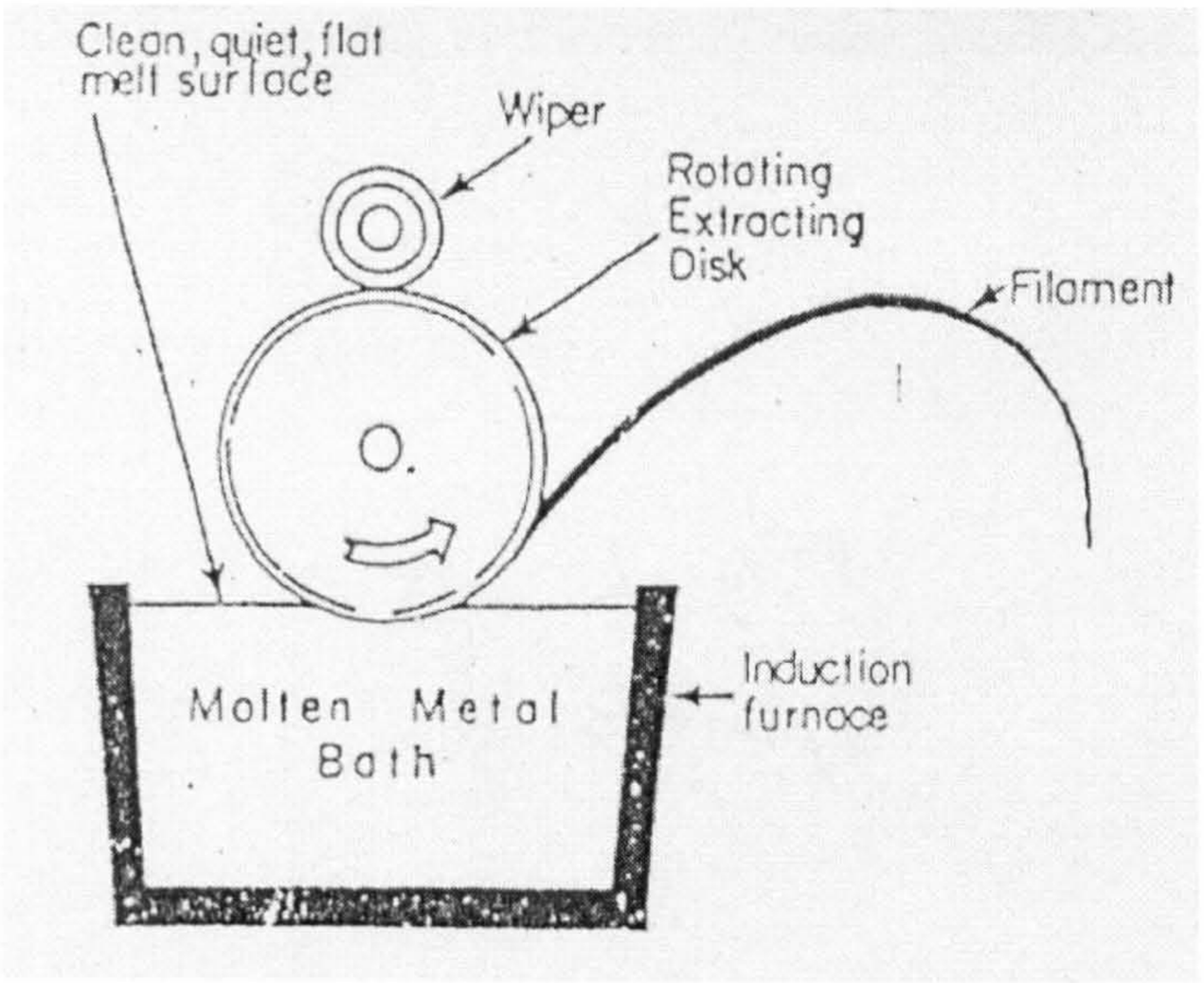

Figure 2.5. Schematic illustration of the, "crucible melt extraction" process [44].

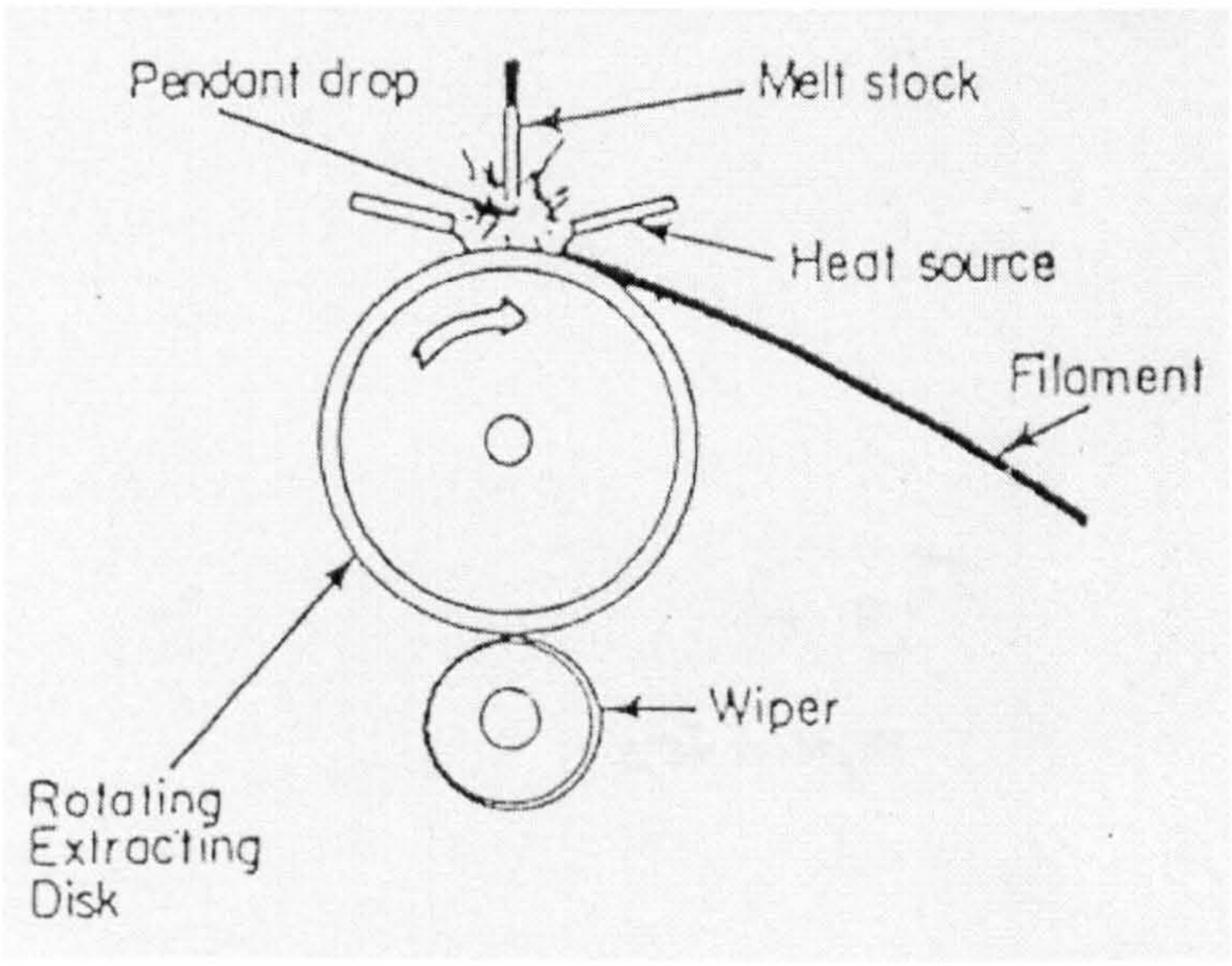

Figure 2.6. Schematic illustration of the "pendant drop extraction" process [44].

In CBMS the material is melted in a crucible and the molten alloy is ejected through a small orifice by gas pressure, generally argon. The free jet of molten metal impinges on the surface of the rapidly rotating wheel where the melt solidifies and ribbon is formed, (figure 2.7(*a*)). On the other hand, the PFC process [45] which is an improved CBMS technique, uses a slotted nozzle orifice maintained very close to the substrate. The resultant ribbon is more uniform because the mechanical constraint of the melt puddle by the

crucible nozzle stabilises it, allowing the casting of wider ribbons equal to the slot width (figure 2.7(*b*)).

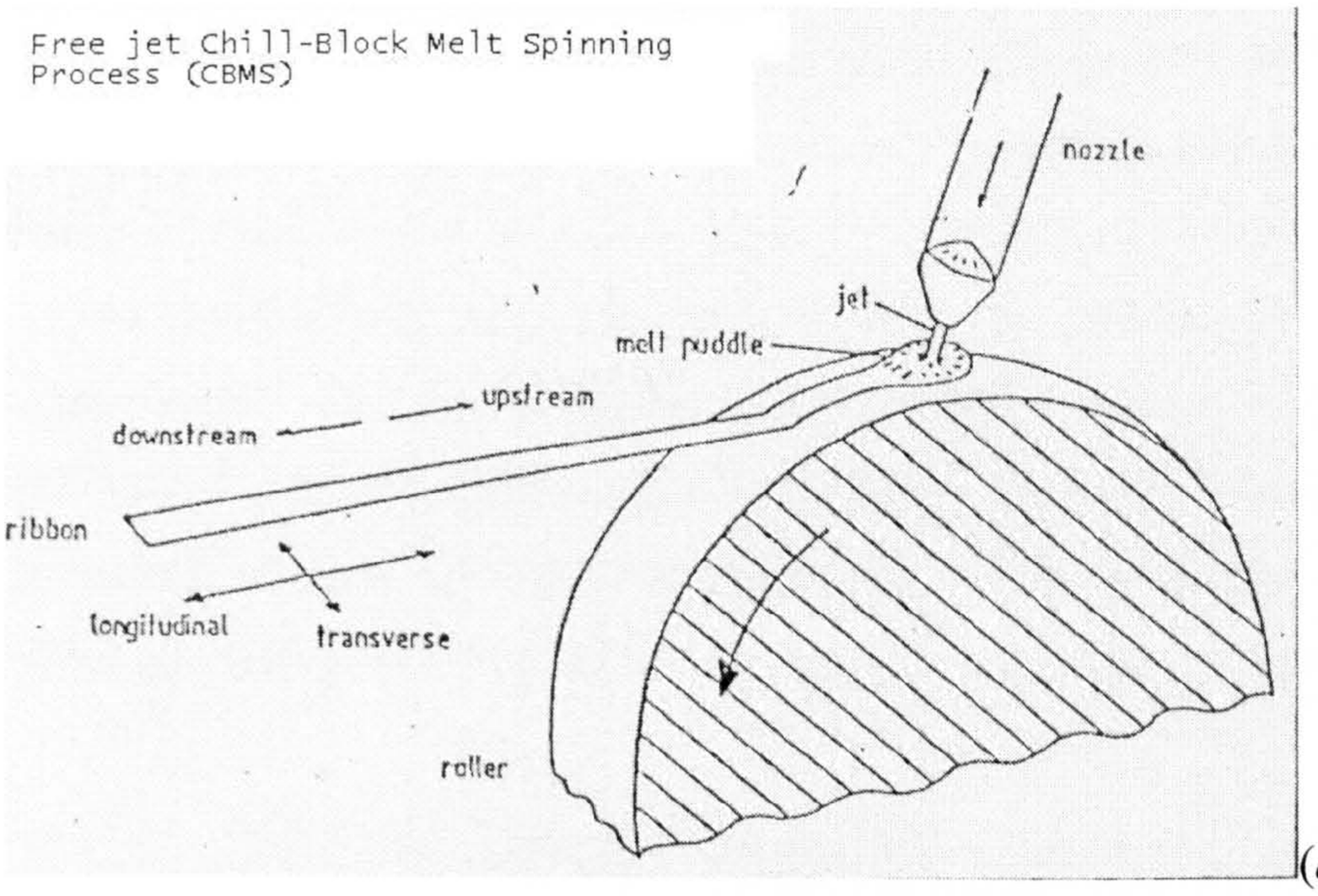

(*a*)

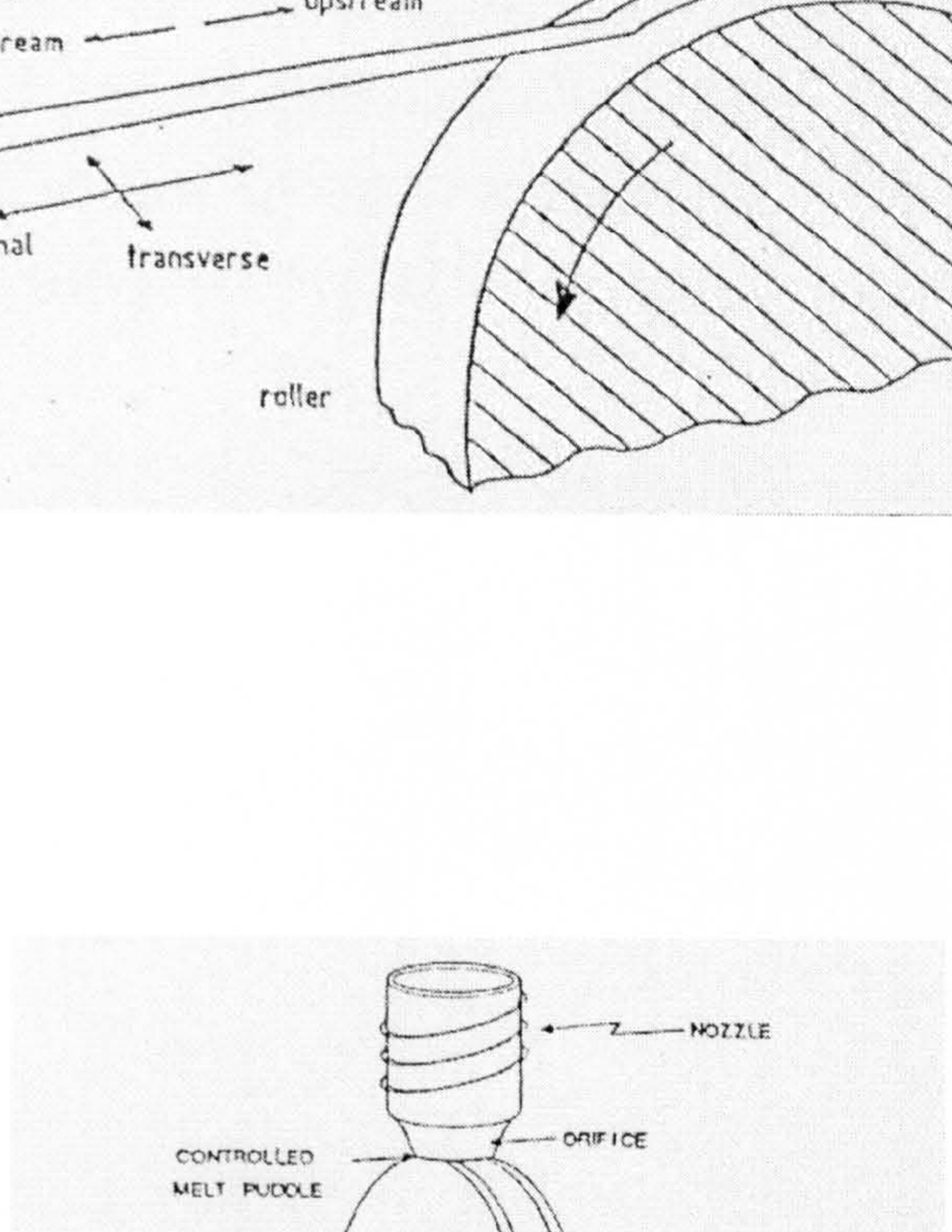

(*b*)

Figure 2.7. Schematic illustration of the (*a*) free jet chill block melt spinning process, and (*b*) planar flow casting process.

2.3.2 Wires

The first method for producing wires directly from the melt was proposed in 1882 and exploited by *Small* [46]. This process produced wire solder by ejection of molten lead-tin alloy through a nozzle into a tank of stagnant liquid, (figure 2.8). In 1924, Taylor developed a process known as the *Taylor Wire Process* [44], for producing very small diameter metallic filament. As can be seen in figure 2.9, metal is melted and encapsulated in a stable viscous sheath of a silicate glass that is drawn down continuously and solidified to form a coated filament. This fibre is circular in cross section and its surface is smoother than filaments from the solid chill process. This process was shown subsequently to be capable of quenching alloys at a cooling rate in the range of 10^3 to 10^5 Ks^{-1}. Fe- and Ni-based amorphous filaments was reportedly cast in diameters ranging from 4 to 12 μm.

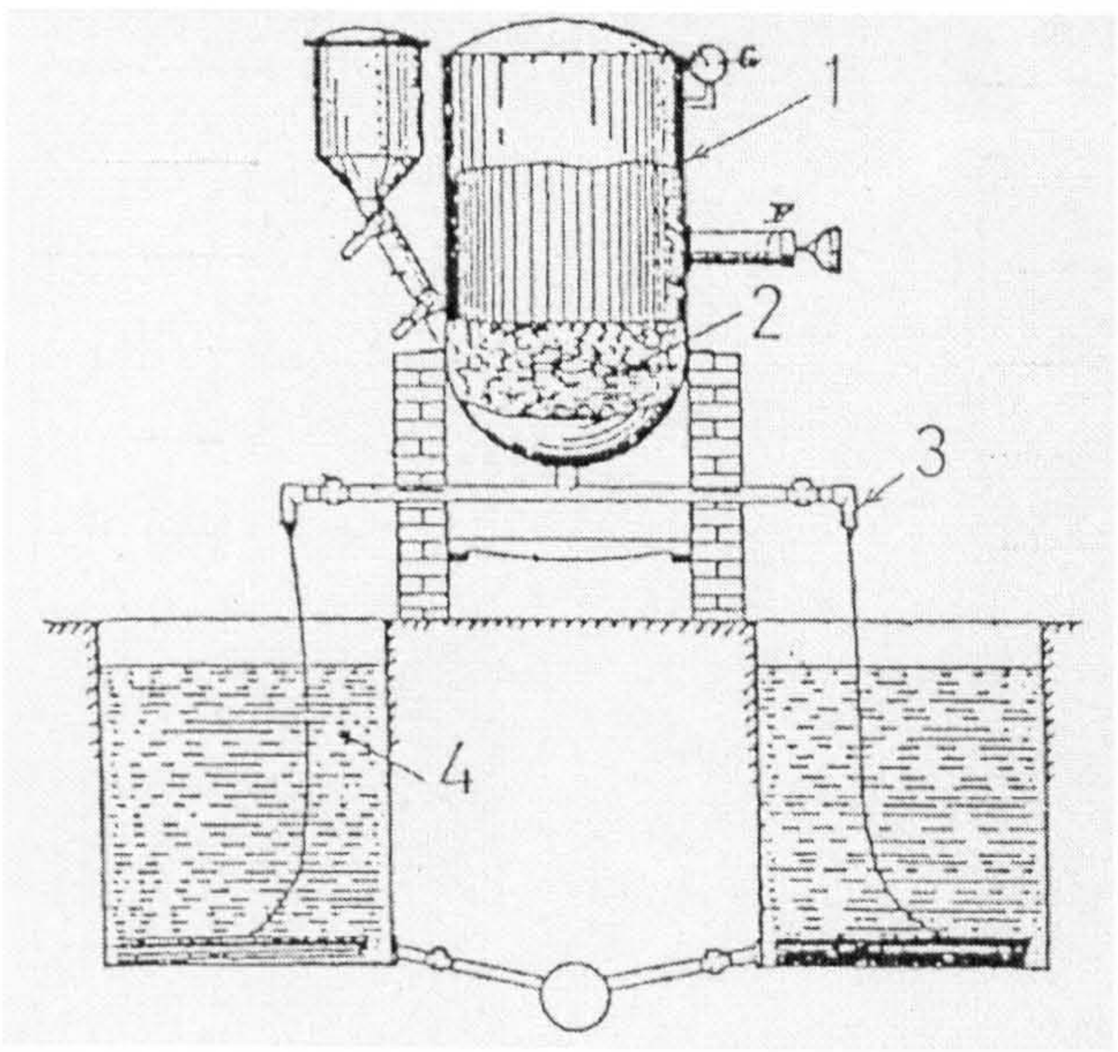

Figure 2.8. Schematic illustration of Small's method of wire casting, (1) solder tank, (2) molten solder, (3) nozzle, and (4) water tank [46].

Leghorn [47] proposed the stream casting technique in 1969 (figure 2.10). In this process, liquid metal is ejected into a flowing liquid medium. In contrast to the Small process, this method maintains close control over melt jet stability. However, these three processes were not specifically designed for rapid solidification and generally are not suitable for producing amorphous metallic filaments with a wide range of compositions and glass forming abilities.

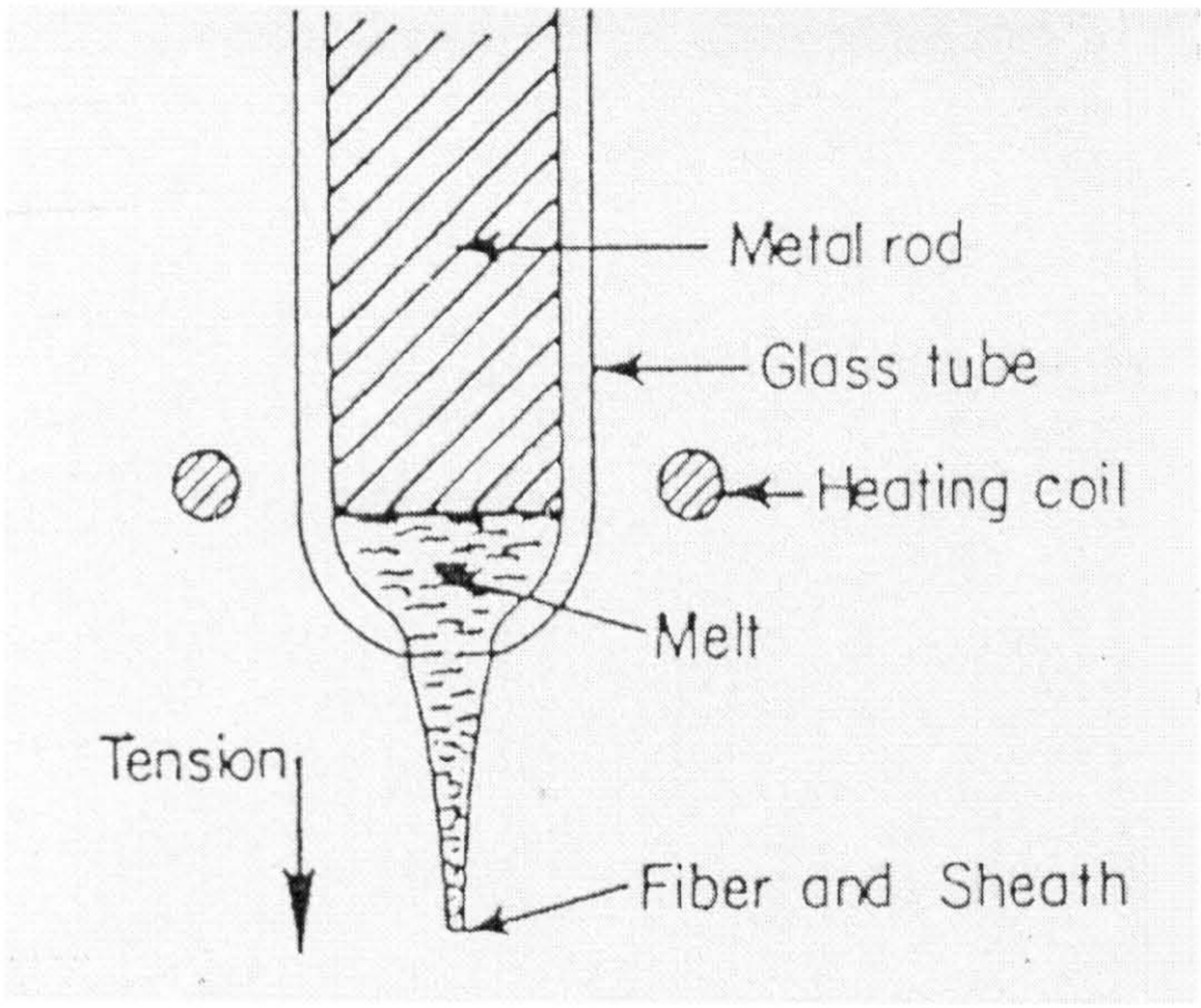

Figure 2.9. Schematic illustration of the Taylor wire process for glass coated melt spinning [44].

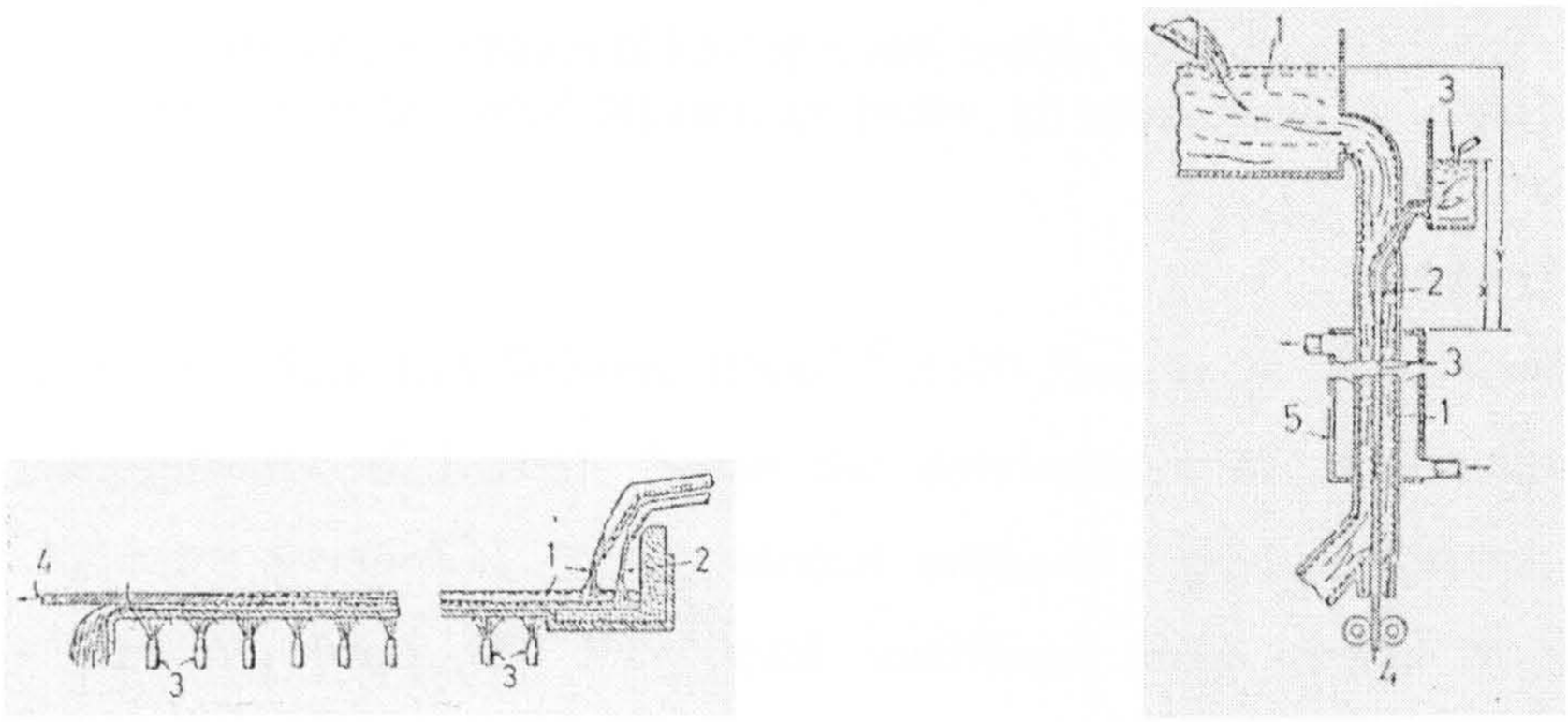

(*a*) (*b*)

Figure 2.10. Schematic illustration of Leghorn's method, (*a*) Stream casting into flowing, (1) molten metal, (2) liquid coolant, (3) spray nozzle, and (4) solidified metal; (*b*) Stream casting in flowing liquid, (1) liquid coolant, (2) nozzle, (3) molten metal, (4) solidified metal, and (5) coolant medium [47].

Kavesh [48] proposed a method where a melt jet is ejected within a tube into a confluent stream of chilled cooling water driven by the force of gravity, (figure 2.11). This process was shown to be capable of producing amorphous and microcrystalline filaments. Ohnaka and co-workers, however, reported difficulty in consistently producing round

section samples by this process, because of jet disturbance due to the turbulence at the confluence.

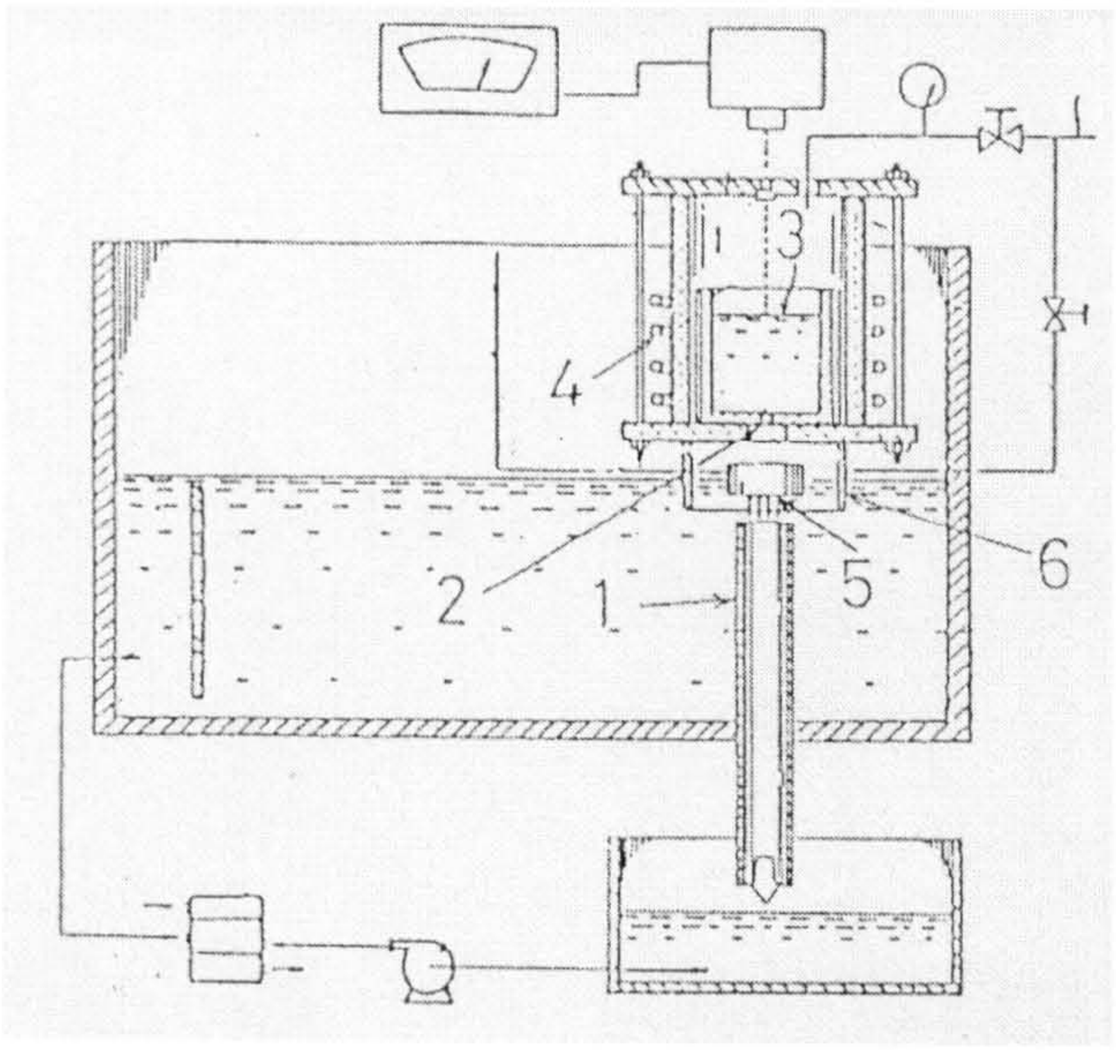

Figure 2.11. Schematic illustration of Kavesh's wire casting technique, (1) quartz stand pipe, (2) nozzle, (3) molten metal, (4) induction heater, (5) sparger, and (6) vortex baffle [48].

Rotating Water Bath Melt Spinning (INROWASP) *Process*. In 1971, Ohnaka and co-workers, independently of Kavesh, began the development of other melt spinning processes for wire production, trying various methods including ejection into the atmosphere and into water [4]. They used centrifugal force instead of gravity or mechanical forces in order to achieve completely controlled laminar flow of the coolant and molten metal; figure 2.12 shows a schematic illustration of this equipment [49]. It uses an induction coil which melts metal in a quartz crucible; once the metal is molten it is ejected by pressured inert gas, usually argon, through the nozzle into the cooling layer of water formed by centrifugal force on the inner surface of a rapidly rotating drum. Drum rotation controls the coolant speed, while ejection pressure controls the molten jet velocity. Continuous wires with smooth surfaces are obtained under the correct casting conditions. The process parameters such as nozzle material and nozzle diameter, distance between the nozzle tip and the coolant surface, ejection angle, depth of the coolant layer, coolant temperature, cooling rates, heat transfer [4, 50], and melt jet - water velocity ratio [4, 51], have been discussed. With this technique it has been possible to produce continuous amorphous structured wires in the following alloy systems: Ni-Pd-P [52], Ni-Pd-Si [52],

Ni-Si-B [53], Ni-P-B [53], Pd-Cu-Si [49], Fe-Si-B [5-7, 54, 55], Fe-P-C [56], Fe-Si-RE (rare earth) [57], Co-Si-B [58], Co-M-Si-B [58] and Metal-Zirconium [59] (Metal = Cu, Cu-Nb and Cu-Ta) and crystalline wires for the alloys in the following systems: Ni-Al-Fe [60], Mn-Al-C [61], Fe-Ni-Cr-Al [62], Fe-Mn-Al-C [63], Fe-Mn-Cr-Al-C [64], Fe-Ni-Si-C [62] and Fe-Ni-Cr-Si-C [65].

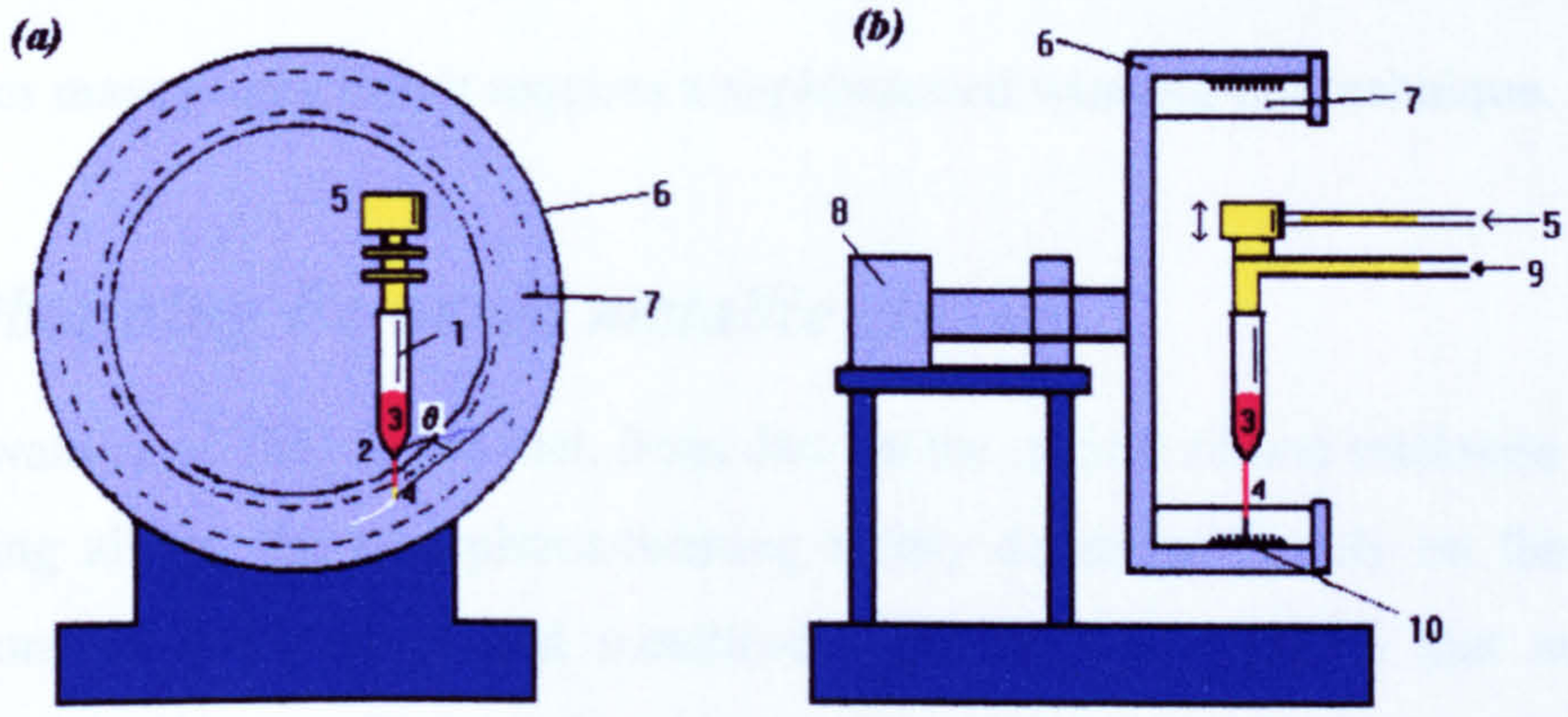

Figure 2.12. Schematic illustration of the rotating water bath melt spinning process.

Ohnaka [4], has discussed some advantages and disadvantages of producing high strength wire by his so-called INROWASP process; these can be summarised as follows:

***Advantages*:**

a) It can produce wires with round cross sections.

b) It is a rapid solidification process that can produce metastable phases.

c) The wire is cooled rapidly down to room temperature.

d) It can produce small diameter wires in compositions which are difficult to draw down by conventional methods

e) It can use liquids effective for coating the wire product as well as for cooling (e.g. cyclohexanol or hexilenglycol to prevent oxidation of Pb-Bi).

***Disadvantages*:**

a) It requires carefully planned process control because of the unstable free jet flight, prior to entry into the coolant bath (the vulnerable length).

b) There are approximate limits on the ranges of melt temperature (lower than 1400 °C) and wire diameter (between 80 and 250 μm) that can be handled.

c) For mass production it requires a sophisticated winding-out technique.

2.3.3 Obtaining Fe-based metallic glasses

Hagiwara *et al.* [66] found that, from data on the critical ribbon thickness for several glass forming alloys, the amorphous-forming ability depended largely on the types and concentrations of base metals and metalloid elements. They argued that most of the previous investigations made up to that time had focused only on the composition range of the formation of an amorphous phase and there were hardly any systematic data on the maximum ribbon thickness obtained at a given imposed cooling rate.

They measured the critical ribbon thickness where a crystalline particle was first observed by optical microscopy for the Fe-Si-B, Co-Si-B and Ni-Si-B ternary glassy alloys. They found that the largest critical thickness was located near the centre of their amorphous-forming regions and that it decreased with increasing or decreasing silicon and/or boron. The compositional dependences of the maximum ribbon thickness for the formation of an amorphous single phase for these systems are illustrated in figure 2.13.

The easiest amorphous-forming ability in each alloy system was located around a total metalloid content of about 25 at% and the ratios of boron to silicon were in the range of 1.2 – 2.0. The maximum values of critical thickness were obtained around 15 at% of boron.

It was estimated that the samples with the maximum ribbon thickness were cooled at rates of $7x10^4$ for $Fe_{75}Si_{10}B_{15}$, $2x10^5$ for $Co_{72.5}Si_{12.5}B_{15}$ and $8x10^4$ Ks^{-1} for $Ni_{75}Si_8B_{17}$.

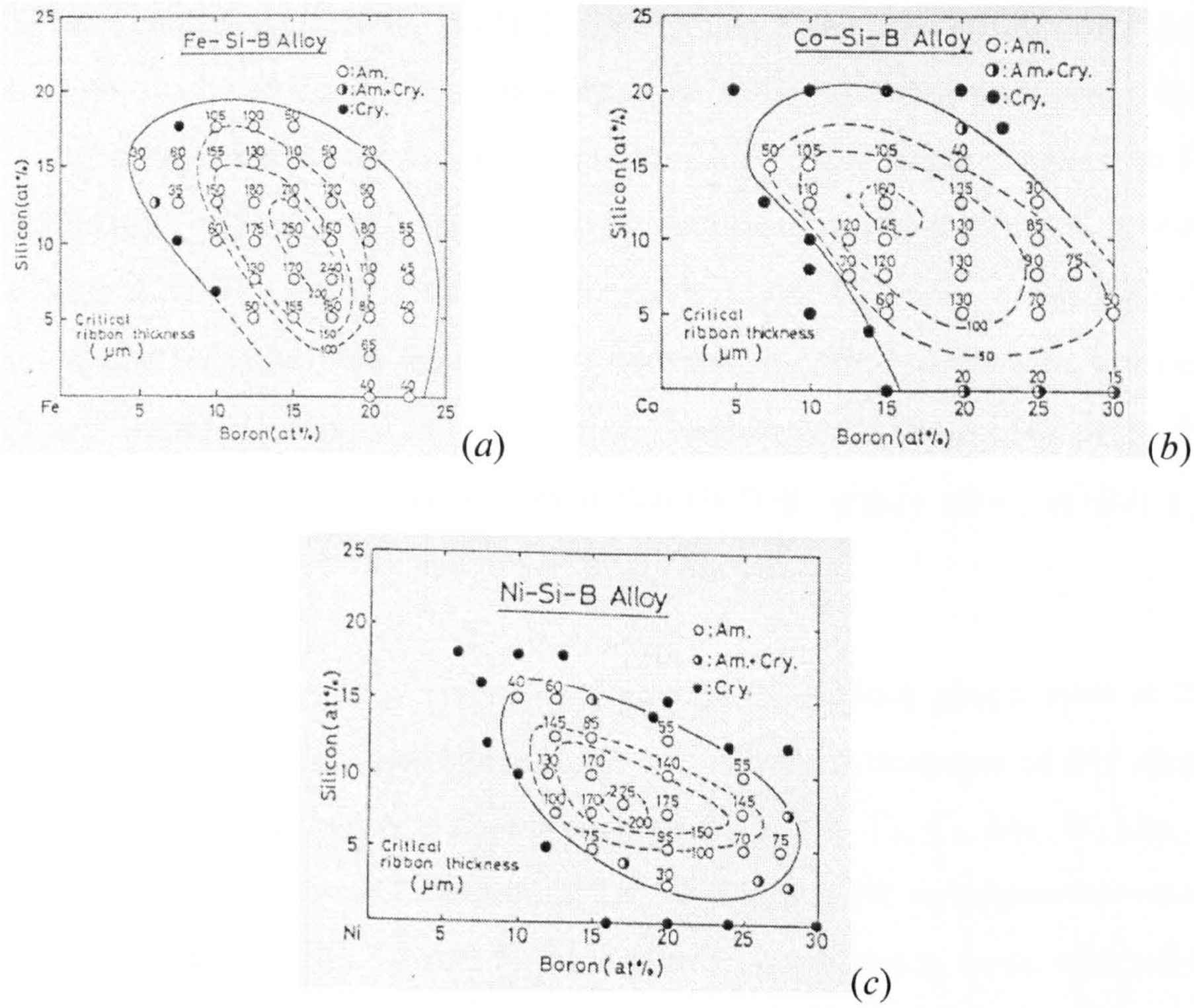

Figure 2.13. Composition ranges and critical ribbon thicknesses for the formation of and amorphous single phase in (*a*) Fe-Si-B, (*b*) Co-Si-B, and (*c*) Ni-Si-B ternary alloys [66].

Hagiwara *et al.* also investigated the effects of metalloid composition on the critical ribbon thickness for the formation of the amorphous phase for $Fe_{80}M_{20}$ (M = P, B, Si and C). The critical thickness increased in the order of Fe-P-Si < Fe-B-C < Fe-B-P < Fe-Si-B < Fe-P-C. It was observed that Fe-P-C and Fe-Si-B had much greater glass forming ability compared with the other alloys and the same tendency was recognised for $Fe_{75}M_{25}$ alloys. In addition, they considered that the remarkable enhancement in the glass forming ability located in the vicinity of about 14 at% phosphorous and boron (with C and Si contents respectively) was because these elements lowered the melting points of the alloys and increased rapidly the temperature coefficient of viscosity of the melt. In addition, the simultaneous dissolution of phosphorus and carbon or boron and silicon led to an increase in the negative heat of formation in the liquid state and to an increase in their glass transition temperatures. This investigation demonstrated that Fe-Si-B and Fe-P-C alloys possessed much higher amorphous-forming tendency than other Fe-based alloys

The first studies undertaken to obtain information about the wire forming ability for Fe-Si-B alloys were carried out by Hagiwara *et al.* [54]. As stated previously, they first measured the critical sample thickness for the formation of an amorphous phase in Fe-Si-B alloy ribbons [66], which is necessary for the production of amorphous wires. It was found that the largest value of the critical thickness is about 250 μm, around $Fe_{75}Si_{10}B_{15}$ composition, and the value near the boundary between amorphous and crystalline phases is about 20 μm, indicating a marked composition dependence of amorphous phase-forming ability (figure 2.13(*a*)). These results showed that Fe-Si-B ternary alloys exhibit a greater amorphous phase forming ability than Fe-B binary alloys.

Since the $Fe_{75}Si_{10}B_{15}$ alloy ribbon exhibited an amorphous phase, even at 250 μm thickness, they also examined the change in the critical ribbon thickness of this alloy when replacing iron by various transition metals such as Zr, V, Nb, Ta, Cr, Mo, W, Mn, Co, Ni or Al. It was found that a small amount of Ta, W, Mo and Nb enhances the amorphous phase-forming tendency, that Co and Ni hardly have an influence, even with substantial additions; and that Cr, V, Mn, Zr and Al significantly decrease it.

Hagiwara *et al.* [54] reported that the iron-based amorphous wires produced in the rotating water bath melt spinning process exhibit a good uniformity of shape, indicating the high stability of the molten jet in rotating water. However, they also reported that in general, it is difficult to form continuous metallic wires by melt quenching methods because of the inherent instability of a jet, due to the low viscosity and high surface tension typical of molten metal jets. Hence, the melt spinning condition must be adjusted by trial and error, based on close examination of the wires spun.

Figure 2.14 [54] shows the maximum diameter for the formation of an amorphous wire of some Fe-Si-B alloys. Around $Fe_{75}Si_{10}B_{15}$, the largest diameter value was found to be about 270 μm, and this tended to decrease with silicon and boron contents away from the optimum values. This compositional dependence agreed well with that of the critical ribbon thickness, seen in figure 2.13(*a*).

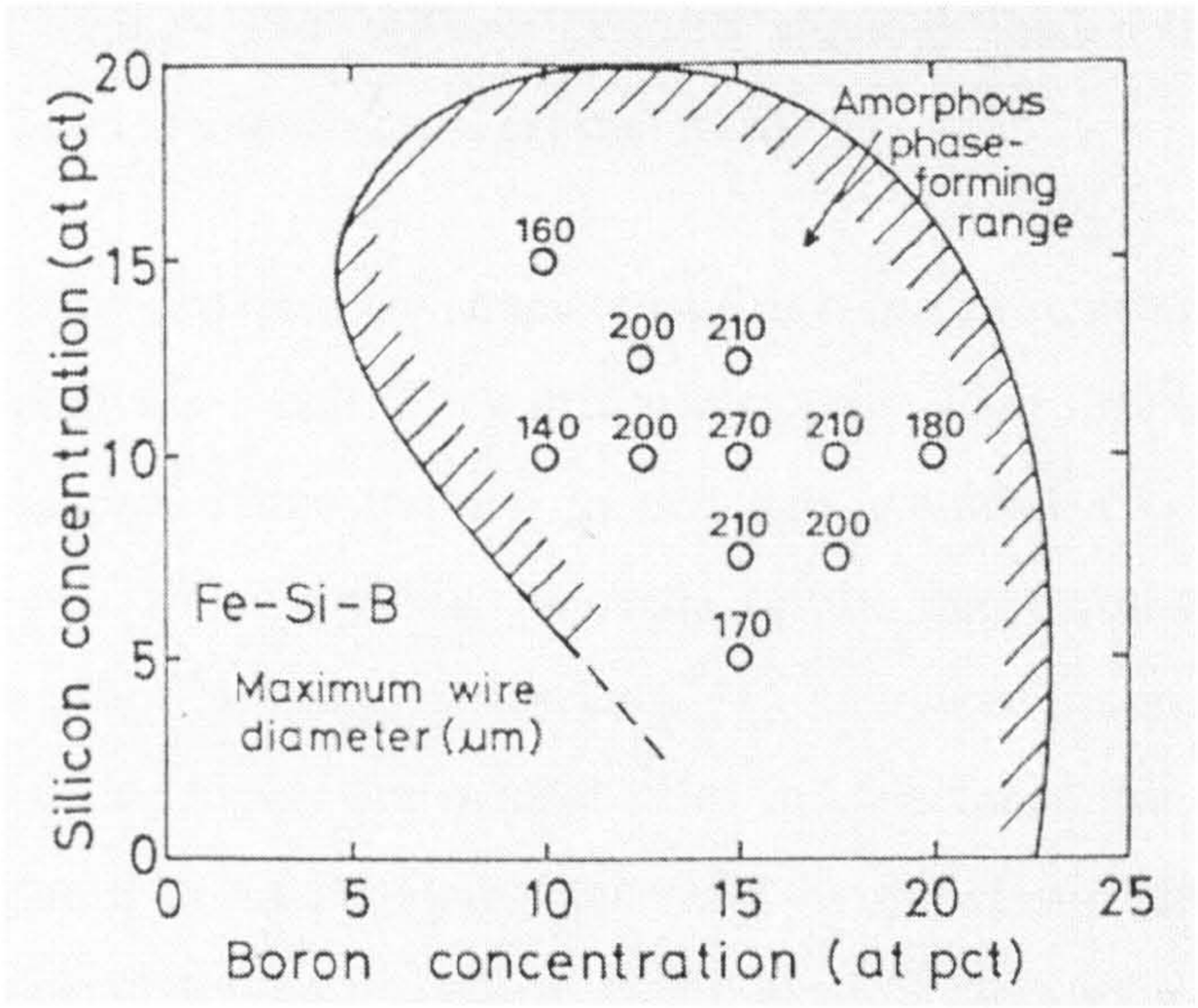

Figure 2.14. Dependence of Si/B metalloid contents in the maximum diameter for the formation of and amorphous wire in Fe-Si-B ternary alloys [54].

Hagiwara *et al.* [54] claimed that the ability to form amorphous wire of a given composition is controlled by several parameters such as melt viscosity and surface tension, the ease of formation of a surface oxide film which stabilises the melt jet, and by the critical ribbon thickness.

2.4 Mechanical properties of metallic glasses

Although amorphous alloys retain the main characteristics of metals, they are free of imperfections such as grain boundaries and stacking faults. For this reason, the mechanical properties of some metallic amorphous alloys are different from those of the corresponding crystalline metals and alloys [67].

2.4.1 Tensile strength

Masumoto and Maddin [68] first showed that amorphous alloys have high elastic limit, high fracture strength and remarkable deformability; however, such characteristics disappear when crystallisation occurs and they become very brittle. They also demonstrated [69] that amorphous alloys have certain mechanical properties superior to those of conventional crystalline alloys. They found that Fe- and Co- based amorphous alloys exhibit very high values of hardness and strength. Amorphous alloys can undergo a

severe bending test through 180° without fracture, although their tensile elongations are much smaller than those of conventional crystalline alloys.

Amorphous alloys also have the characteristic of being strong and, at least in bending and compression, relatively tough. They differ from crystalline metallic materials in not possessing a metallurgical microstructure so that they manifest a very localised plastic deformation process in which yielding proceeds by the nucleation and propagation of discrete shear bands [70]. Davis and co-workers [71], compared the mechanical properties of metallic glass wires and highly drawn steel wires and concluded that the high strength of the latter wires is due to work hardening generated by the elastic interactions of a high density of dislocations; under tensile deformation it experiences very localised plastic flow as its ability to further work harden decreases due to the high dislocation density. On the other hand, metallic glasses exhibit similarly high strength and intensely localised flow that is indicative of the absence of work hardening. Therefore metallic glasses may be considered, on one view, to be composed of an extremely high density of dislocations and/or *disclinations*. Davis [72] found that, in uniform cross-section filaments, deformation initiates at the grips, coincident with a clear departure from linearity of the load-elongation curve, and that the stress at failure, σ_f, is approximately equal to its yield stress, σ_y.

Table I shows the mechanical properties of some amorphous wires, together with those for some steel wires which are included for comparison. It can be seen in this table that stress at failure, σ_f, for $Co_{77.5}Si_{12.5}B_{10}$ amorphous wire is higher (3580 MPa) than both $Fe_{75}Si_{7.5}B_{17.5}$ amorphous wire (3550 MPa), piano wire (3020 MPa) and SUS 304 (729 MPa) steel wires. It is important to add that the deformation to fracture, ε_f, of SUS 304 steel wire is much higher (30.0 %), than for $Co_{77.5}Si_{12.5}B_{10}$ (3.0 %) and $Fe_{75}Si_{7.5}B_{17.5}$ amorphous wires (2.5 %) and piano wire (2.0 %); if the $Fe_{75}Si_{7.5}B_{17.5}$ amorphous wire is cold-drawn to 46 % reduction in area, σ_f increases to 3765 MPa, probably because of a more uniform diameter and removal of necks.

Table I Mechanical properties for some amorphous and steel wires.

ALLOY	STRUCTURE	(σ_f) MPa	(ε_f) %	(H_v) (VHN)	Ref. No.
$(Ni_{40}Pd_{60})_{80}P_{20}$	amorphous	1440	2.2	-	52
$(Ni_{60}Pd_{40})_{82}Si_{18}$ R = 56 %	amorphous	1710 2030	2.0 2.7	-	52
$(Ni_{75}Si_8B_{17})_{99}Al_1$	amorphous	2730	2.9	-	53
$(Ni_{78}P_{12}B_{10})_{99}Al_1$	amorphous	2170	2.4	-	53
$Ni_{53}Al_{20}Fe_{27}$	duplex phase	1285	17	-	60
$Pd_{77.5}Cu_6Si_{16.5}$ R = 17 %	amorphous	1560 1575	2.3 3.25	380 -	49
$Mn_{74.5}Al_{20.5}C_5$ R = 60 %	metastastable fcc	960 1460	- -	285 -	61
$Cu_{60}Zr_{40}$ R = 26 %	amorphous	1810 1950	2.7 3.6	440 -	59
$Co_{77.5}Si_{12.5}B_{10}$	amorphous	3580	3.0	1112	58
$Fe_{75}Si_{7.5}B_{17.5}$ R = 46 %	amorphous	3555 3765	2.5 4.6	960 -	54
$Fe_{75}Si_{10}B_{15}$	amorphous	3510	1.6	1035	7
$Fe_{69.5}Cr_8Si_{7.5}B_{15}$	amorphous	3550	2.5	1006	7
$Fe_{73.5}Ni_8Cr_{10}Al_{7.5}C_1$	lath martensite	1530	17	-	62
$Fe_{75}P_{10}C_{15}$	amorphous	3000	2.8	895	56
$Fe_{54}Mn_{20}Al_{16}C_{10}$	austenite	1000	2.0	-	63
$Fe_{78}Si_{10}B_{12}$	amorphous	3334	-	910	73
Piano wire	crystalline	3020	2.0	-	5
SUS 304 wire	crystalline	720	30.0	-	5

R indicates that the wire has been cold-drawn at the per cent indicated reduction in area; *amorphous ribbon; σ_f Tensile fracture; ε_f Elongation at fracture; H_v Vickers Hardness

2.4.2 Flow

The mechanical response of a material can be categorised according to reversibility and time dependence. The elastic response is instantaneous and reversible, the anelastic response is reversible and time dependent, and the plastic response is irreversible and time dependent. In metallic glasses, the plastic response occurs in two distinct regimes, homogeneous and inhomogeneous flow [74].

Homogeneous flow

Here, each volume element of the material contributes to the strain, resulting in uniform deformation for a uniformly stressed specimen.

Almost every intrinsic property of amorphous alloys has been shown to vary as the structure changes [75], with perhaps the greatest effect being the change in the homogeneous flow resistance. Structural relaxation increases the viscosity, a direct measure of the flow resistance, in some cases by more than five orders of magnitude [76].

Figure 2.15 illustrates the variation of the viscosity of a glass-forming alloy with temperature. If an alloy is at a temperature above the melting temperature T_m, the atomic structure and physical properties of the alloy in this regime are determined by the equilibrium state. If the alloy is cooled below T_m, its atomic structure continuously adopts configurations dictated by equilibrium, until the region of the glass transition temperature T_g is reached. At some temperature near T_g, the atomic configuration begins to 'freeze'. The resistance to atomic motion becomes large enough to restrict structural rearrangement, resulting in the time required for atoms to adopt their equilibrium configurations becoming greater than the time allowed by the cooling process. The atomic structure then begins to deviate from the configuration required by equilibrium. As the temperature continues to decrease, the resistance to atomic motion increases even more and the time required for structural rearrangements become larger. Eventually, significant structural change on the time scale of the cooling process ceases and the atomic configuration is 'frozen in'.

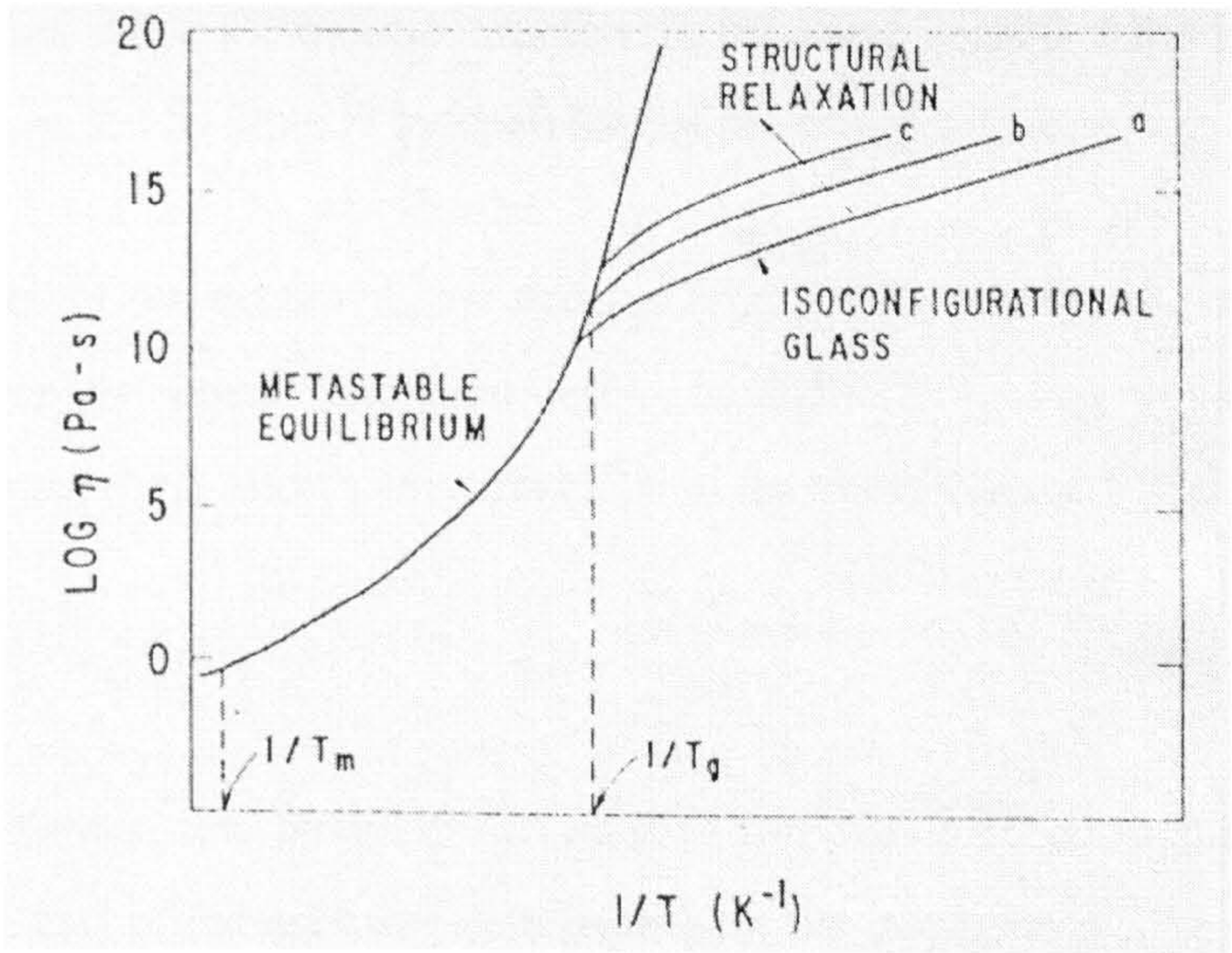

Figure 2.15. Schematic plot of the temperature dependence of the viscosity in a glass forming alloy during quenching and reheating. Curve *a* represents the deviation of the viscosity from the equilibrium curve during quenching. Curves *b* and *c* illustrate the shift in the isoconfigurational viscosity towards the equilibrium curve during annealing [74].

Subsequent heat treatment of the alloy at temperatures below T_g allows the atomic structure to relax and approach somewhat its equilibrium configuration before crystallisation begins.

The viscosity of a glass former is therefore not a unique function of temperature in the range $T < T_m$. In other words the viscosities of the metastable equilibrium liquid, the isoconfigurational glass and the crystallised alloy need to be distinguished.

Inhomogeneous flow

Here, the deformation is localised in discrete, thin shear bands, leaving the rest of the material plastically undeformed [74].

Metallic glasses are in a metastable thermodynamic state. As a result, they continuously change their structure to lower free energy states when the temperature is raised to a suitable fraction of T_g. This structural relaxation process affects all the physical properties, but most strongly the atomic transport properties. This is a most important consideration in homogeneous flow. Inhomogeneous flow is much less sensitive to

structural relaxation since the atomic structure in the shear band is a function of stress and temperature, and, at steady state is independent of the initial structure.

Homogeneous flow occurs at low stresses ($\sigma < \mu/100$, μ is the shear modulus) and is measured in creep or stress relaxation tests. At sufficiently low stresses, the flow is Newtonian viscous, which allows determination of the shear viscosity.

At an atomistic level:

a) Plastic flow at low temperatures relative to T_g is confined to shear bands, whose number and orientation are determined by the geometry of the deformation; the rest of the specimen deforms only elastically.

b) The shear bands are very thin, form very quickly when the yield stress is reached and result in sharp slip line-like marks at the specimen surface.

c) The strain inside the band is very large, and is accompanied by chemical disordering (observed by etching [77]) and dilatation (observed by density measurements).

d) Over a large temperature range, the flow stress is only very weakly temperature dependent [78], and is very strain rate-insensitive [79].

Inhomogeneous flow occurs at high stresses ($\sigma > \mu/50$) and low temperatures ($T < 0.7T_g$) and is observed in tensile tests, hardness tests and cold working processes such as rolling and wire drawing. The flow is strain rate insensitive, exhibits no work hardening (i.e. is almost ideally plastic) and is only very weakly temperature dependent.

Although the local plastic strain in a shear band is very large, the number of shear bands determines the overall strain, which depends on the geometrical constraints of the deformation process. For example, in rolling or wire drawing, the reductions can be 50 %. In a tensile test only a few shear bands are active and fracture occurs soon after initiation of the flow. The total plastic strain in this case is only a few tenths of a percent, which makes the stress-strain curve resemble that of a brittle material. However, the fracture

process is still "ductile" because it occurs along a 45°shear band (not normal to the tensile axis) and forms a "vein" morphology on the fracture surface, which involves extensive local plastic flow. This fracture process is a special case of a general set of instability phenomena.

For instance, Leamy *et al.* [80], using stereo-microscopy experiments, found that the vein structures were apparently *protrusions* which occurred on *both* fracture surfaces. These observations were taken as evidence for the occurrence of local necking during the fracture of metallic glasses.

The point of crack initiation was evidently near the centre of a smooth region by a pattern of veins. Long, necked filaments were commonly observed at triple point junctions of local necking ridges. These filaments appeared to have relaxed into a curved position. In every case, the tips of the filaments were rounded, as if by viscous flow.

Polk and Turnbull [81] suggested that the flow resistance should be increased greatly by compositional disordering. From this and under some conditions, the flow could be sustained by the softening arising from the attendant disordering.

Computer [82, 83] and bubble raft [84, 85] modelling of deformation at high stresses show that flow is governed by a variety of localised shear rearrangements, but this cannot be identified with long-lived extended line defects such as dislocations. On a macroscopic level, the dislocation models have, so far, not accounted for the localisation of flow into a small number of shear bands, nor for the subsequent fracture along the shear band resulting in a very characteristic vein-like fracture morphology.

The latter phenomena can be explained by any model that leads to a strong softening, i.e. lowering of the viscosity, in the shear band. Softening concentrates the deformation into the band and weakens the band against fracture by an instability that produces the vein pattern. The lowered viscosity also explains the decrease in chemical order or, as expected from a free volume model, the decrease in density.

Argon [86] proposed a model in which inhomogeneous flow is governed by localised shear transformations, analogous to the formation of dislocation loops. The parameters are

assumed to operate at steady state and can be adjusted to account for the temperature and stress regimes. The dilatation is introduced as an independent free volume creation parameter accompanying the shear transformation. By assuming that the threshold stress is lowered by an increase in the free volume, the required softening is achieved and localisation of the flow can be demonstrated.

Spaepen and Turnbull [87] proposed an explanation for the strength and plasticity of metallic glasses, based on the concept that the shear viscosity should be lowered sharply in regions which are dilated by stress concentrations. Such a marked lowering of viscosity with dilatation would be in accord with the free volume model for transport, as developed by Cohen and Turnbull [88]. In alloy glasses it is possible that, in addition to the free volume effect, the compositional short range order may decrease with increasing isothermal dilatation with resultant disorder softening.

Spaepen and Turnbull [87] considered the behaviour of Pd_4Si based glasses. They used a simple free volume model that states that the viscosity of a glass should decrease with increasing temperature because of thermal expansion. For instance, the thermal expansion coefficient for Pd_4Si based glasses was estimated to be no greater than 10^{-4} K^{-1}, as between room temperature and the glass transition temperature (350 °C), the viscosity changes by many orders of magnitude whereas the accompanying volume increase was about 3.5 %. They assumed that such a dilatation can easily be obtained in a region where the stress is concentrated. To test this assumption, they took the example of a small edge crack in a ribbon pulled in tension (figure 2.16).

For a volume element on the x axis, the principal stresses are [89]:

$$\sigma_x = \sigma_y = 1.2\sigma_0 \left(c/x\right)^{1/2} \tag{2.17}$$

where c is the crack length and x the distance from the crack tip. For a thin ribbon, plane stress conditions apply and $\sigma_z = 0$. In the middle of a thick specimen plane strain applies and $\sigma_z = 2\upsilon\sigma_y$, where ν is the Poisson ratio, taken as 0.33. The hydrostatic tension is given by:

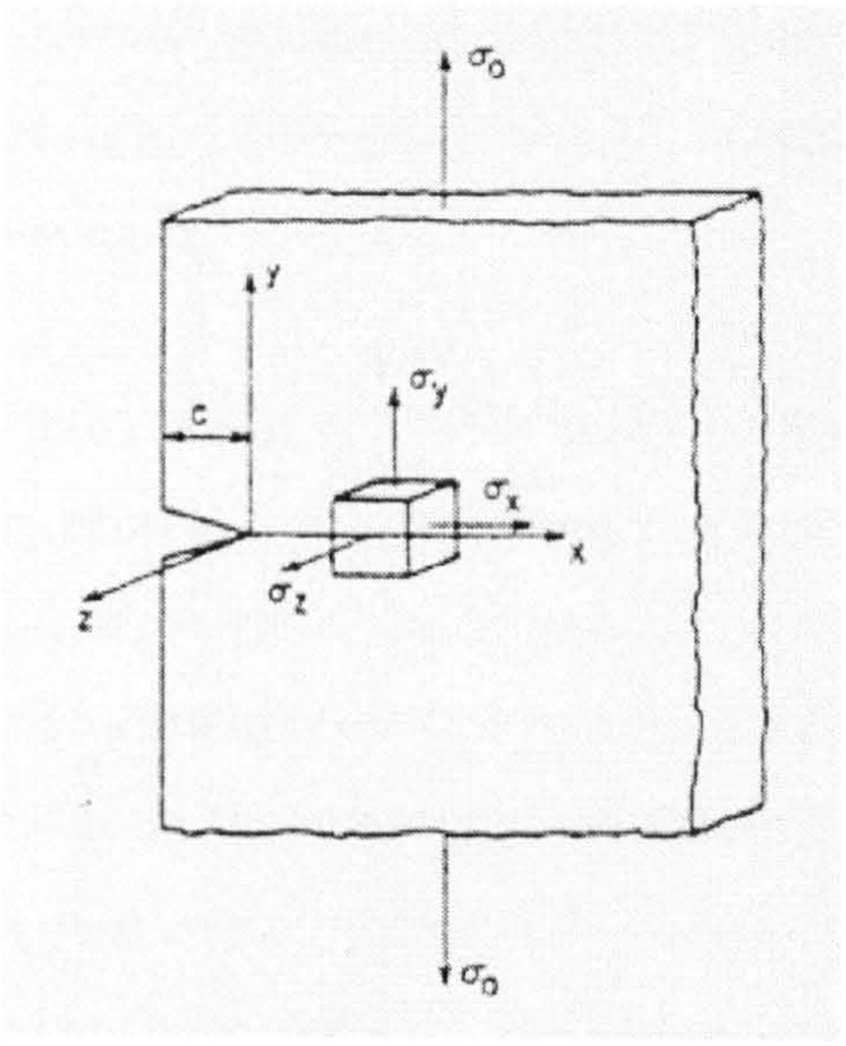

Figure 2.16. Schematic illustration of a small edge crack in a ribbon pulled on tension [87].

$$p = \frac{1}{3}\left(\sigma_x + \sigma_y + \sigma_z\right) = \frac{2}{3}\sigma_y \qquad \text{(plane stress)} \qquad (2.18)$$

$$= \frac{2}{3}(1+\upsilon)\sigma_y \qquad \text{(plane strain)} \qquad (2.19)$$

The dilatation caused by this tension is P/K, where K is the compressibility. Cleavage in the xz-plane would occur when σ_y reached the theoretical fracture stress of the material:

$$\sigma_y = \sigma_{th}\left(E\gamma/a\right)^{1/2} \qquad (2.20)$$

where E is the Young's modulus; γ the surface energy; a the average interatomic distance. The dilation at this point is then:

$$\frac{\Delta V}{V} = \frac{2}{3}\frac{\sigma_{th}}{K} \qquad \text{(plane stress)} \qquad (2.21)$$

$$= \frac{2}{3}(1+\upsilon)\frac{\sigma_{th}}{K} \qquad \text{(plane strain)} \qquad (2.22)$$

Inserting appropriate values for the variables in these equations, they obtained dilatations of 15% (plane stress) and 20% (plane strain), which was more than sufficient to obtain a dramatic viscosity decrease.

They considered the results of this dilatation in the deformation of an amorphous thin ribbon. The behaviour would be sensitive to the many cracks that are always present in the thin edge. Plastic flow would occur when the hydrostatic dilatation at the tip of the most susceptible crack had reached a certain level which corresponds to the apparent yield point on the load-displacement curve. In the stress state of figure 2.16, the plane of maximum shear stress, on which flow will occur, makes 45° angles with the y and z axes. Since plastic deformation occurs at constant volume, the density of the material that has flowed does not change. This also means that the viscosity remains relatively low, because no work hardening can occur. Thus, they deduced that the zone of plastic deformation consists of a low viscosity layer between two solid planes. In time, the dilatation in this molten zone would be decreased by configurational and volume relaxation processes which would transfer elastic strain to the adjacent solid zones.

The flow mechanism can repeat itself since the elastic stress field of the plastic zone changes as if the crack length had increased. The plastic zone will propagate and might eventually reach the other side of the specimen. When this happens, there are two 45° solid planes separated by a fluid layer. This layer will remain fluid until it reaches fracture, because all the deformation will happen there and keep the density low. At some point, the two parts will have slid off so much that the net cross section of the specimen becomes small enough to induce fracture, forming the typical "vein pattern" surface morphology.

This pattern is precisely that expected from the breaking of a fluid layer between two solid surfaces. The instability if the interface motion, which produces the vein pattern, is the fastest mode by which the two solid surfaces can be separated for a certain viscosity of the fluid layer.

Without flow, the normal stress σ_y at the sharpest crack would quickly reach the theoretical fracture stress σ_{th} and the specimen would break in a brittle way at very low external loads σ_0.

Spaepen and Turnbull [87] considered that this mechanism does not operate in crystalline metals nor in covalent glasses because, in these materials, the yield stress is determined, respectively, by workhardening or bond breaking. The maximum shear stress near a crack is also smaller than in pure tension. In metallic glasses, this effect is negligible compared to the dramatic decrease in viscosity, but in crystals and covalent glasses, it is the cause of the brittle behaviour induced by cracks. Spaepen [79] made this model more quantitative by assuming that disordering is a shear-induced free volume creation process, as a result of atoms pushing their neighbours aside at high stress levels. An ordering process during which free volume is annihilated balances this process. It was first [79] assumed that the annihilation process consisted simply of a series of diffusional jumps. However, in a later study of homogeneous flow, he showed that the annihilation process is one of structural relaxation, with kinetics that can be quite different from those of the purely diffusional process, at least in the high-viscosity regime. The original model assumed that the creation and annihilation processes establish a steady state, in which the free volume, and hence the viscosity, is a strong function of the stress. This is contrasted with homogeneous flow, where the viscosity is determined by the thermal history (below T_g) or the equilibrium structure (above T_g).

Bengus *et al.* [90] proposed that the combination of high local plasticity and high strength of ribbons leads to interesting physical peculiarities of ductile shear failure under "quasi-static" uniaxial tension, i.e.

a) relativistic regime of shear crack propagation.

b) repeated alternation of shear crack orientation during crack propagation

c) plastic corrugation as a result of post-failure deformation by various types of elastic waves

d) extreme local heating up to or close to the melting point at shear crack front.

e) non- zero plastic resistance in the so-called "liquid-like" layer.

Kinetics of the shear crack propagation

Studies made on $Ni_{78}Si_8B_{14}$ and $Fe_{70}Ni_{10}B_{20}$ amorphous ribbons [90] demonstrated that the maximum velocity of crack propagation was about $2.2x10^3$ ms^{-1}. Thus, in amorphous materials, the velocity of shear crack propagation is close to the maximum theoretical limit (2.5×10^3 ms^{-1}).

It was observed from crack front velocity *V(t)* curves coupled with fractographic morphologies, that the fracture surface was quite simple in regions where the crack propagated with high velocity. This surface lay close to one of the planes of maximum shear stress. The fracture surface was more complex in regions where the crack velocity decreased for which it had a faceted appearance (one smooth shear and one veined). The crack propagated alternately along one of the two planes of maximum shear stress. Fractographic observations indicated that the process of shear crack propagation from one edge of the ribbon to the other was step-like.

It was believed that two factors were important for the formation of the "faceted" surface. One was the presence of local internal stress and the other was local bending at the shear crack that violated the symmetry of the ribbon stress state under uniaxial tension. This latter reason for the alteration of the shear crack orientation was physically similar to the formation of conjugate shear bands under plane strain in crystalline solids.

It was observed that some folds of corrugation were formed by aggregates of shear bands. This was taken as evidence of the high local plasticity of amorphous alloy ribbons. The origin of those folds of corrugation could be then easily understood, considering that the velocity of the crack was close to the sound velocity. It was believed that elastic waves formed in the specimen during the time t_f for the crack to propagate from one edge of the specimen to the other.

On the other hand, based on creation and annihilation of the free volume, Steif *et al.* [91] analysed the establishment of inhomogeneous flow as a transient, i.e. time-dependent, problem, together with the requirements for localisation of the plastic strain. They concluded that the free volume creation model indeed leads to catastrophic softening and formation of shear bands. It also became apparent that the band forms so quickly that the steady state is probably never reached. In that case, the annihilation process can be

neglected and their precise nature does not have to be identified to describe inhomogeneous flow. The time-dependent analysis can account for the experimentally observed stress for onset of the strain localisation and its temperature dependence.

The mechanism regimes for homogeneous and inhomogeneous flow are illustrated schematically in figure 2.17 [74].

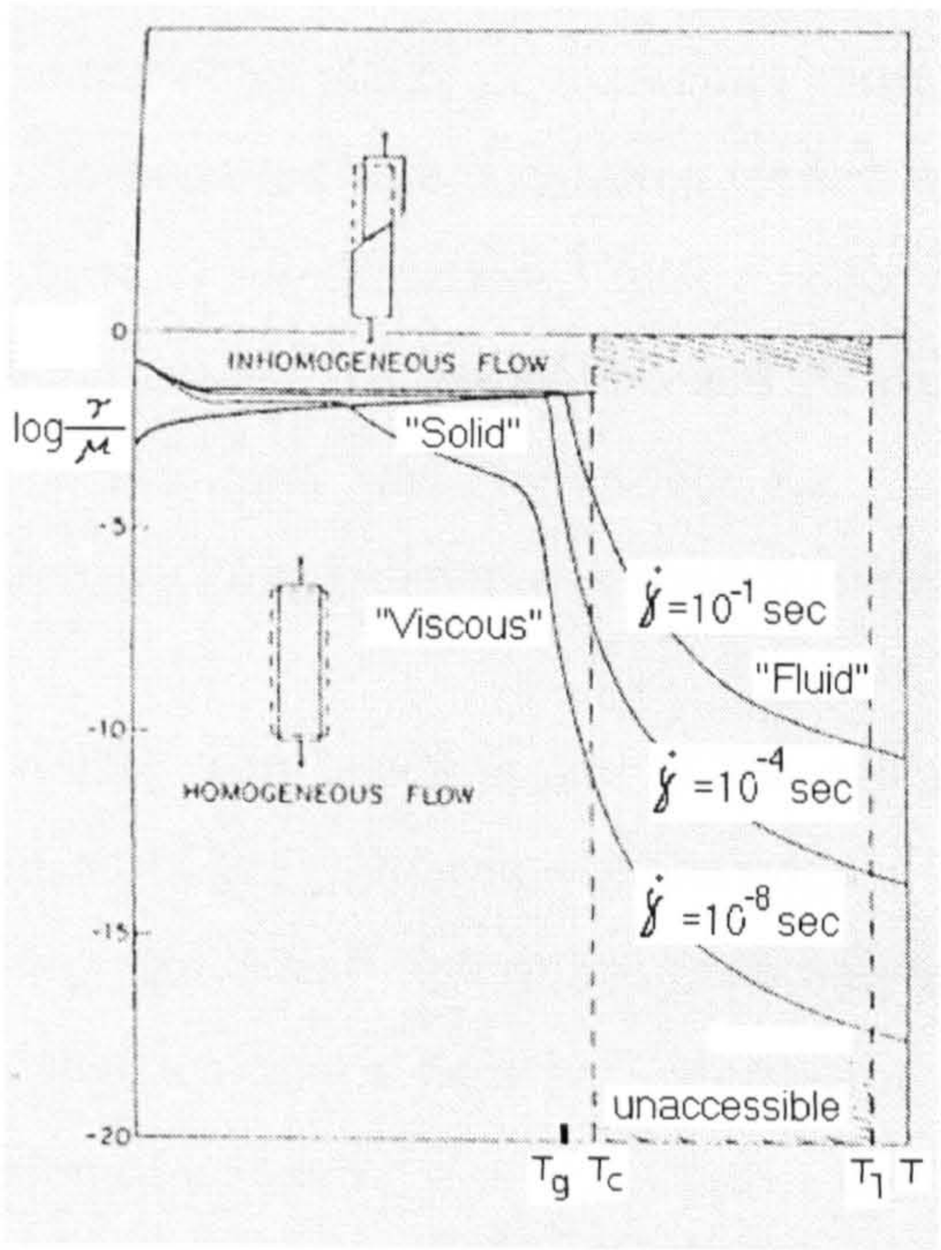

Figure 2.17. Schematic deformation mechanism map for an amorphous alloy (in a particular state of annealing), showing the temperature and stress regions for homogeneous and inhomogeneous plastic flow [74].

Kimura and Masumoto [92] reported that plastic flow in metallic glasses occurs locally (local yielding) in the form of slip bands and then proceeds through the entire cross-section of the round specimen (general yielding). The angle of the slip band to the tensile axis has the constant value of 55 degrees. General yielding appears to occur before the application of maximum load.

Evidence of an ideal plastic solid

The plastic behaviour of an amorphous $Pd_{78}Cu_6Si_{16}$ alloy was examined in terms of reasonable macroscopic variables in continuum plastic theory [92]. Simple torsion theory gives the relationship for the pure shear stress τ as:

$$\tau = \frac{3M_T + \theta \dfrac{dM_T}{d\theta}}{2\pi d^3} \tag{2.23}$$

where M_T is the torsional moment, θ the torsional angle, and d is the diameter of a round-bar specimen. The torsion moment-torsion angle curve in the region of the elastic-plastic flow allows an adjustment to a simple torsion theory prediction for an elastic-perfectly plastic solid. The morphology of slip bands in torsion is characterised by the two sets of intersecting straight slip bands along planes of maximum shear stress. It was also found that the density of slip bands increased with decreasing torsion strain, indicating the stable deformation of torsional flow. Amorphous $Pd_{78}Cu_6Si_{16}$ under torsion gave evidence of elastic-perfectly plastic deformation. The nucleation and propagation of slip bands at a stress concentration in the specimen was responsible for local yielding appearing in tension, but an inherent micro-yielding behaviour in uniaxial tension was not expected.

The angle of the 'visible' slip bands is one of the characteristics of flow for an amorphous alloy. The concept of the strain-rate component can describe plastic flow of a highly local nature by noting that 'local' deformation can only occur on planes in which, on general yielding, the extension rate is zero [93]. According to this idea, an observed angle of 45° for compression of a round bar of $Pd_{78}Cu_6Si_{16}$ corresponds to that for plane-strain deformation; the observed 55° for tension is equal to the predicted value for uniaxial extension. The difference between the slip band-angle in tension and compression is not due to a normal stress induced variation of 45° shear yielding (i.e., plane strain extension with a volume dilatation). The small pressure coefficient of shear stress does not account for such a large deviation from 45°, as pointed out by Davis and Kavesh [94].

Micro-mechanics of plastic deformation

The near-equality of the value for 'microscopic' critical shear stress acting on a single shear band and for macroscopic yield stress proves that the inhomogeneity of the flow is of an elastic-perfectly plastic nature.

If an amorphous alloy is plastically deformed in a multiple axial stress state, e.g. in drawing, rolling and V-notch bending, it proceeds by gross yielding, exhibiting an intersection and multiplication of slip bands. In contrast the plastic deformation in uniaxial

stress occurs by highly localised shear (i.e., along a single slip plane) wherein the general yielding stress is adequate as a variable for the flow. Tensile tests on undrawn and drawn $Pd_{77.5}Cu_6Si_{16.5}$ amorphous wires [95] showed that the fracture stress of drawn wires increased slightly (~ 7%) from that of undrawn wire, and macroscopic elongation to fracture increased considerably after drawing. Considering the mechanics of gross yielding and 'apparent' strain hardening, intrinsic (physical) strain hardening was not responsible for these events, since an individual slip was of an ideal-plastic nature. The intersecting of shear bands inhibited further sliding of pre-existing shear bands and further deformation promoted creation and propagation of new shear bands ahead of terminal shear bands through undeformed material; an increase in the density of mobile shear bands could be created only by raising the applied stress. The pre-existing shear bands tended to slide at a smaller applied stress below macroscopic general yielding under a stress concentration (i.e., local yielding); an increase in the density of such pre-existing shear planes accounted for an increase in the elongation of drawn wire.

2.4.3 Fracture

The first fractographic studies on amorphous metallic alloys were carried out by Masumoto and Maddin on $Pd_{80}Si_{20}$ filaments tested in tension [68]. As discussed above it was found that fracture occurred by plastic flow but by a process different from those of crystalline metals when a fluid layer was formed in the shear planes. The following summary points concerning the deformation of the amorphous alloy were made:

a) Apparent yielding occurred, evidenced by a region of the stress-strain curve that deviated from elastic behaviour. The surface showed evidence of markings that produced by shear displacements (bending).

b) In the region of the initiating defect, limited to a few ten of nm, there was evidence of plastic flow.

c) The microscopic aspects of the fracture surface were quite similar to that of silicate glasses at room temperature; however on a microscopic scale, tearing was visible.

Masumoto and Maddin [68] assumed that amorphous alloys behave as other amorphous materials, such as silicate glasses, with brittle fracture characteristics, i.e. little plastic deformation. However, amorphous $Pd_{80}Si_{20}$ (the first metallic glass studied with respect to its mechanical properties) was found to depart from purely glassy behaviour in the following way:

a) A crack appeared after yielding but remained stable in a region showing evidence of "plastic flow".

b) The "plastic flow region" at the tip of the crack was limited to a few tens of nm.

c) Viscous-type tearing occurred on the fracture surface.

From these observations, it was concluded that deformation and fracture occurred through the stabilisation of cracks by limited "plastic" flow, followed by the propagation of these cracks. There, plastic deformation was needed to nucleate a crack but the absorption of energy by the deformation in advance of the crack rendered the crack somewhat stable. In this type of material, strain is a function of stress and time and there exists a region near the glass transition temperature where "*viscous flow*" occurs. According to this model if a crack is accompanied by "viscous" flow the fracture stress will be strongly dependent upon strain rate. At low strain rate the fracture stress should increase because more energy is needed to continue the propagation of the crack. These predictions appeared to agree with the results which indicated that the fracture stress decreased by about 200 MPa with a 100 fold increase in the strain rate.

Ductile fracture

If fracture in a metallic glass occurs as a result of large plastic strain, at least locally, this fracture is said to be "ductile" [74]. Specifically, this applies to the fracture process that terminates inhomogeneous flow. In uniaxial tension, it occurs along the plane of the shear band, not along the plane normal to the tensile axis, which has the largest normal stress. Fracture morphology results in a characteristic 'vein' or 'river' pattern. Figure 2.18 shows how the direction of the veins is related to the shear band and the direction of the fracture process [74]. The similarity between this pattern and that obtained by separating

two solid surfaces containing a fluid layer, such as vaseline or grease [86] supports the softening mechanism for inhomogeneous flow.

Leamy *et al.* [80] suggested that a portion of the mechanical work expended during rupture produced local heating of the material in the necked regions resulting in the apparently viscous relaxation of the necked filaments at vein triple points.

They summarised their observations of the tensile deformation and fracture behaviour of amorphous and microcrystalline alloys as follows:

a) Tensile stress was accompanied by hardening rate plastic shear deformation.

b) Fracture occurred on surfaces of maximum resolved shear stress and was preceded by a plastic shear strain of as much as 40 %.

c) Fracture was accompanied by local heating and viscous flow necking of material between propagating cracks or voids.

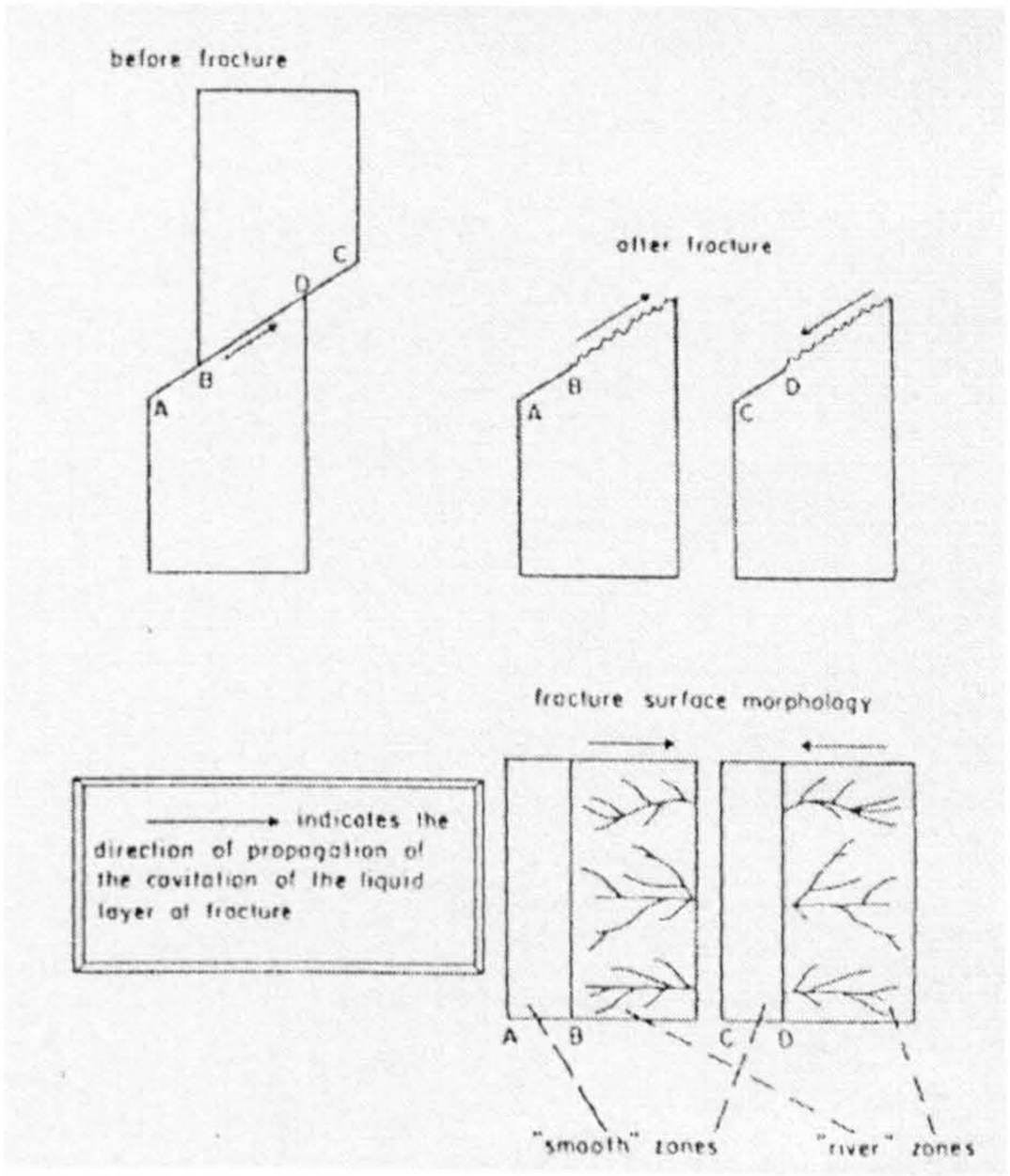

Figure 2.18. Diagram showing the origin of the features of a ductile fracture and their relation to the shear band. Arrows indicate the direction of propagation of the cavitation of the liquid layer at fracture [74]

These observations formed the basis for speculation that plastic flow occurs via motion of localised strain concentrations and that fracture is initiated by macroscopic "adiabatic" shear.

Aside from the local necking patterns, macroscopic shear has commonly been observed in crystalline specimens when the work-hardening rate was near zero [96-98]. This phenomenon is commonly referred to as "adiabatic shear", and occurs catastrophically whenever the rate of decrease in strength due to "adiabatic" heating of the deforming region equals or exceeds the rate of strengthening due to the increased strain and strain rate.

If the elimination of all the increase in energy associated with deformation was achieved through complete relaxation of all atoms in the stressed volume, a viscous, zero hardening rate, shear deformation would result [80].

The fracture surface morphology is the result of an instability that occurs during the motion of the interface between the fluid and the outside air. This is a special case of a general type of instability. Pitts and Greiller [99] give an approximate analysis of the conditions for instability, which is illustrated schematically in figure 2.19.

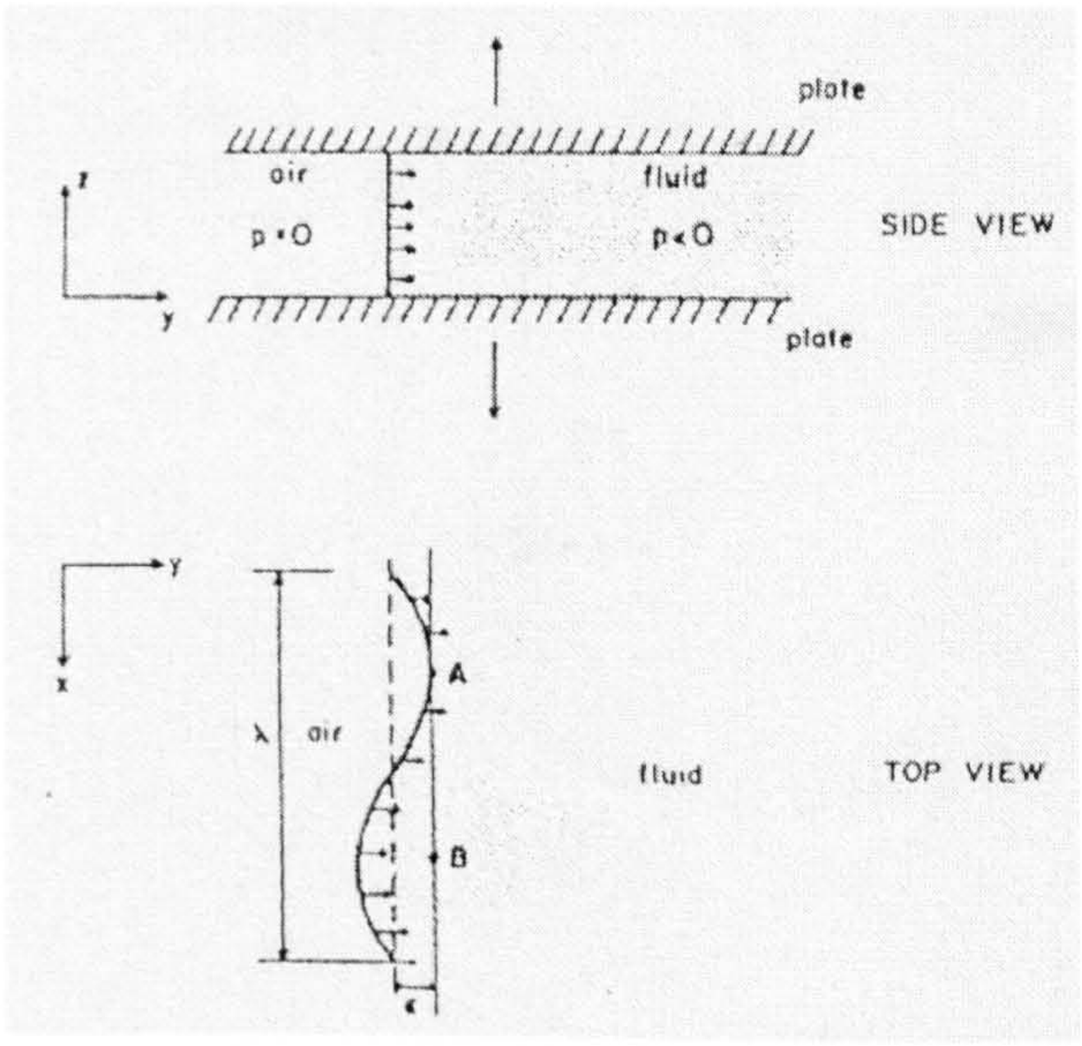

Figure 2.19. Schematic illustration of the instability of a perturbation in a moving fluid-air interface [74].

The fluid-air interface lies in the *xy*-plane and is driven in the *y*-direction by an externally applied negative pressure gradient ($\partial p/\partial y$). An infinitesimal sinusoidal perturbation:

$$y = \varepsilon \sin\left(\frac{2\pi x}{\lambda}\right) \tag{2.24}$$

causes the pressure P_A, at a point A, just inside the fluid, to be determined by the surface tension γ, and the local curvature k, such that:

$$P_A = \gamma k = -\gamma\varepsilon\left(\frac{2\pi}{\lambda}\right)^2 \tag{2.25}$$

At point B, the pressure effect due to capillarity has the reverse sign and the effect of the applied pressure gradient over a distance 2ε has to be taken into account as well:

$$P_B = \gamma k + 2\varepsilon\frac{\partial p}{\partial y} \tag{2.26}$$

If $P_A < P_B$, matter will flow from B to A and the perturbation will die. If $P_A > P_B$, the reverse will happen and the perturbation will grow as a protrusion into the fluid layer. These protrusions then run into one another on an increasingly larger scale, resulting in the overall '*vein*'-*pattern* effect. The critical wavelength that can still grow corresponds to $P_A = P_B$, so that

$$\lambda = 2\pi\sqrt{\frac{-k}{\varepsilon}} \tag{2.27}$$

The scale of the instability is seen to be the result of the balance between the pressure gradient driving the interface motion, and the surface tension resisting growth of perturbation. This is similar to the dendritic instability in crystal growth, which is governed by the balance between a temperature or concentration driving gradient and the crystal-melt surface tension. It has been found that the wavelength of the fastest growing perturbation is $\lambda_m = 3\lambda$.

On the other hand, Spaepen [100] proposed that the applied stress σ can be resolved in two components: a shear stress τ in the plane of flow, which makes the two parts of the specimen slide over each other, and a stress σ_n, normal to the plane of flow, which tries to pull them apart. Therefore, σ_n at fracture can be considered as the fracture stress (σ_n^f) of the liquid layer. When the specimen breaks, a vein-like morphology is formed on the fracture surface. The shape and direction of the 'river' pattern suggests that fracture happens when a perturbation in one of the moving edges of the layer goes unstable and sweeps across the fracture plane towards the other edge.

Investigations of the river or vein pattern [100] showed that the "tributaries" which are most finely spaced are the ones that are closest to the edge where the fracture originated. An analogue experiment by Pampillo *et al.* [101] showed clearly how the initial perturbation forms the first, most finely spaced, tributaries, which then run into each other and form the veins. Figure 2.20 shows a schematic representation of this phenomenon. If the edge that develops the instability also has a slight, long wavelength perturbation to it, this will cause the tributaries to run into each other. Since the liquid layer in a metallic glass wets the solid surface very well (both are chemically identical), more of the fine initial tributaries will be preserved after fracture than in the experiments by Pampillo where grease and glass were used.

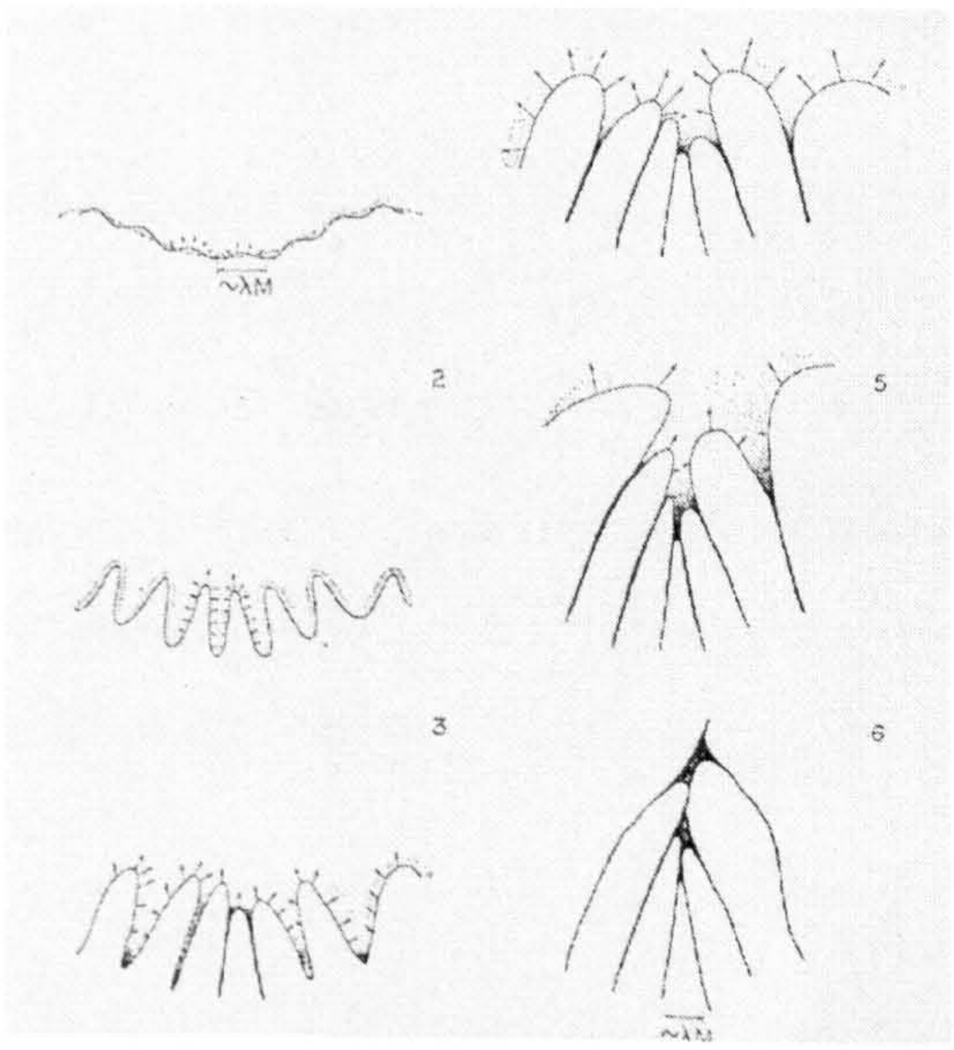

Figure 2.20. Schematic representation of the successive stages in the formation of the "veined" pattern from the initial perturbation. The shading is qualitatively proportional to the density [100].

Bengus *et al.* [90] predicted that the dissipation of the plastic deformation energy in the region of localised shear will result in the local heating of this region. The greater the specific power of plastic deformation (i.e. the higher the stress and the strain rate) in this volume the greater will be the temperature rise.

Unique conditions for initiation of extreme heating are realised under low-temperature ($T < 0.6T_g$) shear failure under uniaxial tension of amorphous alloy ribbon, where:

a) the failure stress σ_f is of the order of the theoretical strength.

b) catastrophic shear strain ($\Delta\varepsilon$), which precedes the rupture, was of the order of 100, because the typical magnitude of the shear displacement S_s was about 10 μm, and the shear band width d was only about 0.02 μm.

c) the duration Δt of the catastrophic shear and failure was of the order of 10^{-6} s.

The specific work of plastic deformation W_p in the volume of the catastrophic shear region could be estimated, on the basis of the cited data, using:

$$W_p = \int_0^{\Delta t} \sigma(t)\dot{\varepsilon}_p(t)dt = \sigma^* \Delta\varepsilon \tag{2.28}$$

where σ^* is the average stress acting during the time Δt of catastrophic shear at a shear rate $\dot{\varepsilon}_p$. On the basis of $\Delta\varepsilon = S_s/d$ and ≈100 and $\sigma^* \sim \sigma_f \sim 2$ GPa a value of $W_p \sim 100$ GJ/m^3 was obtained. However, the sum of the energy $q_t = C_p\Delta T$ required for the heating to the melting temperature (where C_p is the mean specific heat and ΔT is the temperature internal) and the heat of melting q_m does not exceed W_p since $q_t = 10$ GJ/m^3 and $q_m \sim 0.1$ GJ/m^3. In this way, melting on the catastrophic shear surface was possible if the following condition of adiabaticity was fulfilled; i.e.

$$\sqrt{\Delta tD} \sim d \tag{2.29}$$

where D is the thermal diffusion coefficient (of the order of 10^{-7} m^2s^{-1} at room temperature). For a single facet of the failure surface, when $\Delta t \sim 0.01$ μs, the shear is definitely adiabatic. Thus, local strain heating during catastrophic shear was sufficiently high for local melting.

On checking the hypothesis of local melting for a sample length L of 10 mm and $\sqrt{\Delta tD}$ equal to $5x10^{-2}$, $\Delta T_l >> 10^3$ K was obtained, giving $T_m \geq 1800$ K, which is well in excess of the values for all practically important glass forming alloys. Fractographic observations gave evidence of the presence of liquid phase at the moment of rupture of ribbons and wires. However, liquid phase was evidently absent during the process of plastic shear preceding rupture, although the material was already heated close to the melting temperature.

Non-zero value of plastic shear resistance in liquid-like layer

Two theoretical models of "vein" pattern formation on failure surfaces of amorphous ribbons are based on the supposition of a small viscosity of the material in a thin layer along the surface of catastrophic shear. This layer has been referred to as a "liquid-like" layer.

In one model proposed by Spaepen [100] the shear resistance was not considered; apparently it was assumed to be zero. The resulting equation connecting the linear density H of "veins" with the fracture stress σ_f was:

$$H = \frac{\sqrt{\sigma_f}}{2\pi\sqrt{\gamma_f d}} \tag{2.30}$$

where γ_f was the surface energy.

In the other model proposed by Argon [86], the plastic shear resistance of the liquid-like layer was assumed to be non-zero and nonlinearly dependent on the strain rate. This model contained a coefficient $A(n)$, that was dependent on the nonlinearity exponent n for plastic resistance of the material. Thus

$$H = \frac{\sigma_f}{12\sqrt{3}\pi^2 A(n)\gamma_f} \tag{2.31}$$

On the basis of results obtained experimentally and comparisons with the predictions of equations 2.30 and 2.31 it was possible to consider the liquid-like layer as a supercooled liquid. Then it was possible to imagine that the liquid phase was present only in the last stage of the failure because of additional heating at the moment of the rupture. Eberhart [102], found that this additional heating might be connected with complex processes in the electronic subsystem. Observed peculiarities in the behaviour of the liquid-like layer might also be connected to its non-linear properties. However, this possibility has not been studied yet.

Brittle fracture

The principal causes of embrittlement in metallic glasses are *a)* a low temperature of deformation, *b*) relaxation annealing and *c*) crystallisation. The following points can be made about annealing induced embrittlement [74]:

a) it is very composition-dependent: iron-based glasses, especially with large metalloid additions, embrittle very easily; palladium-based glassy alloys, on the other hand, have been annealed for very long times without embrittling, if no crystallisation occurs; similarly, nickel-based alloy glasses are generally also very resistant to thermal embrittlement.

b) it correlates with structural relaxation.

c) it can be reversed by neutron irradiation.

Brittle fracture is a cleavage process that can most simply be said to occur if the tensile stress at a stress concentrator, such as a microcrack, reaches the theoretical fracture stress of the material, σ_{th}, before shear induced plastic flow can blunt the crack and relieve the stress. It seems plausible in view of Spaepen and Turnbull's first argument about the initiation of flow at stress concentrators that the significant viscosity increase resulting from structural relaxation or the viscosity decrease associated with the density decrease upon irradiation [103], should have an effect on this crack blunting process. Spaepen and

Turnbull pointed out that the temperature change ΔT necessary to give dilatation equivalent to that just preceding fracture is:

$$\Delta T \cong \frac{\sigma_{th}}{K\alpha} \tag{2.32}$$

where σ_{th}, the theoretical strength, $\approx E/10$ (E = Young's modulus), the compressibility $K \approx$ E and α is the volume thermal expansion coefficient. Thus, for $\alpha = 10^{-4}\,K^{-1}$, $\Delta T \approx 10^{3}$ K. This corresponds to a drastic decrease in viscosity, more than sufficient to relieve the stress at the singularity.

Leamy [80] found that some amorphous and microcrystalline filaments, containing large amounts of metastable silicide were extremely brittle. The fracture on those specimens consisted of two zones: an area of crack initiation that was quite rough, the fracture being apparently intergranular in this region, while the remaining zone was also rough but on a much finer scale.

The fracture surface features which were common to amorphous and microcrystalline alloys were described as follows:

a) fracture occurred on surfaces whose normals lay at 45° ±2 to the tensile axis in the plane of the tensile axis and the ribbon surface normal. That is, fracture occurred on planes of maximum resolved shear stress.

b) fracture involved one, and occasionally two, transitions from one to the other plane of maximum shear stress.

c) two distinct fracture zones were present: a nearly smooth region, and one in which local necking 'vein' patterns were observed. The veins were of the order of 0.1 μm in width and generally possessed a height-to-width ratio of two to four, except at triple point junctions where elongated necked filaments were often observed.

d) the shear nature of the deformation process was confirmed by bend test experiments. At large radii, bending produced long straight plastic shear deformation steps parallel to the bend axis. Further bending lead to production of secondary steps at small angles to the primary steps and finally to large shear displacements at these steps.

The shear failure of these sample filaments may be envisioned as propagating in several possible modes. These are illustrated schematically in figure 2.21 [80]. In the first case, a shear crack propagates from the surface through a portion of the specimen and creates a smooth fracture zone. At the increased stress levels, shear cracks (voids) in the remaining sound material may link together during fracture to produce the observed vein structure. Alternatively, figure 2.21(*b*), the specimen may undergo plastic shear deformation and subsequently fail by propagation and linking of internal shear cracks or voids. Finally, the alternating shear mechanism proposed to account for observations of shear failure in steels tested near their ductile-brittle transition temperature is shown in figure 2.21(*c*).

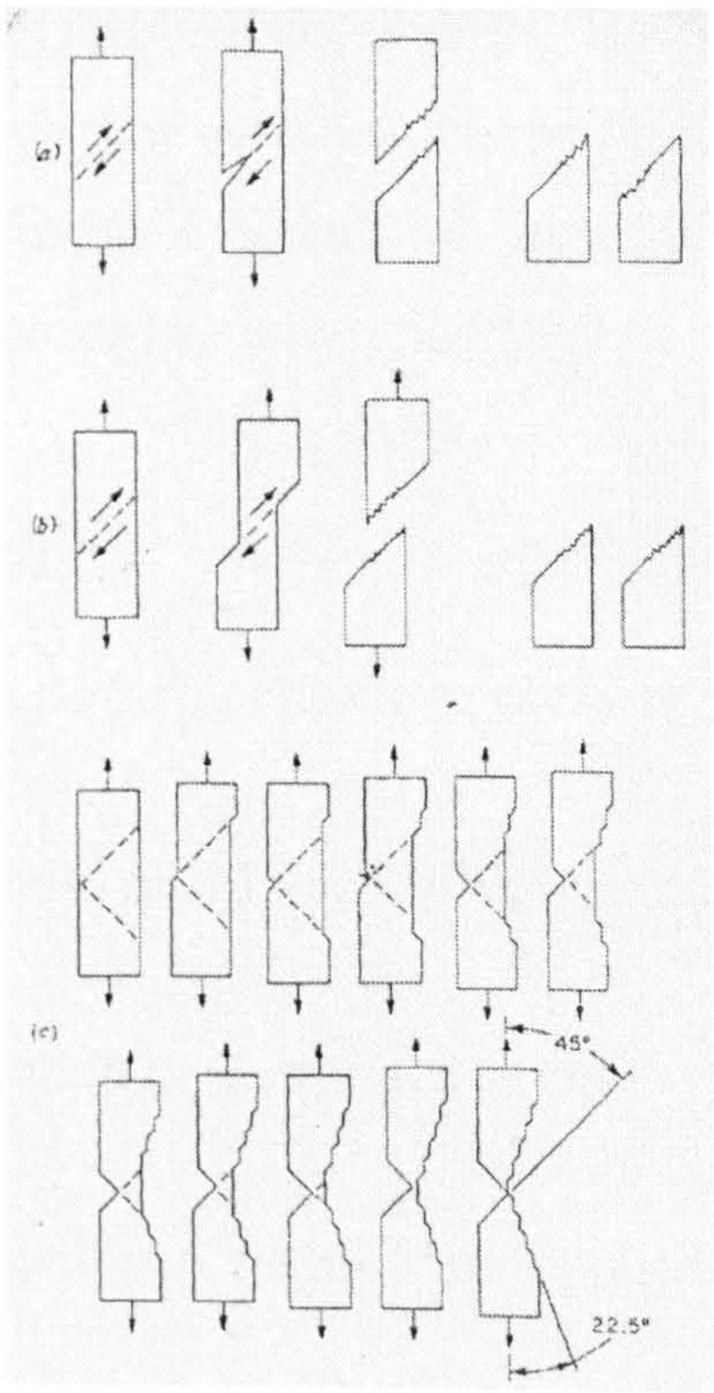

Figure 2.21. Schematic illustration of possible shear fracture modes in ribbon specimens. (*a*) Shear crack propagation; (*b*) Plastic shear and fracture; (*c*) Alternating shear [80].

Of these mechanisms, only those in (*a*) and (*b*) produce fracture surfaces, which possess the characteristics observed in metallic ribbons. Leamy *et al.* [80] found that plastic shear deformation of as much as 40 % precedes failure in $Pd_{80}Si_{20}$-based amorphous alloy ribbons and concluded that plastic shear displacement must therefore have been produced at high stress, just prior to fracture.

Strip specimens of the glassy alloy $Ni_{49}Fe_{29}P_{14}B_6Si_2$ loaded in tension were shown by Davis [104], to have failed simultaneously with general yielding with the fracture surface inclined at an angle of ~53° to the tensile axis. It was found that while the elongation to fracture was minimal for both failure modes noted (ductile and brittle), the 53° mode is technically ductile because general yielding occurred just prior to, or coincident with separation. Antiplane strain failure occurred when an elastic-plastic boundary propagated across the specimen in the direction of the width vector. Plasticity was localised at the crack tip and hence this mode was brittle.

On the other hand, Olofinjana and Davies [55], found that fractures in tensile tests on wire samples occurred by shear-induced deformation, on a plane at ~45° to the tensile axis that is in the plane of maximum resolved shear stress. The fracture surfaces manifested the characteristic vein pattern, which they considered to be fingerprints of crack instability that followed the initial displacement, evidence of local plastic deformation in narrow unseparated regions between the rapidly advancing cracks.

2.4.4 Fatigue Strength

Dieter [105] lists three basic factors that are necessary to cause fatigue failure:

a) a maximum tensile stress of sufficiently high value.

b) a large enough fluctuation in the applied stress.

c) a sufficiently large number of cycles of the applied stress.

In addition, there are a host of other variables such as stress concentration, corrosion, temperature, over-load, metallurgical structure and residual stress, which tend to alter conditions for fatigue.

This section deals with some different fatigue studies by using different types of machines, carried out on amorphous alloys in both forms, wires and ribbons, in some cases, conventional wires are mentioned for comparison.

The first bend type fatigue testing machine used for testing amorphous wires was reported by Hagiwara *et al.* [5], figure 2.22. They tested $Fe_{75}Si_{10}B_{15}$ and $Fe_{77.5}P_{12.5}C_{10}$ amorphous alloy wires and compared the results with those of 0.8 wt % C piano wire and 304 stainless steel wire.

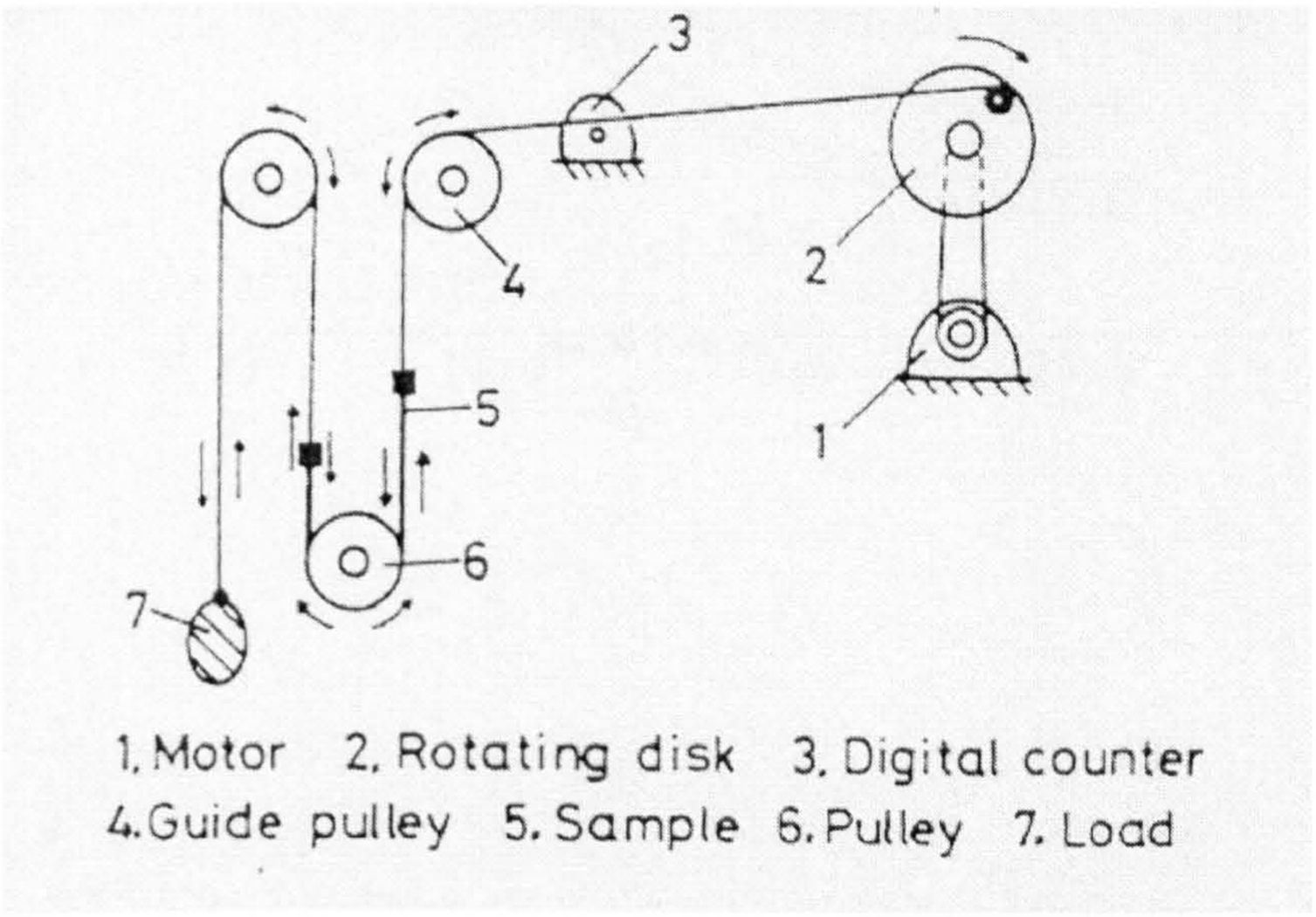

Figure 2.22. Schematic illustration of the first bend type fatigue machine for testing amorphous wires [5].

They found that piano and 304 stainless steel wires had higher fatigue limits than amorphous ribbons and wires when tested at ambient humidity ~85 % relative humidity, RH, (they plotted their results as function of bend strain, λ vs number of cycles to failure, N_f). However, the fatigue limit for the $Fe_{75}Si_{10}B_{15}$ wires improved by about 300 % decreasing the humidity from values of 85 % to 30 % RH (figure 2.23(*a*)). Similarly, when Cr replaced ≥ 8 at % of Fe in the Fe-Si-B alloy, the fatigue limit for amorphous wires was higher than for piano and 304 crystalline wires. This high fatigue strength for Fe-8% Cr-

based amorphous alloy wires was also observed in water, although the fatigue limit decreased about 25 % (figure 2.23(*b*)). The fatigue strength level was higher by a factor about 1.9 than that of 304 stainless steel wire, while no fatigue limit was attained for piano wire or for the $Fe_{75}Si_{10}B_{15}$ amorphous wires. Hagiwara *et al.* concluded that the enhancement of the fatigue strength for the glassy FeSiB wire by the dissolution of Cr was due mainly to the suppression of the initiation of fatigue crack on the sample surface through the effect of Cr in enhancing substantially the corrosion resistance [5].

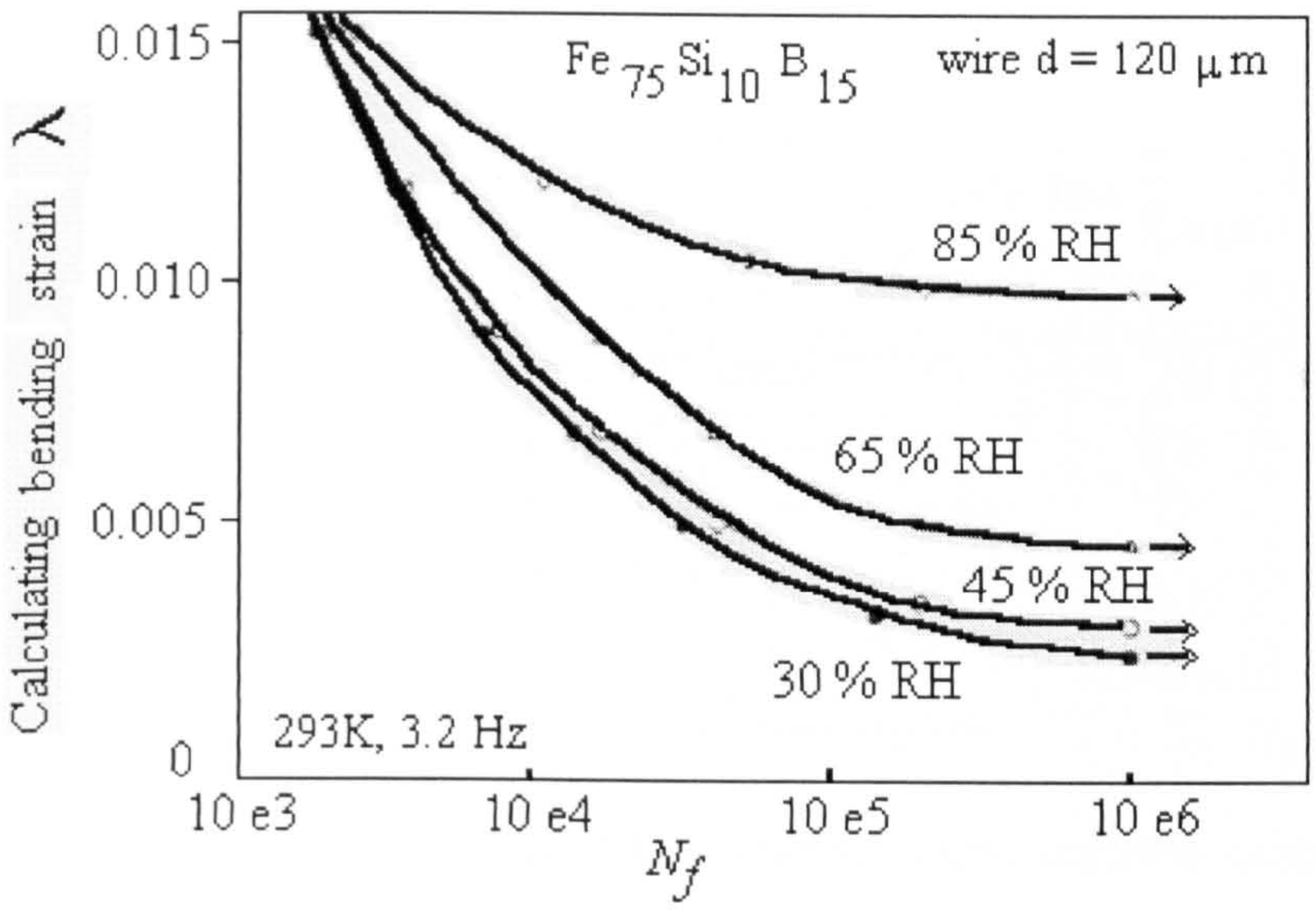

(*a*)

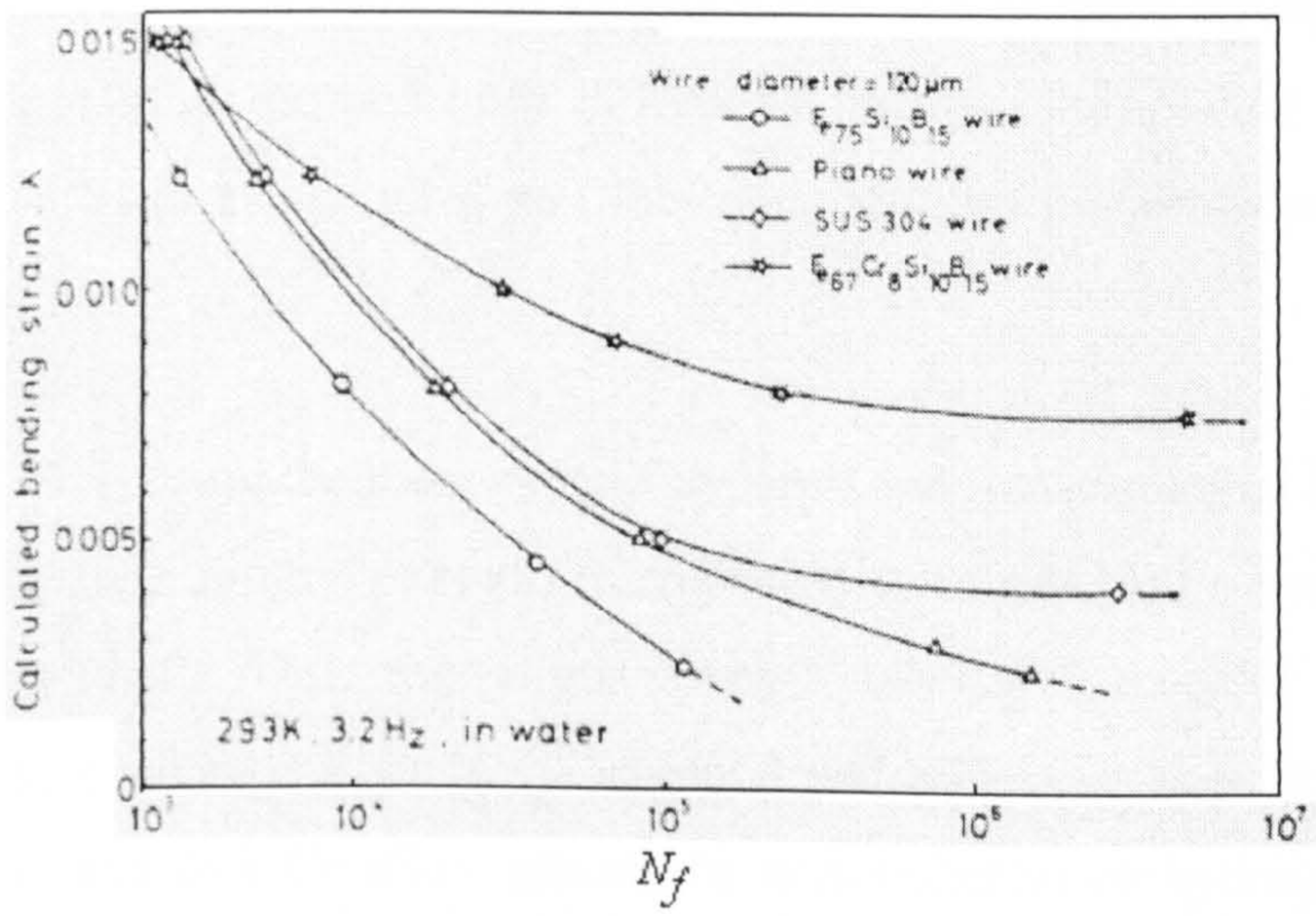

(*b*)

Figure 2.23. Fatigue curves for (*a*) $Fe_{75}Si_{10}B_{12}$ tested in different humidities, (*b*) fatigue curves for FeSiB amorphous alloy and crystalline wires tested in water [5].

Doi *et al.* [106] used an alternative technique for measuring the fatigue lifetime of metallic glass ribbons (figure 2.24). They found that Co_{75} $Si_{10}B_{15}$ alloy had longer fatigue life than both $Fe_{75}Si_{10}B_{15}$ and $Ni_{75}Si_{10}B_{12}$ for all measured bend strains, in spite of the fact that the Co-based alloy glass had the lowest hardness (810 VHN, compared with 950 VHN for $Fe_{75}Si_{10}B_{15}$, and 850 VHN for glassy $Ni_{75}Si_{10}B_{15}$).

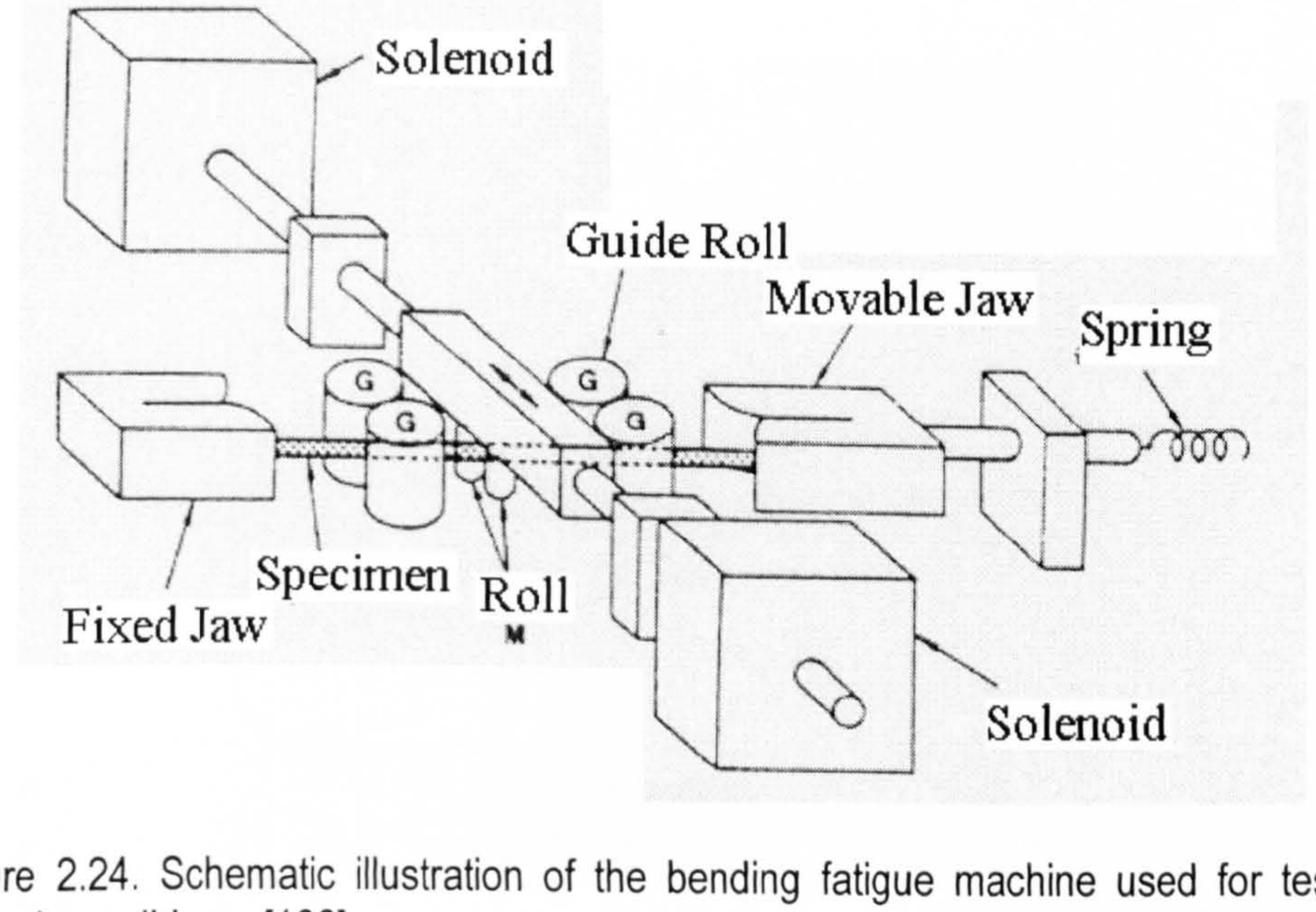

Figure 2.24. Schematic illustration of the bending fatigue machine used for testing amorphous ribbons [106]

Interestingly, they also found that the Vickers hardness increased with increasing number of cycles. They compared the fatigue behaviour of these amorphous alloys with those of polycrystalline molybdenum (99.96 % purity), and polycrystalline type 304 stainless steel (SUS) and concluded that the metallic glass filaments had equal or longer life.

Le *et al.* [107], using the same type of apparatus as that employed by Hagiwara *et al.* [5], found similar high fatigue strength in corrosion solutions for Fe-based wires with the substitution of Cr for Fe. Thus, the fatigue strength was higher than for 304 stainless steel for filaments tested under 3.5 wt % (w/o) NaCl and NH_2SO_4. They attributed the crack initiation in zero and low Cr alloy glasses to accumulation of hydrogen. However, the hydrogen generation was suppressed for glasses with 8 and 11 at % Cr substituted for Fe due to strong passivation of the surface of the wires by Cr oxides which enhanced the corrosion resistance to the media, thus increasing the fatigue performance.

Olofinjana *et al.* [6, 7] reported a higher fatigue limit than that reported by Hagiwara *et al.* [5] and by Inoue *et al.* [108], and attributed this enhancement to the different design of the machine (figure 2.25) [6], where the tensioning load was not connected directly to the test specimen (see figure 2.22), thus eliminating the inertial effects of the reciprocating load which were characteristic of the design of machine employed by the previous workers.

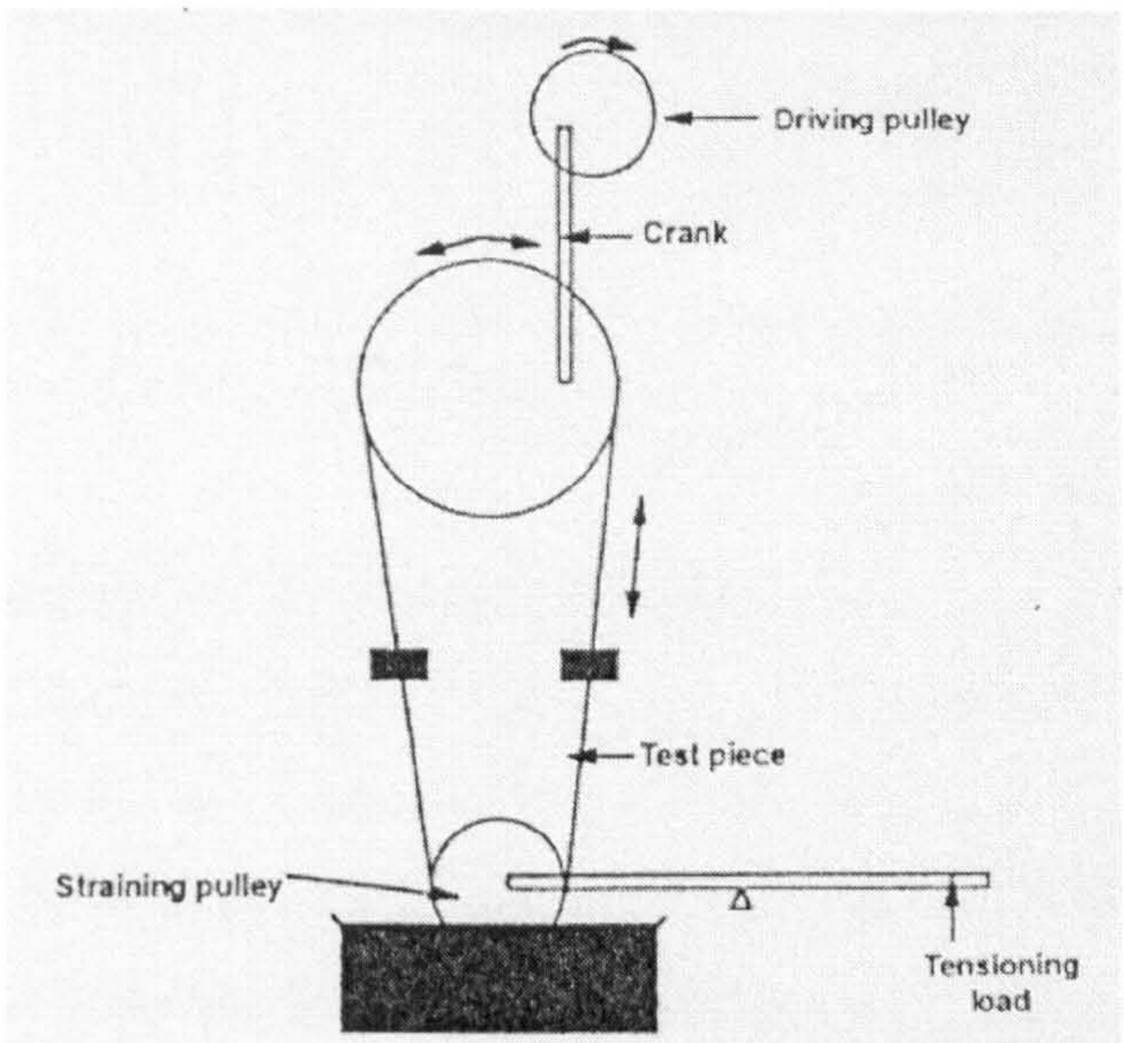

Figure 2.25. Schematic illustration of the bend-type fatigue testing machine used for Olofinjana *et al.* [6].

Figure 2.26 [7] summarises the fatigue limit (bend strain) data obtained by Olofinjana and Davies at normal humidity for two series of Fe-Si-B-based amorphous wires with different contents of Si as a function of Cr content. It can be seen that there is a threshold of Cr concentration, where the fatigue limit began to increase fairly rapidly, at about 2 at % Cr for 10 at % Si, and at about 4 at % Cr for 7.5 at % Si. It was reported [6] that an oxide film composed mainly of Si and Cr oxides or a stoichiometric combination of both (analysed by XPS studies), was probably responsible for the fatigue strength enhancement. Olofinjana and Davies [7] reported that the suppression of fatigue crack initiation by surface films could be viewed in terms of two possible mechanisms: (1) protection against environmental attack, and (2) suppression of surface plasticity.

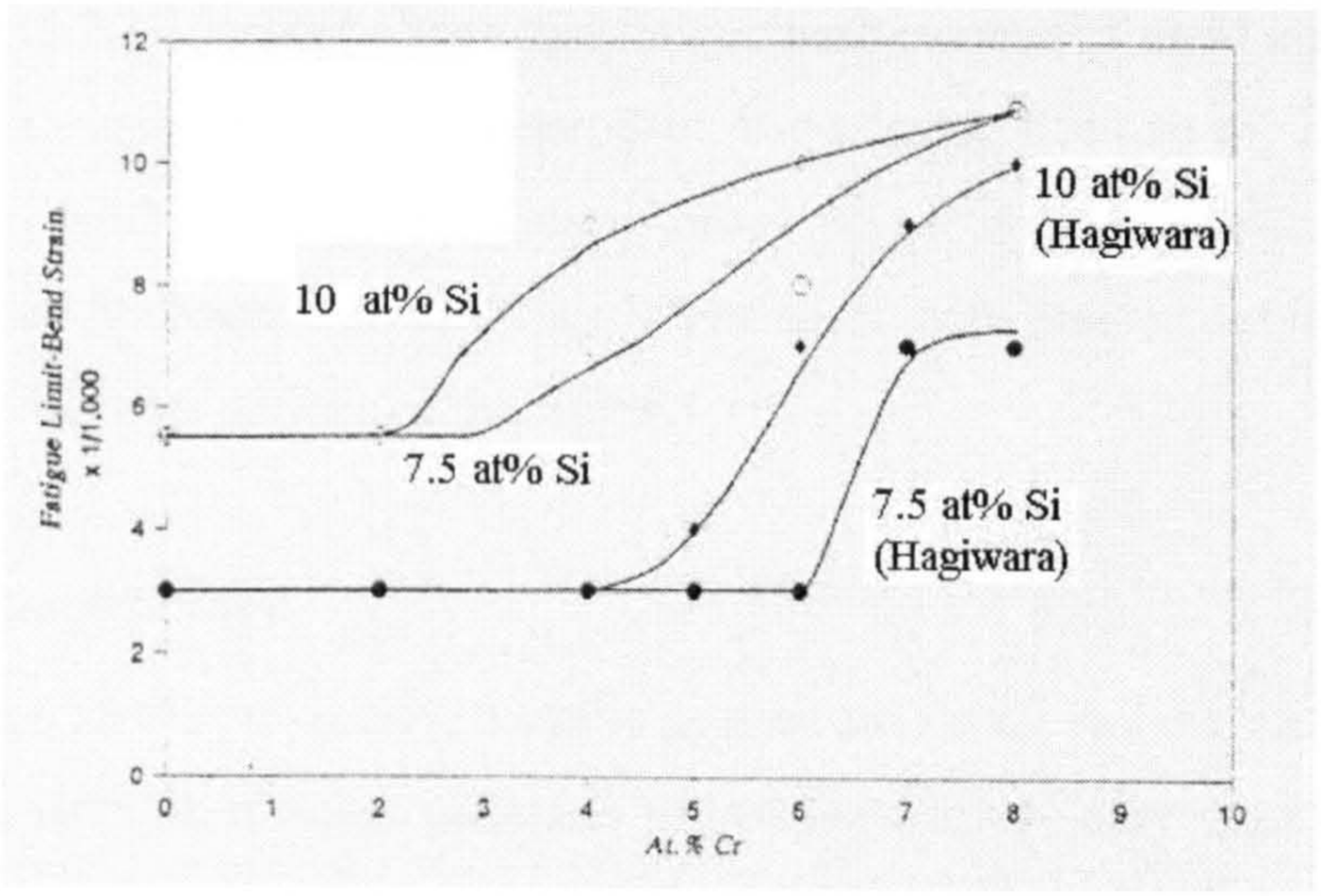

Figure 2.26. Comparison between results obtained using two different fatigue machines designs in function of Cr in $Fe_{85-x-y}Cr_xSi_yB_{15}$ amorphous wires [7].

The fatigue behaviour of the Fe-based amorphous wires tested by Olofinjana *et al.* [6, 7] was similar to that reported [5, 108] under argon atmosphere at 10 % RH. The fatigue limit for 8 at % Cr alloy wire did not change significantly when tested under air humidity (~ 60 % RH), whereas the fatigue limit of $Fe_{77.5}Si_{7.5}B_{15}$ alloy tested at 10% RH increased to a level equivalent to that of $Fe_{69.5}Cr_8Si_{7.5}B_{15}$ alloy wire when tested in ambient humidity (figure 2.27). In deionised water and in 1M NaCl solution, no fatigue limit appeared for the ternary alloy, but the wire containing 8 at % Cr showed a clear fatigue limit in both media.

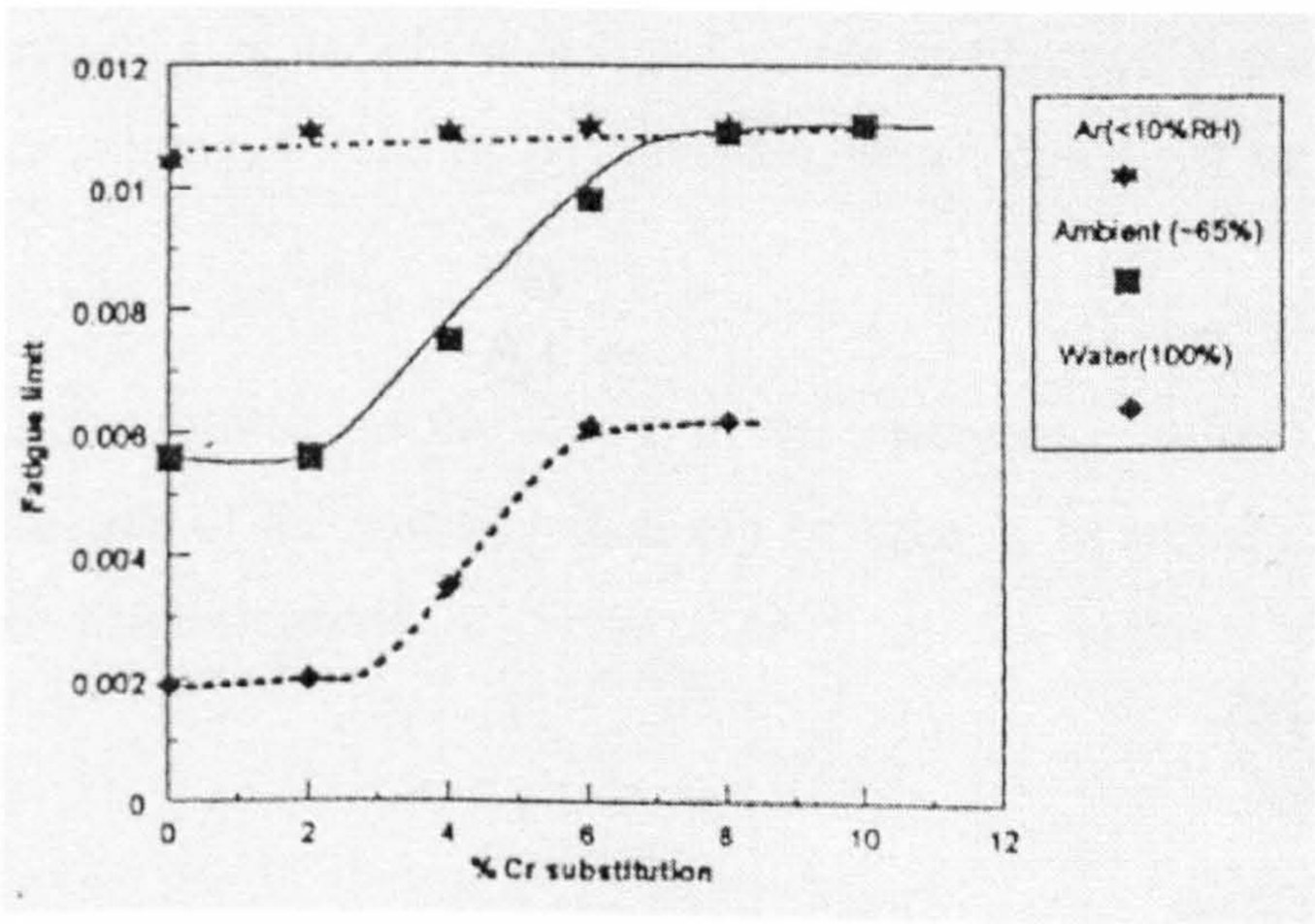

Figure 2.27. Effect of Cr substitution and humidity on fatigue behaviour of $Fe_{77.5-x}Cr_xSi_{7.5}B_{15}$ metallic glass wires [6].

From figure 2.27, it can be seen that fatigue performance of these metallic glasses is both environment- and composition- dependent. It was suggested that the protective action of the oxide film (Si/Cr) prevents or at least substantially retards the corrosive attack which otherwise generate hydrogen ions especially at the shear steps created during the process of bend fatigue on the outer surface of the wires.

Fatigue fracture

As has been stated previously, metallic glasses are strong and ductile. But they differ from other high strength metallic materials in that they do not have normal metallurgical microstructure and that they manifest a very localised nature of the plastic deformation process, where yielding proceeds by nucleation and propagation of discrete shear bands. Amorphous metals are particularly suited for testing the fracture theory of an ideal material, which is assumed to be homogeneous, elastic and perfectly plastic.

The first fatigue tests carried out on amorphous alloys were performed in ribbons ($Pd_{80}Si_{20}$) using an electrohydraulic (SUM SVF 1-10 type) fatigue machine based on tension/tension stress cycles. The ratio of the fatigue limit to the tensile strength was found to be about 0.33 [109].

The fracture surface consisted of two regions, one being a plane making an angle of about 45° to the stress axis and containing a vein pattern that was perpendicular to tensile fracture. This surface was assumed to be formed by unstable shear rupture in the final stage of fracture. The other region had characteristic features peculiar to fatigue-induced fracture surfaces, often containing a void or an inclusion which could act as a fatigue crack initiator.

Some striations formed on the slopes of the plateau (or valley). Such striations covered the whole area of the slopes, which can be seen in figures 2.28(*b*) and 2.28(*c*), which are higher magnifications of figure 2.28(*a*) of the regions marked *a* and *b*, respectively.

(*a*)

(*b*)

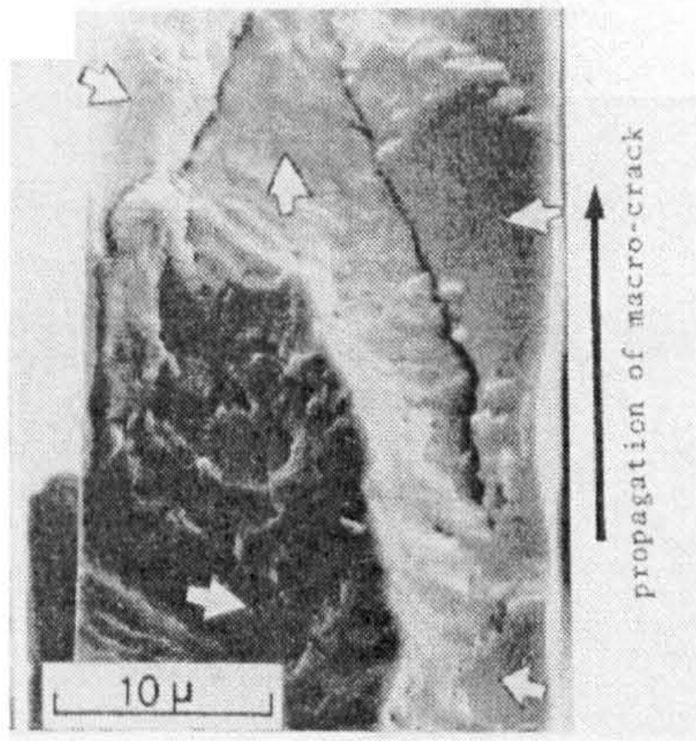

(*c*)

Figure 2.28. (*a*) Fatigue fracture surface of $Pd_{80}Si_{20}$ amorphous alloy ribbon, (*b*) and (*c*) formation of striations in the region *A* in figure (*a*). Local directions of crack growth are indicated by small arrows [109]

The inter-striation spacing increased with increasing distance from the crack initiator, which suggests that the propagation rate increased with increasing crack length. The formation of the plateau was thought to be caused by the growth of fatigue cracks on planes inclined at about 45° to the stress axis. Some shear markings were observed on the surface of the specimen near a fatigue crack. On the other hand, spaced striations and many fissures, visible in the fracture surface, indicated violent fracture, which was followed by unstable rupture in the final stage. These results suggested that immediately after the critical length of a stable fatigue crack, or a critical value of the elastic stress at the tip of the crack, was attained, unstable growth of the crack occurred.

In fatigue tests carried out on $Pd_{80}Si_{20}$ ribbons [110] on tensile to tensile stresses, Ogura *et al.* observed shear markings around a fatigue crack formed after 2.8×10^4 cycles at 245 MPa. A plastic zone was observed around the fatigue crack. A large number of lines were concentrated exclusively in this zone, whose size increased with increasing crack length. Apparently fatigue crack propagation on the specimen surfaces occurred along shear lines, which were formed ahead of the crack. A fatigue shear band in an amorphous alloy is not a so-called persistent shear band, which is generally observed in a crystalline

metal, but is one having a single slip step. An incubation period was anticipated for a fatigue crack to start from the root of a notch. The lower the fatigue stress, the longer the incubation period. The fatigue crack grew at first very slowly then gradually increased its propagation rate and finally caused unstable tensile fracture. The length of fatigue crack, l_c, which caused the unstable fracture, decreased with increasing fatigue range stress. It was suggested that the plastic deformation near a fatigue crack was controlled by the stress intensity factor near the tip of the crack.

In fatigue tests carried out on Ni-Fe-based alloy centre cracked ribbon by Davis [111] in the tensile to tensile mode, it was found that the fatigue crack section and the rapid fracture section lie at 90° to the tensile axis on a microscopic scale. Shear lips about 2 to 4 μm wide at 45° to the tensile axis occurred on either side of the rapid fracture surface. As the crack propagated, the plastic zone size increased so that the shear lips increased in width until the fracture surface underwent transition from square (plane strain) to slant (plane stress). It was assumed that catastrophic failure ensued immediately when the initial popping beyond the fatigue crack occurred.

Fracture toughness values for the centre cracked tension configuration were K_C = 19.23 MPa√m. Average K_C values of 37.22 and 9.3 MPa√m were observed for Ni-Fe-based alloys. Fatigue zones indicated the presence of surface striations. The fracture toughness, K_C increased as the mode of fracture changed from almost fully square (plane strain) to a mixed mode exhibiting increasingly greater amounts of slant (plane stress) fracture. This variation occurred with decreasing sample thickness as the ratio of plastic zone size to specimen thickness increased. It was concluded that the variation in K_C for Ni-Fe-based alloys was primarily a thickness effect.

Examination of the plane strain fracture region (chevron pattern), indicated that it was perpendicular to the tensile axis only on a gross scale. In detail, it consisted of a sawtooth pattern with surfaces inclined to the tensile axis. Examination of opposing fracture surfaces indicated that a 'valley' on one surface was matched by a 'peak' on the other surface. Closer inspections revealed that the chevron surfaces were marked by a fine scale, equiaxed vein pattern. It seemed likely, that these surfaces were produced by shear rupture. The striations on the fatigue fracture surface showed no evidence of a vein pattern. It appeared that the fatigue crack was produced under pure alternating shear conditions.

Fatigue cracks associated with shear bands usually nucleate at the surface of specimens. The propagation behaviour of fatigue cracks in metallic glasses is largely based on the fact that crack tips are attended by plastic zones composed of intense shear bands. At high ΔK levels striations are seen, but at low ΔK levels they are absent. Initiation of fatigue cracks may be delayed in heat-treated metallic glasses that contain a dispersion of soft metallic crystals [112].

In $Ni_{78}Si_{10}B_{12}$ amorphous ribbons fatigued under monotonic loading conditions [70], the fracture surfaces near the fatigue threshold stress intensity range, ΔK_{th}, were perpendicular to the loading axis and exhibited fine ridges extending in the direction of crack propagation. The crack tip was attended by a plastic zone, which consisted of a single shear band about 0.5 μm long. It was proposed that the ridges were the decohered ligaments of the shear band, and that the very low ΔK_{th} value found in the alloy could be attributed to the ease of nucleation of such localised shear bands in metallic glasses.

It was found [70] that with crack growth rates above 10^{-6} mm cycle^{-1} ($\Delta K \geq 2$ MPa$\sqrt{m}$) fracture morphologies started to change and fracture surfaces become characterised by paraboloidal facets. The crack tip plastic zone was no longer a single shear band but was comprised of a number of bands that form a pattern similar to a slip line field. On increasing ΔK from 5 to 9 MPa$\sqrt{m}$, the size of the plastic zone increased form 20 to 45 μm and the length of the paraboloidal facets enlarged from 30 to 50 μm. This correlation between the size of the facets and the size of shear bands implies that the crack growth in this region occurred by the advance of the crack front along one of the bands within the plastic zone. At growth rates above 10^{-5} mm cycle^{-1} ($\Delta K \geq 10$ MPa$\sqrt{m}$) the proportion of the facets tended to decrease in favour of areas covered by periodic fracture markings in the form of curved lines parallel to the crack front, and the plastic zone was then composed of a much larger number of shear bands than those for lower ΔK levels. Thus, with an increase in shear band density, crack growth occurred by the rupture of ligaments between the bands and led to the formation of periodic fracture markings. Striations appeared at $\Delta K \geq 30$ MPa$\sqrt{m}$, and exhibited spacings that correlated with the macroscopic crack growth rate. Above a critical ΔK ($\approx 0.75\ K_c \approx 50$ MPa$\sqrt{m}$) shear lips started to develop at the edges of the ribbons, the size of which was controlled by the maximum static load K_{max}.

Annealing the amorphous alloy to yield a partly crystalline structure produced an increase in ΔK_{th} and reductions in both the near-threshold and intermediate crack growth rates. The heat treatment for 7 min at 440 °C did not change the fatigue crack propagation rate. The fracture morphology contained facets of 5-10 μm, which was smaller than the facets in the initial amorphous alloy. This decrease in facet size was thought to be due to homogenisation of the slip distribution caused by nickel particles. Boron enrichment of the amorphous matrix could play a major role in reducing near-threshold crack growth rates. It was found that at $\Delta K \geq 10$ MPa$\sqrt{m}$ crack growth occurred by the decohesion of the nickel particle-matrix interfaces.

Olofinjana and Davies [6, 7, 55] found fracture surface morphologies similar to those observed for silicate glasses and ceramics failed in fatigue or in tension, where the primary fracture characteristics were classed as "mirror", "mist", "hackle" and crack branching patterns, shown schematically in figure 2.29 [55]. Based on their observations, they found that for high strains (low cycles) these characteristic features were not fully developed during fracture whereas, in contrast, for low strains (high cycles), these features were clearly manifested.

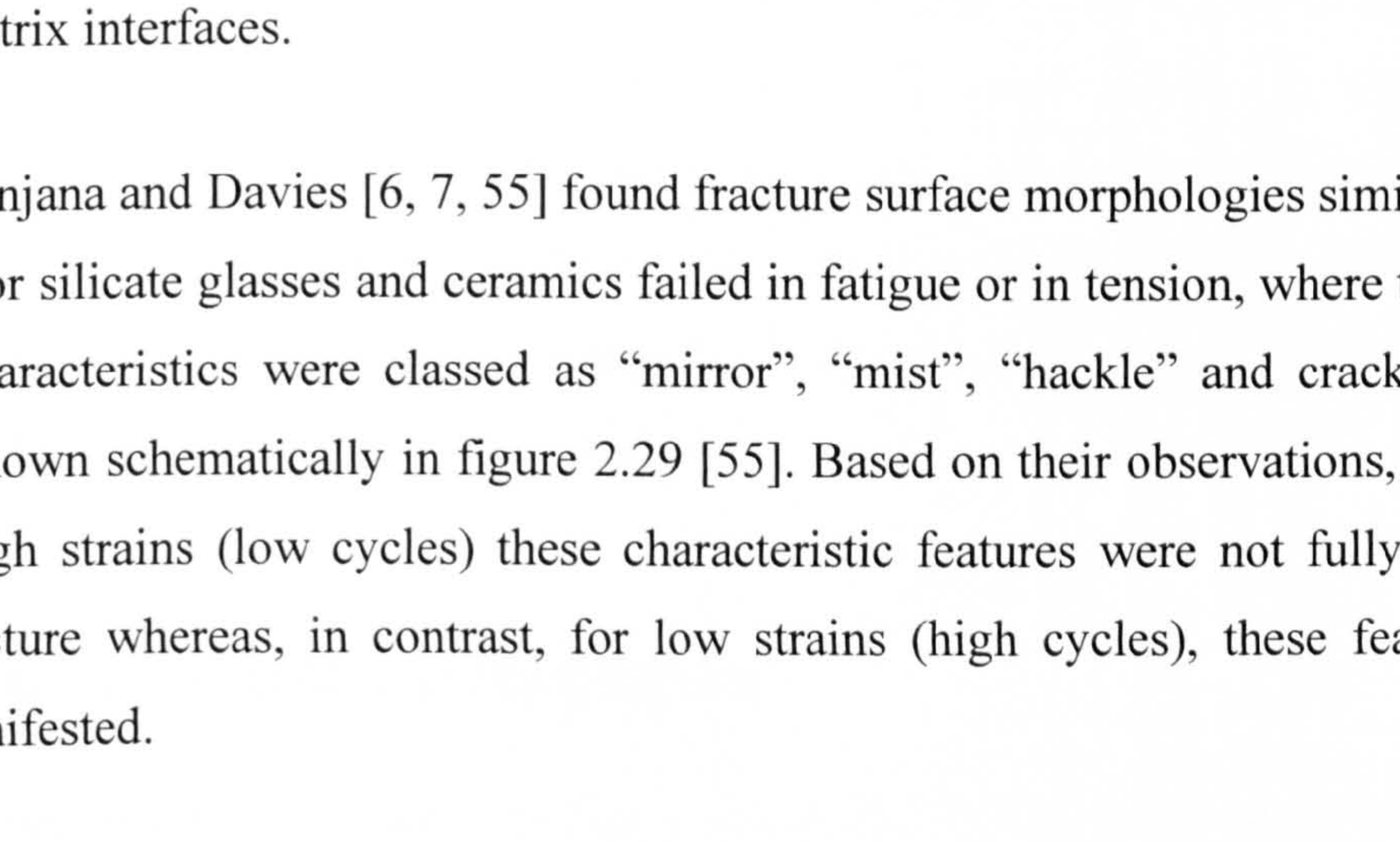

Figure 2.29. Schematic illustration of the nomenclature for fatigue fracture features reported by Olofinjana and Davies [55].

Similar mechanisms of crack propagation were found in wires tested in four different media, air at normal humidity (65% RH), dry argon, deionised water, and 1M NaCl solution [6, 7, 55]. Olofinjana and Davies [7, 55] proposed on the basis of these

observations, the following mechanism: in the absence of a minimum level of chromium in the alloy or in the presence of atmospheric moisture, corrosion cracking is thought to occur at shear bands. The bands would be expected to act anodically with respect to the matrix material because of its increased structural disordering. The increased free volume within the glass structure in the band would also provide a preferential path for the diffusion of hydrogen, produced as a corrosion product, thus embrittling the alloy preferentially along the band.

The fatigue threshold stress intensity (in this case when transition to crack branching began and was marked by the mist and hackle pattern,) was estimated to be approximately 14 MPa$\sqrt{m}$. The stress intensity at the start of the crack branching ΔK_B, was estimated to be 20 to 24 ΔK_B [55]. It was reported that this ΔK_B value is in good agreement with the fracture toughness of metallic glasses which is reported to vary between 10 and 70 MPa$\sqrt{m}$ for samples loaded in tension and pure shear [92, 111].

2.5 Corrosion resistance

Amorphous alloys are free of defects associated with the crystalline state such as grain boundaries, and stacking faults. Rapid quenching prevents solid state diffusion during solidification. Hence, they are also free of defects formed by solid state diffusion such as second phases, precipitates, and segregates. Amorphous alloys are, therefore, regarded as ideally chemically homogeneous materials. Since ordinary crystalline metals often suffer localised corrosion, owing to the presence of chemically heterogeneous sites on the metal surface, the chemically homogeneous amorphous alloys should be resistant to localised corrosive attack [113]. A large fraction of metalloid atoms contained in the alloys greatly affects their corrosion behaviour.

Polarisation measurements are used in order to describe the corrosion behaviour of metallic glasses [113]. When a potential rise in an electrochemical reaction of metals with environments results in the formation of a new corrosion product, which is a stable solid in the corrosive media and able to cover the metal surface, the dissolution rate of the metal substantially decreases. This corresponds to passivation and the corrosion product film covering the metal surface is called a passive film. If the solution contains aggressive ions

such as halides, then a further rise in potential leads to pitting corrosion for crystalline corrosion-resistant metals such as stainless steels; a major area of metal surface is covered by a passive film, but its localised breakdown by halide ions results in the formation of pits, where preferential corrosion attack proceeds deeply into the material. The nucleation and growth of pits are easily detected by a sharp increase in the current density by anodic polarisation.

Amorphous iron-metalloid alloys, without addition of a second metallic element generally show higher corrosion rates than crystalline iron, presumably because they are in a higher state of free energy . However, their corrosion resistance is improved by addition of almost any metallic element [114] such as Ti, Zr, V, Nb, Ta, Cr, Mo, W, Co, Ni, Cu, Rh, Pd, and Pt. In particular, the addition of Cr is very effective. Cr is more active than iron, and hence the addition of Cr to crystalline iron gives rise to an increase in corrosion rate in aggressive hydrochloric acids. On the contrary, the addition of Cr to amorphous iron-metalloid alloys significantly decreases the corrosion rate [115]; for instance, amorphous Fe-Cr-$P_{13}C_7$ alloys containing 8 at% or more Cr do not show a detectable weight loss, even in 2 *N* HCl at ambient temperature, due to spontaneous passivation. Except for tantalum, all commercial corrosion-resistant crystalline alloys such as stainless steels, high nickel alloys, etc. are not able to passivate spontaneously even in 1 *N* HCl at room temperature.

The combined addition of Cr and Mo to a glass forming alloy further improves the corrosion resistance; some Fe-Cr-Mo-metalloid alloys passivate spontaneously even in hot concentrated hydrochloric acids such as 12 *N* HCl at 60 °C. The addition of Cr is also effective in increasing the corrosion resistance of amorphous cobalt- and nickel- based alloys.

2.5.1 Passive film

Almost all metallic species occur naturally as oxides or salts, indicating that the oxidised state is more stable than the metallic state in natural environments. In other words, corrosion is unavoidable for the majority of metals in natural environments. However, when corrosion products cover the metal surface, they are able to act as a barrier against further corrosion attack. Their chemical stability and uniformity determine the protective quality of the corrosion product films.

As can be seen in figure 2.30, the corrosion resistance of amorphous iron-metalloid alloys without adding a second metallic element is generally lower than the crystalline iron [113]. Nevertheless, the corrosion resistance of amorphous metal-metalloid alloys increases by the addition of a second metallic element. This is due mainly to the formation of a protective corrosion product film in which cations of the second metallic element are concentrated. The metallic elements that play such a role in amorphous iron-metalloid alloys are Ti, Zr, V, Nb, Ta, Cr, Mo, W, etc. [116]. Among them, Ti, Zr, and Cr form their own passive films which have a highly protective quality, and hence the alloys containing these metallic elements generally have high corrosion resistance.

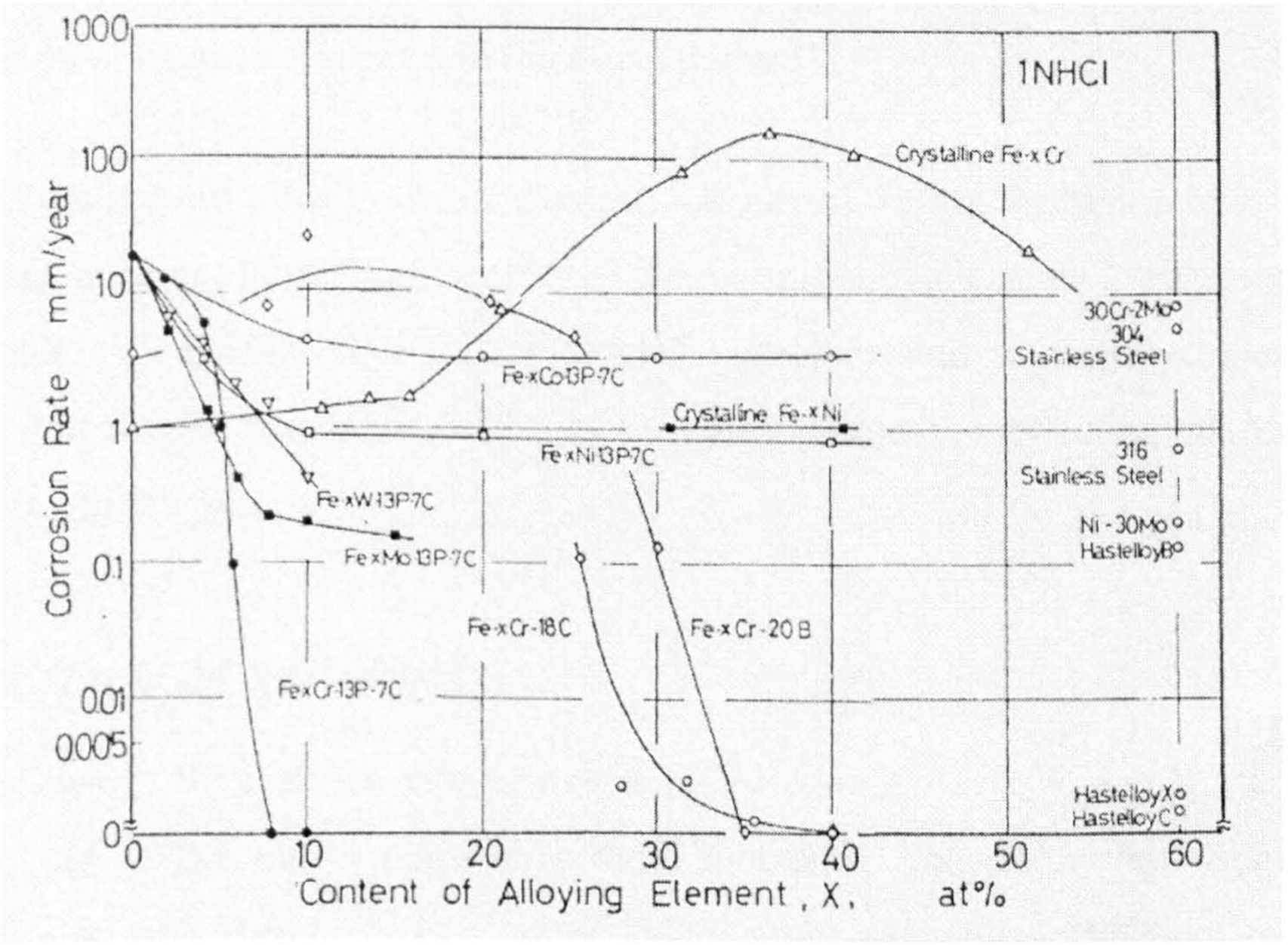

Figure 2.30. Changes in average corrosion rates of amorphous Fe-M-metalloid alloys in 1 *N* HCl at 30 °C as a function of alloying element M. Corrosion rates are also shown for comparison [113].

One of the differences between passive films and ordinary corrosion product films is that the cations that are beneficial in improving the protective quality of the films are highly concentrated in the passive films.

Amorphous metal-metalloid alloys are able to accumulate protective hydrated chromium oxyhydroxide in the passive film, and accordingly the passive films formed on them have quite a high protective quality [113]. In fact, alloying elements are generally

more beneficial to the corrosion resistance of amorphous alloys than of crystalline alloys. This is attributable to the rapid formation of a protective film and the chemical homogeneity of the amorphous alloys.

2.5.2 Rapid film formation

When a protective film on the surface of a metallic material is mechanically or chemically broken, rapid repassivation prevents serious corrosion attack. Such passivation and a high concentration of beneficial elements in the passive film provide the high corrosion resistance. When alloys that are able to passivate are exposed to an aggressive solution, the faster the active dissolution, the faster is the passivation the higher the concentration of beneficial species in the passive film [113].

If an amorphous alloy contains elements beneficial for the formation of a protective passive film, such as Cr, the high activity of the amorphous state leads to rapid enrichment of the beneficial species at the alloy-solution interface and to rapid formation of a relatively rich passive film which will thus be highly protective, reflecting the low current density through the film.

2.5.3 Effects of metalloids

Increases in the content of minor metalloid elements Si, B, C and P increases the corrosion rate of the alloys containing these elements. The phosphorus-bearing alloy exhibits the highest current density immediately after mechanical abrasion, that is, the highest initial reactivity of the alloy but then shows the lowest steady state current density corresponding to the highest protective quality of the film. It is evident that phosphorus is the most effective metalloid element in increasing the rate of protective film formation.

The presence of silicon and boron in amorphous alloys does not greatly accelerate active dissolution of alloys, and hence these elements are less effective than phosphorous or carbon in increasing the rate of passive film formation. Furthermore, they form silicate or borate films, and accordingly prevent the formation of a passive hydrated oxyhydroxide film with a high protective quality. Consequently, although the addition of boron and/or

silicon to amorphous alloys is effective in improving the corrosion resistance, it is less effective in comparison with the addition of phosphorus and/or carbon [113].

2.5.4 Homogeneity of the alloy

In general, the corrosion resistance of almost all metallic materials is determined by the composition, stability, and uniformity of the surface film formed as well as by the kinetics of formation. It has been explained above that amorphous metal-metalloid alloys can be highly corrosion resistant with a protective passive film containing a high concentration of beneficial species with high stability. When the amorphous alloys possess such superior characteristics, the corrosion resistance will depend upon the uniformity of the passive film formed, since in crystalline metals and some amorphous alloys it generally contains weak points whose activity is responsible for the passive current density in aggressive solutions. In this connection, the homogeneous nature of amorphous alloys is responsible for their high passivating ability and their high resistance against pitting. Crystalline defects are often chemically heterogeneous and tend to act as initiation sites for corrosion. Amorphous alloys are, however, free of defects associated with the crystalline state. In addition, rapid quenching from the liquid state prevents solid state diffusion during quenching and precludes segregation, precipitation, and formation of other compositional fluctuations. Accordingly, the amorphous alloys are regarded as ideal alloys that are chemically homogeneous and single phase, which provides the high corrosion resistance.

The chemical heterogeneity in crystallised amorphous alloys leads to a high density of weak points in the passive film and to localised corrosive attack. Heat treatment of amorphous alloys gives rise to the formation of various crystalline metastable phases in the amorphous matrix before the formation of stable crystalline phases. For instance, Kulik *et al.* [117], studied the change in the corrosion behaviour of amorphous $Ni_{36}Fe_{32}Cr_{14}P_{12}B_6$ alloy by heat treatment and found that crystallisation of the alloy resulted in a decrease in the corrosion resistance to the level of ferritic 17Cr stainless steel.

After isothermal heat treatment at 430 °C for different times, amorphous $Fe_{70}Cr_{10}P_{13}C_7$ alloy [118], initially passivates spontaneously in 1 *N* HCl. However, as soon as the first metastable crystalline phase is formed in the amorphous matrix, the anodic

current density increases and the corrosion potential suddenly changes from the passive region to the active region, indicating the detrimental effect of the formation of compositional heterogeneity.

Grain boundaries are considered to act as active surface sites with respect to corrosion. The density of grain boundaries in rapidly quenched crystalline alloys is significantly higher than the conventional crystalline alloys. Nevertheless, the rapidly quenched alloys possess a considerably higher corrosion resistance than conventional crystalline alloys with the same average composition [118].

Anthony and Cline [119] found that rapidly quenched crystalline type 304 stainless steel after laser surface melting possesses an enhanced corrosion resistance because of the avoidance of various compositional fluctuations by rapid solidification.

Rapidly quenched single phase alloys show significantly high corrosion resistance than crystalline stainless steel, even if the rapidly quenched alloys are crystalline [113]. If the crystalline phase formed in the amorphous matrix is not different from the amorphous matrix in terms of apparent average composition, heat treatment considerably decreases the corrosion resistance. Crystal defects, such as grain boundaries, formed during rapid quenching from the liquid state may be chemically clean and may not act as preferential active surface sites with respect to corrosion. In contrast, heat treatment inevitably induces solid state diffusion and hence results in various compositional fluctuations such as precipitation, segregation, and other compositional gradients, and they may thus act as dominant active surface sites with respect to corrosion.

2.5.5 High resistance to localised corrosion

If the high corrosion resistance of amorphous alloys is mainly attributed to their homogeneity, the alloys should be quite resistant against initiation of localised corrosion attack. However, when a crevice assembly exists, they may suffer serious corrosion attack, since crevice corrosion does not require surface heterogeneity for initiation. For instance, Devine [120] and Lee and Devine [121] found that plastic deformation to a total strain of 3.6 % in $Ni_{35}Fe_{30}Cr_{15}P_{14}B_6$ amorphous alloy, had no effect on the passive corrosion rate nor on the pitting corrosion resistance. However, cold-rolling the alloy to 32 % reduction

in thickness markedly increased the corrosion rate. After anodic polarisation in 1 % NaCl solution, severe pitting corrosion was found due to crevice corrosion at the interactions of surface microcracks which were formed by heavy cold-rolling.

Amorphous metal-metalloid alloys containing Cr possess high resistance to propagation of pitting and crevice corrosion owing to high passivation ability arising mainly from the high reactivity of metalloid-containing amorphous alloys, which results in the rapid formation of a thick and impermeable chromic oxide film.

2.5.6 Stress corrosion attack and hydrogen embrittlement

Stress corrosion cracking of crystalline solids is associated with grain boundaries or certain crystallographic planes. Pampillo [122] reported that $Ni_{49}Fe_{29}P_{14}B_6Al_2$ amorphous alloy failed by immersion in a 3.5 % NaCl solution at 26 °C after 117 hr under an applied tensile stress, of about 75 % of the fracture stress in air.

Some amorphous alloys suffer hydrogen embrittlement when they are corroded under an applied tensile stress or when hydrogen is charged into them [123, 124]. When a metallic specimen is corroded by immersion in an aqueous solution, the following cathodic reactions take place:

$$2H^+ + 2e \rightarrow H_2 \qquad (2.a)$$

$$O_2 + 2H_2O + 4e \rightarrow 4OH^- \qquad (2.b)$$

The sum of these cathodic reaction rates is equal to the corrosion rate of the metal. Reaction (2.*a*) consists of the following elementary reactions:

$$H^+ + e \rightarrow H_{ads} \qquad (2.c)$$

$$2H_{ads} \rightarrow H_2 \qquad (2.d)$$

or

$$H_{ads} + H^{+} + e \rightarrow H_2 \qquad (2.e)$$

Accordingly, corrosion of metal results in the formation of hydrogen atoms adsorbed on the metal surface, H_{ads} being an intermediate species of cathodic reaction. Some of the adsorbed hydrogen atoms are then absorbed in metals as

Consequently, aqueous corrosion leads to absorption of hydrogen into metal and often to hydrogen embrittlement.

The fracture strength of $Fe_{53}Cr_7Ni_{20}P_{14}C_6$ alloy in $5N$ H_2SO_4 + $0.1N$ NaCl, for instance, decreases with increasing time of a tensile test in the aqueous solution, indicating that embrittlement results from deformation in the aqueous solution [123]. It is evident that the decrease in fracture strength and strain is due to hydrogen embrittlement, since the fracture strength of the specimen embrittled by the tensile test in the solution is completely recovered by a subsequent heating in oil. 5Cr alloys, for instance are more susceptible to hydrogen embrittlement than the 10Cr alloys [123]. This indicates that an improvement of the corrosion resistance greatly increases the resistance to hydrogen embrittlement. In addition, the types of metalloid species contained in the alloys significantly affect the susceptibility to hydrogen embrittlement.

Chapter III: EXPERIMENTAL

Two series of metallic glass alloys were produced in the form of ribbon and wire. Series A had the general formula $Fe_{78-x}Cr_xSi_{10}B_{12}$ with x = 0, 3.5, 6.25 and 8 at. %; and series B had the general formula $Fe_{77.5-x}Cr_xSi_{7.5}B_{15}$ with x = 0, 4 and 8 at %. Crystalline high tensile (HT) steel wire was also used in some experiments for comparison. The HT steel wire studied is a standard brass plated tyre reinforcement filament (245 μm diameter) supplied by Goodyear, Luxembourg.

3.1 Ingot preparation

30 g ingots of each alloy were prepared from high purity electrolytic iron (99.9 %), chromium (99.9 %), silicon (99.999 %) and boron (99.9 %). The elements were weighed using a precision balance and the resulting mixtures were placed in crucibles machined from graphitic boron nitride. The crucible and its contents were placed in a small scale radio-frequency (R.F.) induction melting unit, figure 3.1. The system was evacuated to a pressure of approximately 13.3 Pa and then flushed with pure argon at atmospheric pressure. It was evacuated again to a pressure of about 6 Pa and finally refilled with pure argon at atmospheric pressure. The alloys were melted under a flow of pure argon for approximately 4 minutes and allowed to cool under vacuum. This procedure ensures homogenisation of the alloys, resulting in the production of ingots with weight losses typically less than 0.3 % for boron which was confirmed by chemical analysis using gravimetric methods. Hence, the agreement between nominal and actual composition was generally satisfactory (see table 3.I).

Table 3.I Chemical analysis results

	wt % before ingot melting				wt % after ingot melting			
ALLOY	Fe	Cr	Si	B	Fe	Cr	Si	B
$Fe_{78}Si_{10}B_{12}$	91.39	-	5.88	2.72	91.18	-	5.91	2.51
$Fe_{74.5}Cr_{3.5}Si_{10}B_{12}$	87.52	3.83	5.9	2.73	87.45	3.96	6.11	2.48
$Fe_{71.75}Cr_{6.25}Si_{10}B_{12}$	84.15	6.84	5.92	2.73	84.85	6.76	5.94	2.45
$Fe_{70}Cr_{8}Si_{10}B_{12}$	82.6	8.8	5.9	2.7	82.86	8.51	6.1	2.53
$Fe_{77.5}Si_{7.5}B_{15}$	92.1	-	4.5	3.4	92.34	-	4.51	3.15
$Fe_{73.5}Cr_{4}Si_{7.5}B_{15}$	87.6	4.4	4.5	3.5	88.1	4.55	4.58	2.77
$Fe_{69.5}Cr_{8}Si_{7.5}B_{15}$	83.1	8.9	5.5	3.5	83.47	8.72	4.6	3.21

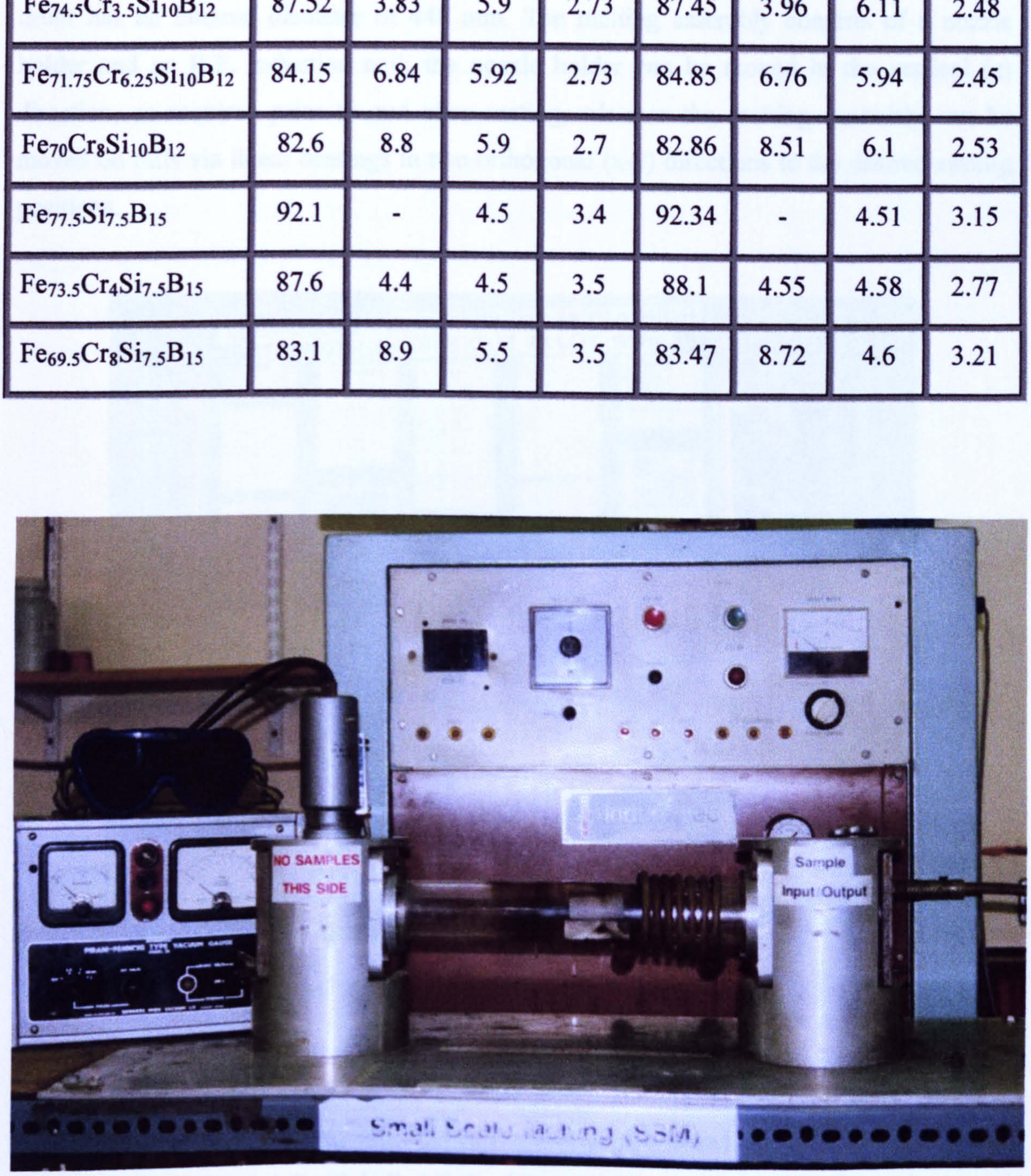

Figure 3.1. Photograph of the small scale melting unit used to melt the series A and B alloy systems.

3.2 Wire casting

Continuous amorphous wires were produced using the rotating water bath melt spinning process [4], (see figure 3.2). This process involves the streaming of a fine jet of molten alloy into a fluence of cold water (moving in a rapidly rotating drum at almost the same velocity as the jet) such that the alloy rapidly solidifies and vitrifies. The casting drum has an internal diameter of 440 mm. The melting assembly consists of a nozzle holder and an R.F. induction coil; the nozzle holder can be moved in the vertical (z) direction, as required prior to and after casting, whereas the melting assembly can be moved on rails via linear bearings in two orthogonal (x-y) directions to the desired casting positions.

Figure 3.2.- Photograph of the rotating water bath melt spinning apparatus.

To produce amorphous wires, a round orifice of the desired diameter (typically within the range 90 - 135 μm) was opened (measured with a travelling microscope) at the tip of a sealed quartz tube (labelled 2 in figure 2.12) by grinding on emery paper to produce a nozzle. The nozzle was then washed, rinsed with acetone and dried; the ingot was loaded into the tube after washing it with acetone. The quartz tube was mounted

with its axis along the centre line of an induction R.F. coil. At this stage the quenching water was mixed with ice to cool it down to approximately 1 °C. The drum was accelerated to the selected angular speed, measured with an optical tachometer, allowing enough time so that it reached a steady velocity. The water was then introduced into the drum to a depth of about 19 mm, previously set with a depth indicator. A rotating liquid layer was thus established at the inner surface of the drum by centrifugal force. The melting assembly, which was in the elevated position during melting, was lowered down to the ejection position. A jet of molten alloy was ejected from the nozzle into the rapidly rotating layer of quench liquid (figure 3.3) by application of an appropriate predetermined argon over-pressure (typically 400 kPa). After molten metal ejection, the melting assembly was then removed from the drum, and the latter was rotated to the horizontal position before stopping the driving motor for removal of the cast wire. The drum was then slowly brought to an angle of ~45° to the vertical in order to empty it of water. The wire casting parameters are given in table 3.II.

Figure 3.3. Stream of molten alloy during the process of wire casting.

Table 3.II. Wire casting parameters

Nozzle orifice diameter	90 - 135 μm
Distance water/nozzle	2 - 5 mm
Water depth	19 mm
Ejection over pressure	354.5 - 405 kPa
Angular drum velocity	320 - 370 rpm
Casting angle	~60°

Because of the difficulty of employing a thermocouple for measuring the melt temperature, the initial castings for each alloy were carried out by trial and error and the melting conditions employed for subsequent runs were based on this empirical experience.

3.3 Ribbon casting

Amorphous ribbons having the same compositions as wire samples were required for assessing the fracture toughness of these materials, since the geometrical form of the wire renders them less suitable for this purpose.

Long lengths of amorphous ribbons were produced in a stainless steel sealed-atmosphere chill block melt spinning process (CBMS) chamber, The process involves the streaming of the melt onto the circumferential surface of a rotating copper roll rather than into a bath of water as for wire. The ribbons were prepared from identical alloy ingots to the wires. In this case, the alloy ingot was broken up into several pieces and approximately 10 g of these pieces were normally used. These were washed with acetone and subsequently placed into quartz nozzles with an orifice (~0.8 mm) produced in the same way as those used for casting amorphous wires. The quartz nozzle containing the alloy was accommodated in the centre of an R.F. induction coil. The nozzle was inclined at about 15° to the radial direction, the tip of the nozzle being approximately 5 mm from the roll surface, which was previously polished with emery paper down to 1200 grit followed by

cleaning and thorough degreasing with acetone (see figure 3.4). The chamber was then closed and pumped down to 10^{-4} torr and then back filled to atmospheric pressure using high purity helium in order to obtain dimensionally uniform and ductile ribbons free of entrapped gas pockets on the surface; less uniform ribbons were produced when argon at atmospheric pressure was used. The roll was then accelerated to the selected angular speed, previously calibrated with an optical tachometer. The small pieces of the alloy were melted and ejected under pre-set argon pressure, to produce long lengths of ribbon with thicknesses varying from 34 to 40 μm, and widths ranging from ~1.2 to 1.5 mm. Typical ribbon casting parameters are shown in table 3.III.

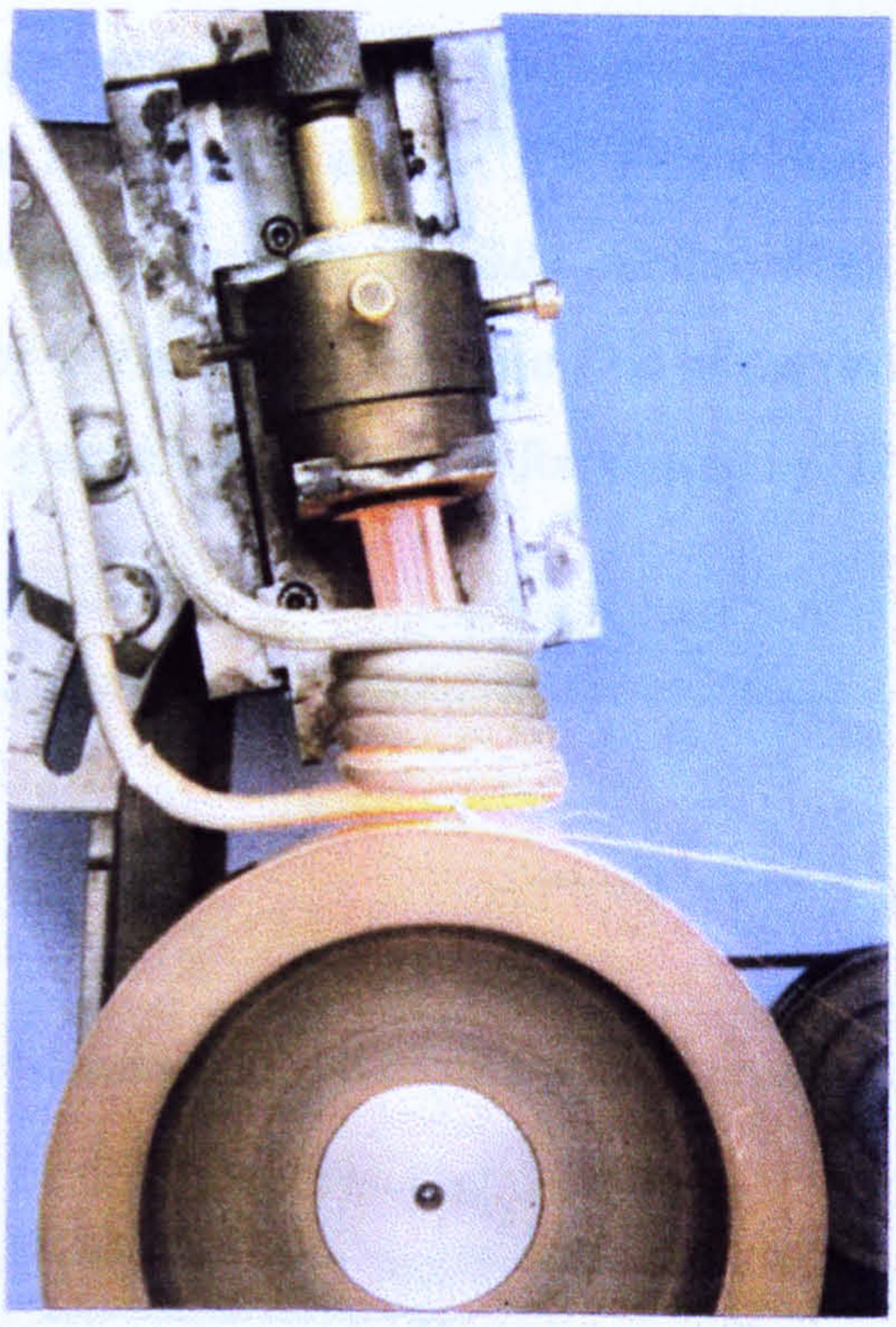

Figure 3.4. Melt spinning apparatus.

Table 3.III. Ribbon casting parameters

Nozzle orifice diameter	~0.8 mm
Wheel velocity	30 - 34 ms^{-1}
Argon over pressure	~15 kPa

3.4 Structure

In order to initially characterise the as-quenched wire and ribbon, specimens approximately 5 mm in length were placed in a simple bend testing rig (figure 3.5). The ductility of both wires and ribbons, was then estimated using the maximum bend strain (λ) on the outer surface of the bent specimen. Assuming that the bend is semicircular, it can be shown that:

$$\lambda = \frac{d_w}{D - d_w} \tag{3.1}$$

where d_w is the wire diameter and D is the distance between the plates at fracture. The sample was considered to be: *a*) *fully ductile*, if the specimen could be completely bent over without fracture, $D=2d_w$ $\lambda = 1$; *b*) *partially ductile*, when some measurable plastic deformation occurred prior to fracture, in this case D is of the order of $2d_w$; and *c*) *brittle*, if fracture occurred without considerable plastic deformation, i.e. $D >> 2d_w$

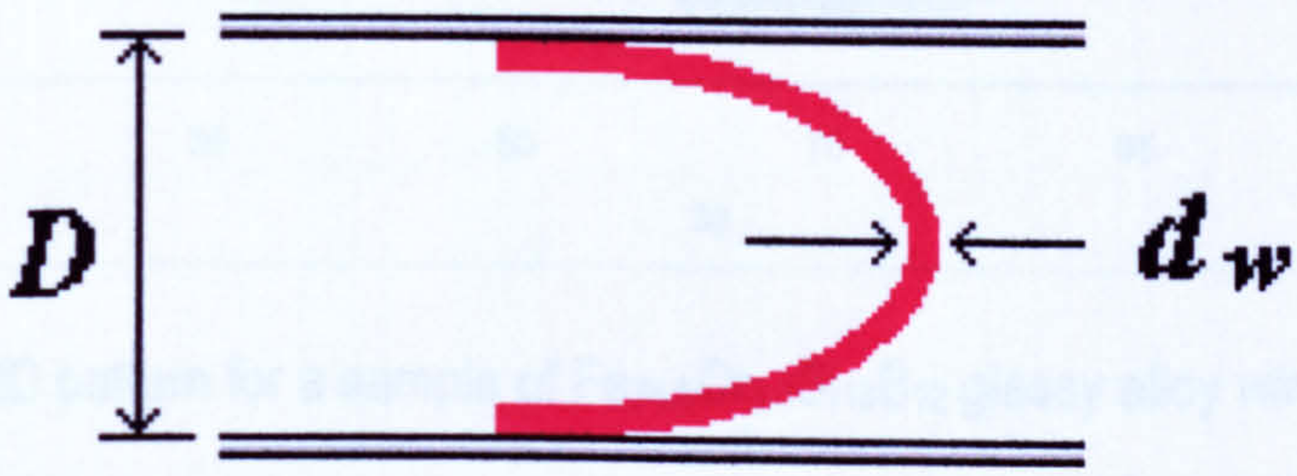

Figure 3.5. Schematic illustration of the ductility test.

3.4.1 X-ray diffraction

In order to obtain more detailed information about the structure, wires showing a bend angle range of 150 to 180° (ribbons for all the alloys studied produced 180° bend without fracture) and ribbons were analysed using x-ray diffraction. Samples were prepared by cutting lengths about 20 mm and gluing them to a flat glass slide using double sided adhesive tape. For ribbons, the surface not in contact with the roll during casting, i.e. the free surface was investigated, since crystallisation during quenching generally initiates

on this surface where the cooling rate is generally lowest, especially in the absence of gas pockets on the roll contact surface.

The samples were mounted in a Phillips PW 1710 computer controlled diffractometer and scanned using Co Kα (λ = 0.179 nm) radiation at 40 kV and 20 mA. Scans were performed over the range 15 to 90° 2θ or 15 to 120° 2θ, in order to check for the presence of any crystalline phases. Both wires and ribbons were classified as being amorphous when the x-ray intensity as a function of diffraction angle showed a typical, modulated liquid-like pattern, (a typical example is shown in figure 3.6).

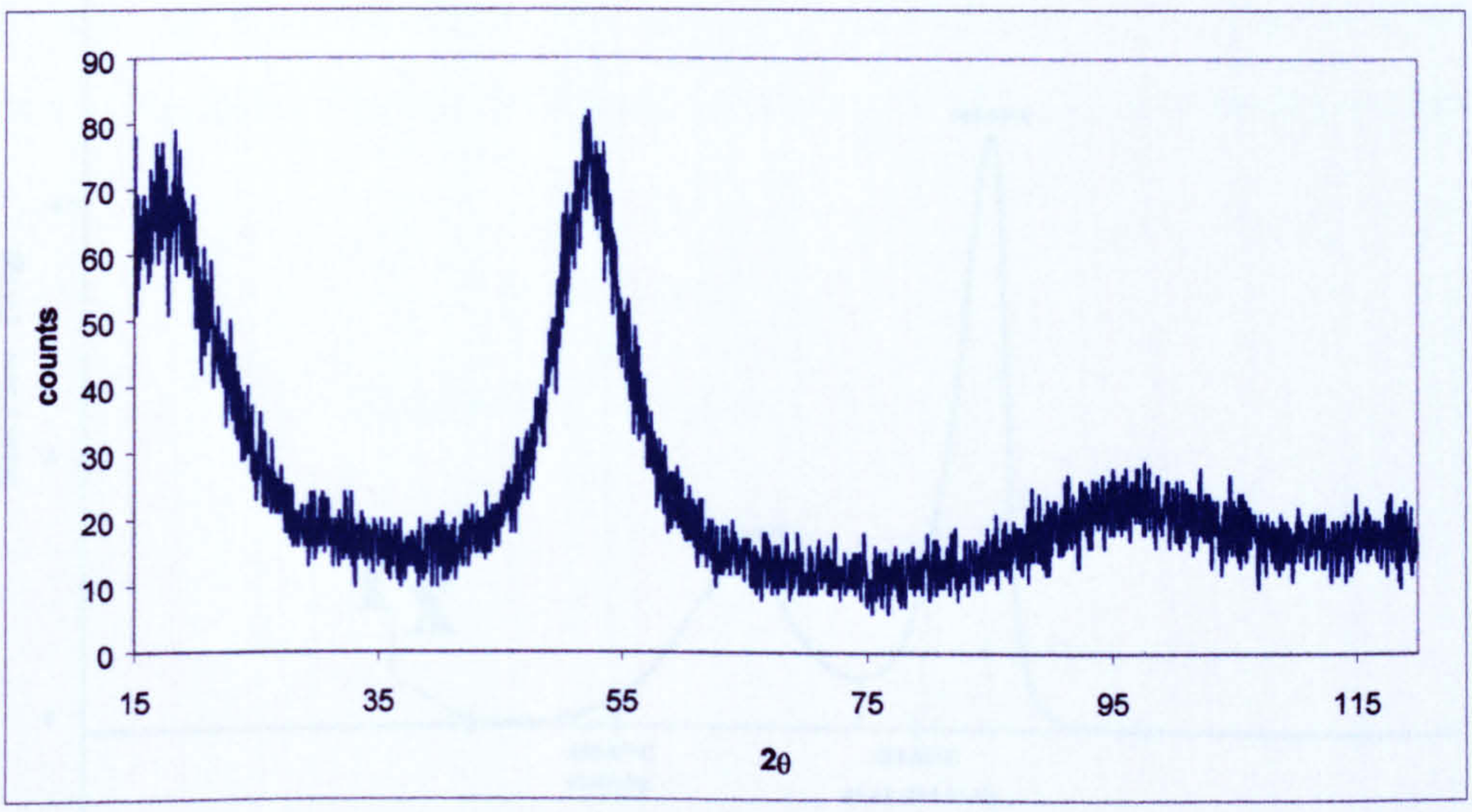

Figure 3.6. XRD pattern for a sample of $Fe_{74.5}Cr_{3.5}Si_{10}B_{12}$ glassy alloy wire.

3.4.2 Differential Scanning Calorimetry

Crystallisation temperatures and the enthalpies of crystallisation of the alloy wires were investigated by differential scanning calorimetry (DSC), using a computer controlled Perkin Elmer DSC-7 series calorimeter with TAS-7 software. Initially, the DSC was calibrated with the melting points of indium and tin, by comparing the scan results at 5 $Kmin^{-1}$ with the published equilibrium data for the standards.

Small lengths of wire ~40 mm in length were washed in a Transsonic T 460/H ultrasonic cleaning unit for 15 min at 25 °C, using acetone, in order to remove any contamination. Once the samples were cleaned, they were cut into smaller lengths (~3mm)

weighing a few milligrams (9-15 mg) and loaded in aluminium pans. The sample was heated at a rate of 20 °C min^{-1} from 20 to 600 °C, employing a nitrogen flow at rate of 120 ml min^{-1} (an empty aluminium pan was used as a reference). Aluminium sample pans were used instead of gold pans because they are cheaper and importantly, give better thermal contact with the calorimeter base, since their bottoms are generally much more uniform.

The onset of crystallisation, defined as the initial deviation from the base line, was considered to be the crystallisation temperature, for all instances, see figure 3.7.

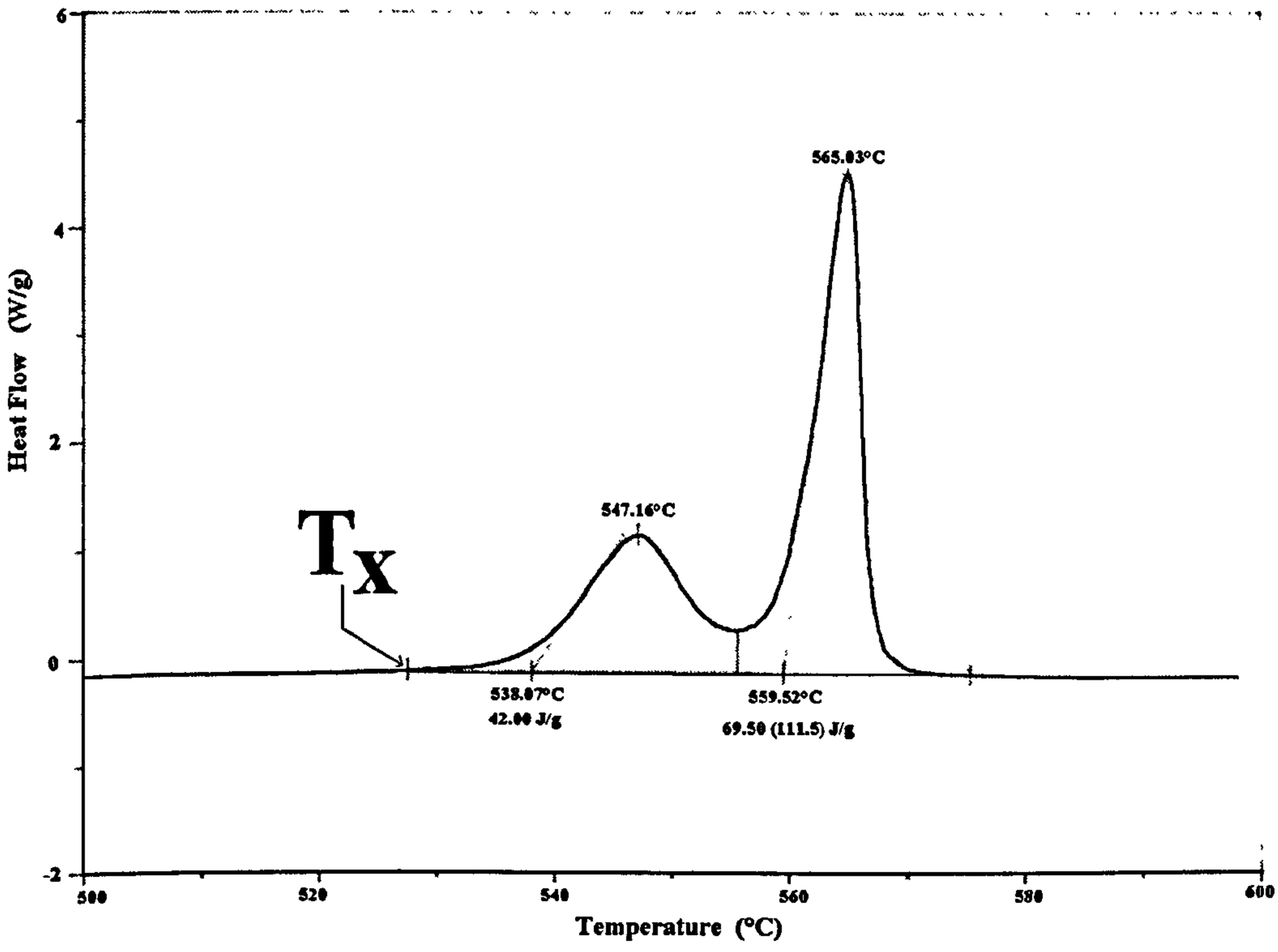

Figure 3.7. Typical DSC curve, showing the point of crystallisation temperature, T_x.

3.5 Mechanical properties

The mechanical properties of the amorphous alloy wires were measured and compared with the properties of HT steel wire which was a standard, brass plated tyre reinforcement filament of 245 μm diameter.

3.5.1 Tensile

The tensile strength of the alloys was measured on wires samples using a Hounsfield universal testing machine at a strain rate of 1.66×10^{-4} s^{-1}. Conventional tensile testing methods are generally unsuitable for this type of wire; therefore, the test samples were mounted over pulleys as shown in figure 3.8. A typical force-extension graph is shown in figure 3.8.A. The gauge length was 60 mm. The fracture stress was calculated using:

$$\sigma_f = \frac{F}{A} \tag{3.2}$$

where F was the force at which the sample fractured and A the fractured wire area determined using SEM. The quoted results are the mean of 5 separate measurements.

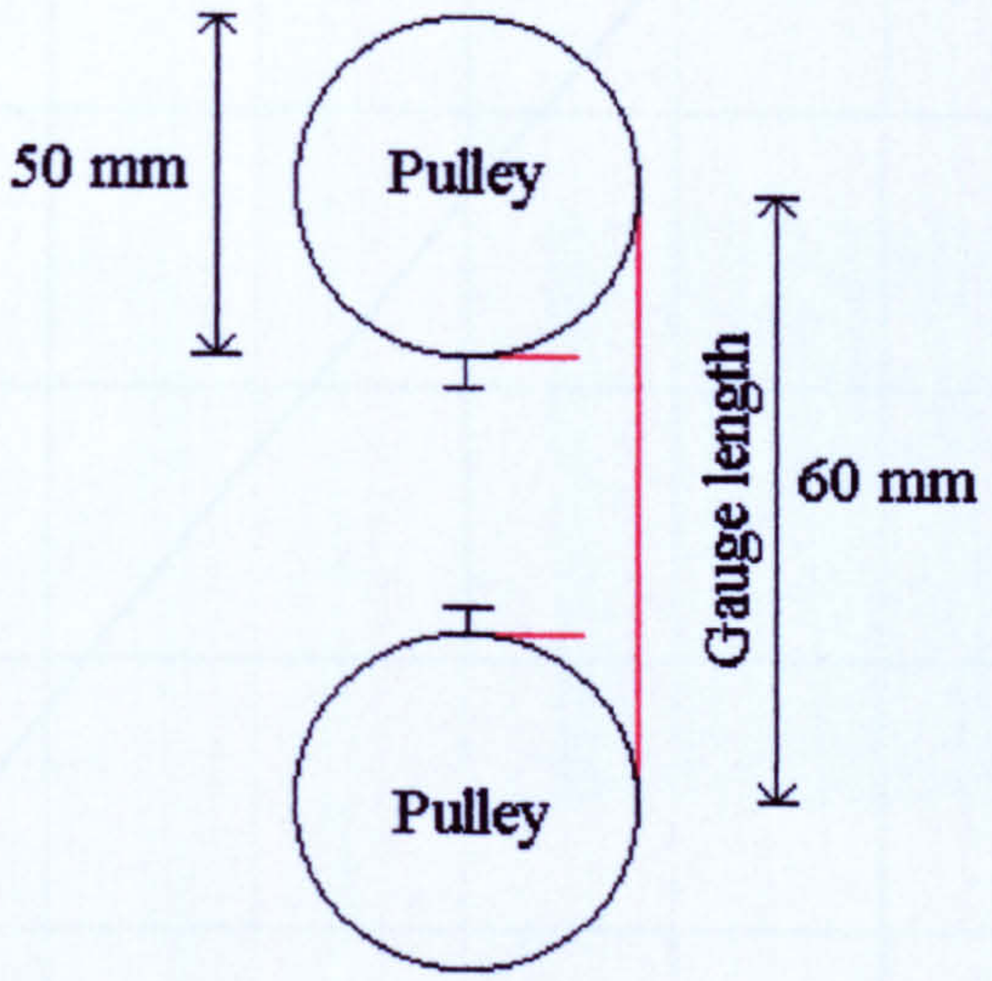

Figure 3.8. Schematic illustration of the gripping method for wire tensile tests.

3.5.2 Fracture toughness

The fracture toughness of the alloys was measured on notched ribbons (mode I) again using a Hounsfield universal machine at a strain rate of 1.66×10^{-4} s^{-1}. A notch was made with scissors in one edge of the ribbon, which was then mounted at each end on a specially prepared tab (which consists of 120 grade emery paper, placed against both surfaces of the sample in order to avoid slipping during the test) and fixed with cold setting resin for 24 hours (see figure 3.9). The prepared sample was mounted in the testing

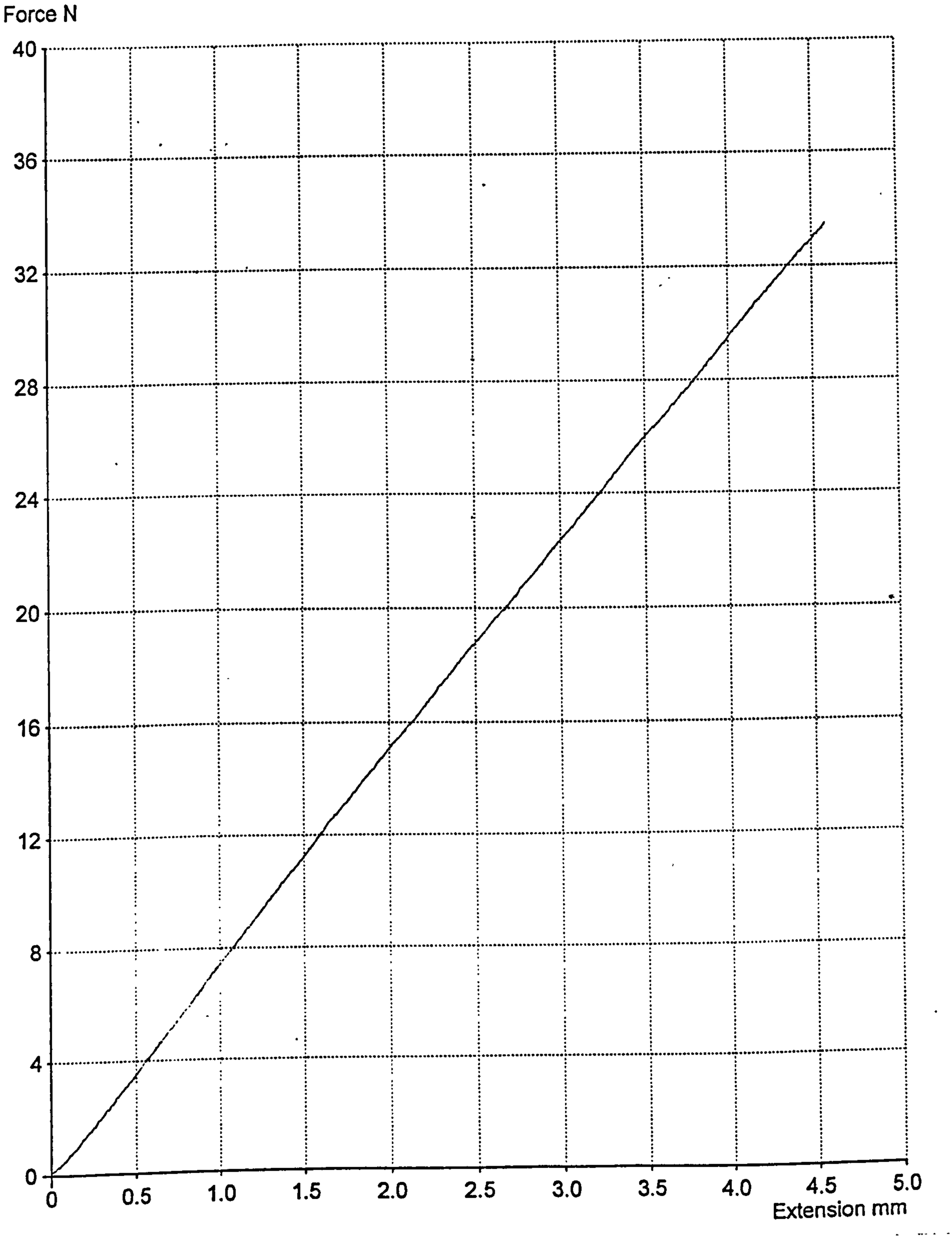

Figure 3.8.A. Typical force-extension graph for a tensile test on wire.

machine, the central longitudinal axis of the ribbon aligned with the axis of loading, and then the paper sides were cut -see figure 3.9(*a*)- before testing. A typical force-extension graph is shown in figure 3.8.B. The fracture toughness K_c was obtained from the resultant failure load using [125]:

$$K_c = C\sigma\sqrt{\pi a} \tag{3.3}$$

where σ is the stress at which sample fractured, a is the initial crack length and C is given by [125]:

$$C = 1.12 - 0.231\left(\frac{a}{W}\right) + 10.55\left(\frac{a}{W}\right)^2 - 21.72\left(\frac{a}{W}\right)^3 + 30.39\left(\frac{a}{W}\right)^4 \tag{3.4}$$

where W is the ribbon width.

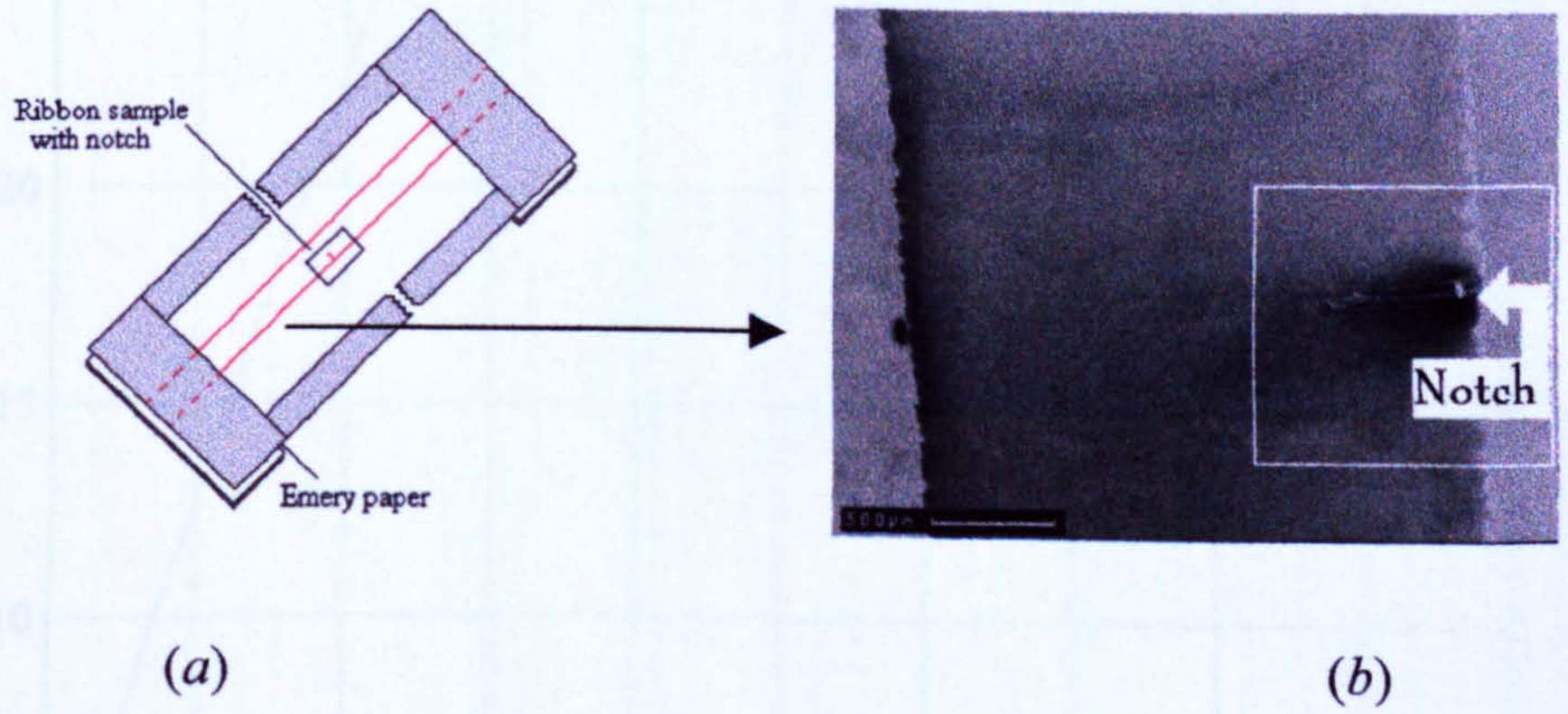

Figure 3.9. (*a*) schematic illustration of the fracture toughness test specimens and (*b*) micrograph of a typical notch.

3.5.3 Fatigue

Fatigue tests on the glassy alloy wires in the compositional series $Fe_{78-x}Cr_xSi_{10}B_{12}$ were carried out using both an existing single pulley bend type fatigue testing machine (SP) [7], which produces only tension/tension loading (figure 3.10), and a modified fatigue machine developed as part of the present project, which uses two pulleys (DP) to facilitate tension/compression loading (figure 3.11). In both cases, testing was carried out until the wire sample failed had undergone 10^7 cycles.

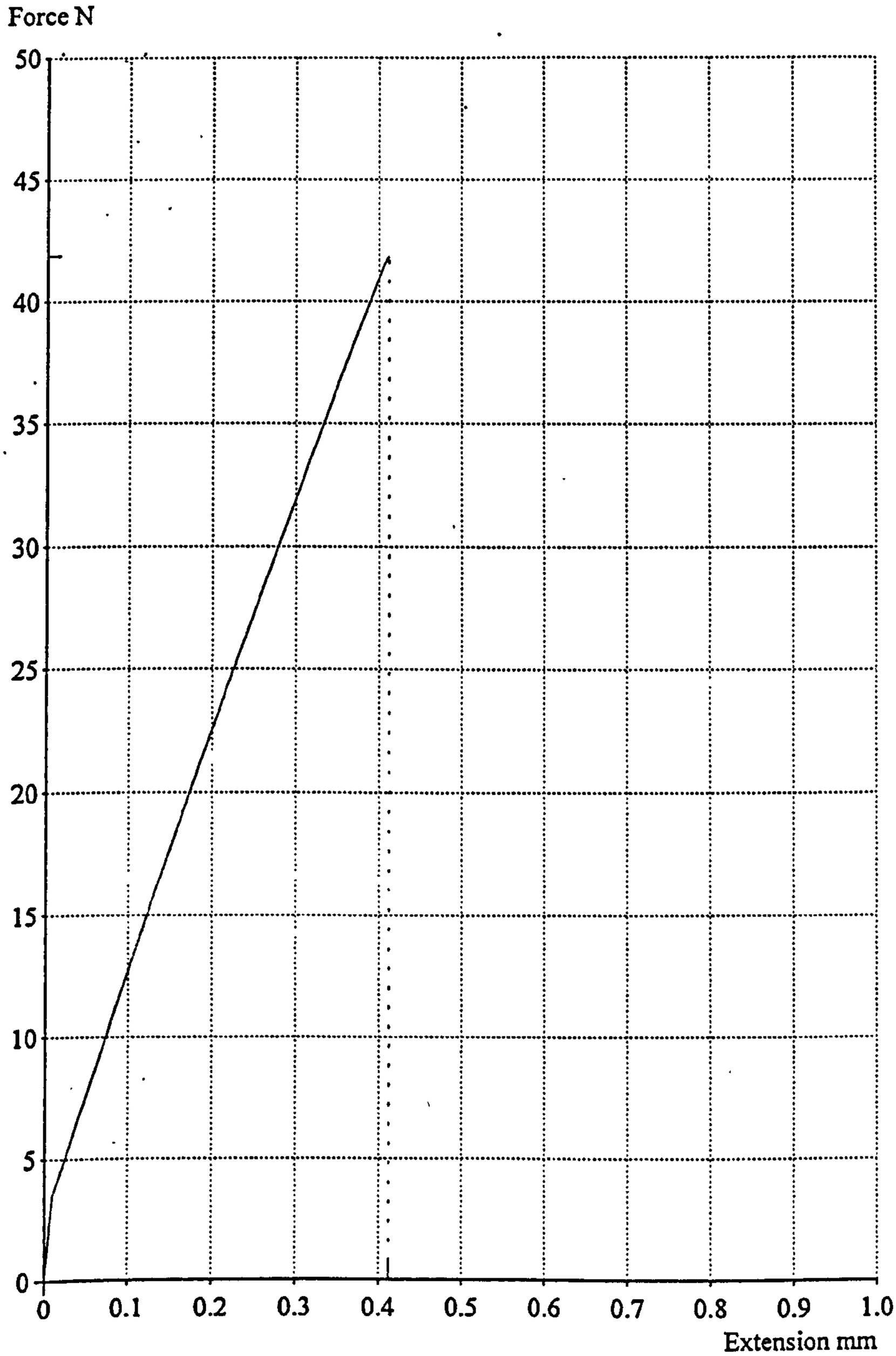

Figure 3.8.B. Typical force-extension graph for a fracture toughness test on ribbon.

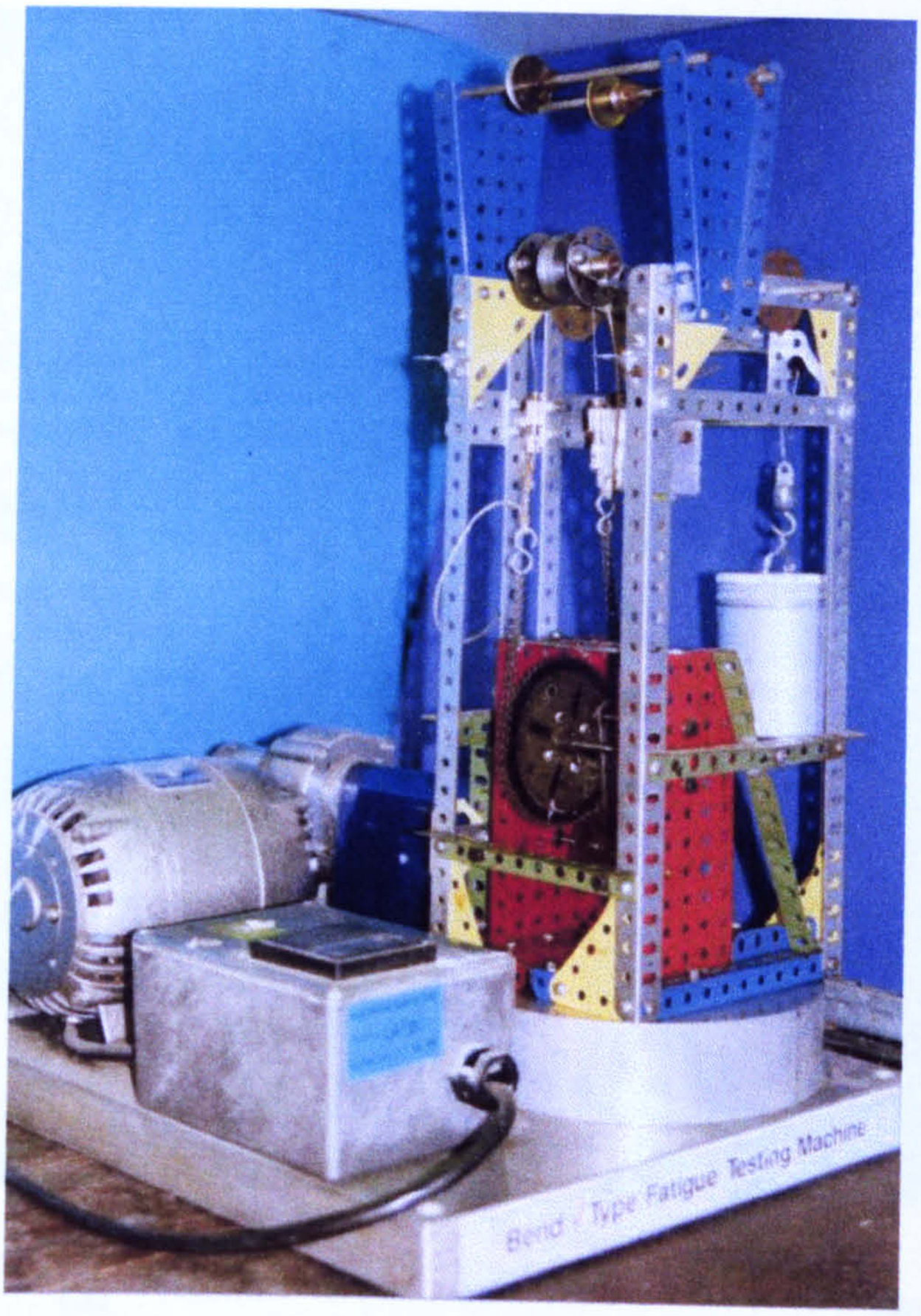

(a)

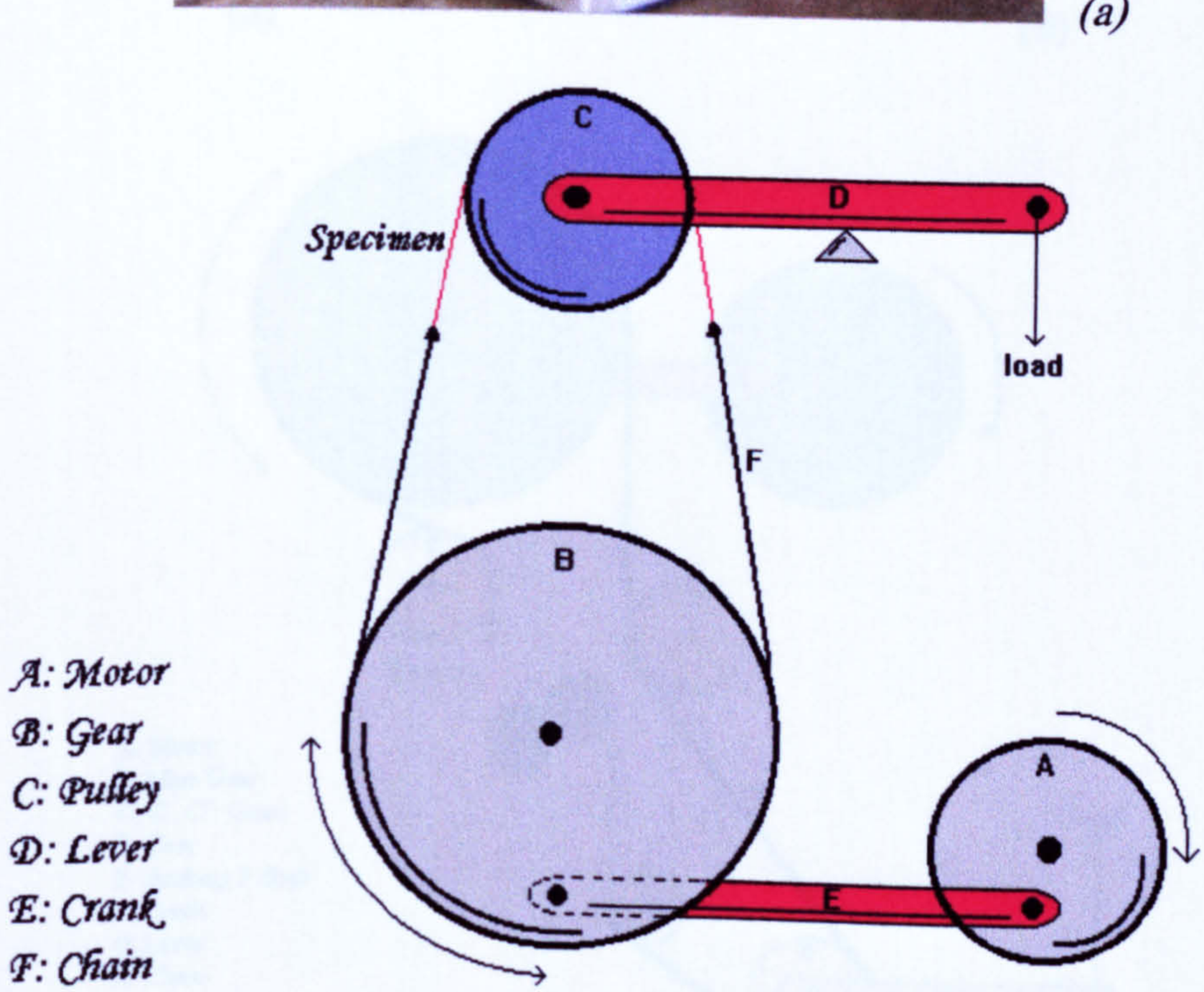

(b)

Figure 3.10. Single pulley bend type fatigue testing machine, *(a)* photograph and *(b)* schematic illustration.

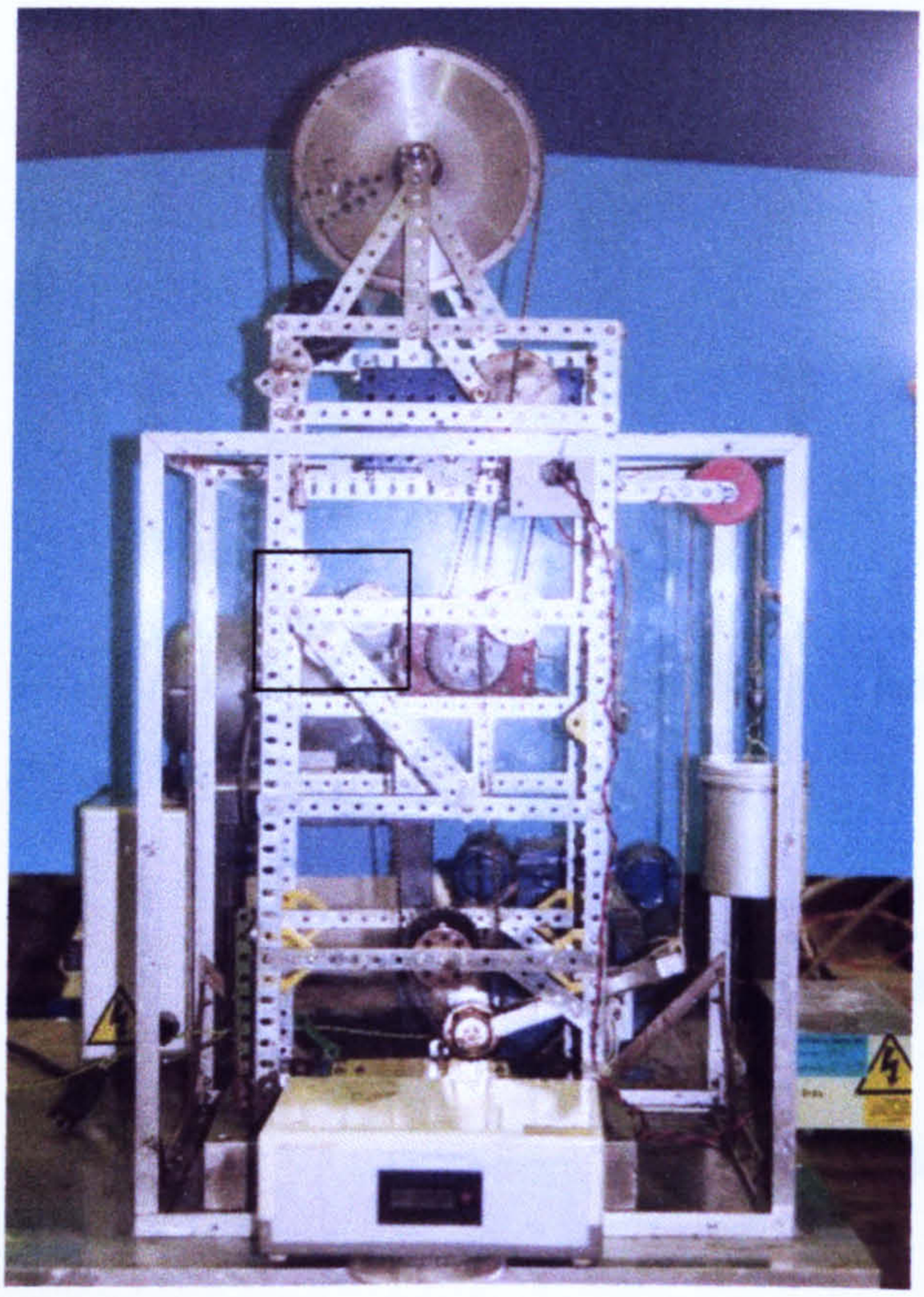

(a)

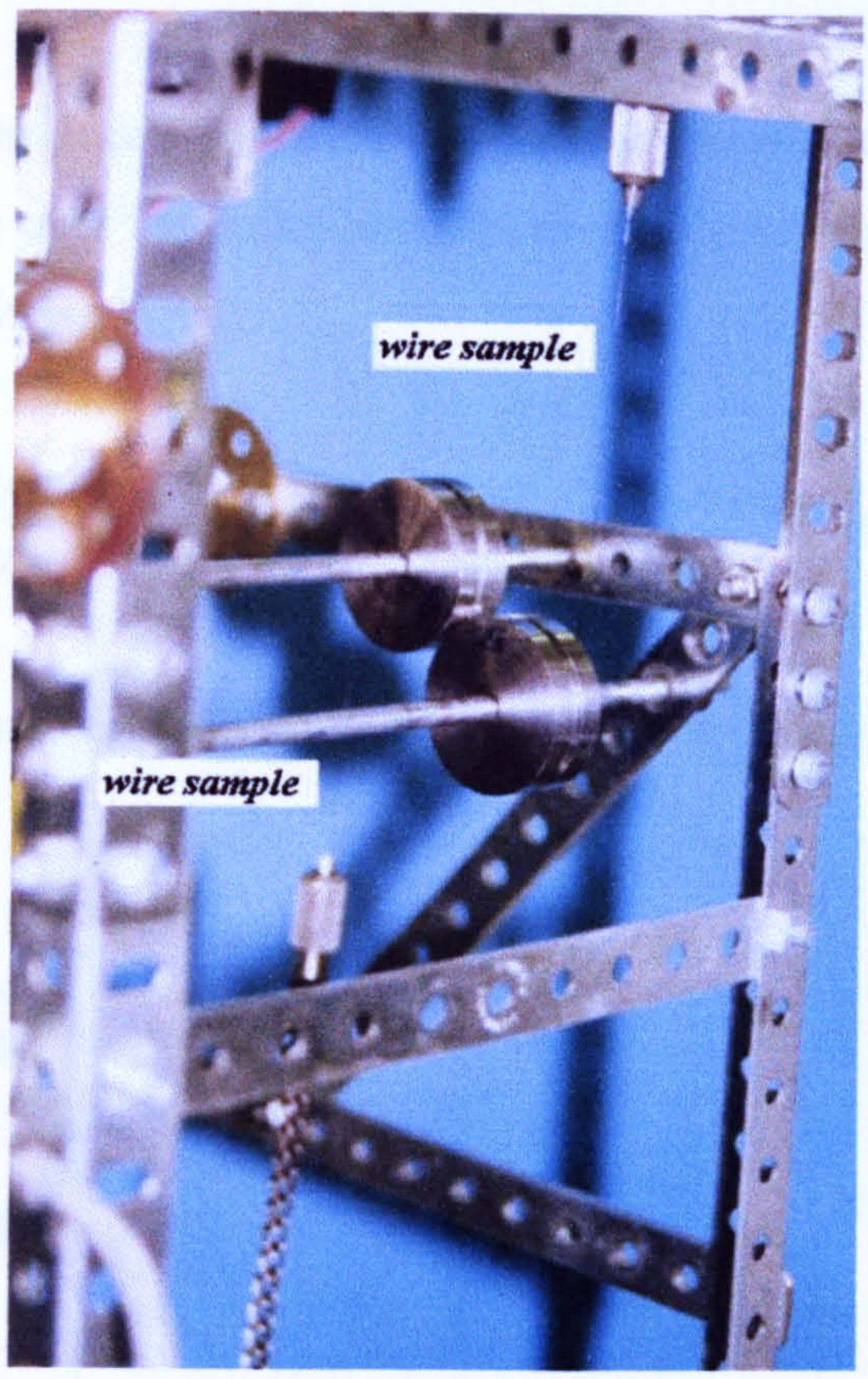

(b)

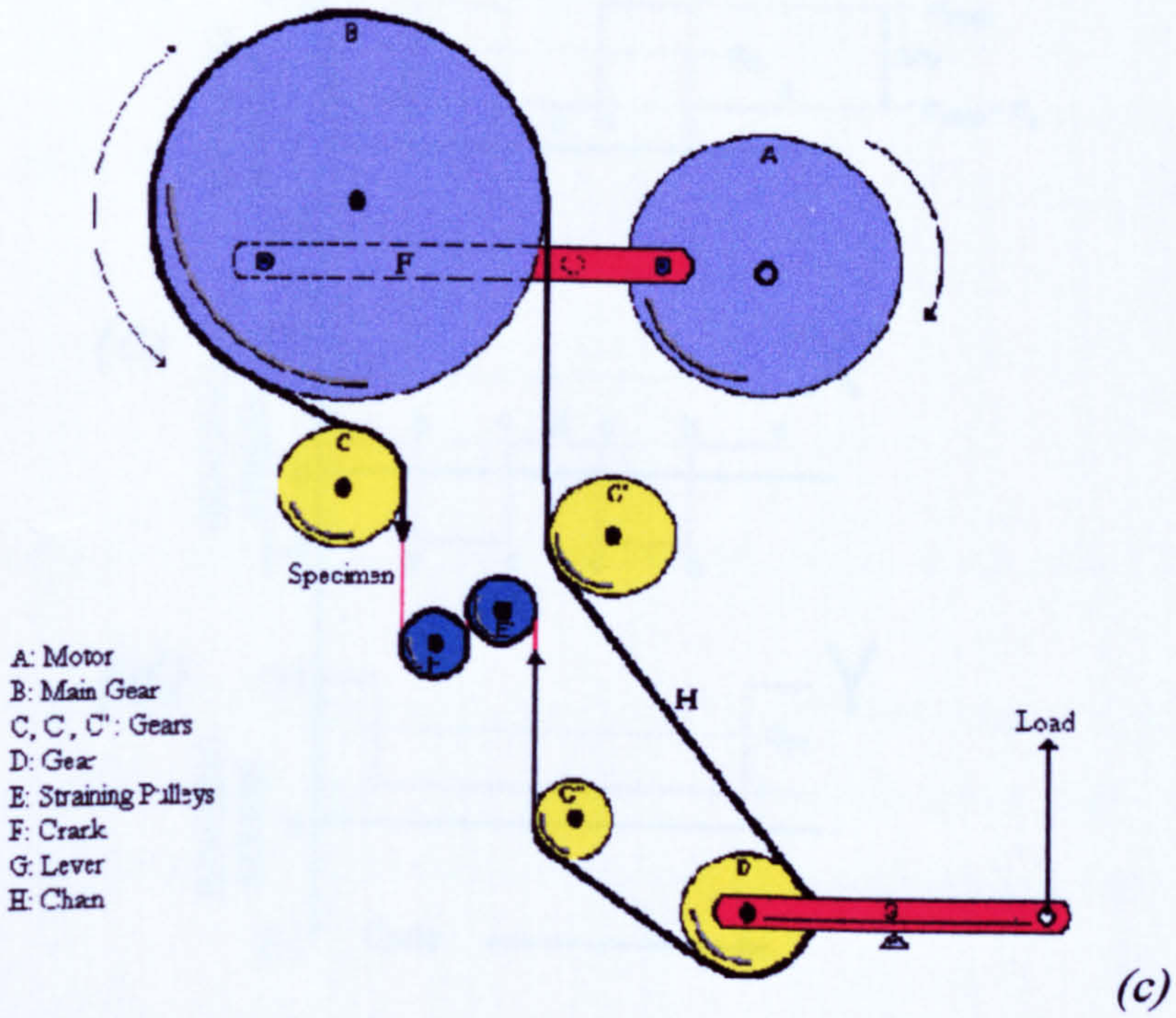

(c)

Figure 3.11. New designed double pulley bend type fatigue testing machine *(a)* photograph of; *(b)* higher magnification of *(a)*, showing the sample where the test is being carried out; and *(c) schematic illustration.*

SP machine.

A schematic diagram of the stress cycle produced by the SP machine is shown in figure 3.12(*b*). Parts of the wire that do not pass over the pulley are subjected only to the tensioning load, which gives rise to a tensioning stress

$$\sigma_t = \frac{m \cdot g}{A} \tag{3.5}$$

where m is the loading mass, g is the gravitational constant, and A is the cross sectional area of the wire.

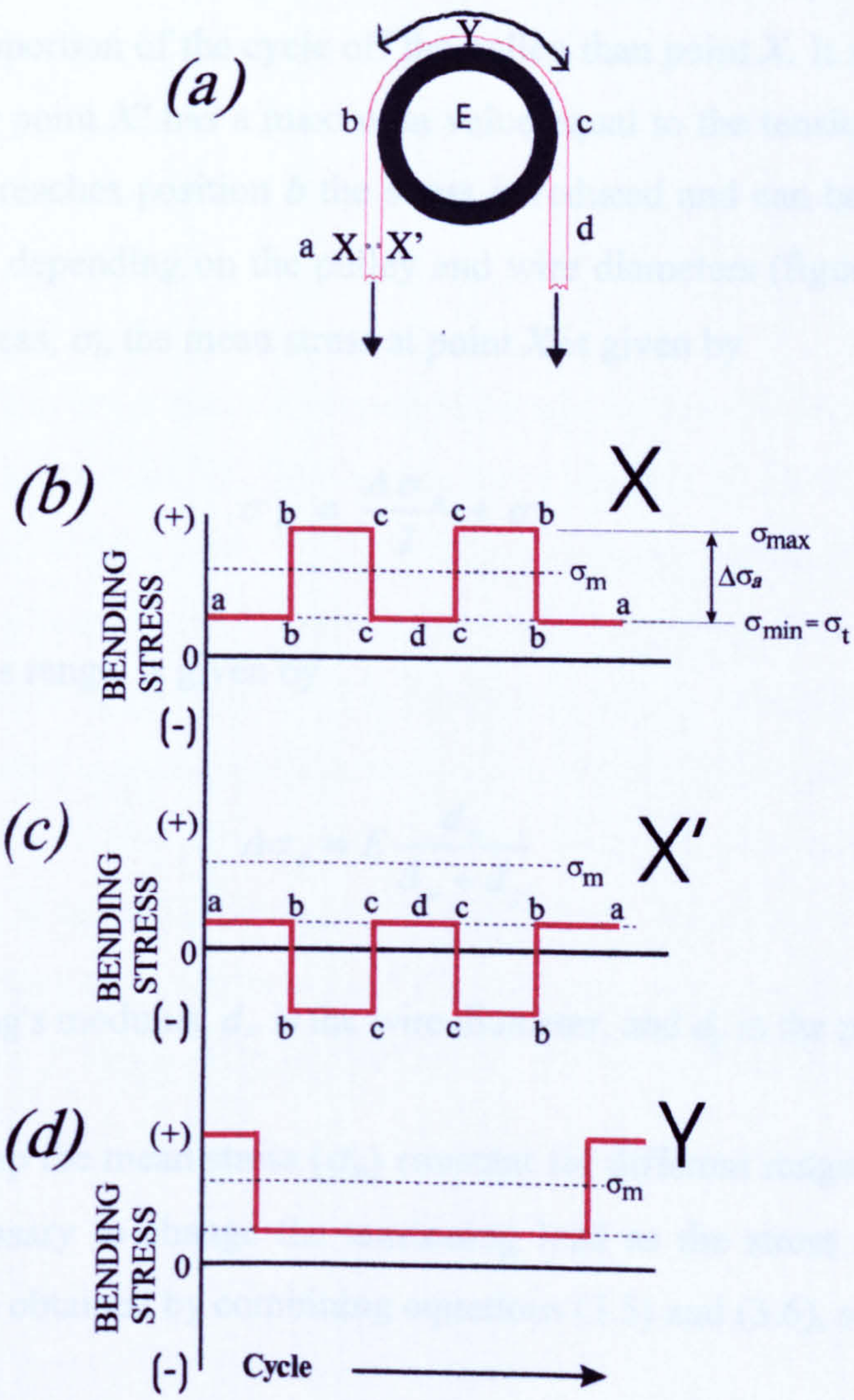

Figure 3.12. Bending stress cycles produced in the SP machine, (*a*) equipment, (*b*) stress-cycle for point *X*, (*c*) stress-cycle for point *X'*, (*d*) diagram stress-cycle for point *Y*; $\Delta\sigma_a$, σ_m, and σ_t, σ_{min} and σ_{max} are the stress range, mean stress, tensioning load, minimum and maximum stress, respectively.

Hence at the start of a cycle when point *X* on the wire is at point *a* the stress equals a minimum value determined by the tensioning load. When point *X* reaches position *b* its outer surface achieves the maximum stress, the sum of the tensioning stress and the bending stress, instantaneously and this is maintained until position *c*, when point *X* parts with the pulley and the bending component of the stress falls to zero instantaneously. The bending stress at point *X* remains at zero until the cycle reverses and it again reaches the pulley and the stress rises again to its maximum value instantaneously. This is maintained until point *X* reaches position *b*, where the bend stress falls again to zero instantaneously. Obviously the same basic cycle is seen by all other points on the wire that move onto and off the pulley in the forward direction, however, the detailed cycle seen by point *Y* is slightly different as shown in figure 3.12(*c*) because *Y* starts the cycle on the pulley and spends a greater proportion of the cycle off the pulley than point *X*. It should also be noted that stress cycle for point *X'* has a maximum value equal to the tensioning stress and that when this point *X'* reaches position *b* the stress is reduced and can become negative if is under compression, depending on the pulley and wire diameters (figure 3.12(*c*)). Because of the tensioning stress, σ_t, the mean stress at point *X* is given by

$$\sigma_m = \frac{\Delta\sigma_a}{2} + \sigma_t \tag{3.6}$$

where $\Delta\sigma_a$, the stress range, is given by

$$\Delta\sigma_a = E\frac{d_w}{d_w + d_p} \tag{3.7}$$

where E is the Young's modulus, d_w is the wire diameter, and d_p is the pulley diameter.

In order to keep the mean stress (σ_m) constant for different ranges of stress in the SP machine, it is necessary to change the tensioning load as the stress range changes. The required load can be obtained by combining equations (3.5) and (3.6), so that:

$$m = \frac{\left[\sigma_m - \frac{\Delta\sigma_a}{2}\right] \cdot A}{g} \tag{3.8}$$

DP machine

The design of the double pulley (DP) fatigue testing machine system developed for this project was based on that of the single pulley machine but with the addition of an additional bending pulley. The modifications made for the new system are shown in the figure 3.13. The principle of this machine is as follows: It uses a motor ***A*** which drives gear ***B*** through the crank ***F*** giving reversible movements of the same form as the single pulley machine. The main modification is that the new design uses two pulleys, ***E*** and ***E'***, where the testing of the filament is carried out in a reversible form, as follows: As the gear ***B*** is in the position shown in figure 3.13(*a*), the point ***X*** of the wire contacts the pulley ***E***, then this point travels round the outer side of pulley ***E*** and inner side of pulley ***E'*** until it reaches the situation shown in figure 3.13(*b*). The cycle is then reversed. Gear ***D*** is fastened to a lever ***G*** which is pulled up by applying a force ***P***, this force pulls the chain ***H*** down, placing a tensioning stress on the specimen. Gears ***C***, ***C'*** and ***C''*** have the function of reducing vibrations in the chain and therefore producing a more uniform movement of the specimen.

A schematic diagram of the stress cycle produced by this DP is shown in figure 3.14. When the point ***X*** (figure 3.14(*a*) is at position ***a*** the stress is as for the SP machine, equal to the tensioning load stress, (figure 3.14(*b*)). When point ***X*** contacts pulley ***E*** at position ***b*** the specimen reaches instantaneously the maximum tensile stress. This stress is maintained until ***c***, when the stress again drops to the tensioning stress. When point ***X*** then contacts pulley ***E'*** at position ***d*** the stress reaches instantaneously the maximum compressive stress, which is maintained until position ***e***. When point ***X*** parts with the pulley ***E'*** and comes to position ***f***, the stress is again equal to the tensioning load. The process is now reversed. As before, ***X'*** sees a different stress cycle to ***X*** although the overall cycle is the same as that seen at ***X*** (see figure 3.14(*c*)). Furthermore some points such as ***Y*** again see a different cycle (see figure 3.14(*d*)).

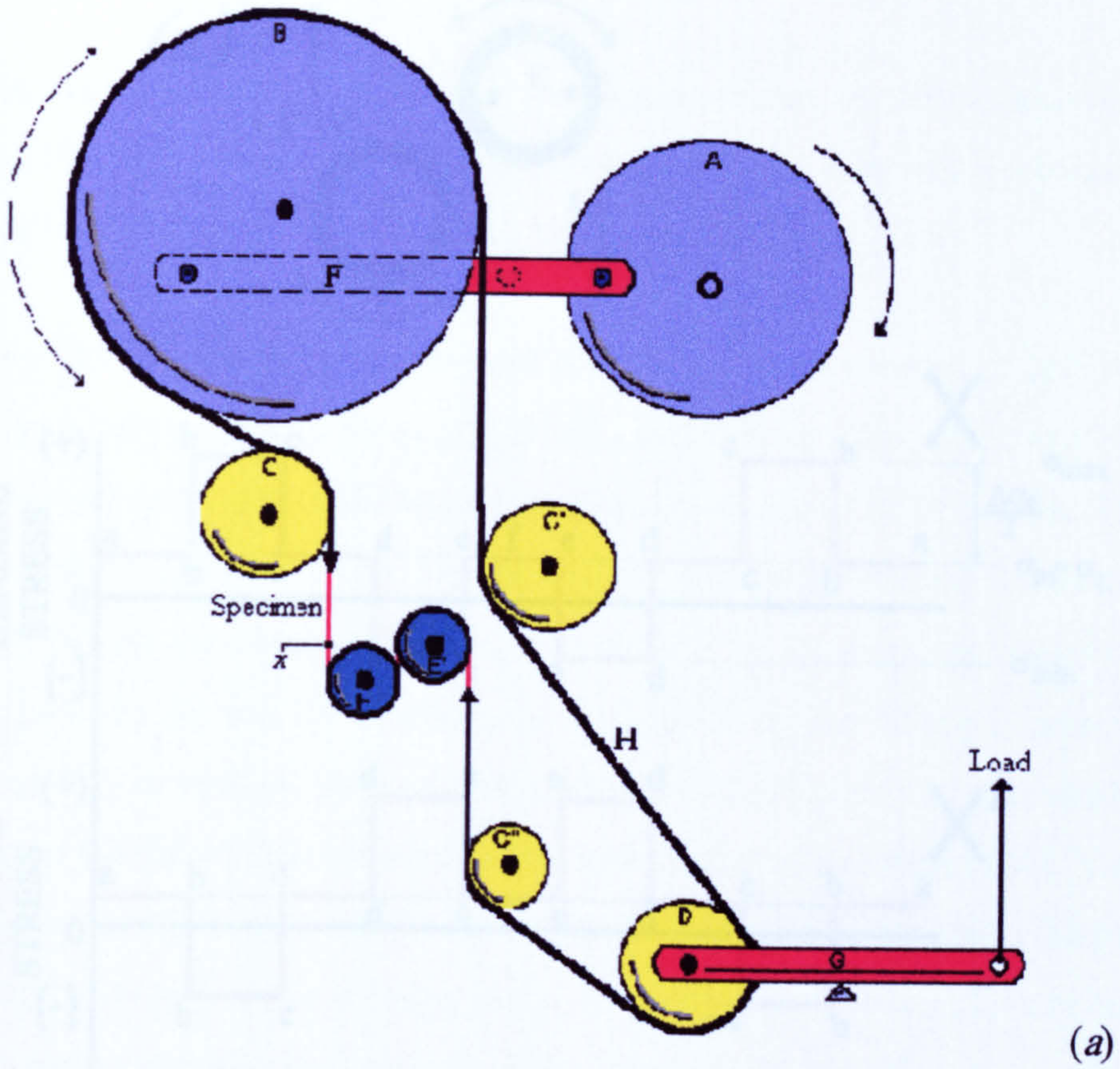

(a)

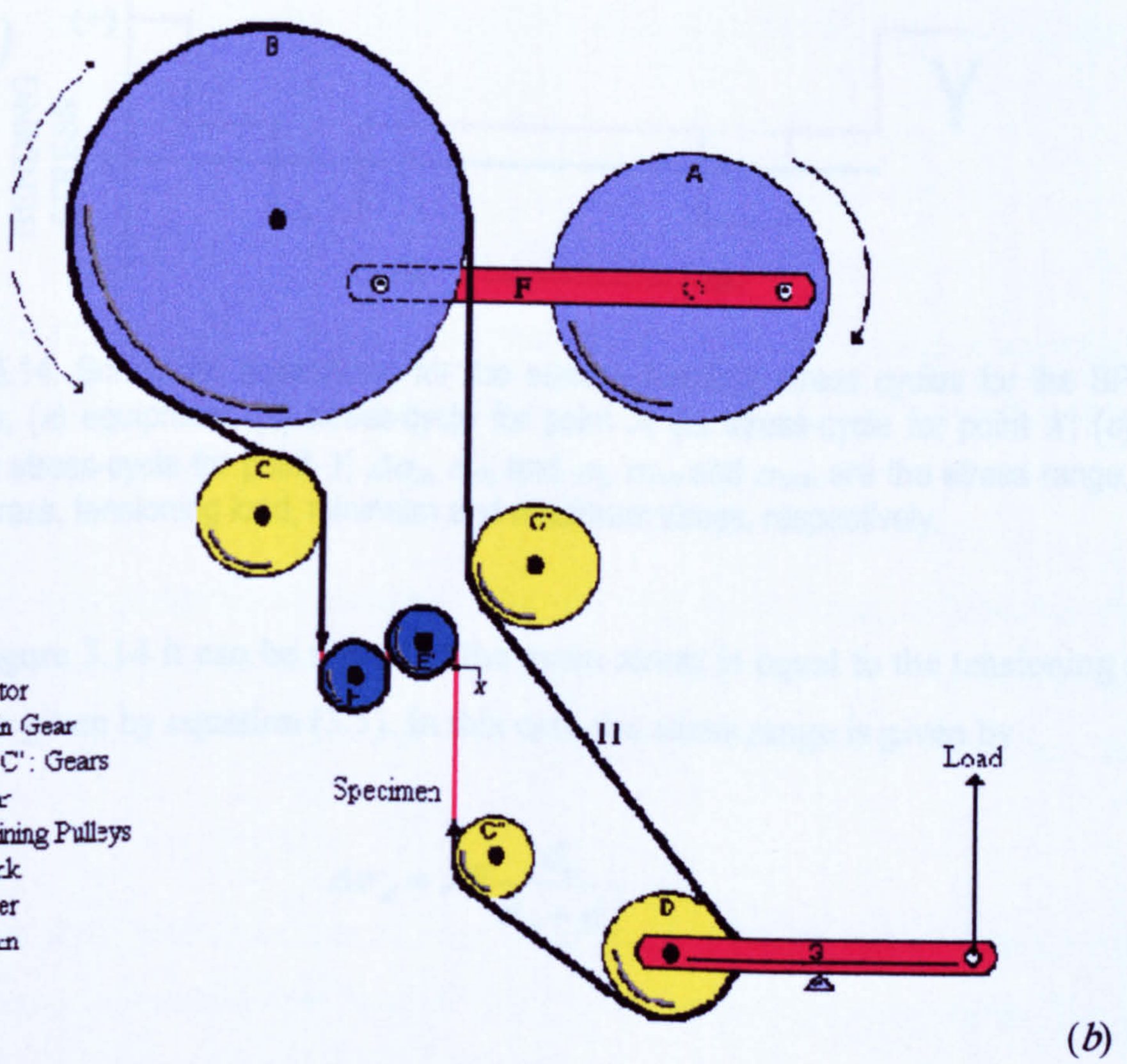

(b)

Figure 3.13. Schematic illustration of the new twin pulley fatigue testing machine.

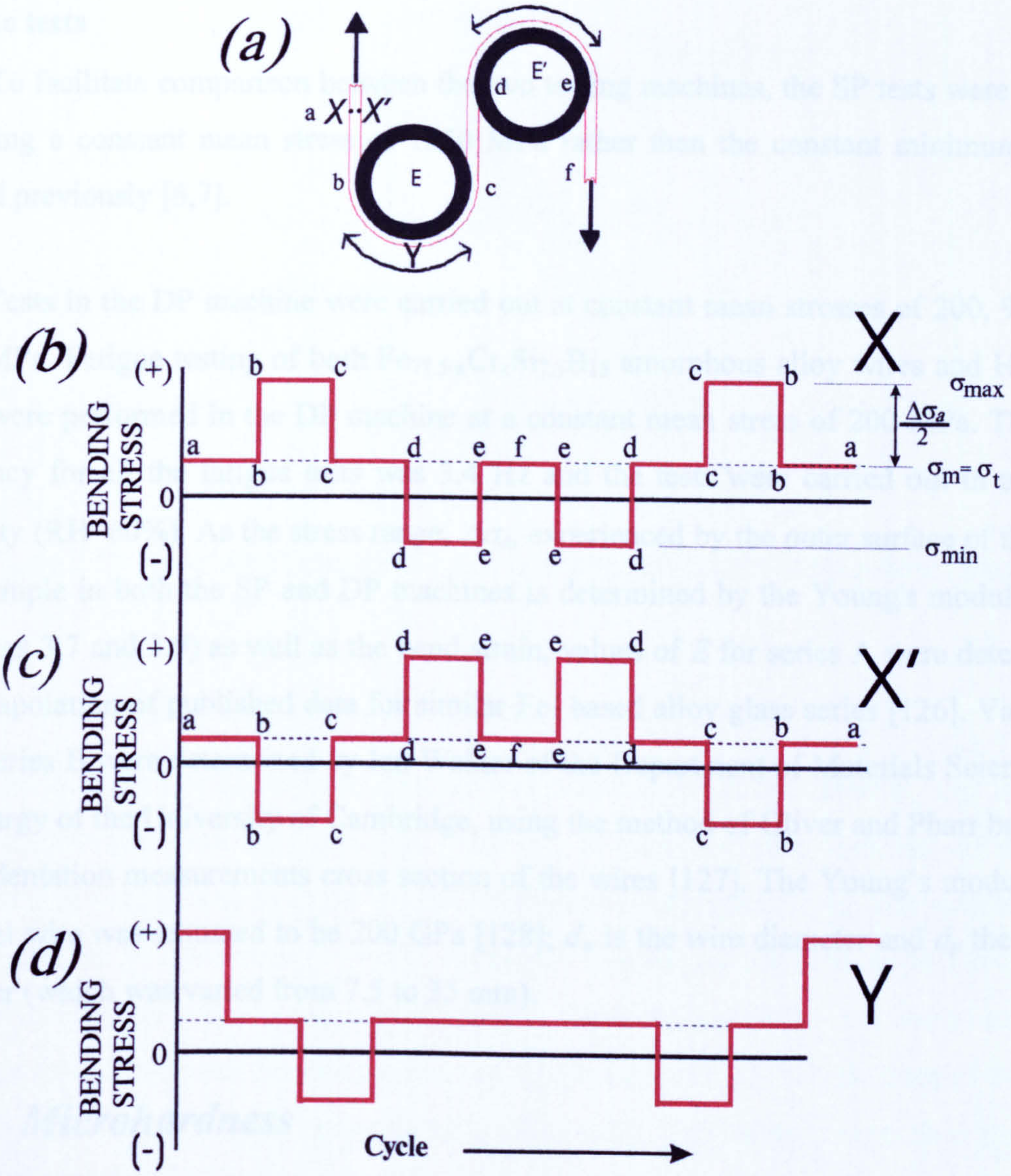

Figure 3.14. Schematic illustrations for the surface bending stress cycles for the SP machine, (*a*) equipment, (*b*) stress-cycle for point *X*, (*c*) stress-cycle for point *X'*, (*d*) diagram stress-cycle for point *Y*; $\Delta\sigma_a$, σ_m, and σ_t, σ_{min} and σ_{max} are the stress range, mean stress, tensioning load, minimum and maximum stress, respectively.

From figure 3.14 it can be seen that the mean stress is equal to the tensioning stress, which is again given by equation (3.5). In this case the stress range is given by

$$\Delta\sigma_a = 2E\frac{d_w}{d_w + d_p} \tag{3.9}$$

Fatigue tests

To facilitate comparison between the two testing machines, the SP tests were carried out using a constant mean stress of 1550 MPa rather than the constant minimum stress utilised previously [6,7].

Tests in the DP machine were carried out at constant mean stresses of 200, 900 and 1550 MPa. Fatigue testing of both $Fe_{77.5-x}Cr_xSi_{7.5}B_{15}$ amorphous alloy wires and HT steel wires were performed in the DP machine at a constant mean stress of 200 MPa. The load frequency for all the fatigue tests was 3.4 Hz and the tests were carried out in ambient humidity (RH~60%). As the stress range, $\Delta\sigma_a$, experienced by the outer surface of the bent wire sample in both the SP and DP machines is determined by the Young's modulus (see equations 3.7 and 3.9) as well as the bend strain, values of E for series A were determined by extrapolation of published data for similar Fe- based alloy glass series [126]. Values of E for series B were determined by Ian Walker of the Department of Materials Science and Metallurgy of the University of Cambridge, using the method of Oliver and Pharr based on nanoindentation measurements cross section of the wires [127]. The Young's modulus for HT steel wire was assumed to be 200 GPa [128]; d_w is the wire diameter and d_p the pulley diameter (which was varied from 7.5 to 35 mm).

3.5.4 Microhardness

Vickers microhardness measurements were carried out on both the amorphous wires and HT steel wires prior to and after fatigue testing, in order to monitor for either hardening or softening during the process of fatigue.

Samples were prepared by mounting wire sections vertically in cold setting Araldite for 24 hours, as illustrated schematically in figure 3.15. The samples were then polished to a ¼ μm finish in order to facilitate the imaging of clearly defined microhardness indentations.

The tests were performed on a Leco M-400 microhardness tester using a diamond pyramid indentor. An indentation load of 100 g was applied for 20 seconds. The quoted results are the mean value of at least 30 measurements.

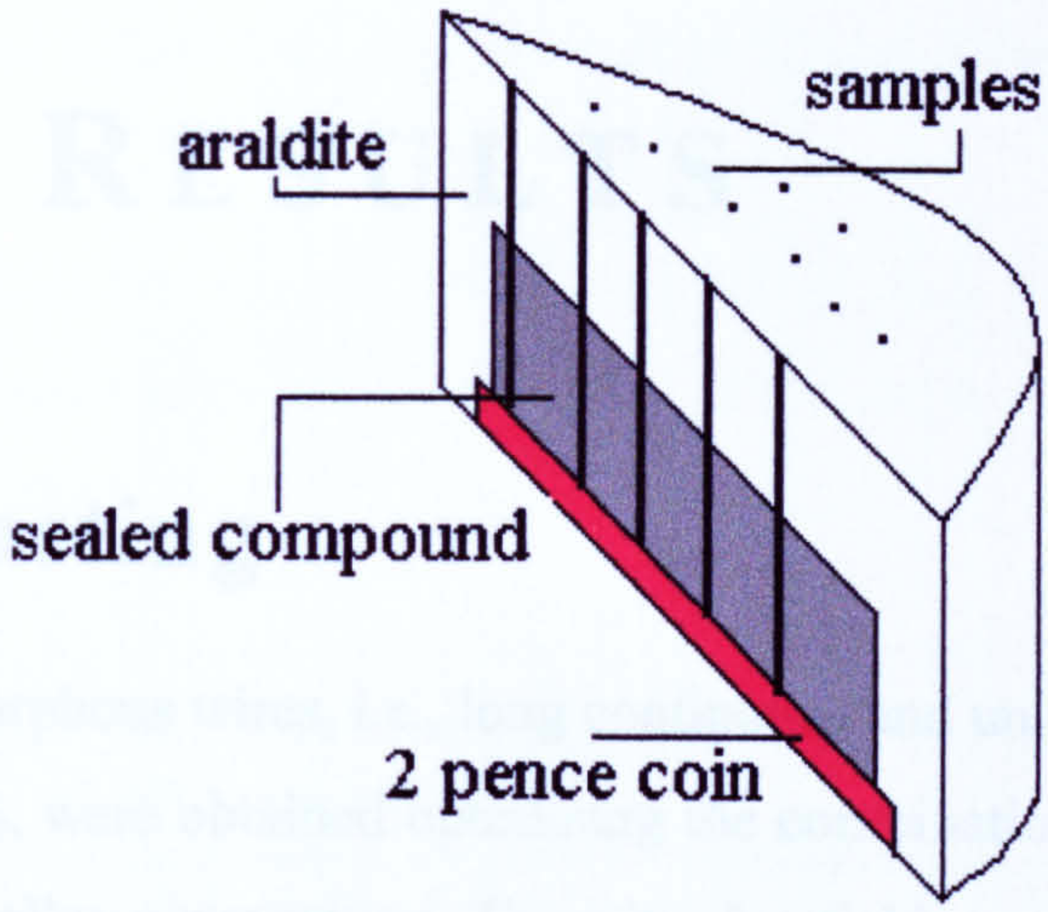

Figure 3.15. Schematic illustration of the mounting preparation for microhardness tests

3.5.5 Scanning Electron Microscopy

The fractured samples from fracture toughness tests on the ribbons, and from the tensile and fatigue tests on the wires, were cut 15 mm from the fractured surface and mounted in a similar way to those for microhardness tests (figure 3.16). The samples were also washed in a Transsonic T 460/H ultrasonic cleaner for 30 minutes at 25°C, using acetone in order to remove any contamination. Once the samples were clean, to ensure electrical contact between the sample and the aluminium stub, the bottom ends of the wires were coated with a thin layer of conducting silver paint. The samples were then examined in a Camscan S2 Scanning Electron Microscope operated at 20 kV.

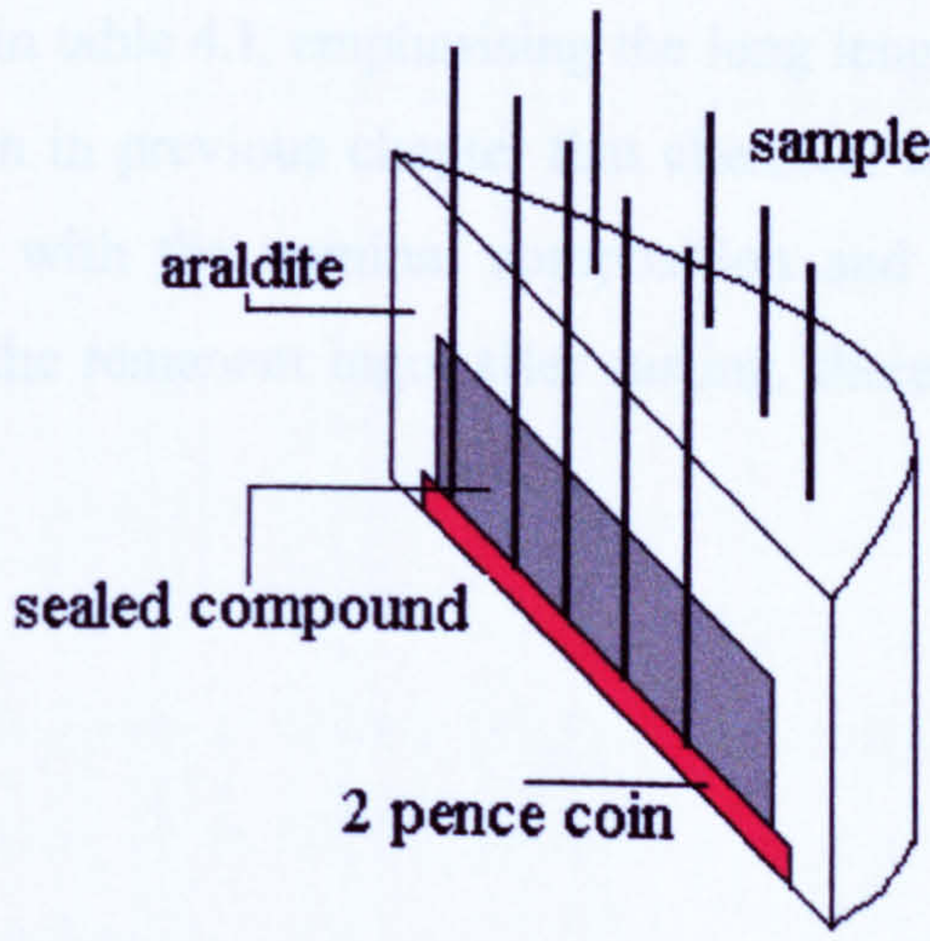

Figure 3.16. Schematic illustration of the samples mounted in araldite for SEM. Transverse cut.

Chapter IV: RESULTS

4.1 Wire Casting

Good quality amorphous wires, i.e., long continuous and uniform lengths > 10 m and good roundness > 99 %, were obtained optimising the combinations of casting conditions, which depended on the alloy composition. The critical variables were:

- Nozzle diameter
- Nozzle/water distance tip
- Melt superheat
- Melt jet velocity (determined by ejection over pressure and nozzle diameter)
- Drum/water velocity (angular drum velocity)

Table 4.I presents a summary of the critical values for the parameters listed above employed for casting amorphous wires of good quality for various alloy compositions. Figure 4.1(*a*) and (*b*) show an example of good quality ($Fe_{73.5}Cr_4Si_{7.5}B_{15}$) wire cast with the parameters presented in table 4.I, emphasising the long length and round cross-section, respectively. It was shown in previous chapter that chemical analysis of some test ingots were in good agreement with the nominal composition and there was no evidence of compositional change in the remanent ingot after casting, therefore nominal compositions are given in table 4.I.

4.1.1 Process parameters for casting amorphous wires of good quality

The effects of individual process parameters on the cast wire are described below. The nozzle/water distance, melt superheat, melt jet velocity and drum velocity were optimised by trial and error.

Table 4.I. Some of the critical conditions for casting good quality wires for the alloy studied.

Composition (at %)	Nozzle diameter (μm)	Drum speed (rpm)	Ejection pressure (kPa)	Dwell time (sec)	Diameter wire (μm)	Wire Diameter Contraction (%)
$Fe_{78}Si_{10}B_{12}$	120	324	400	30	110	8.3
$Fe_{74.5}Cr_{3.5}Si_{10}B_{12}$	130	360	400	60	124	4.6
$Fe_{71.75}Cr_{6.25}Si_{10}B_{12}$	120	345	400	30	106	11.6
$Fe_{78}Cr_{8}Si_{10}B_{12}$	110	344	400	60	95	18
$Fe_{77.5}Si_{7.5}B_{15}$	130	320	400	270	116	10.7
$Fe_{73.5}Cr_{4}Si_{7.5}B_{15}$	130	358	354	90	123	5.3
$Fe_{69.5}Cr_{8}Si_{7.5}B_{15}$	120	345	400	90	115	4.1

Nozzle diameter

Taking into account previous experience regarding optimal nozzle diameter [129], diameters ranging from 110 to 130 μm were used for the present project. This range was chosen in order to avoid problems of nozzle blockage for smaller diameters, or at the other extreme for larger diameters, to avoid fragmentation of the wire into short lengths, or ultimately formation of powder.

During the casting, the jet contracts, generally resulting in a slight reduction on wire diameter relative to the nozzle diameter. The measured diameter contraction varied from 4.1 to 18 %. Around 100 measurements of wire diameter were made for each alloy wire. Table 4.I gives the data for wire diameter contraction in relation to nozzle diameter for each alloy studied.

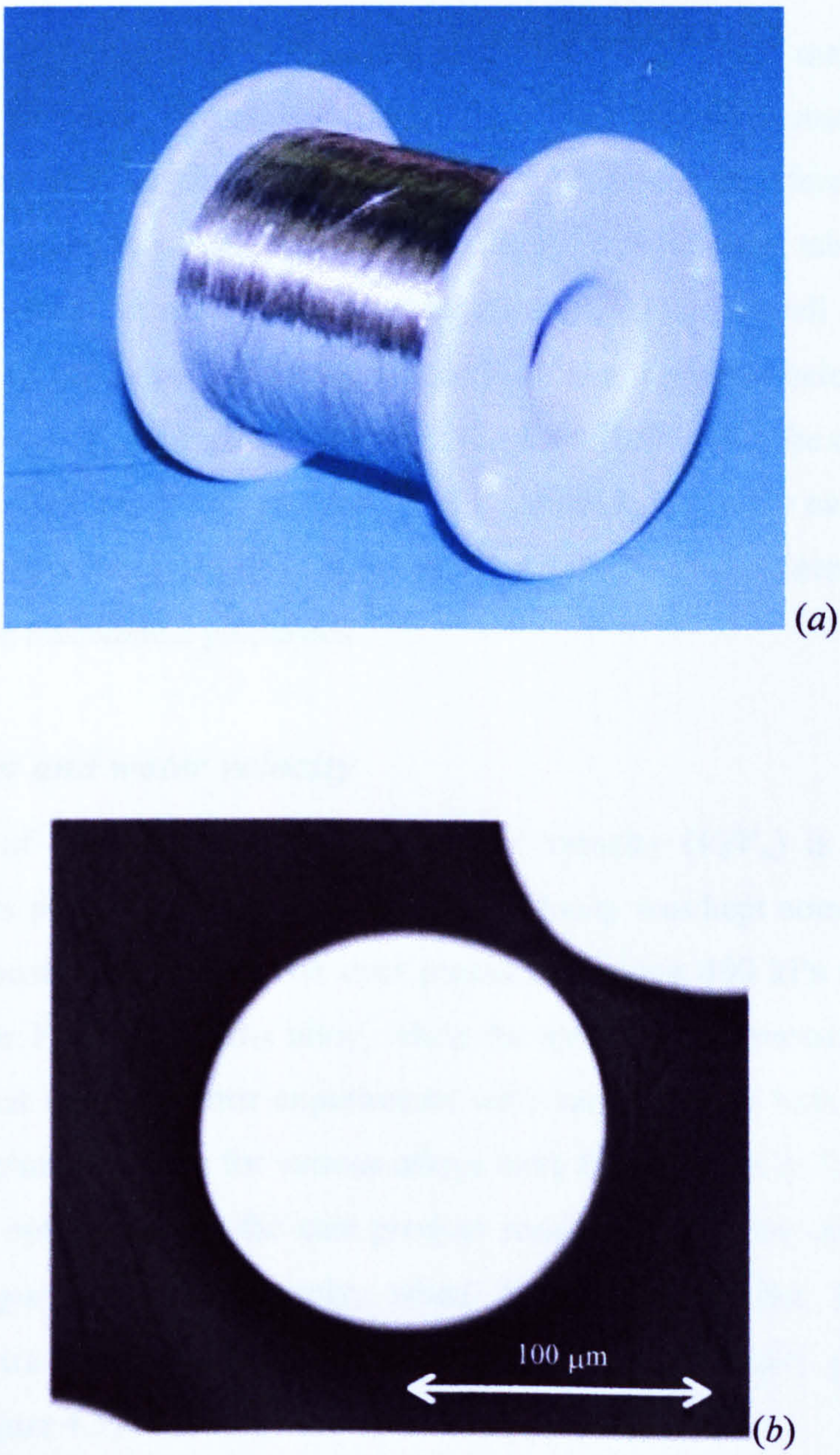

(*a*)

(*b*)

Figure 4.1 Good quality $Fe_{73.5}Cr_4Si_{7.5}B_{15}$ amorphous alloy wire; *(a)* long length > 300 m, *(b)* optical photomicrograph of the cross-section.

Distance water/nozzle

The optimum clearance between the nozzle tip coolant surface was found to be about 3 to 4 mm. A shorter distance led to melt solidification in the nozzle and blockage while, on the other hand, large distances led to short lengths of brittle wire.

Melt superheat

Several attempts were made to adapt a thermocouple to the melting assembly in order to monitor the casting temperature; however, all attempts were unsuccessful. Thus as indicated in section 3.2, empirical experience was used, taking as reference the total time elapsed after melting until casting was initiated, i.e. the "dwell" time, table 4.I presents the optimum dwell times for each alloy composition cast. Longer dwell times, i.e. higher superheat, led to jet instability, shortened nozzle life and the product being cast in the form of powder or, at best, short lengths which were often also brittle. On the other hand, shorter dwell times, i.e. lower superheat, resulted in melt solidification in the nozzle or in the best of the cases, very short lengths of wire not suitable for further characterisation and study and especially the mechanical properties.

Melt jet and water velocity

The ratio of the melt jet velocity to water velocity (V_j/V_w) is one of the more important process parameters to consider. The jet velocity was kept nominally constant by maintaining a constant argon ejection over pressure of about 400 kPa for all the casting alloys, except for $Fe_{73.5}Cr_4Si_{7.5}B_{15}$ alloy, when the ejection over pressure was about 354 kPa. After several trial and error experiments with various water bath velocities, it was found that the optimum values for various alloys were those shown in Table 4.I. If V_w was slower than the optimal value, the cast product resulted in sinuous wire and eventually powder (see figure 4.2). Conversely, when V_w was faster that the optimal one, discontinuous wire with short thin and necked ends and eventually powder was again obtained, (see figure 4.3).

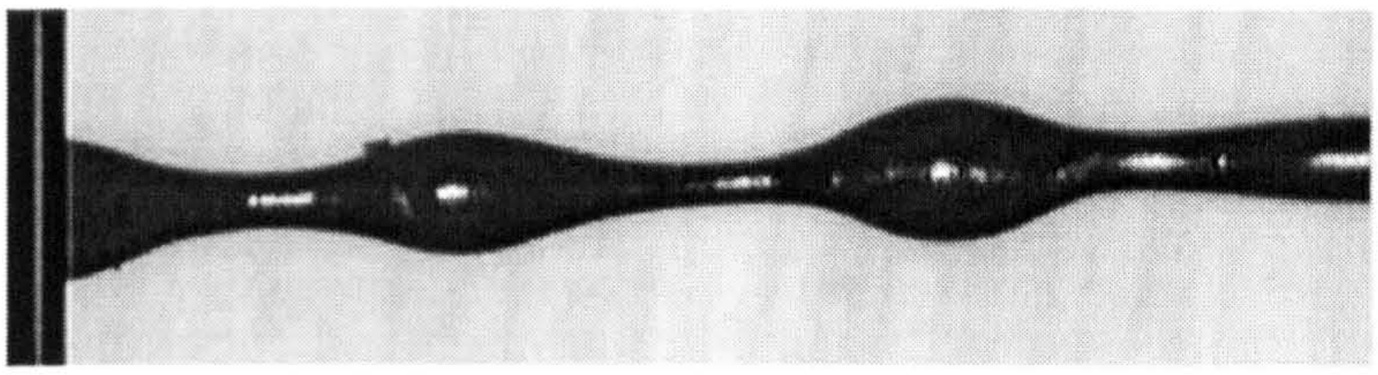

Figure 4.2. Sinuous wire obtained when V_w was slower than the optimal value.

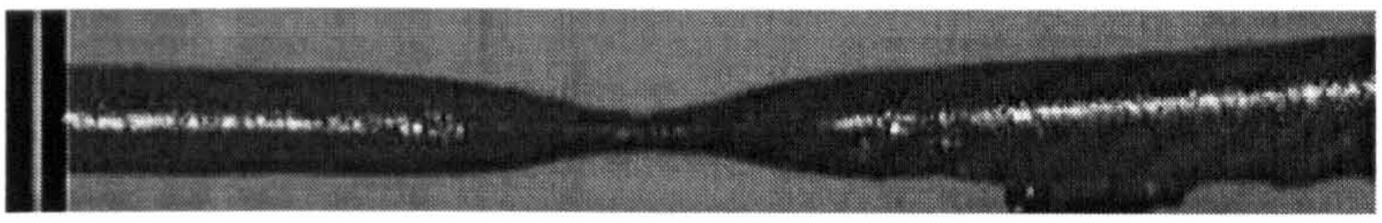

Figure 4.3. Discontinuous necked wire obtained when V_w was faster than the optimal value.

Alloy composition

In order to obtain uniform and continuous amorphous wires, the alloy must contain a melt jet stabiliser to promote a suitable balance between surface tension and viscosity in order to inhibit jet break-up. It has previously been reported [129, 130] that Si has proved to be acceptable as a melt jet stabiliser for Fe-based compositions, even at Si contents as low as 7 at % for FeSiB alloys. However, in the present study, it was found to be difficult to cast uniform amorphous wires of the $Fe_{78}Si_{10}B_{12}$ alloy, and it was frequently necked. Nevertheless, the wire quality for $Fe_{77.5}Si_{7.5}B_{15}$ was higher than for $Fe_{78}Si_{10}B_{12}$, although the alloys contain less Si, but more B, which suggests that B also plays significant role in the ability to obtain wires of good quality. The quality was also improved when Cr replaced Fe, indicating that Cr helps greatly in the enhancement of melt jet stabilisation evidently because of the formation of a film of Cr oxide [7]. Figure 4.4 shows the surface morphologies of the wires obtained using the optimal parameters presented in table 4.I.

4.2 Ribbon casting

Some ribbons were cast for fracture toughness tests. However, good quality ribbons could not be cast within an atmosphere of argon, since they were brittle and rough in all compositions, and could not be used for fracture toughness measurements, as it was not possible to notch the edges of these samples. Figure 4.5 (*a*) shows an example of this type of ribbon. Attempts to cast good quality ribbons were then made within an atmosphere of

helium, now with excellent results, since the products were completely ductile and uniform for all compositions. Table 4.II(*a*) and (*b*) presents the nozzle diameter and speed roll used to cast good quality ribbons as well as the dimensions obtained for each alloy ribbon cast under Ar and He atmospheres respectively. Figure 4.5 (*b*) shows an example of a good quality alloy ribbon.

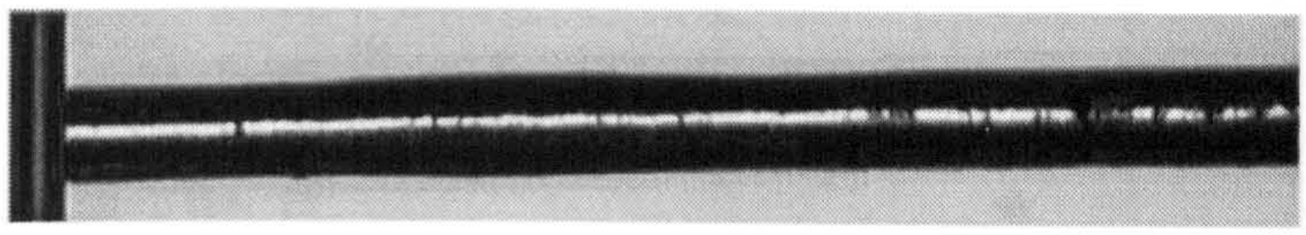

$Fe_{78}Si_{10}B_{12}$

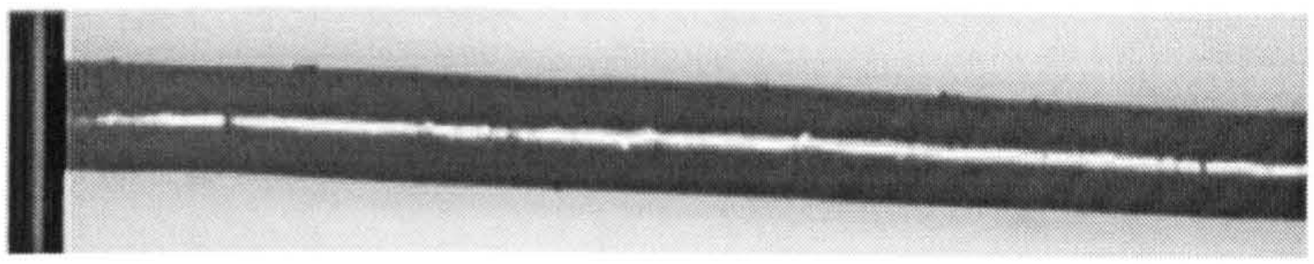

$Fe_{74.5}Cr_{3.5}Si_{10}B_{12}$

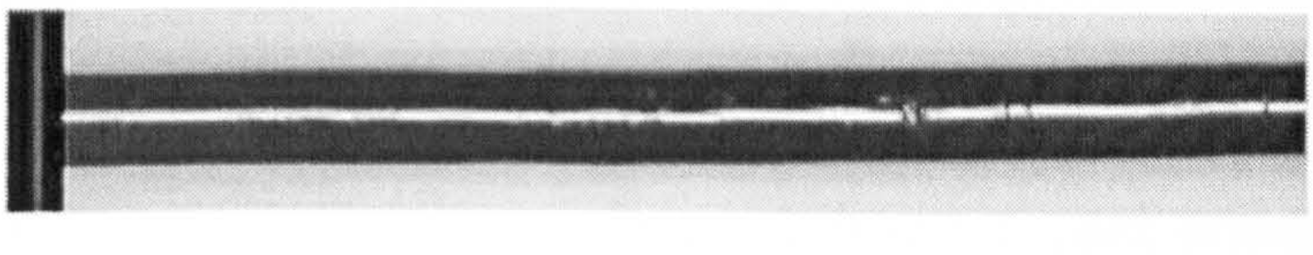

$Fe_{71.75}Cr_{6.25}Si_{10}B_{12}$

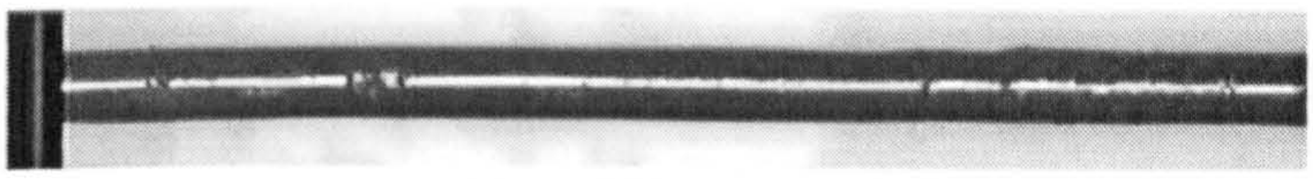

$Fe_{70}Cr_8Si_{10}B_{12}$

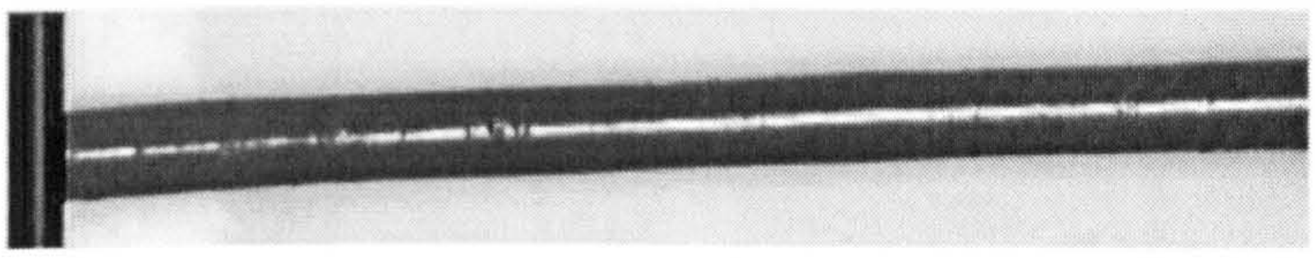

$Fe_{77.5}Si_{7.5}B_{15}$

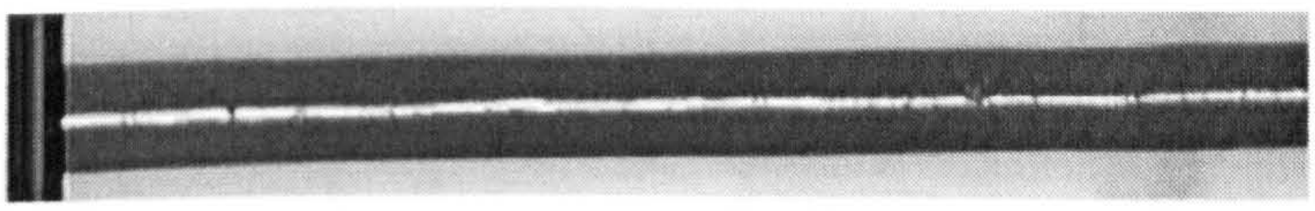

$Fe_{73.5}Cr_4Si_{7.5}B_{15}$

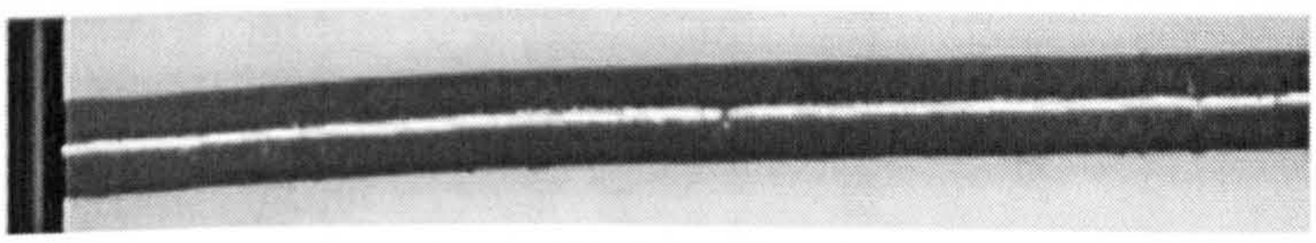

$Fe_{69.5}Cr_8Si_{7.5}B_{15}$

Figure 4.4. Surface morphology of the cast wires for all the alloys, obtained using the optimal parameters presented in table 4.I. —— 100 μm.

Table 4.II(*a*). Ribbon casting parameters cast under an atmosphere of Ar (all ribbons were brittle).

	at % Cr	Diameter nozzle (mm)	Roll speed (ms^{-1})	Thickness (μm)	Width (mm)
Series A	0	0.9	28	33.5 ±3	1.4 ±0.07
	3.5	0.95	20	55 ±5.5	1.8 ±0.15
	6.25	0.9	22	43 ±7	1.6 ±0.1
	8	0.95	25	38.5 ±3.5	1.5 ±0.2
Series B	0	1.01	30	37 ±4.5	1.5 ±0.08
	4	1	28	45.5 ±6	1.9 ±0.1
	8	0.9	30	36.5 ±5	1.7 ±0.15

Table 4.II(*b*). Ribbon casting parameters cast under an atmosphere of He (all ribbons were ductile).

	at % Cr	Diameter nozzle (mm)	Roll speed (ms^{-1})	Thickness (μm)	Width (mm)
Series A	0	1.01	32	39.5 ±0.9	1.2 ±0.05
	3.5	1	30	39 ±1.5	1.4 ± 0.07
	6.25	1.04	32	38 ±2.5	1.35 ±0.1
	8	1.04	34	37.5 ±1.5	1.35 ±0.02
Series B	0	1.02	32	38.5 ±2.5	1.3 ±0.06
	4	1	32	36.5 ±1.5	1.3 ±0.07
	8	1.01	34	37.5 ±3	1.5 ±0.06

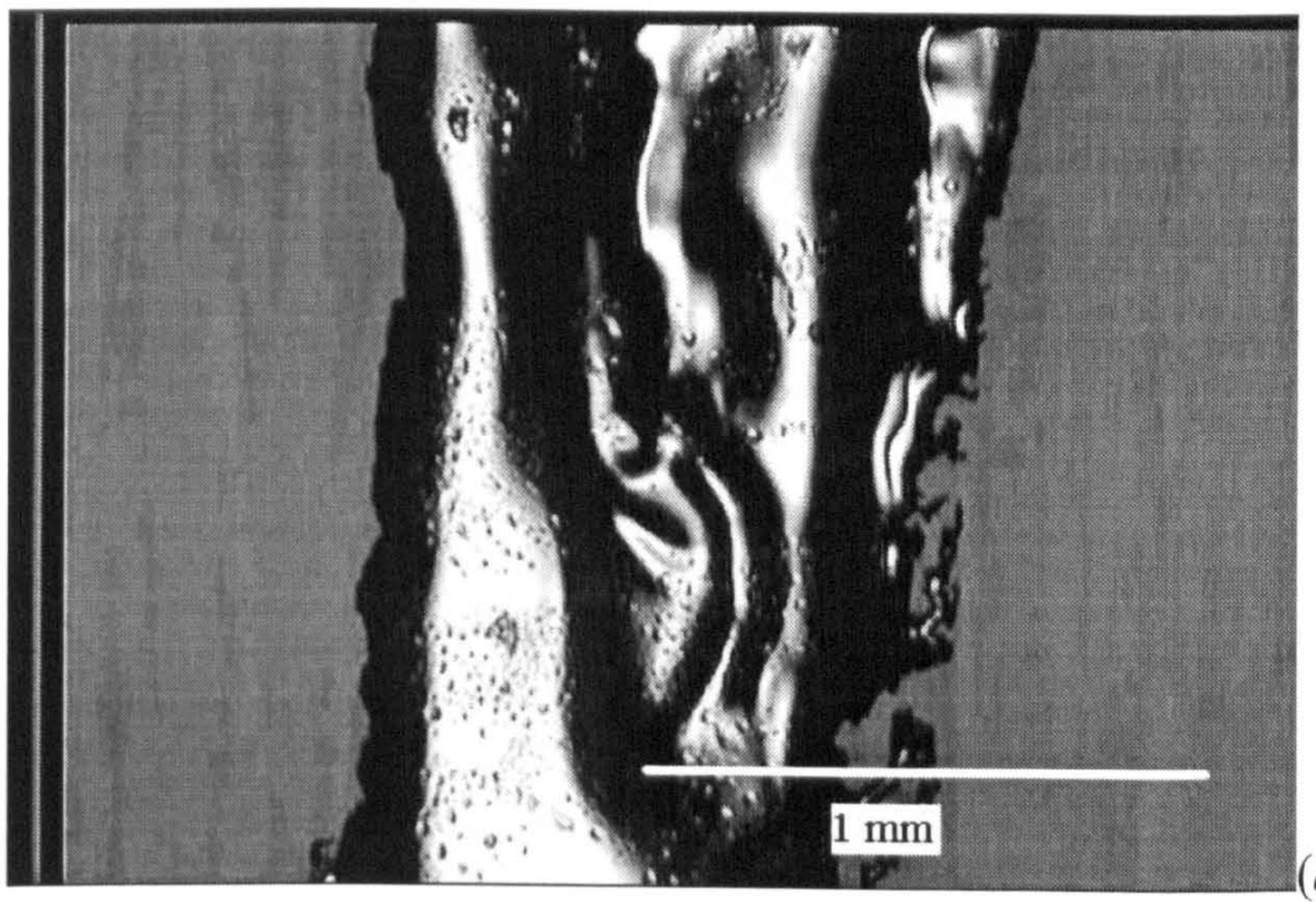

(*a*)

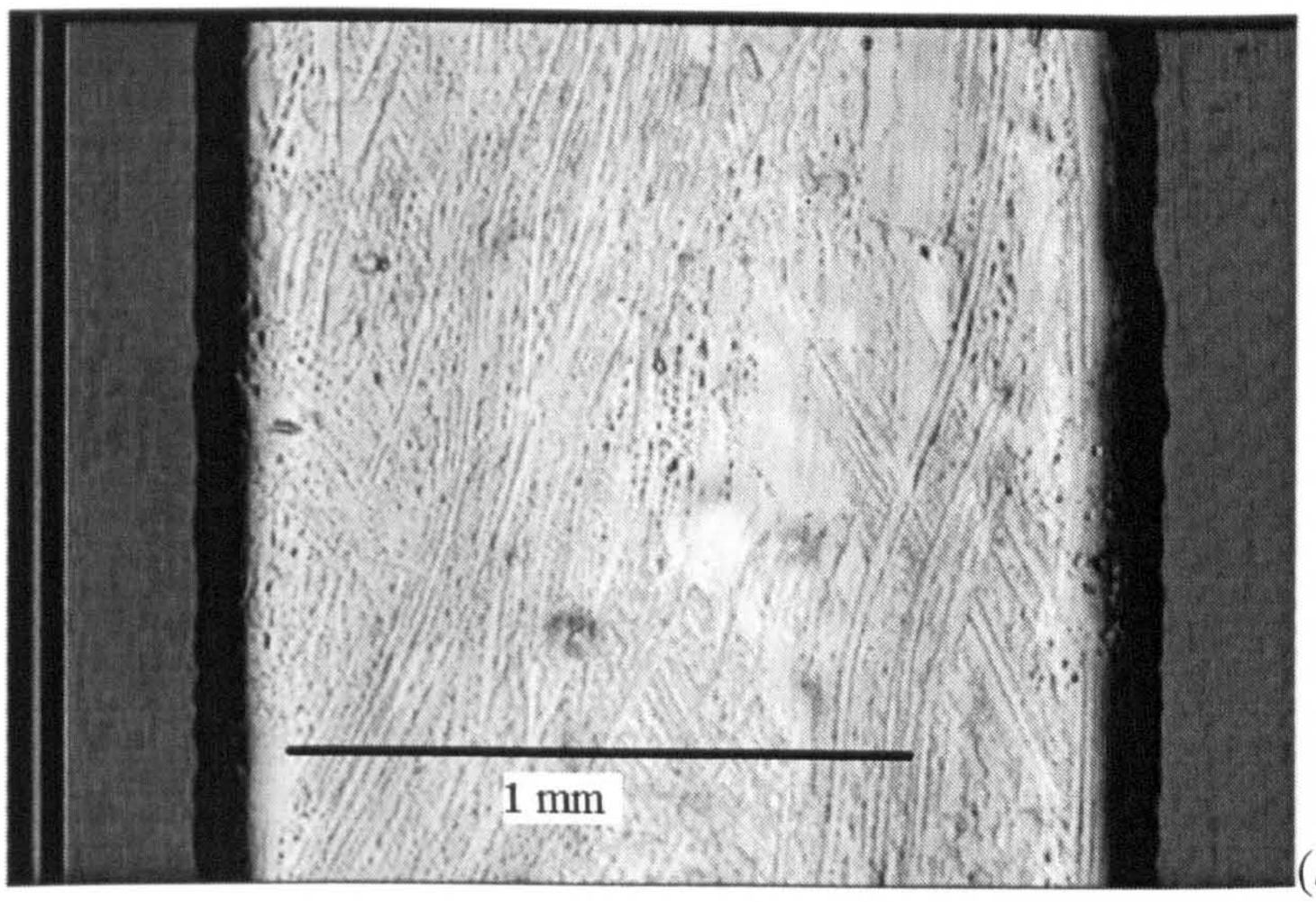

(*b*)

Figure 4.5. Optical photomicrographs of ribbons cast under an atmosphere of (*a*) argon and (*b*) helium.

4.3 Structure and thermal properties

Ductility

Bend tests carried out on the wires demonstrated that all alloys could be bent through 180° without fracture except $Fe_{69.5}Cr_8Si_{7.5}B_{15}$, which fractured when bent beyond 150°. On the other hand, as was mentioned above, casting under argon atmosphere resulted in completely brittle ribbon for all compositions.

X-ray diffraction

XRD diffraction patterns indicated that all alloys in the form of wire had a typical liquid-like diffraction pattern, even for the $Fe_{69.5}Cr_8Si_{7.5}B_{15}$ alloy wire, which was only partially ductile. Figure 4.6 shows a summary of all the data collected for each alloy.

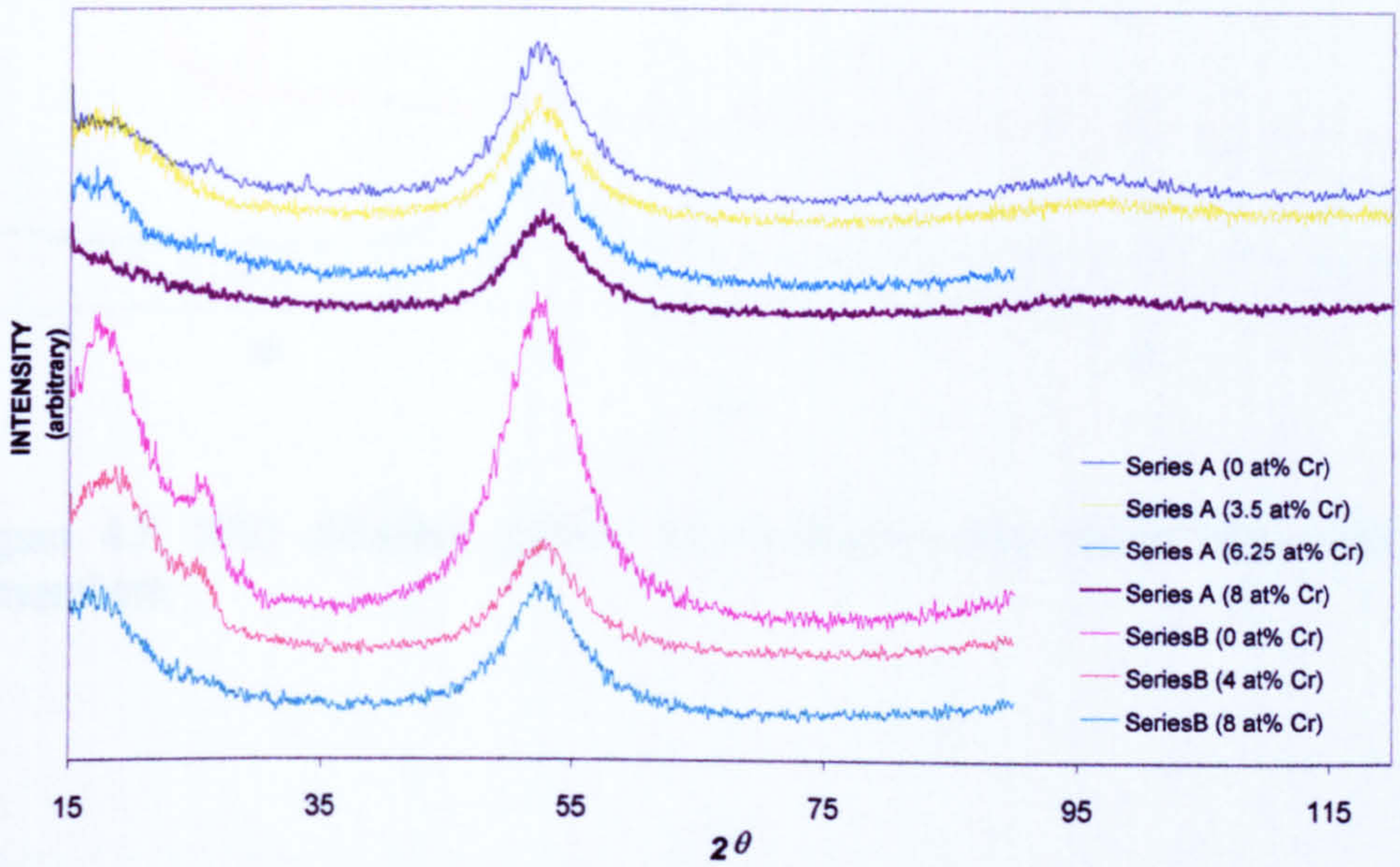

Figure 4.6. XRD diffraction patterns for all alloy wires, series A and B.

X-ray diffraction analysis of ribbons cast under an Ar atmosphere on both surfaces of the ribbon, i.e. free and roll-contact surfaces indicated an amorphous structure, although the samples were totally brittle; figure 4.7 shows examples of the XRD diffractions. The peaks observed before the angle 35° may be the result from the double sided stick tape used for mounting the ribbon samples, which was analysed separately (see figure 4.7).

XRD diffraction patterns for ribbons cast under a He atmosphere, indicated that all the alloys studied had amorphous structures (figure 4.8).

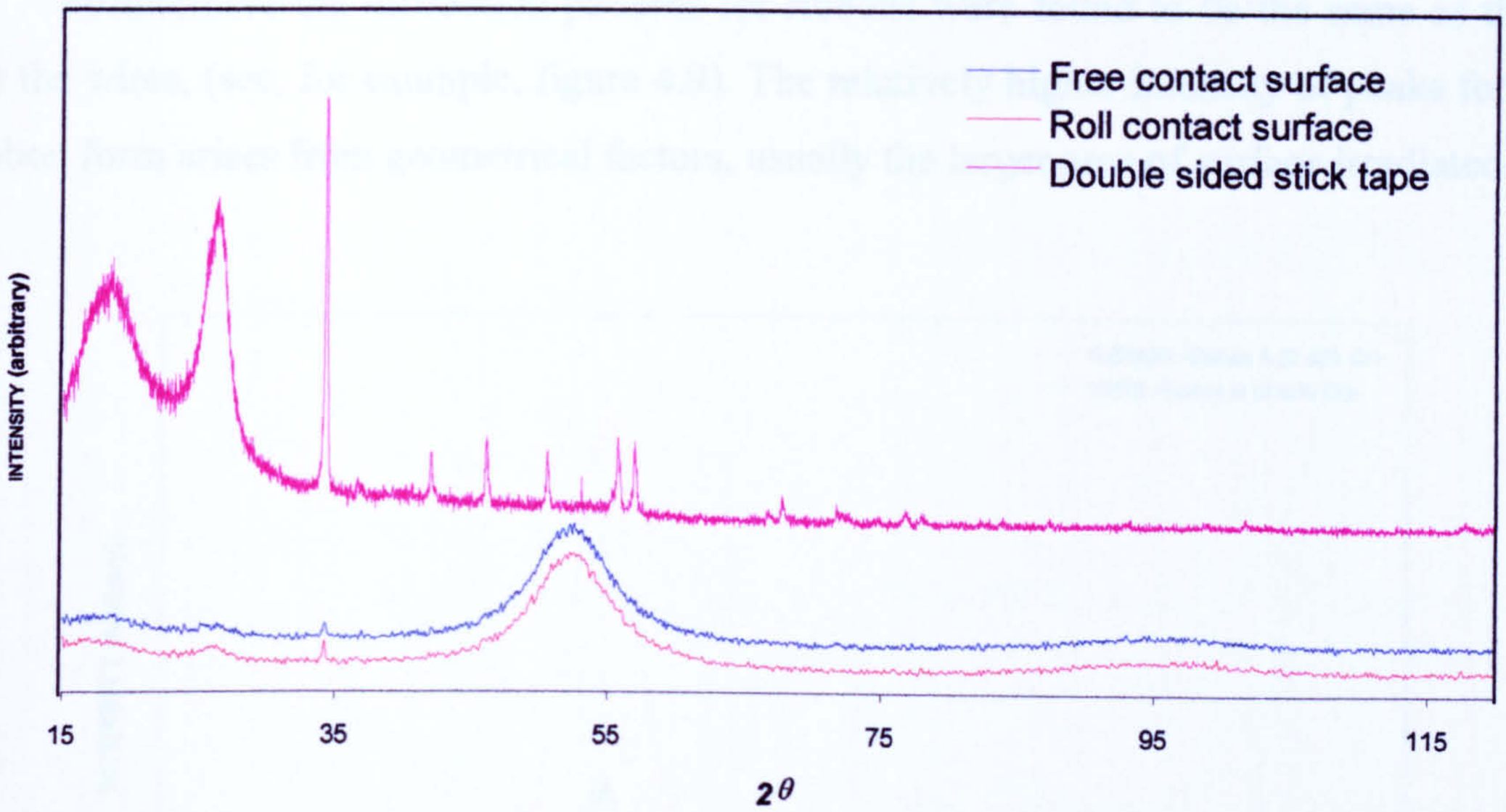

Figure 4.7. XRD diffraction pattern for $Fe_{78}Si_{10}B_{12}$ alloy ribbon cast under Ar atmosphere.

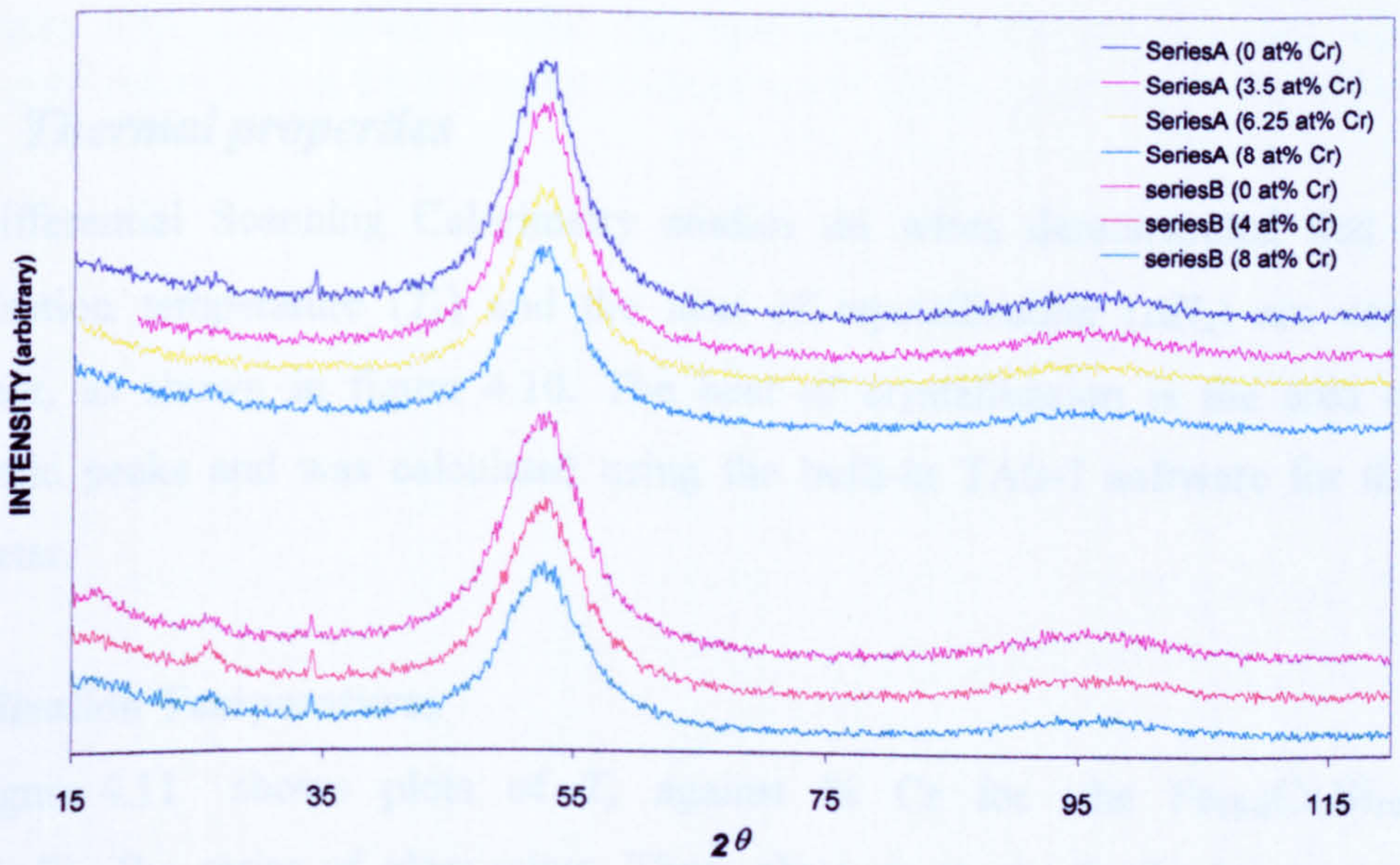

Figure 4.8. XRD diffraction patterns for all alloy ribbons (series A and B), cast under a He atmosphere.

Furthermore the diffraction patterns for ribbons were found to be the same as those for the wires, (see, for example, figure 4.9). The relatively higher intensity of peaks for the ribbon form arises from geometrical factors, usually the larger area of surface irradiated.

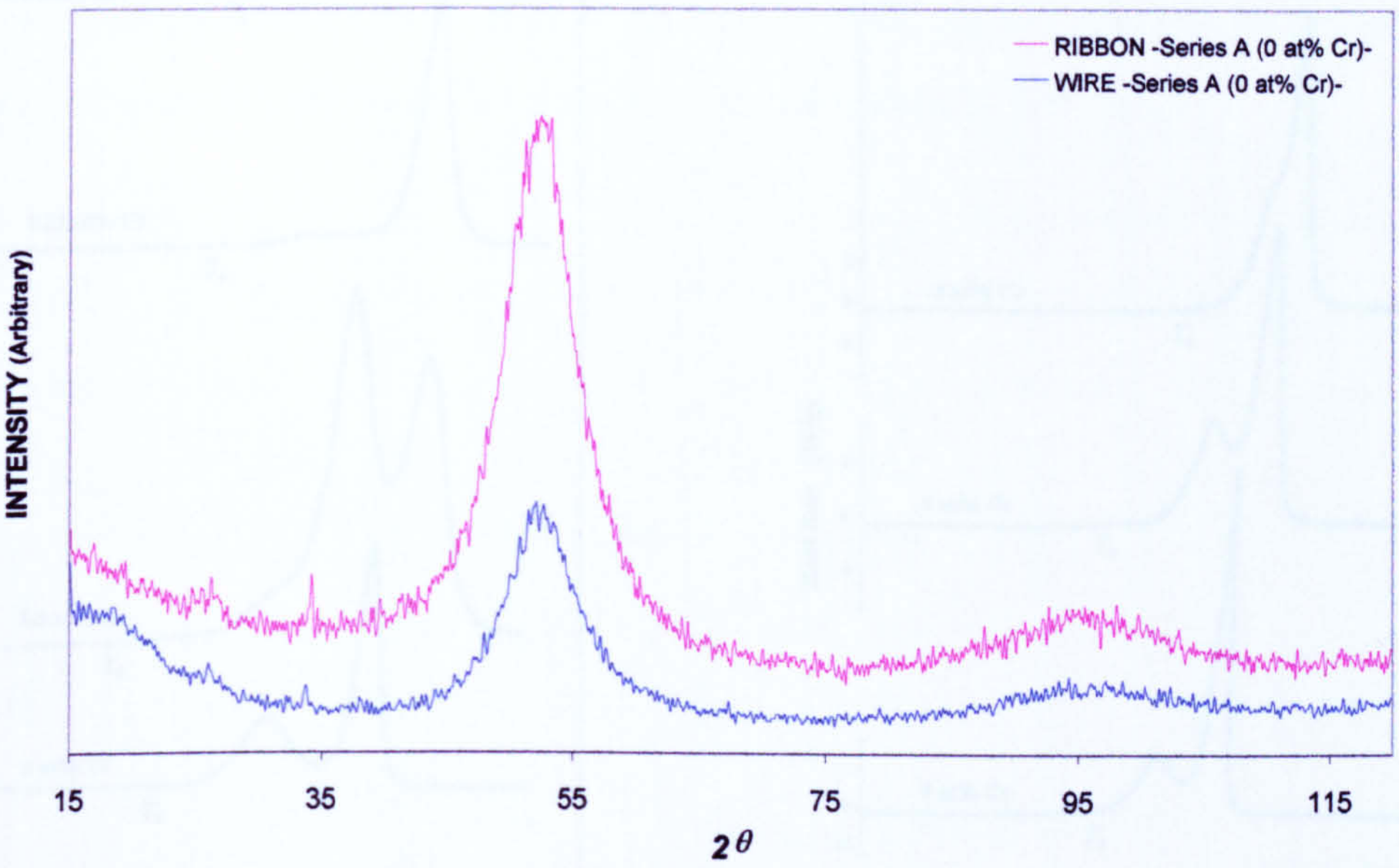

Figure 4.9. XRD diffraction patterns for wire and ribbon forms.

Thermal properties

Differential Scanning Calorimetry studies on wires demonstrated that both the crystallisation temperature (T_x) and the heat of crystallisation (ΔH_x) are composition dependent, as shown in figure 4.10. The heat of crystallisation is the area under the exothermic peaks and was calculated using the built-in TAS-7 software for the DSC-7 calorimeter.

Crystallisation Temperatures

Figure 4.11 shows plots of T_x against % Cr for the $Fe_{78-x}Cr_xSi_{10}B_{12}$ and $Fe_{77.5-x}Cr_xSi_{7.5}B_{15}$ series of glass wires. These show more clearly the increase of T_x and thermal stability with increasing Cr content, which can also be interpreted in terms of the gradual decrease of the first exothermic peak in both series. These plots also show the influence of B and Si on T_x. Clearly the increased B content is more influential in increasing T_x than an increase in Si content since the $Si_{7.5}B_{15}$ alloy series have consistently higher T_x than the $Si_{10}B_{12}$ series for all Cr contents, as was also observed previously [129].

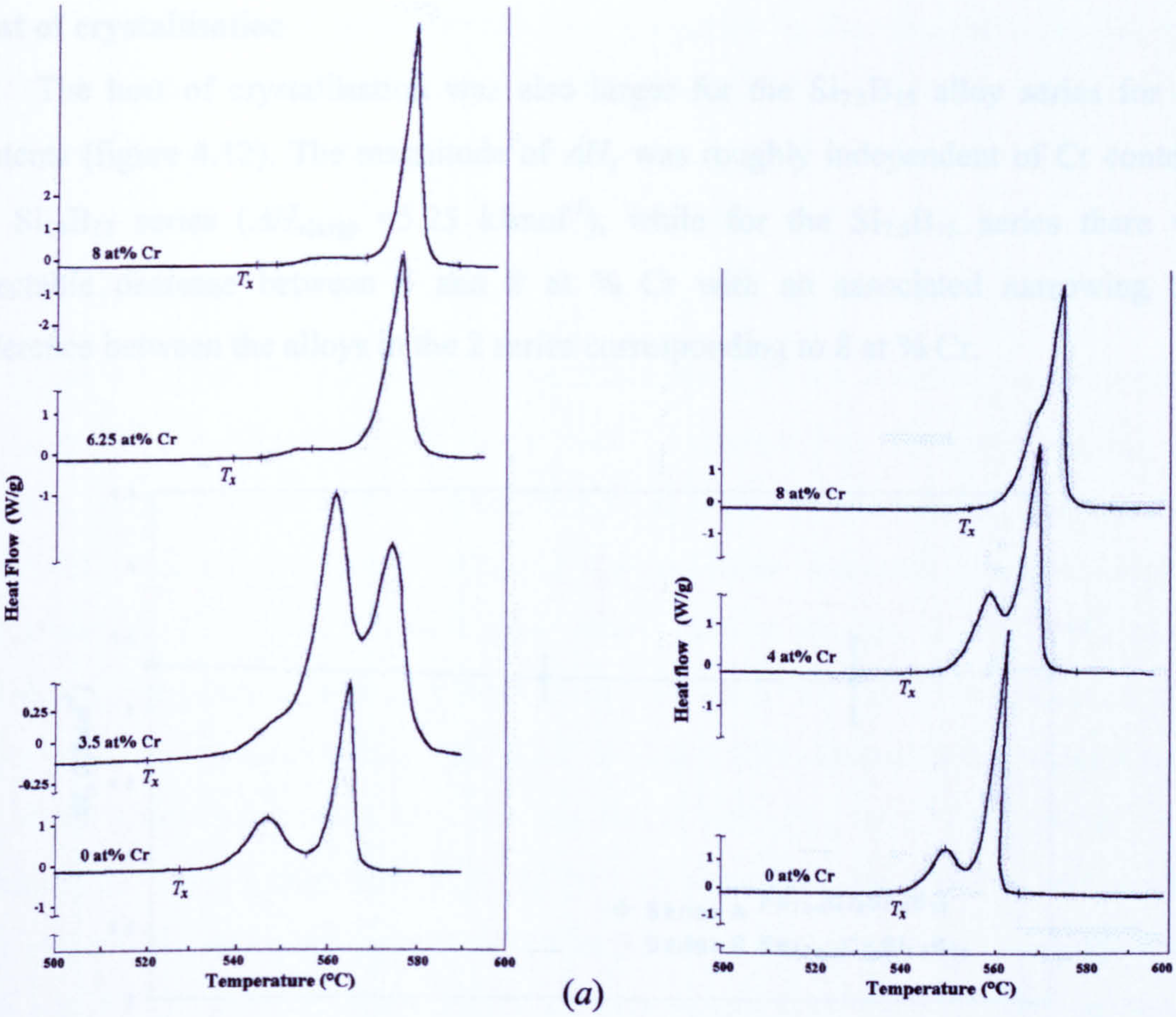

Figure 4.10. DSC curves showing the crystallisation temperature, T_x; the heat of crystallisation, ΔH_x is the area under the exothermic peaks. (*a*) series A, and (*b*) series B.

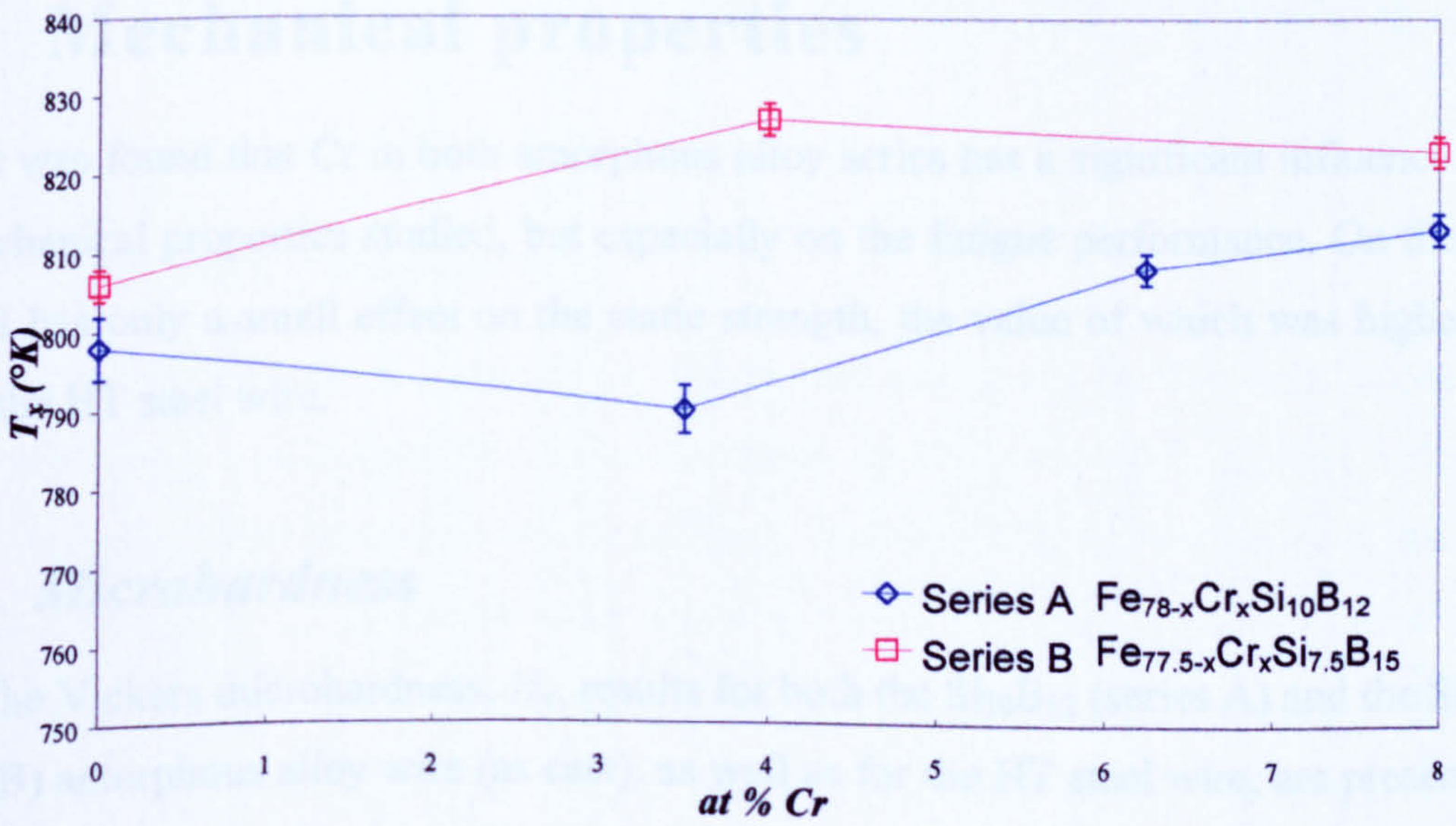

Figure 4.11 Crystallisation temperature, T_x, for both series, as function of Cr content.

Heat of crystallisation

The heat of crystallisation was also larger for the $Si_{7.5}B_{15}$ alloy series for all Cr contents (figure 4.12). The magnitude of ΔH_x was roughly independent of Cr content for the $Si_{10}B_{12}$ series ($\Delta H_{x(avg)}$ =5.25 kJmol^{-1}), while for the $Si_{7.5}B_{15}$ series there was a detectable decrease between 4 and 8 at % Cr with an associated narrowing of the difference between the alloys in the 2 series corresponding to 8 at % Cr.

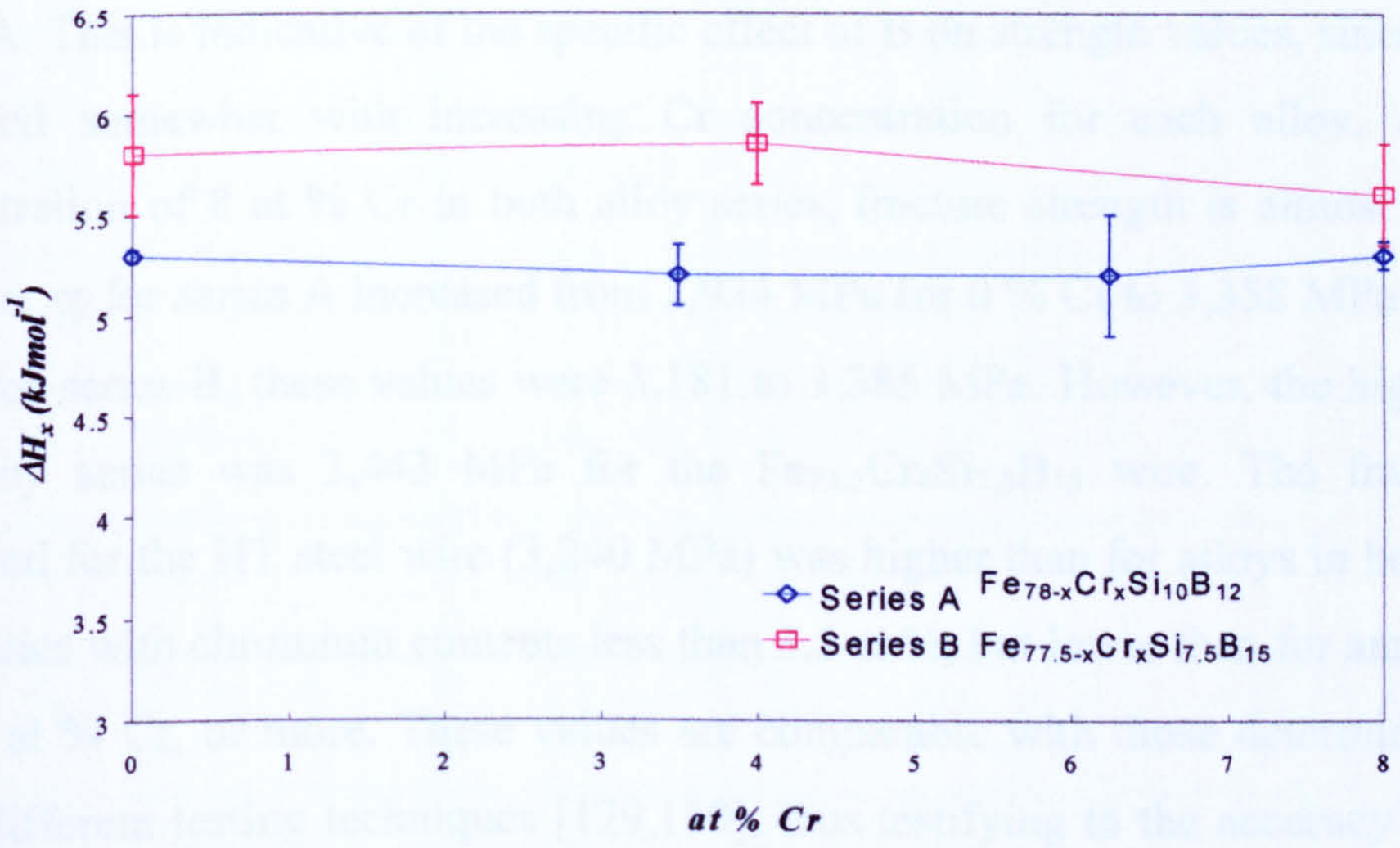

Figure 4.12. Heat of crystallisation, ΔH_x, for all alloy series, as a function of Cr content.

4.4 Mechanical properties

It was found that Cr in both amorphous alloy series has a significant influence on all the mechanical properties studied, but especially on the fatigue performance. On the other hand, B has only a small effect on the static strength, the value of which was higher than that of the HT steel wire.

4.4.1 Microhardness

The Vickers microhardness, H_v, results for both the $Si_{10}B_{12}$ (series A) and the $Si_{7.5}B_{15}$ (series B) amorphous alloy wire (as cast), as well as for the HT steel wire, are presented in table 4.III. The series B wires showed higher H_v values than series A for all compositions, from 0 to 8 at % Cr. For instance, H_v values for series B ranged from 1065 to 1168 VHN

for non- and 8 at % Cr, respectively while, for series A, they ranged from 971 to 1065 VHN. H_v for the HT steel wire was 721 VHN, which is 26 % lower than the smallest value measured for the amorphous wire ($Fe_{78}Si_{10}B_{12}$).

4.4.2 Tensile

Table 4.III shows the tensile strength measured for all the alloy wires studied. The wires in series B showed higher σ_f, for each Cr content than the corresponding wire in series A. This is indicative of the specific effect of B on strength values, since this property increased somewhat with increasing Cr concentration for each alloy, although at a concentration of 8 at % Cr in both alloy series, fracture strength is almost the same. For instance, σ_f for series A increased from 2,924 MPa for 0 % Cr to 3,358 MPa for 8 at % Cr, while for series B, these values were 3,181 to 3,385 MPa. However, the highest value for the alloy series was 3,443 MPa for the $Fe_{73.5}Cr_4Si_{7.5}B_{15}$ wire. The fracture strength measured for the HT steel wire (3,240 MPa) was higher than for alloys in both amorphous wire series with chromium contents less than 3.5 at %, but lower than for amorphous wires with 4 at % Cr, or more. These values are comparable with those determined previously using different testing techniques [129,130], thus testifying to the accuracy of the present testing technique.

Due to the technique employed for these experiments and because it was not possible to use a strain gauge (because of the very fine filaments), strain at fracture, ε_f, was not estimated.

4.4.3 Fracture Toughness

Fracture toughness, K_{Ic}, results for ribbons are also given in table 4.III. Contrary to the hardness and tensile strength values discussed in 4.4.1 and 4.4.2, K_{Ic} did not show a gradual increase with respect to the Cr addition. For instance, K_{Ic} for series A decreased from 70.6 for 0 % Cr to 63 MPa$\sqrt{m}$, for 8 at % Cr, but with smaller values for the intermediate 3.5 and 6.25 at 5 Cr alloy. On the other hand, K_{Ic} for the series B showed a modest increase, from 67.4 for 0 % Cr to 70.6 MPa$\sqrt{m}$ for 8 at % Cr. There is a drop of 53.7 MPa$\sqrt{m}$ for $Fe_{73.5}Cr_4Si_{7.5}B_{15}$. K_{Ic} for X-200 steel and maraging steel are presented in the same table for comparison since it was not possible to measure this property on HT

steel wire; for instance K_{Ic} for X-200 steel is intermediate between the highest and lowest values measured for the alloy glassy ribbons.

Table 4.III. Static properties of amorphous and HT steel wires, and amorphous ribbons

Alloy	H_v (HVN)	σ_f (MPa)	K_{Ic} (MPa$\sqrt{m}$)	E (GPa)
$Fe_{78}Si_{10}B_{12}$	970 ±45	2,925 ±120	70 ±4.5	156 [126]
$Fe_{74.5}Cr_{3.5}Si_{10}B_{12}$	1,040 ±60	3,075 ±120	55.5 ±13.5	156 [126]
$Fe_{71.75}Cr_{6.25}Si_{10}B_{12}$	1,120 ±85	3,265 ±100	59.5 ±7	157 [126]
$Fe_{70}Cr_8Si_{10}B_{12}$	1,065 ±60	3,360 ±350	63 ±10	158 [129]
$Fe_{77.5}Si_{7.5}B_{15}$	1,065 ±50	3,180 ±80	67 ±13	159*
$Fe_{73.5}Cr_4Si_{7.5}B_{15}$	1,110 ±45	3,440 ±100	53.5 ±19.5	176*
$Fe_{69.5}Cr_8Si_{7.5}B_{15}$	1,160 ±55	3,385 ±80	70.5 ±12	157*
HT steel wire	720 ±35	3,240 ±30	-	200 [128]
X-200 steel	-	-	60.4 [69]	-
Maraging steel	-	-	86.8 [69]	-

* Values determined in the University of Cambridge.

4.4.4 Fatigue

The fatigue test results are presented in terms of fatigue limit (stress to failure at 10^7 cycles), the maximum range bending stress, $\Delta\sigma_a$, at which samples did not fracture at an imposed 10^7 cycles, or, when samples fractured prior to 10^7 cycles, at the minimum bending range strain, $\Delta\varepsilon_a$.

In order to see the various effects on fatigue behaviour of the alloy composition and constant mean loading stress, σ_m, initially, the results will be presented as typical fatigue

curves for the compositional series A of wire samples at various σ_m's used, since series B were only tested at one σ_m = 200 MPa. Then the results will be presented for each σ_m used for the different alloy compositions and, finally a summary of both alloy series showing the effect of Cr in terms of stress and strain ranges; HT steel wire results are also included where appropriate for comparison.

Effect of constant mean loading stress

Figure 4.13 shows that for $Fe_{78}Si_{10}B_{12}$ alloy wire no fatigue limit was attained for any of the constant mean loading stresses investigated. On the other hand, it can be seen that the fatigue strength increased on reducing σ_m, from 1550 to 200 MPa in the DP machine. The fatigue strength determined using the SP machine was lower for all compositions than that attained using the DP machine as is shown (using the same nominal parameters) later in this section.

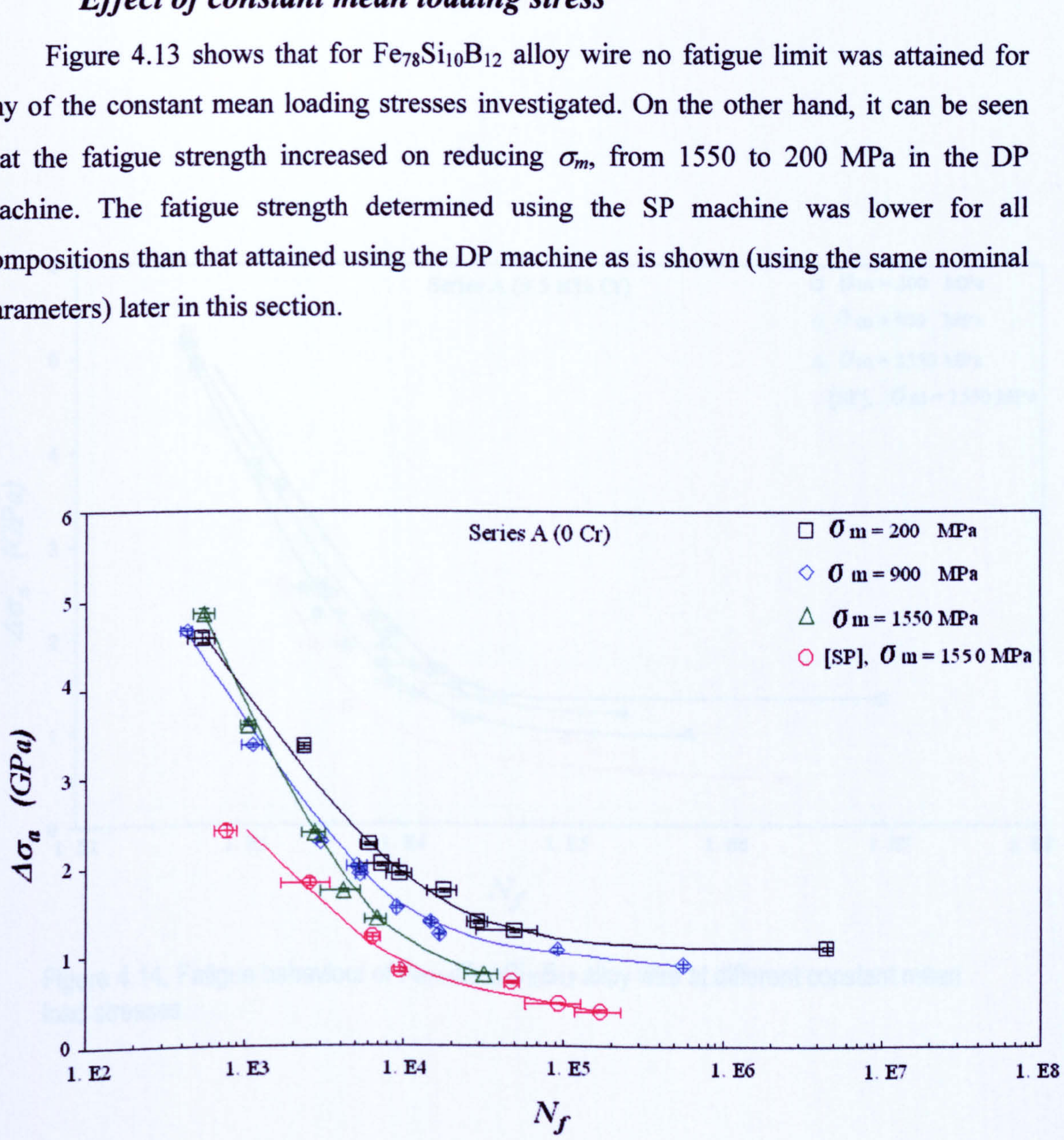

Figure 4.13. $Fe_{78}Si_{10}B_{12}$ alloy wire fatigue behaviour at different constant load mean stresses.

For $Fe_{74.5}Cr_{3.5}Si_{10}B_{12}$ alloy wire a fatigue limit was reached at $\Delta\sigma_a$ = 1.35 GPa when tested at σ_m = 200 MPa. At σ_m's of 900 and 1550 MPa, for the DP machine, as well as for the SP machine no fatigue limit was attained, as can be seen in figure 4.14. Nevertheless, the maximum numbers of cycles to failure were larger than for the $Fe_{78}Si_{10}B_{12}$ alloy wire, tested under the same conditions.

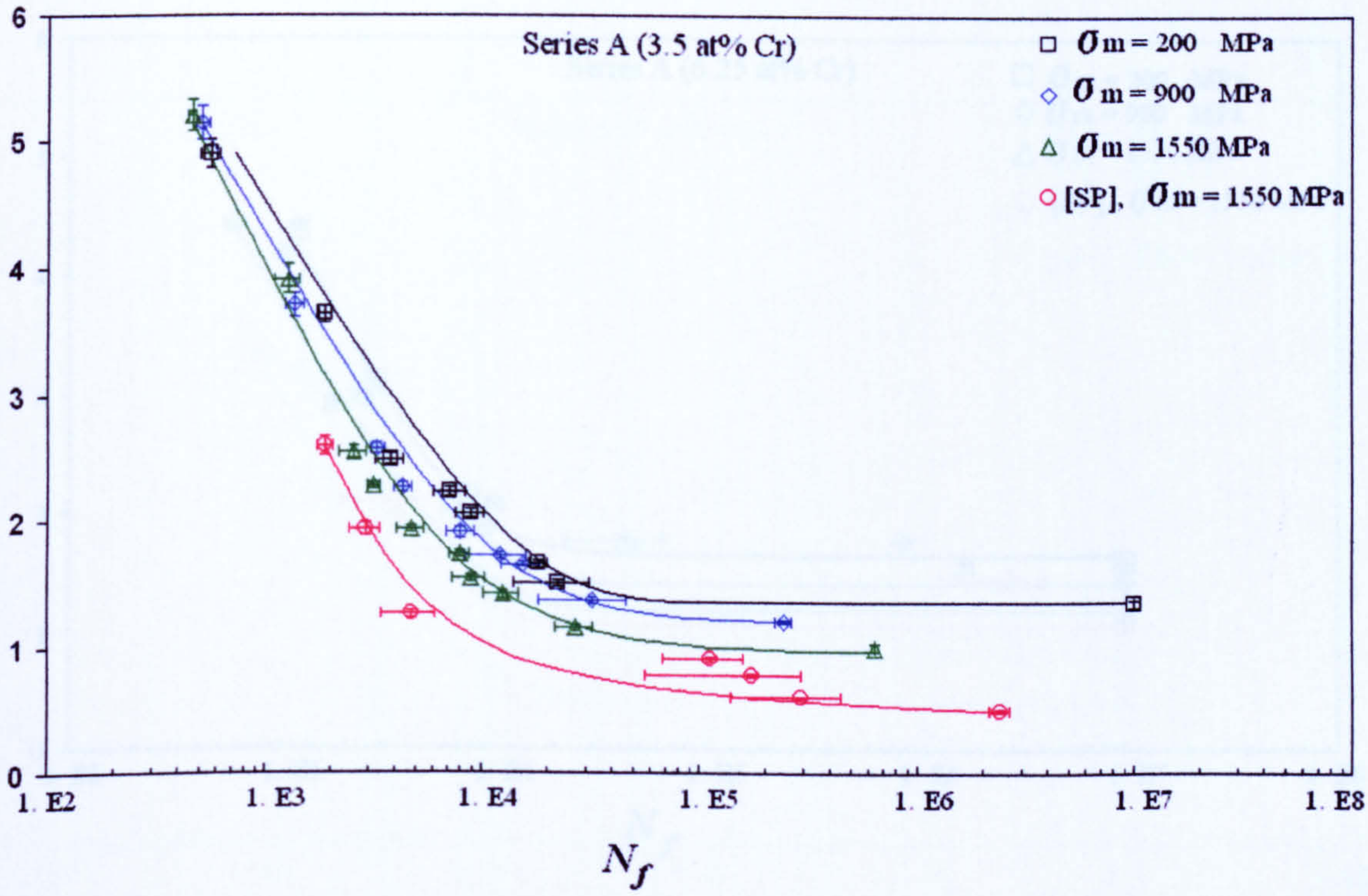

Figure 4.14. Fatigue behaviour of $Fe_{74.5}Cr_{3.5}Si_{10}B_{12}$ alloy wire at different constant mean load stresses.

Fatigue limits were attained for all σ_m's investigated for the $Fe_{71.75}Cr_{6.25}Si_{10}B_{12}$ alloy wire samples tested in the DP and SP machines (figure 4.15). The fatigue limit increased from 1.18 GPa at σ_m = 1550 MPa to 1.59 GPa at σ_m = 200 MPa in the DP machine (17.8 % higher than for the $Fe_{74.5}Cr_{3.5}Si_{10}B_{12}$ alloy wire tested at σ_m = 200 MPa). The fatigue limit determined using the SP machine was about 1.07 GPa.

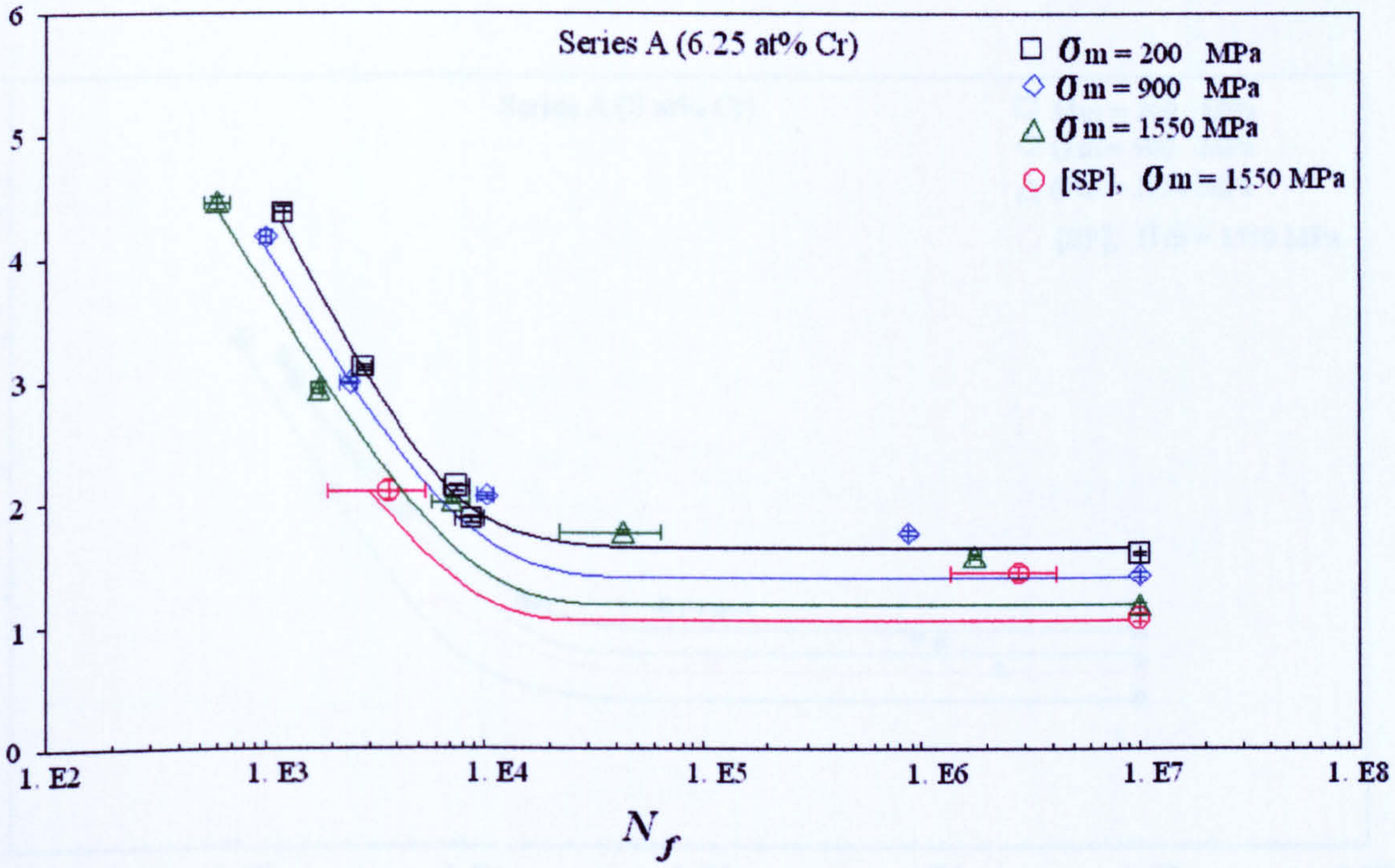

Figure 4.15. Fatigue behaviour of $Fe_{71.75}Cr_{6.25}Si_{10}B_{12}$ alloy wire at different constant mean load stresses.

Effect of composition

Figure 4.17 shows the fatigue behaviour of amorphous alloy wires of compositional series A and B, as well as that of the HT steel wire, tested using the DP machine at a constant mean loading stress of 200 MPa.

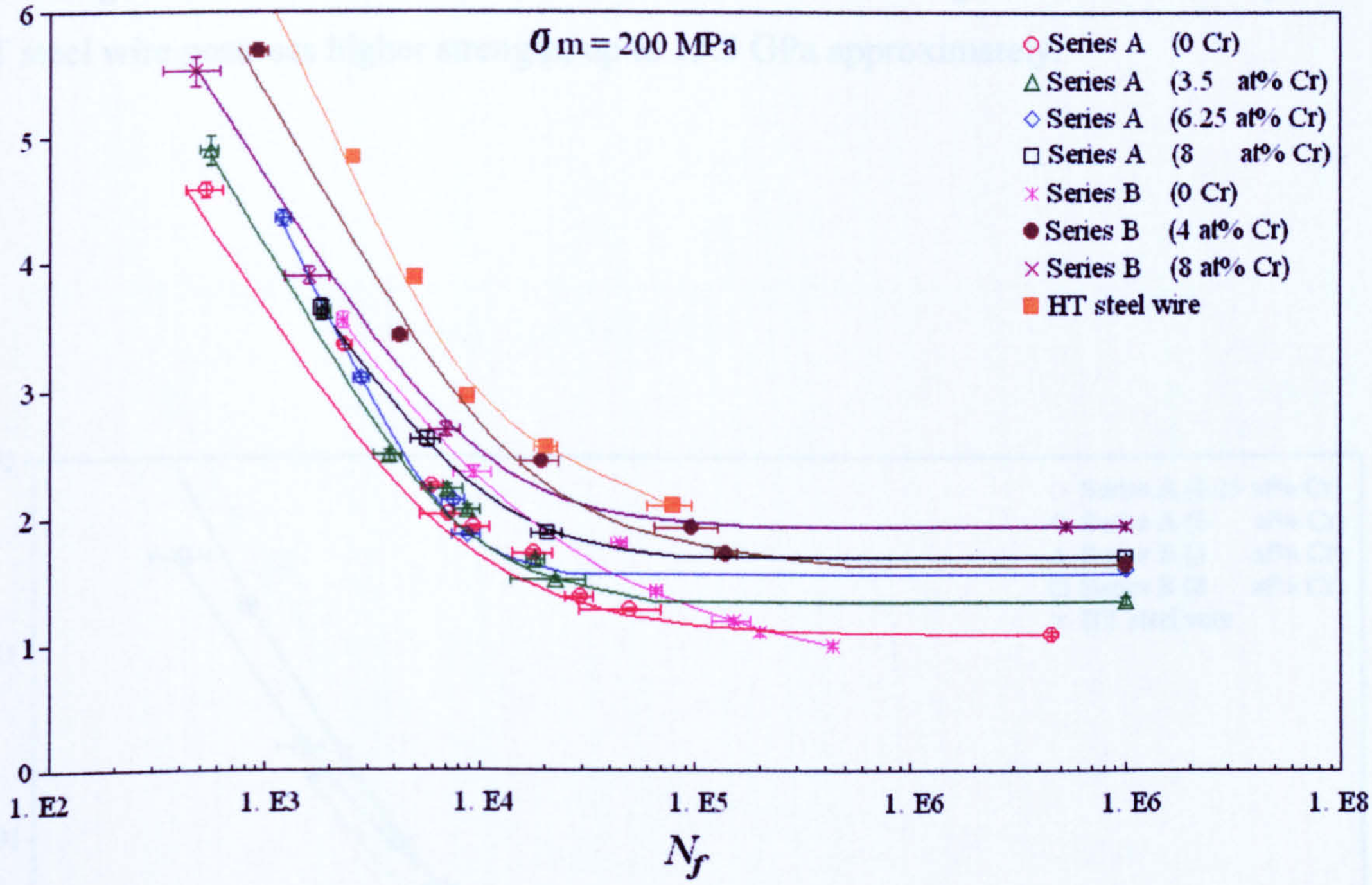

Figure 4.17. Fatigue behaviour of both amorphous alloy wire series and HT steel wire in the DP machine at a constant load mean stress of 200 MPa, as function of $\Delta\sigma_a$.

For both the wires that did not contain Cr, no fatigue limit was reached, the value of $\Delta\sigma_a$ being 1.0 GPa at approximately $4x10^5$ cycles and 1.08 GPa at approximately $4.5x10^6$ cycles for the $Fe_{77.5}Si_{7.5}B_{15}$ and $Fe_{78}Si_{10}B_{12}$ wires, respectively. The fatigue limit increased in the order of $Fe_{74.5}Cr_{3.5}Si_{10}B_{12}$ < $Fe_{71.75}Cr_{6.25}Si_{10}B_{12}$ < $Fe_{73.5}Cr_4Si_{7.5}B_{15}$ < $Fe_{70}Cr_8Si_{10}B_{12}$ < $Fe_{69.5}Cr_8Si_{7.5}B_{15}$. The HT steel wire did not attain a fatigue limit, since it was not possible to decrease $\Delta\sigma_a$ to a suitable low value for this sample due to the much larger wire diameter (245 μm) and sufficiently large pulleys could not be accommodated in the DP machine. Nevertheless, over the range of $\Delta\sigma_a$ the HT steel wire had higher cycles to failure than amorphous alloy wires. This suggests that the fatigue limit performance of the steel wire is superior to that of the amorphous alloy wires. However, in terms of strain range, the fatigue strength of the HT steel wire was lower, as is shown in figure 4.18. At low cycle, the HT steel wire posseses higher strength, up to 13.5 GPa approximately.

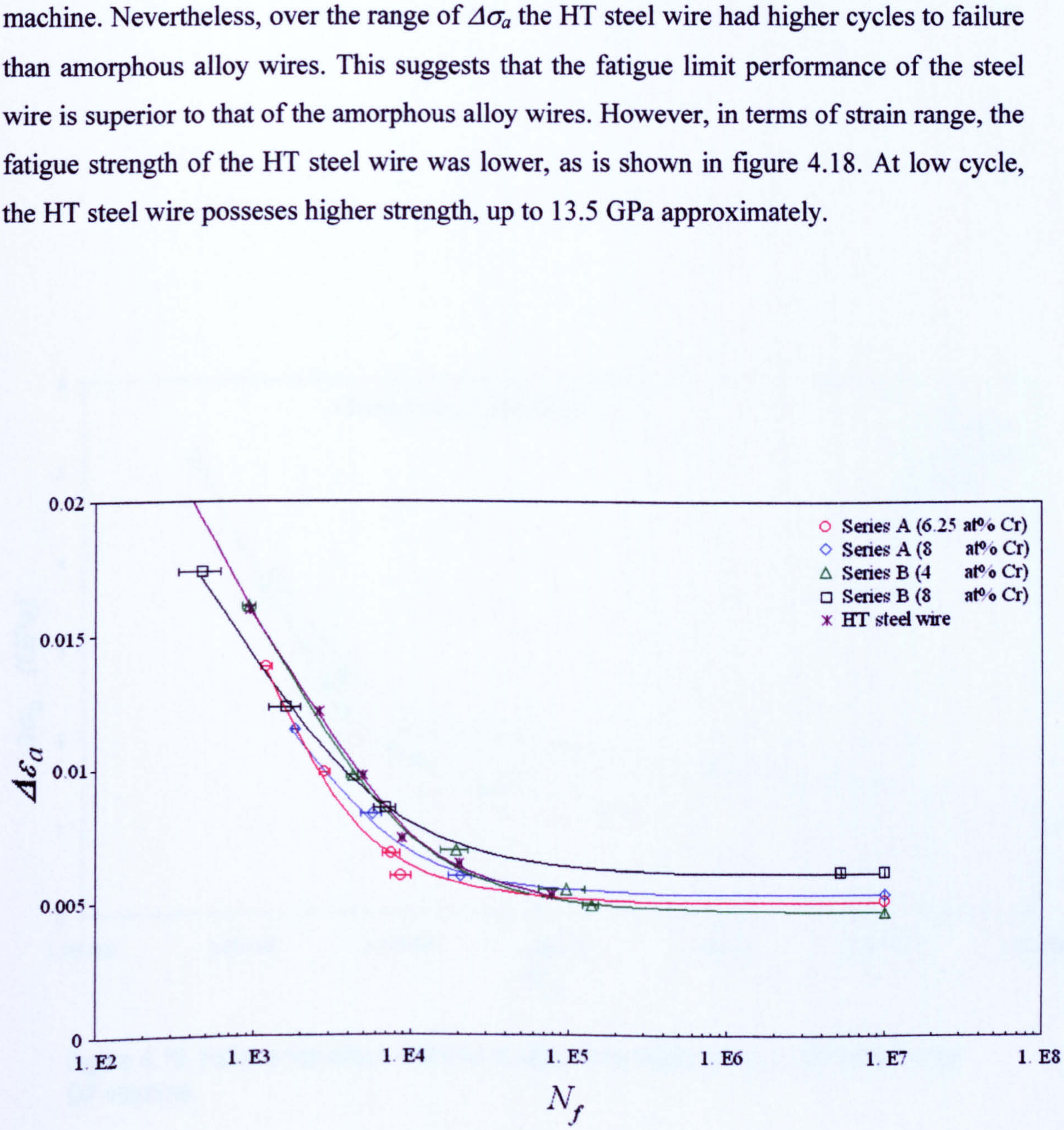

Figure 4.18. Fatigue behaviour of some amorphous alloy wires and HT steel wire in the DP machine at a constant load mean stress of 200 MPa, as a function of $\Delta\varepsilon_a$.

Only amorphous alloy wires of series A were tested at σ_m = 900 MPa. The fatigue behaviour followed a similar pattern to that shown for wires tested at σ_m = 200 MPa. For 0 and 3.5 at % Cr wires no fatigue limit was attained, as seen in figure 4.19. The fatigue limits for amorphous alloy wires containing 6.25 and 8 at % Cr were 1.42 and 1.45 GPa, respectively; these values are lower than those obtained when tested at σ_m = 200 MPa, i.e. 1.59 and 1.68 GPa, respectively.

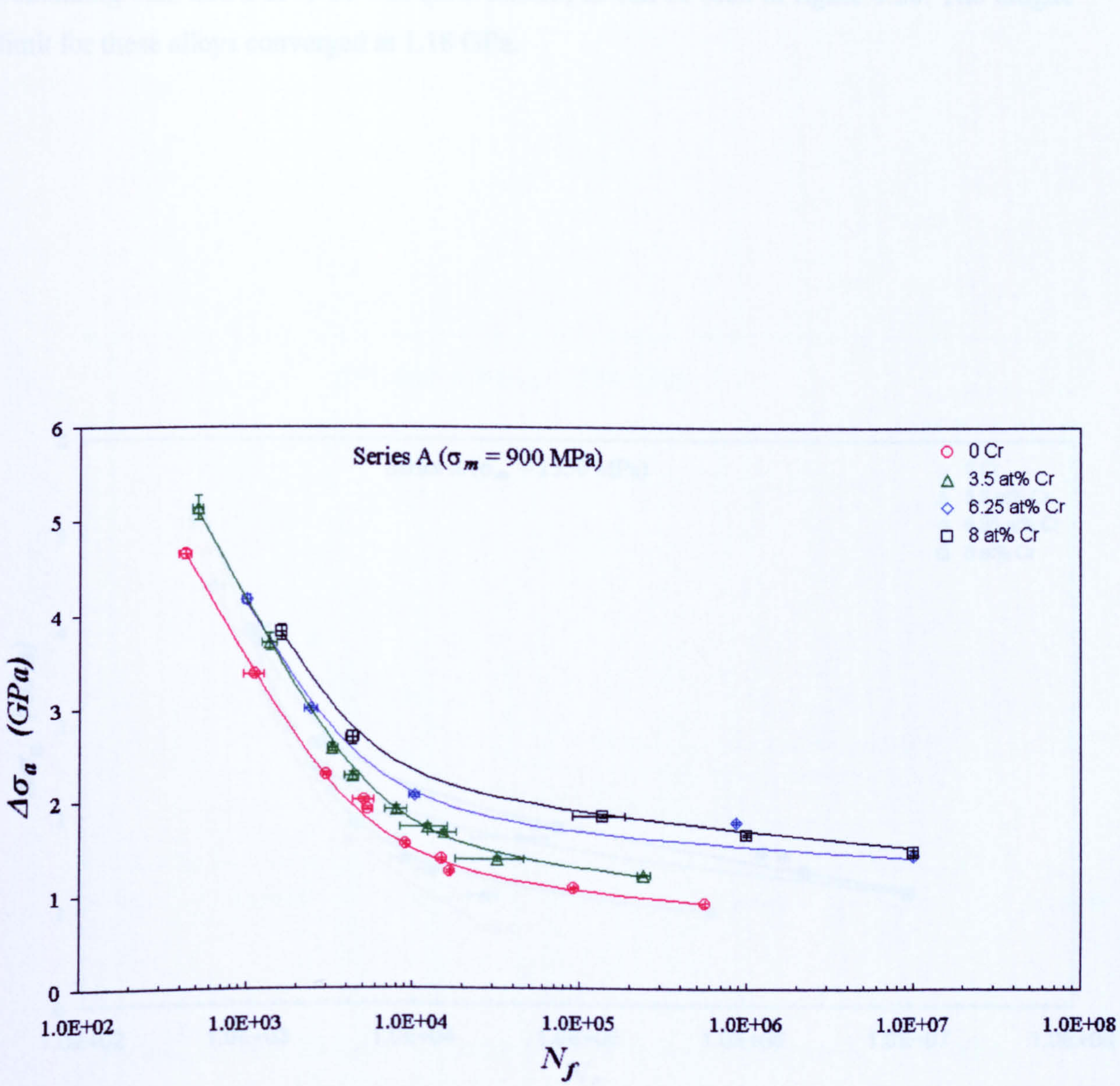

Figure 4.19. Fatigue behaviour of series A alloy wires tested at σ_m = 900 MPa, in the DP machine.

Only series A were tested at σ_m = 1550 MPa; the fatigue behaviour showed the same pattern to that shown at σ_m = 200 and 900 MPa. In this case, the maximum number of cycles reached for 0 and 3.5 at % Cr amorphous alloy wires corresponded to lower stress ranges than those when tested at σ_m = 200 and 900 MPa (0.8 and 1 GPa, respectively). The maximum number of cycles that $Fe_{78}Si_{10}B_{12}$ attained was the lowest for any of the fatigue tests carried out (approximately $3x10^4$ cycles). The fatigue behaviour for alloy wires containing 6.25 and 8 at % Cr was quite similar, as can be seen in figure 4.20. The fatigue limit for these alloys converged at 1.18 GPa.

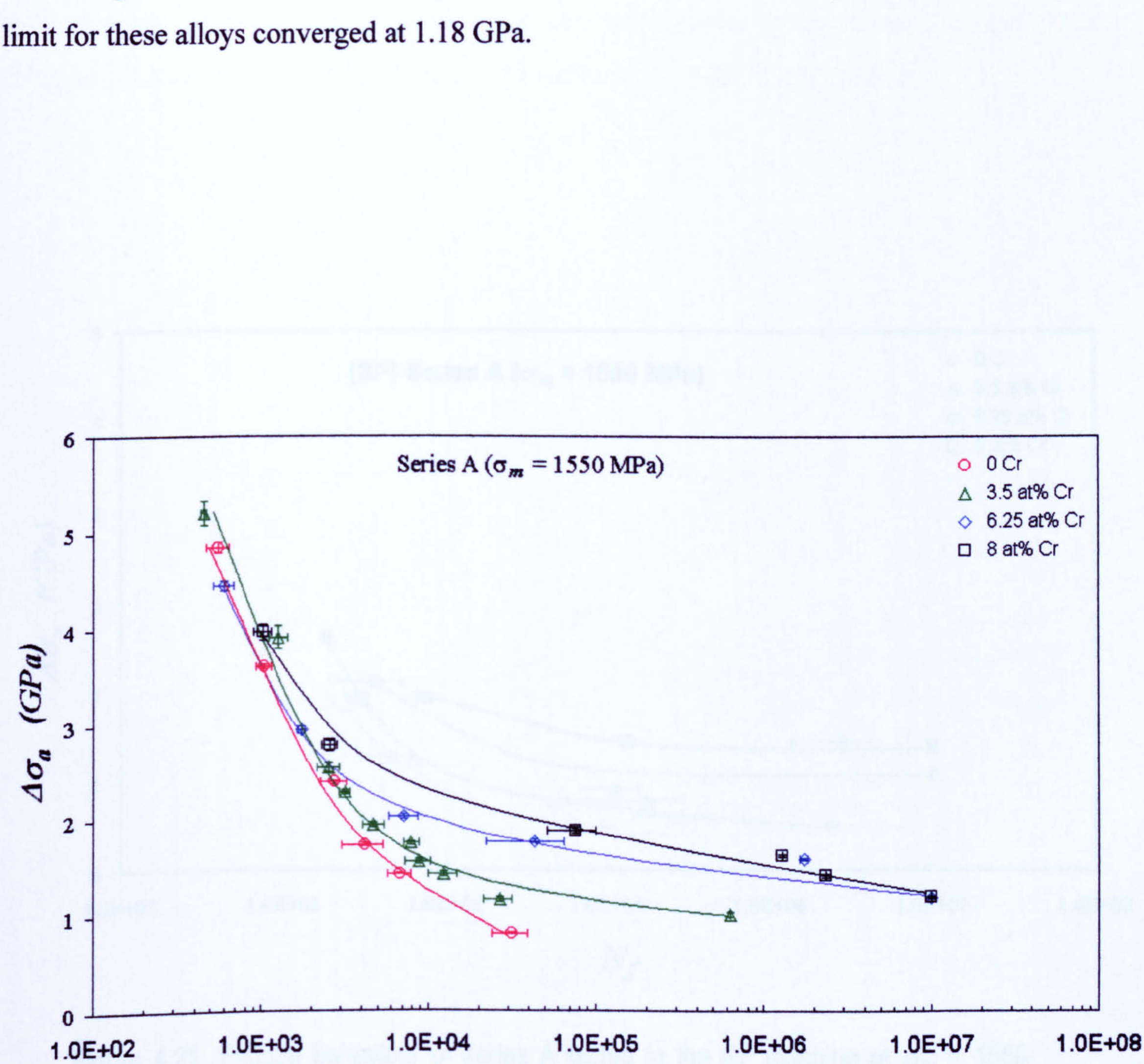

Figure 4.20. Fatigue behaviour of series A alloy wires tested at σ_m = 1550 MPa, in the DP machine.

Figure 4.21 shows the effects of Cr on the fatigue behaviour of the alloy glass series A tested in the SP machine at σ_m = 1550 MPa. It can be seen that the fatigue performance increased with the Cr concentration, in a similar way to that found for the DP machine tests for all the σ_m's studied. Again, for alloys containing 0 and 3.5 at % Cr no fatigue limit was attained and only the alloys containing 6.25 and 8 at % Cr manifested such a limit, at stress ranges $\Delta\sigma_a$ of 1.42 and 1.45 GPa, respectively.

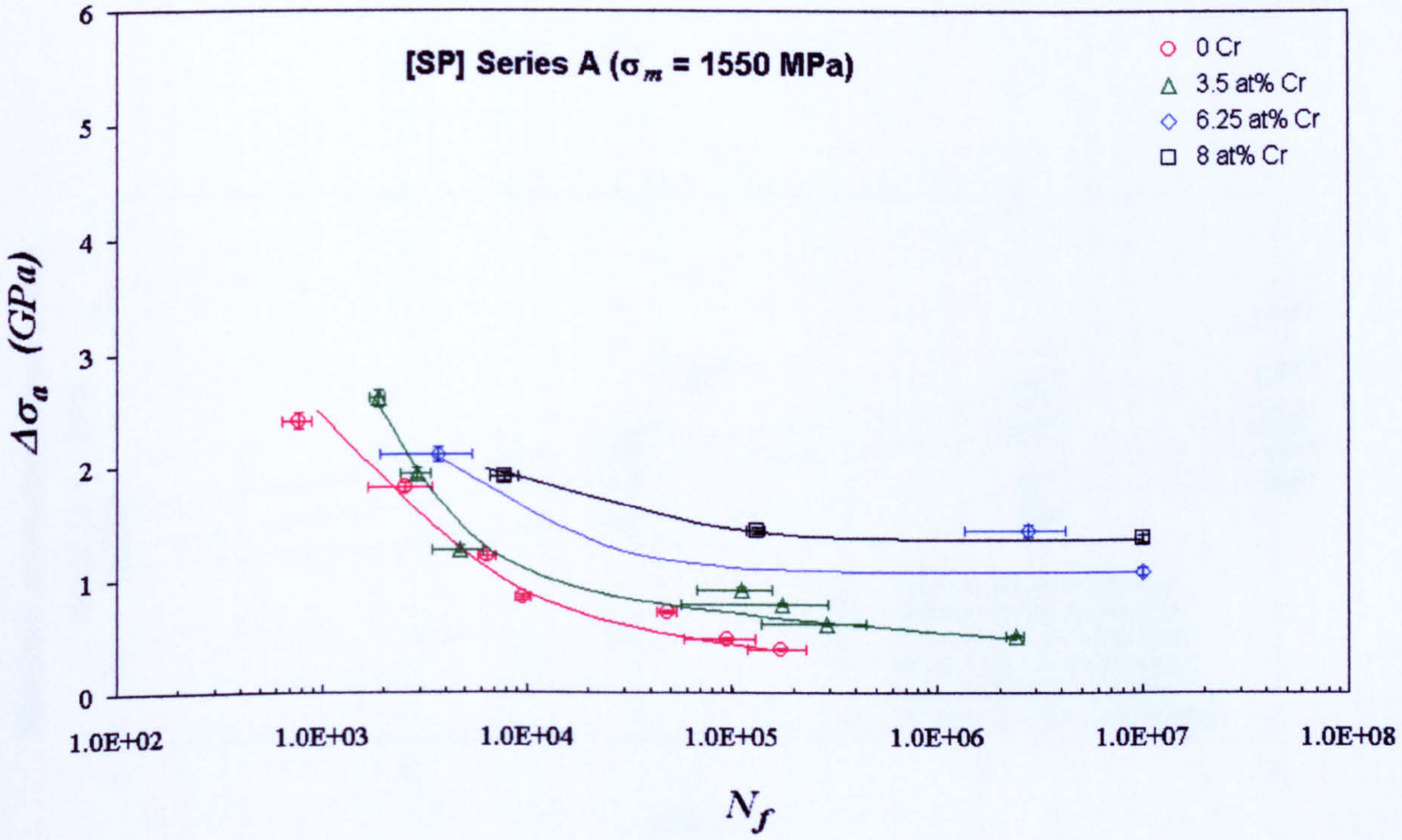

Figure 4.21. Fatigue behaviour of series A tested in the SP machine at σ_m = 1550 MPa.

As seen before, some alloy wires did not attain a clear fatigue limit. The effects of both constant load mean stress and composition on the fatigue behaviour of both glassy wire series are summarised in figure 4.22 with all the results of fatigue limit as a function of chromium content, including those for which no fatigue limit was reached. In the latter case, the maximum stress range that gave rise to a finite lifetime is used. It is important to note that these data can therefore only be used to indicate trends in the fatigue behaviour as a function of composition. This graph clearly shows the great influence of the Cr addition to both alloy wires, as the fatigue performance increases as this element is added. This influence is more marked in series B than in series A, probably due to boron.

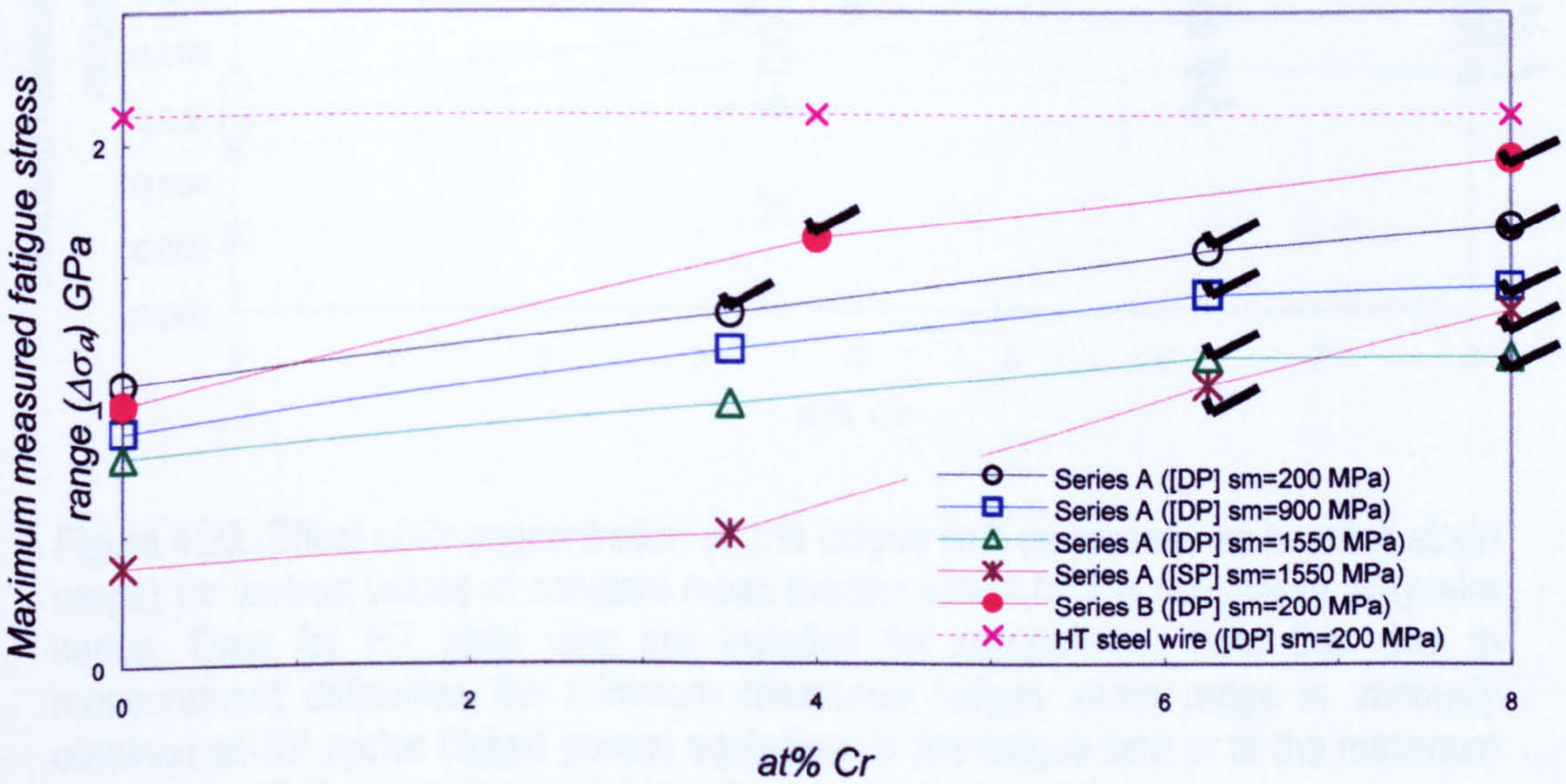

Figure 4.22. Effect of Cr concentration on the maximum measured stress range fatigue limit expressed by bending stress ranges for various values of constant mean loading stress for both glassy alloy wires. Data for HT steel wire are included for comparison. Note that due to measurement difficulties the minimum measured fatigue stress range is variously obtained at 10^7 cycles (ticked points) equivalent to the fatigue limit or at the maximum measurable lifetime with the available pulleys (not ticked points).

On the other hand, figure 4.23 presents the same summary as a function of Cr content, but now with respect to the bending strain range. In this figure it is seen that the maximum bending strain range corresponding to the maximum number of cycles reached by the HT steel wire merges with the fatigue limit of $Fe_{70}Cr_8Si_{10}B_{12}$ amorphous alloy wire, tested at σ_m = 200 MPa, and that is lower than the fatigue limit of $Fe_{69.5}Cr_8Si_{7.5}B_{15}$ amorphous alloy wire tested at the same constant load mean stress.

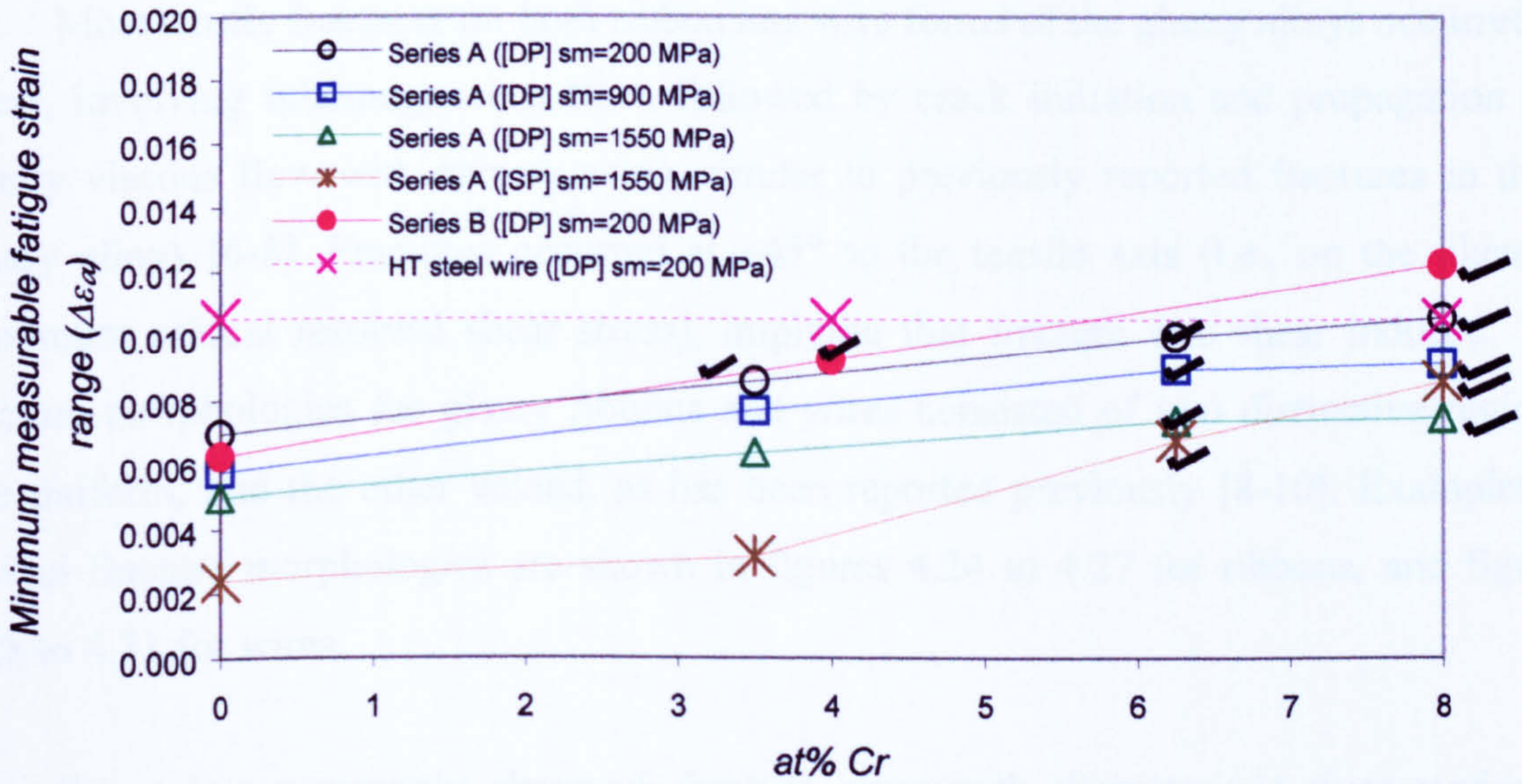

Figure 4.23. Effect of Cr concentration on the fatigue limit (expressed as bending strain range) for various values of constant mean loading stress for the two glassy alloy wire series. Data for HT steel wire are included for comparison. Note that due to measurement difficulties the minimum measured fatigue strain range is variously obtained at 10^7 cycles (ticked points) equivalent to the fatigue limit or at the maximum measurable lifetime with the available pulleys (not ticked points).

4.5 Fracture Morphology

SEM was employed for the observation of the morphologies of both tensile and fatigue fractures. This section is divided in two parts, one covering the tensile fracture morphologies and the other the fatigue fracture surfaces.

4.5.1 Tensile fracture morphology

The fracture morphologies for ribbons presented in this section correspond to those obtained from the tests performed to measure the fracture toughness. These fracture morphologies are similar to those for amorphous wires.

Most tensile fractures for both ribbon and wire forms of the glassy alloys occurred by shear, involving inhomogeneous flow, followed by crack initiation and propagation and finally viscous flow with narrow veins, similar to previously reported fractures in these glassy alloys [6-8]. Fractures occurred at ~45° to the tensile axis (i.e., on the plane of maximum critical resolved shear stress), implying that fracture was shear induced. The fracture morphologies for glassy ribbons and wires consisted of two distinctive regions; one uniform, and the other veined, as has been reported previously [8-10]. Examples of typical fracture morphologies are shown in figures 4.24 to 4.27 for ribbons, and figures 4.28 to 4.31 for wires.

Other, less commonly observed, fracture types with characteristic river markings, were encountered for cases where deformation was not induced on a ~45° shear plane, for both ribbon and wire forms. Figure 4.32 shows an example of this type of fracture for ribbon; in this case, the morphology suggests that fracture initiated from two opposite planes, probably induced by shear. In the case of wires for this type of morphology, shown in figures 4.33 and 4.34, fracture was not initiated by shear and more probably as a result of a load stress concentration, which can be seen from the fact that the crack grew from one point and distributed over the entire cross section. It is evident that this type of the fracture is typically brittle due to the nature of fracture surface and that the fracture planes were approximately normal to the tensile axis.

On the other hand, the tensile fracture morphologies observed for HT steel wire were characterised by the typical features found for this type of crystalline high strength steel. Figure 4.35 shows an example, indicating dimples in the central region and a clear evidence of necking.

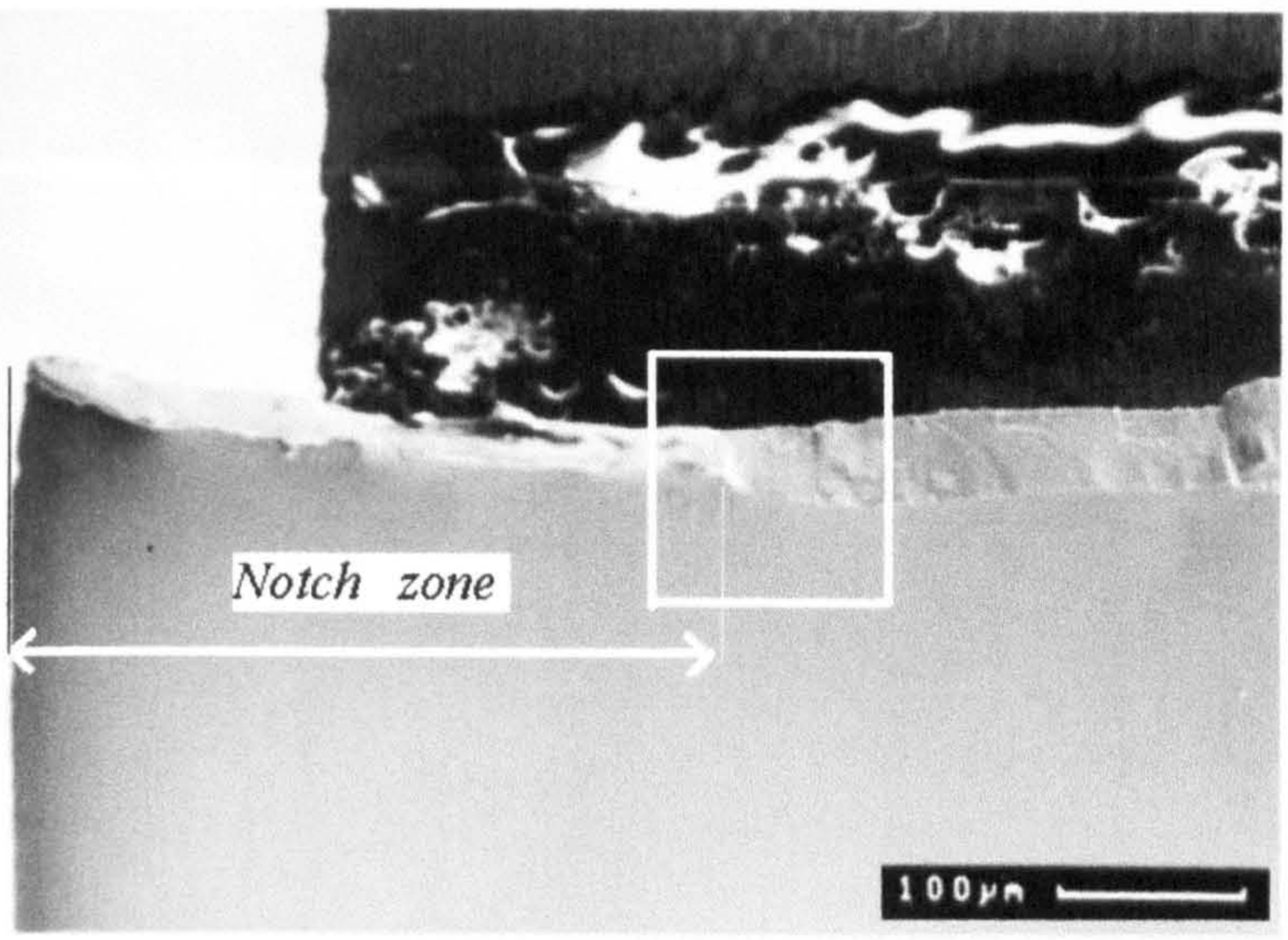

Figure 4.24. SEM photograph of $Fe_{74.5}Cr_{3.5}Si_{10}B_{12}$ glassy ribbon failed in fracture toughness mode I test. K_c = 68.46 MPa$\sqrt{m}$.

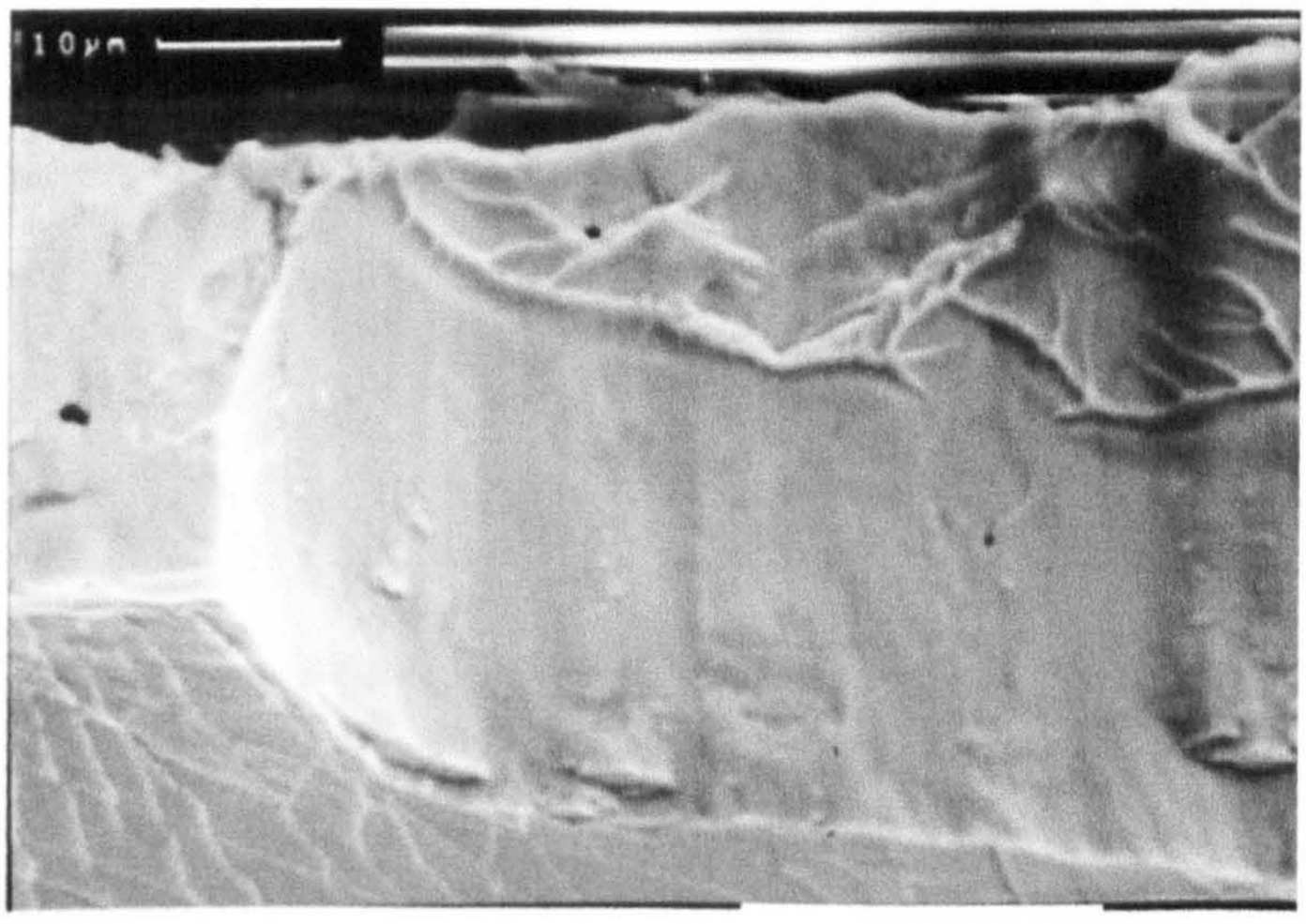

Figure 4.25. Higher magnification of figure 4.24, showing the two distinctive zones on the fracture surface, smooth and veined.

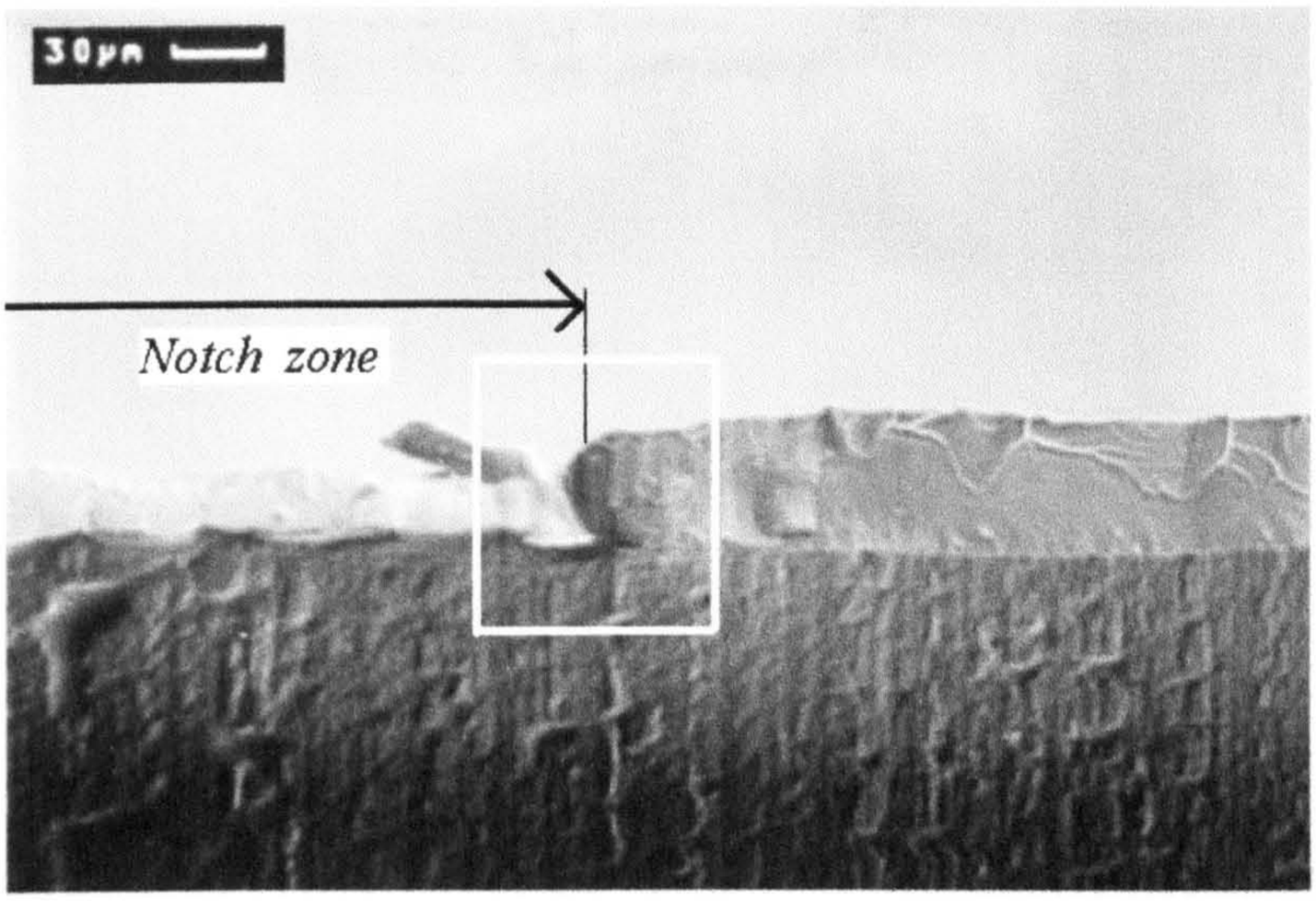

Figure 4.26. SEM photograph corresponding to the counterpart of the fracture surface shown in figure 4.24.

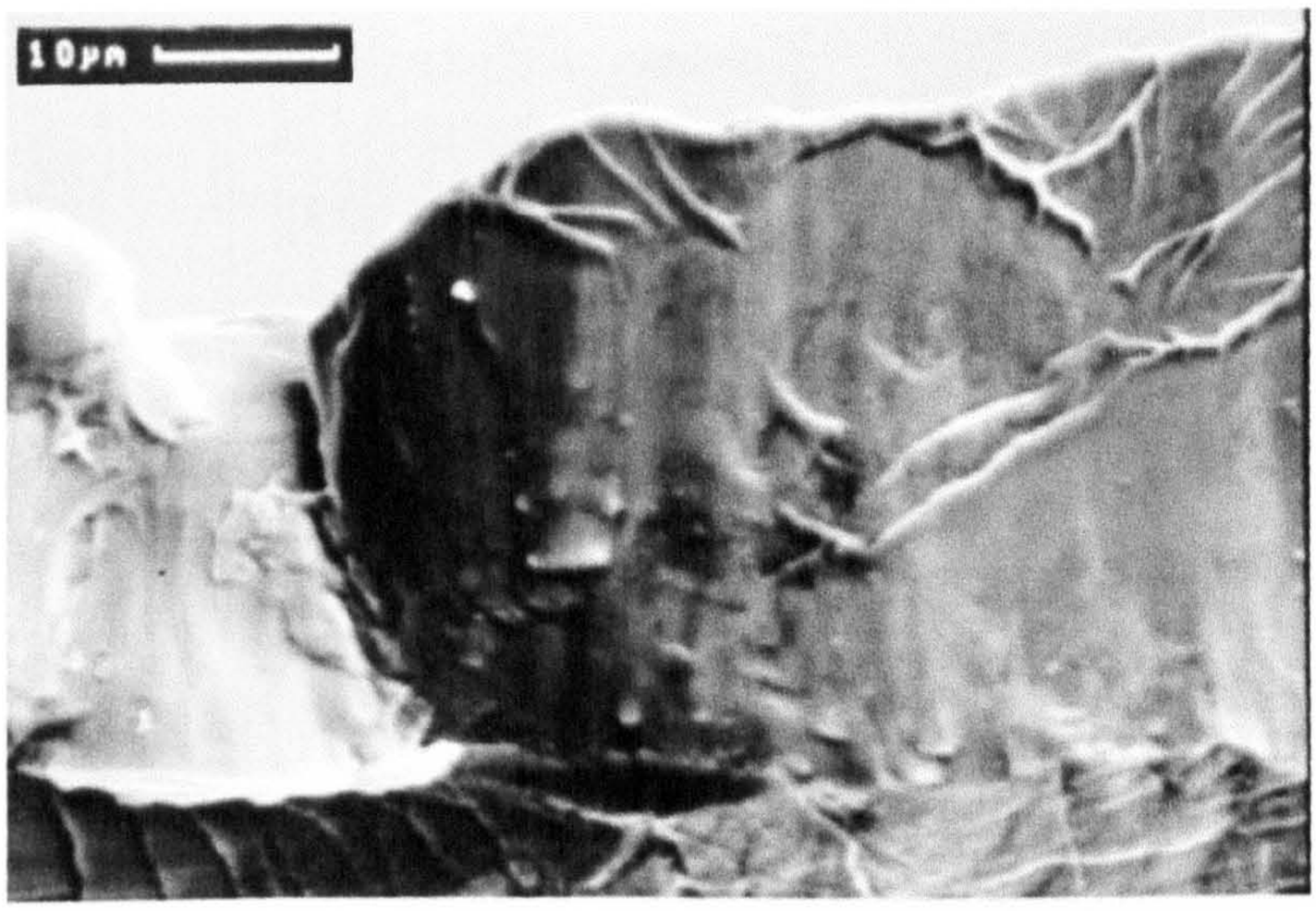

Figure 4.27. Higher magnification of figure 4.26, showing the two detailed distinctive zones on the fracture surface, smooth and veined.

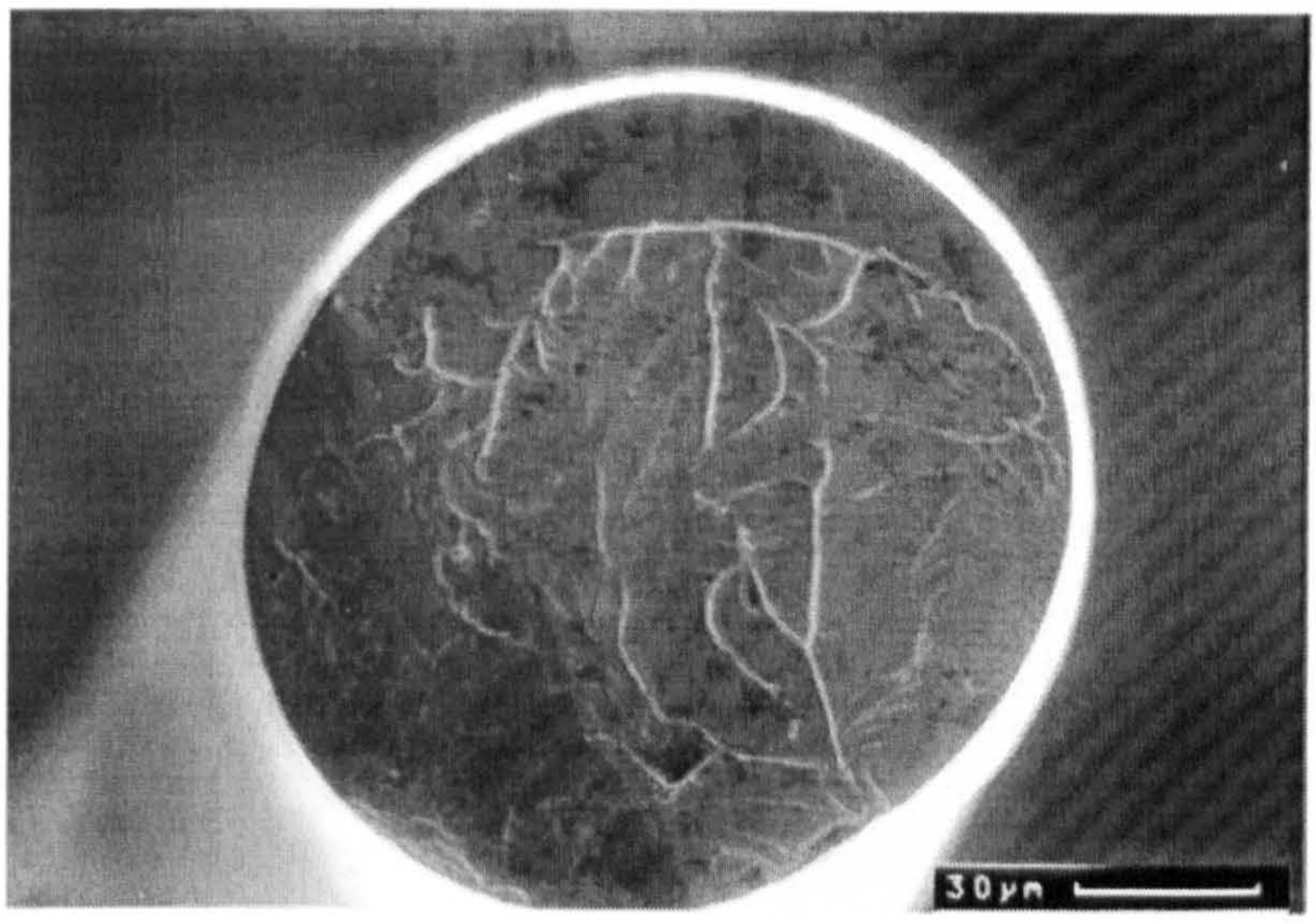

Figure 4.28. SEM photograph of $Fe_{73.5}Cr_4Si_{7.5}B_{15}$ glassy alloy wire failed in tension at a load of 4.6 kg, equivalent to a fracture strength, σ_f = 3,520 MPa.

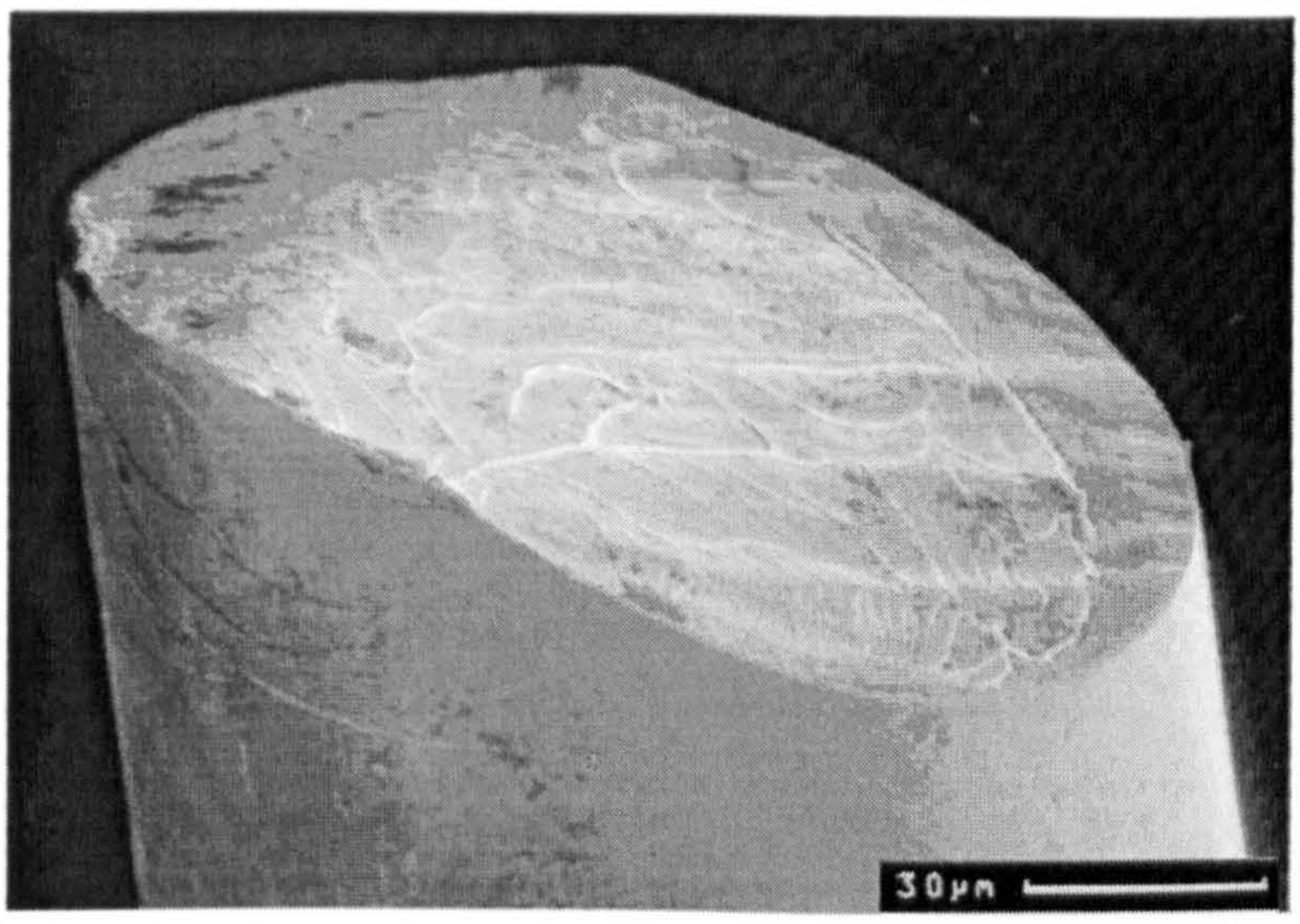

Figure 4.29. Same sample as figure 4.28, tilted ~60° and rotated ~30°.

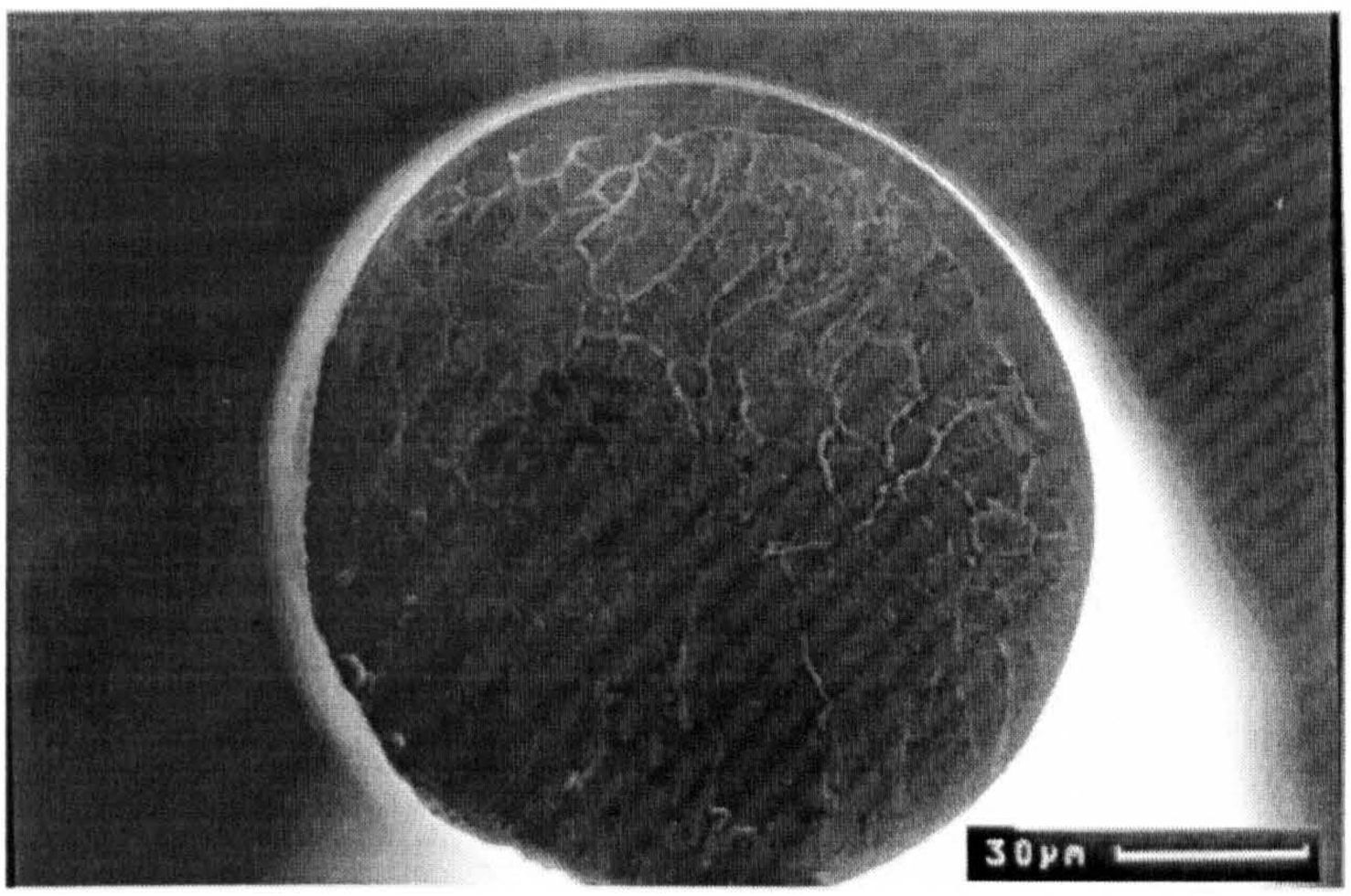

Figure 4.30. SEM photograph of $Fe_{69.5}Cr_8Si_{7.5}B_{15}$ glassy wire failed in tension at a load of 4.11 kg, equivalent to a fracture strength, σ_f = 3,450 MPa.

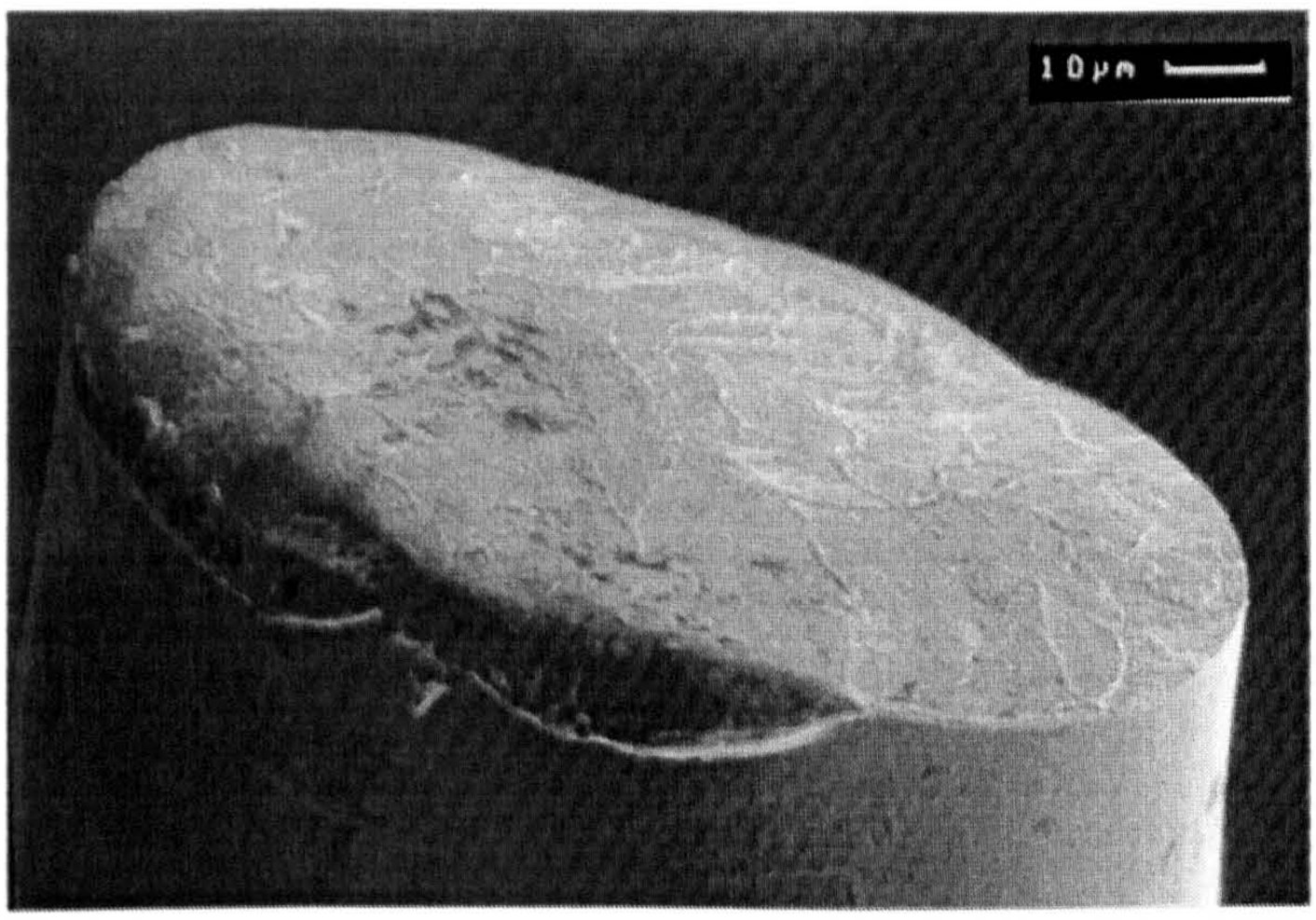

Figure 4.31. Same sample as figure 4.30, tilted ~75°.

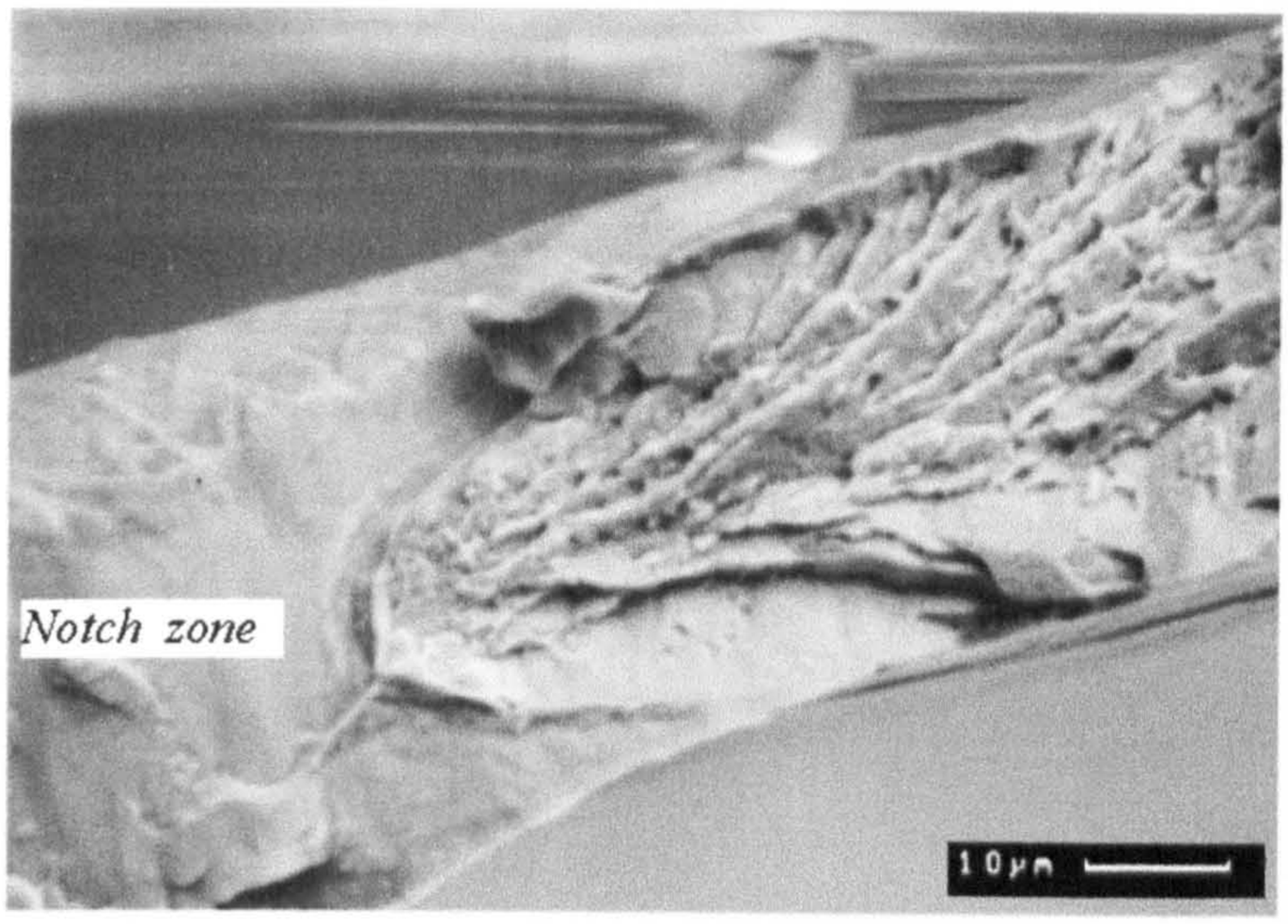

Figure 4.32. SEM photograph of $Fe_{69.5}Cr_8Si_{7.5}B_{15}$ alloy ribbon failed in a fracture toughness mode I test, showing the characteristic river pattern. K_c = 70.5 MPa$\sqrt{m}$.

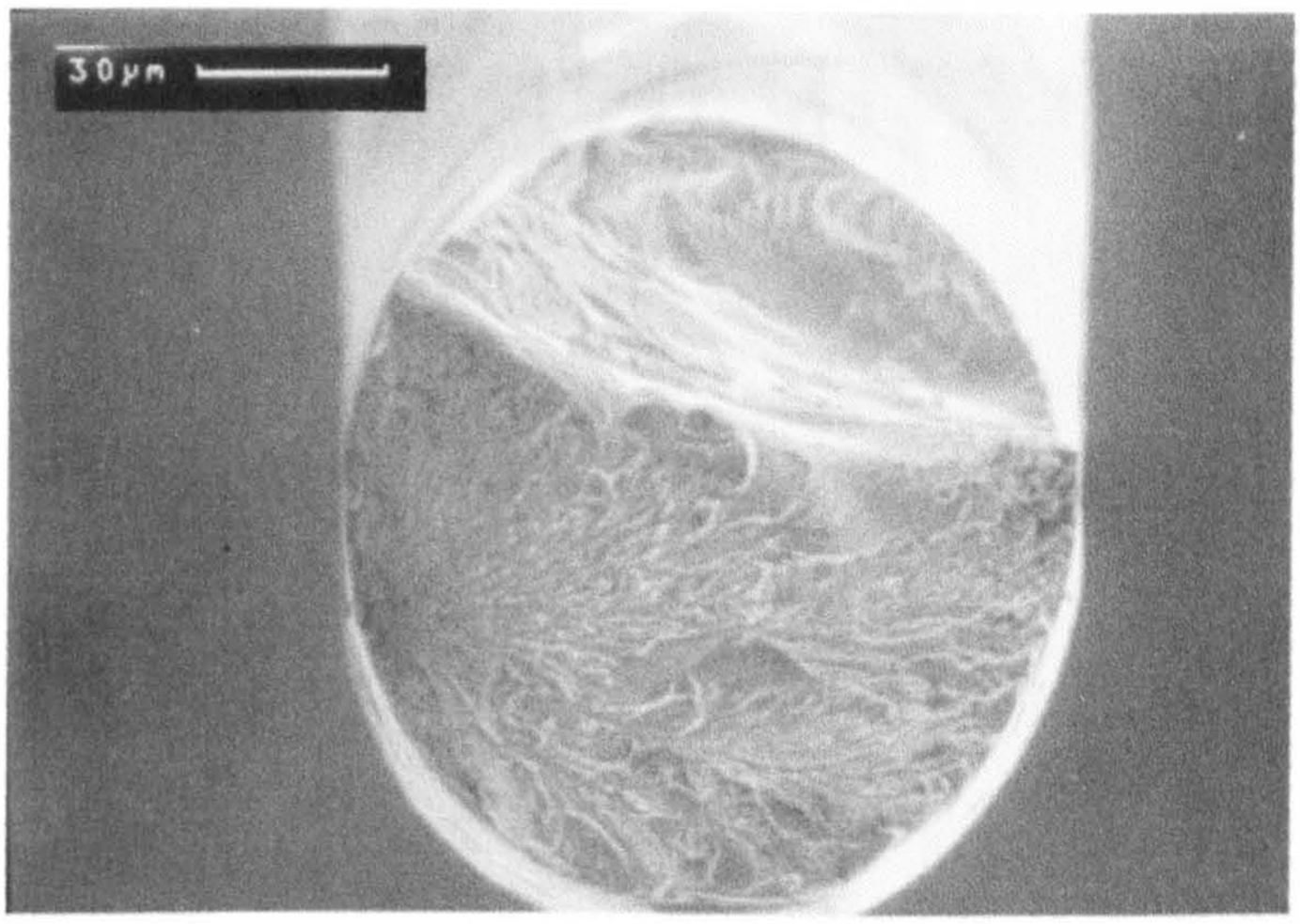

Figure 4.33. SEM photograph of $Fe_{77.5}Si_{7.5}B_{15}$ alloy wire failed in tension, showing the characteristic river pattern. Load = 1.44 kg, σ_f = 1,665 MPa.

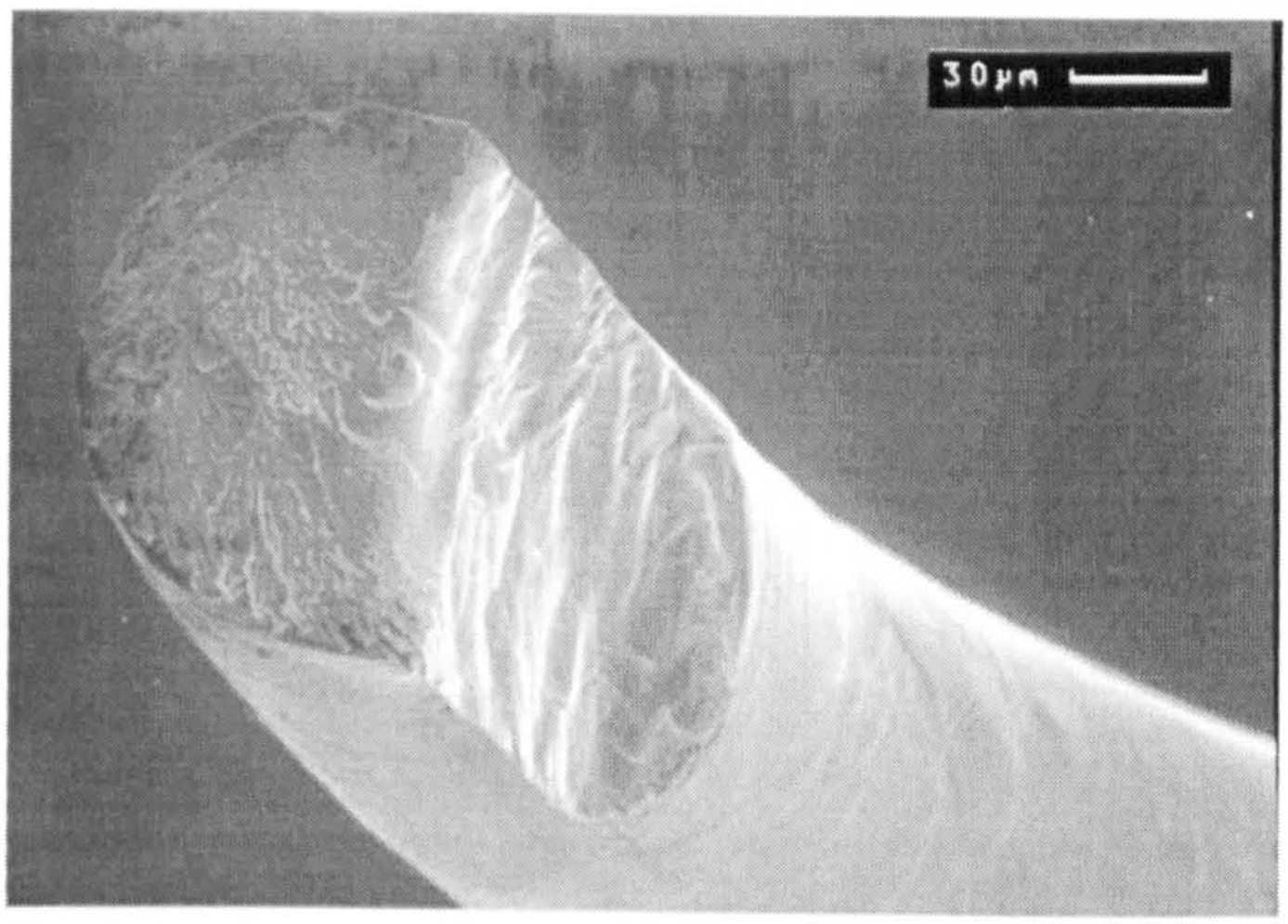

Figure 4.34. Same sample as figure 4.33, tilted ~45° and rotated ~15°.

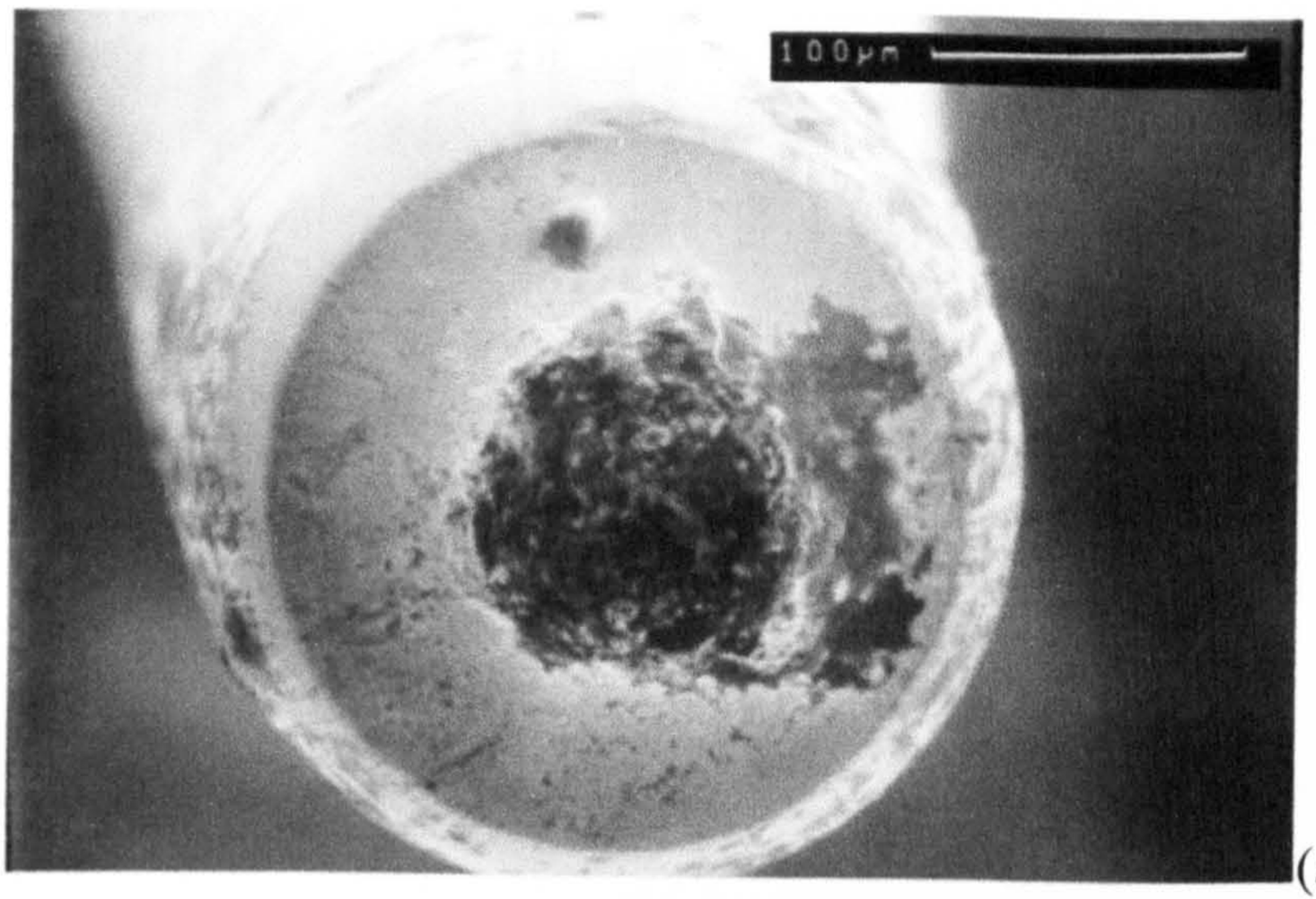

(*a*)

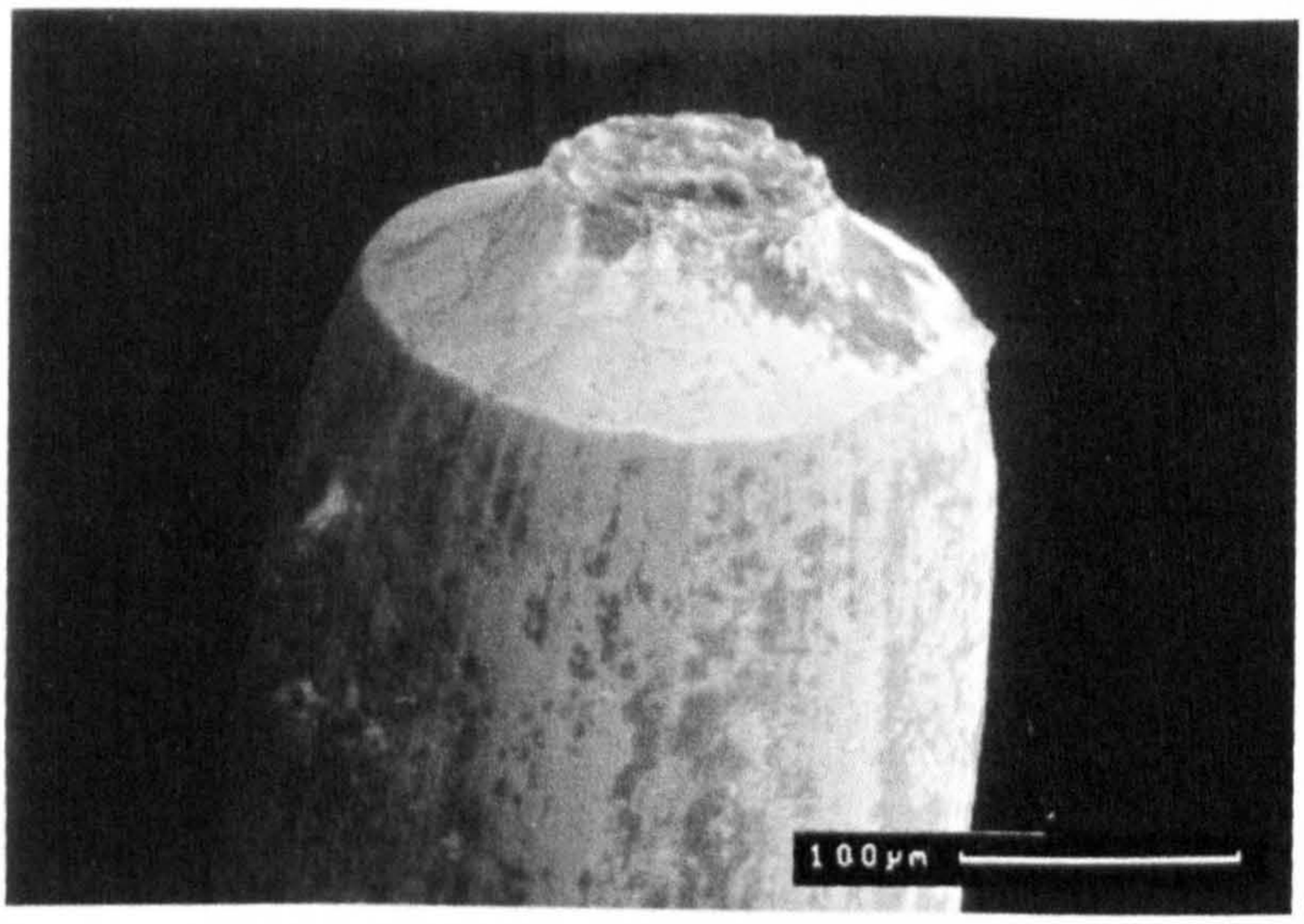

(*b*)

Figure 4.35. SEM photograph showing typical tensile fracture morphology for HT steel wire. Fracture load = 15.51 kg, σ_f= 3,255 MPa. (*a*) view from above, (*b*) tilted ~50°.

4.5.2 Fatigue fracture morphology

Interrupted fatigue tests on $Fe_{71.75}Cr_{6.25}Si_{10}B_{12}$ amorphous alloy wires using large bending stress ranges, were carried out with both machines using a constant mean loading stress of 1550 MPa. The tests were stopped after 400, 800, 1200, 1600, 2000 and 2400 cycles in the SP machine. For $\Delta\sigma_a$ = 2.37 GPa, shear events at 57° to the axis of the maximum stress, started appearing at 2000 cycles (figure 4.36). The tests were stopped at 400, 500 and 550 cycles in the DP machine. For σ_m = 5 GPa, shear events at ~45° to the axis of the maximum stress (i.e., ~45° to the wire axis) started appearing at 400 cycles (figure 4.37)

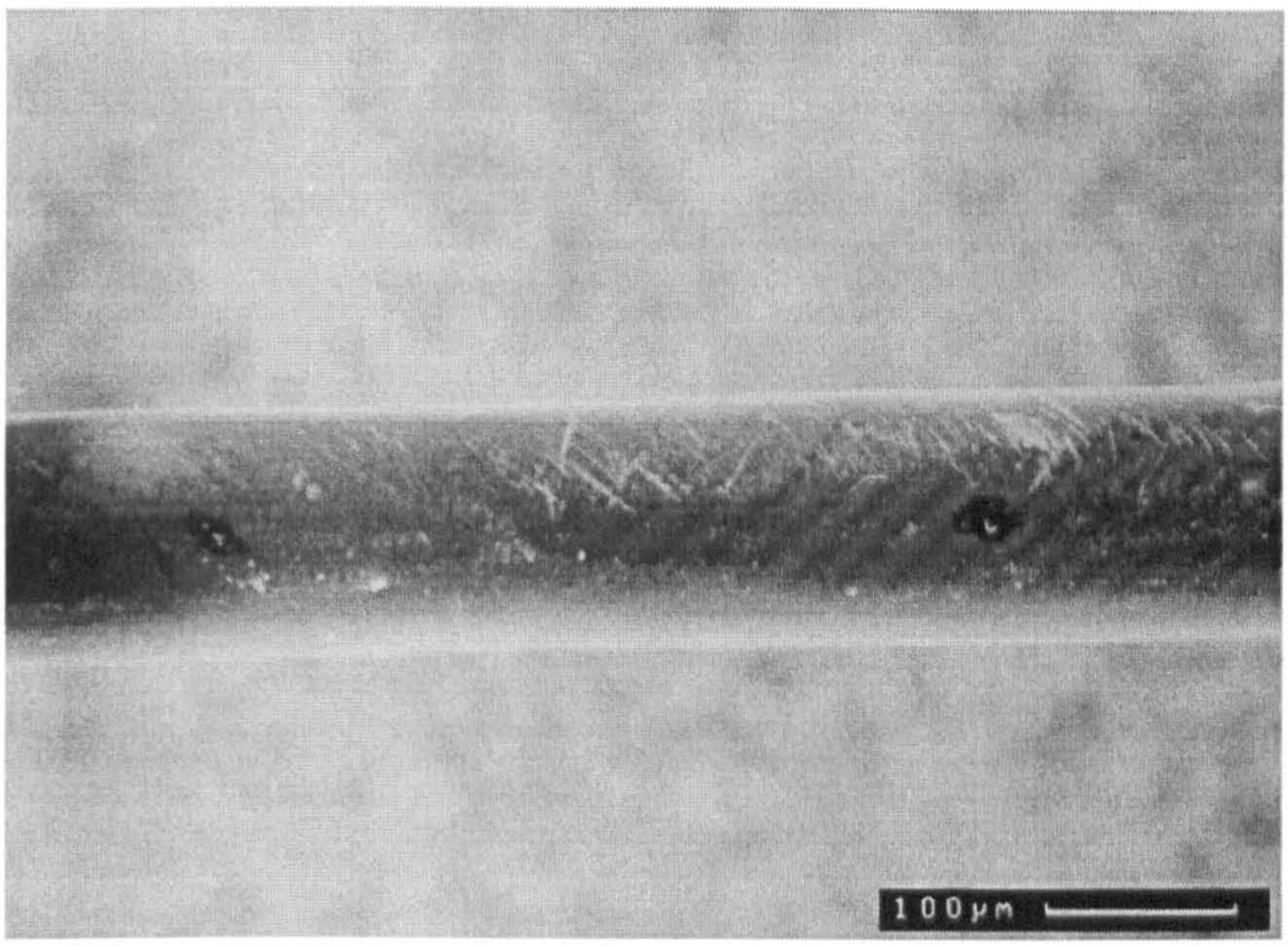

Figure 4.36. $Fe_{71.75}Cr_{6.25}Si_{10}B_{12}$ amorphous alloy wire tested for 2000 cycles in the SP machine at $\Delta\sigma_a$ = 2.37 GPa. Shear events at ~57° to the normal of the applied bending stress can be seen.

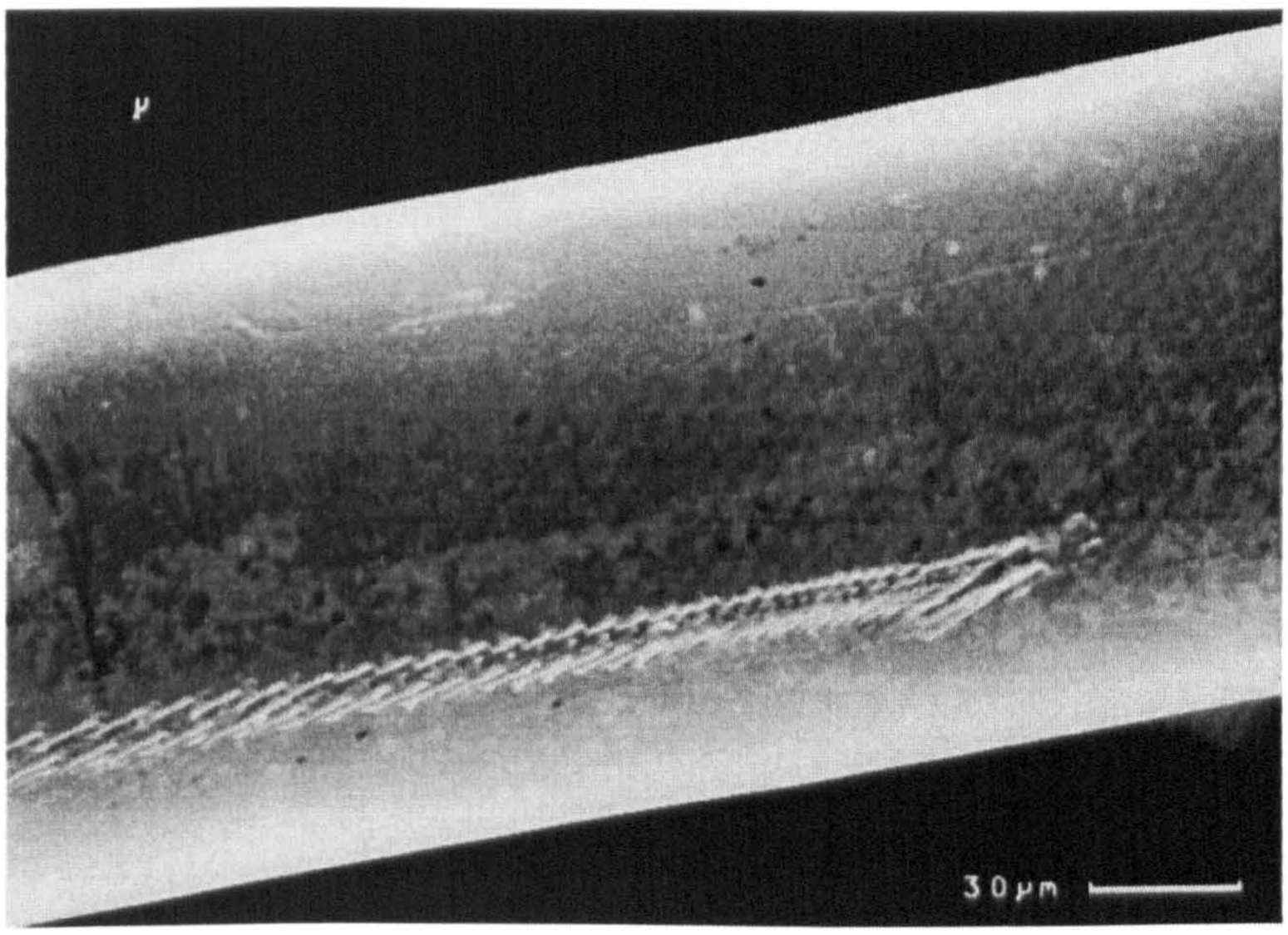

Figure 4.37. $Fe_{71.75}Cr_{6.25}Si_{10}B_{12}$ amorphous alloy wire tested for 550 cycles in the DP machine at $\Delta\sigma_a$ = 5 GPa. Shear events at ~45° to the axis of the maximum stress (i.e., ~45° to wire axis) can be seen.

Different fracture morphologies and crack initiation processes have been found by using the double pulley system, depending on both applied cyclic bend stress range and the

number of cycles to failure, but independent of the mean stress used. Such features are summarised in figure 4.38.

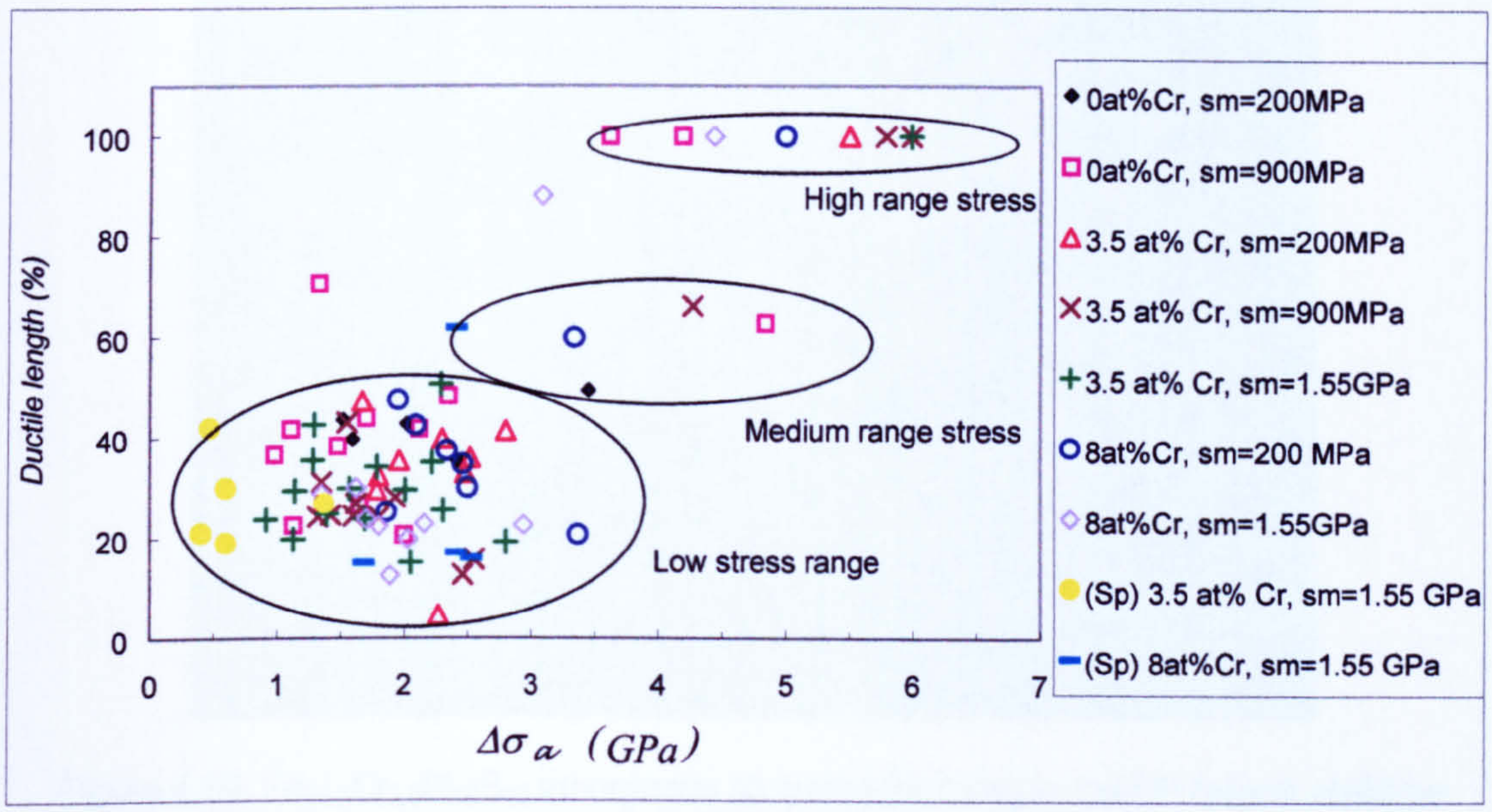

Figure 4.38. Percentage of the ductile fracture length as a function of the applied cyclic stress range (series A).

1) *100 % rough fracture*: For all compositions with large bending stress range (low cycle fatigue). Figure 4.39 shows a clear example of this type of fracture for a $Fe_{74.5}Cr_{3.5}Si_{10}B_{12}$ amorphous alloy wire fractured at 472 cycles with a cyclic stress range of 5.42 GPa. In addition, this figure shows two more cracks originating at shear events below the fracture. The same sample rotated 180° (figure 4.40) shows that there were 2 crack initiation sites, consistent with the two different directions of the crack propagation evident on the fracture surface. The matching fracture surface (figure 4.41) shows evidence of more shear events close to the final fracture.

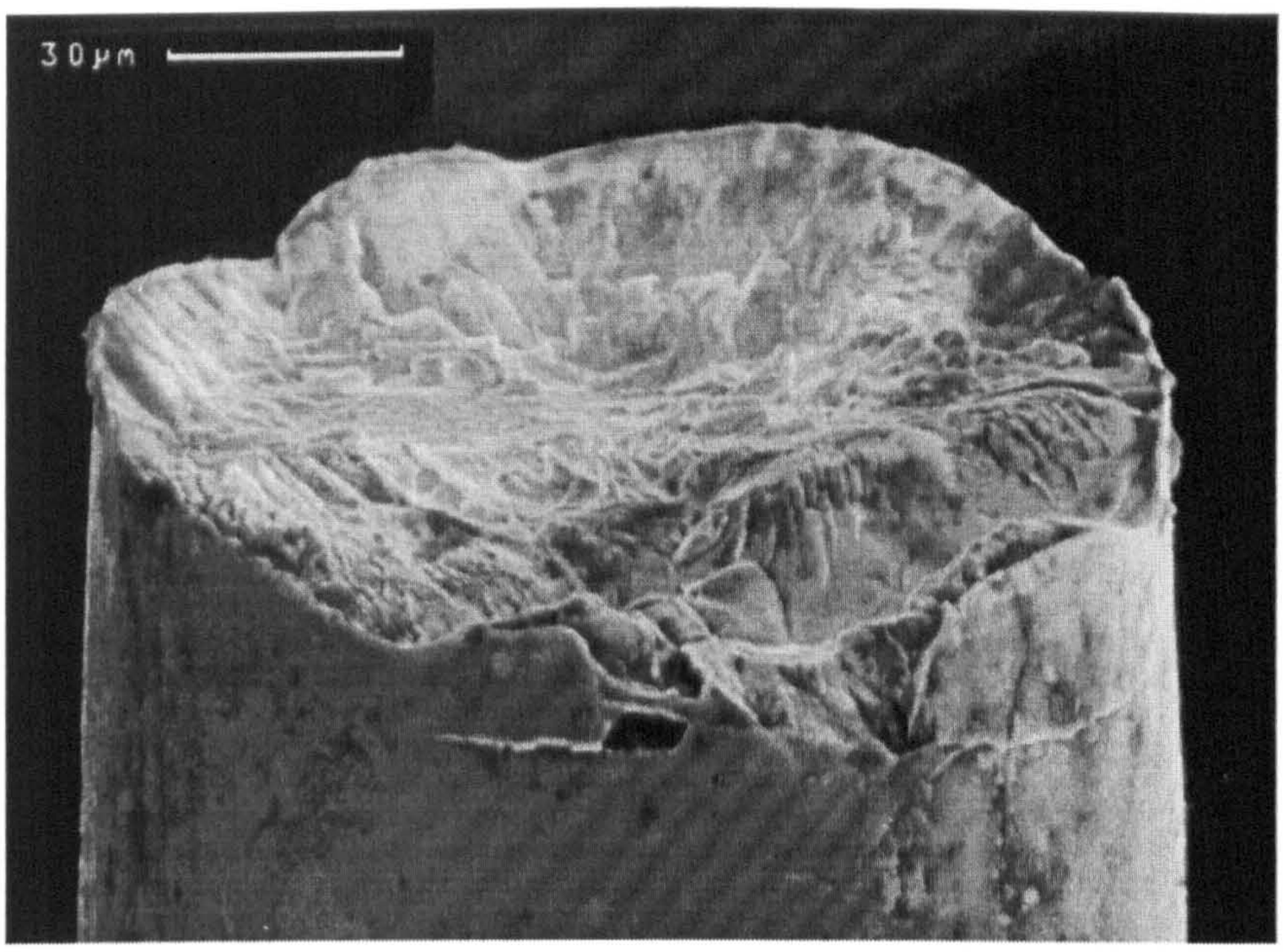

Figure 4.39. $Fe_{74.5}Cr_{3.5}Si_{10}B_{12}$ amorphous alloy wire fractured in the DP fatigue machine at 472 cycles under applied $\Delta\sigma_a$ = 5.42 GPa, using σ_m = 900 MPa.

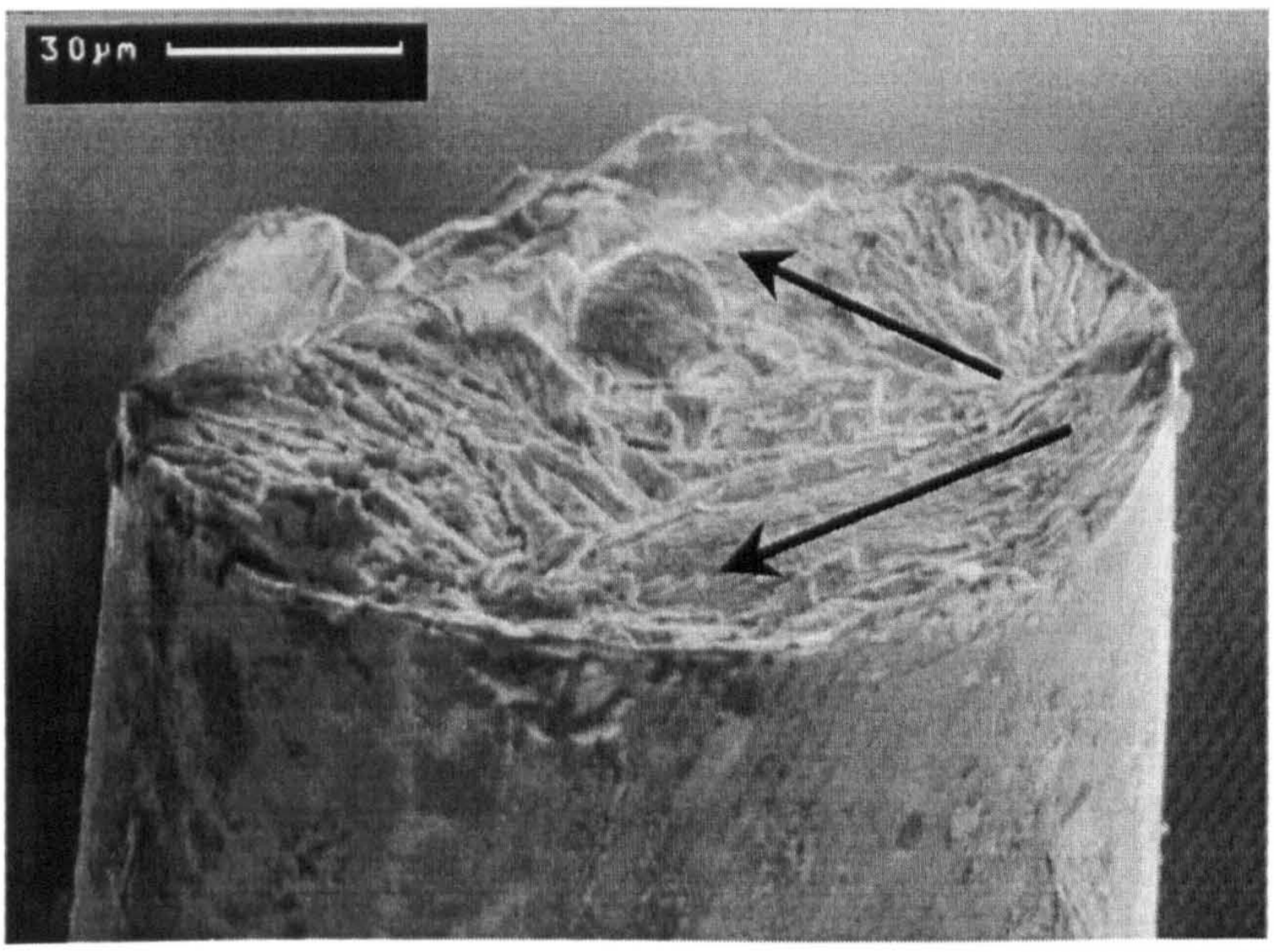

Figure 4.40. Same sample as figure 4.39 rotated 180°, where arrows indicate the crack growths directions.

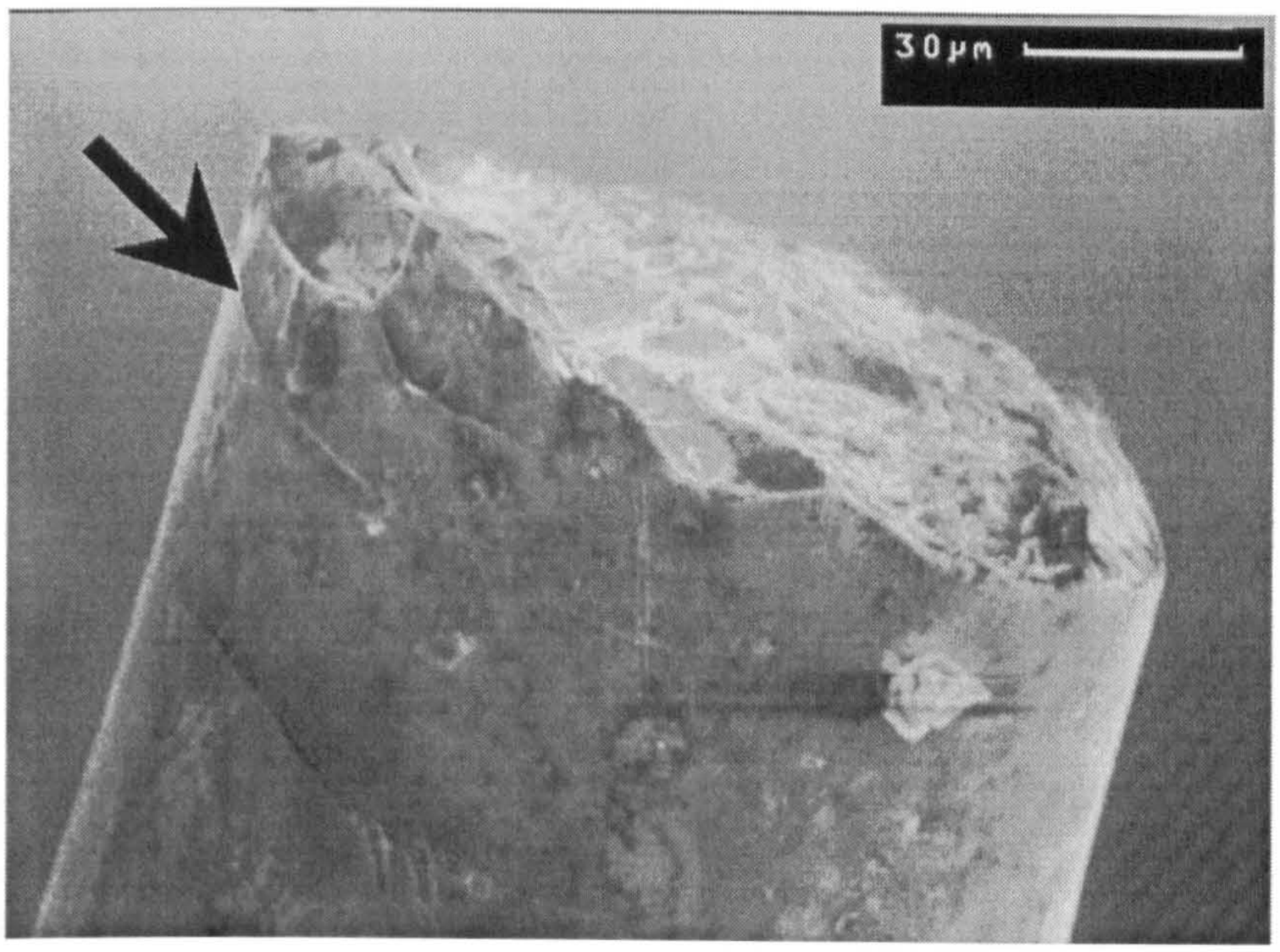

Figure 4.41. Counterpart of figure 4.39 showing some shear events below the final fracture.

2) *50 to 80 % rough fracture*: Here, the ductile (rough) fraction of the fracture was smaller. Only a few samples from the medium to large stress range tests (low cycle), showed this type of fracture (see figure 4.38). Figure 4.42 illustrates this type of fracture. No initiations defect was detected at the point of crack initiation for wires with 8 at % Cr. However for $Fe_{78}Si_{10}B_{12}$ and $Fe_{74.5}Cr_{3.5}Si_{10}B_{12}$ wires, what could have been small surface corrosion pits were found (figure 4.43).

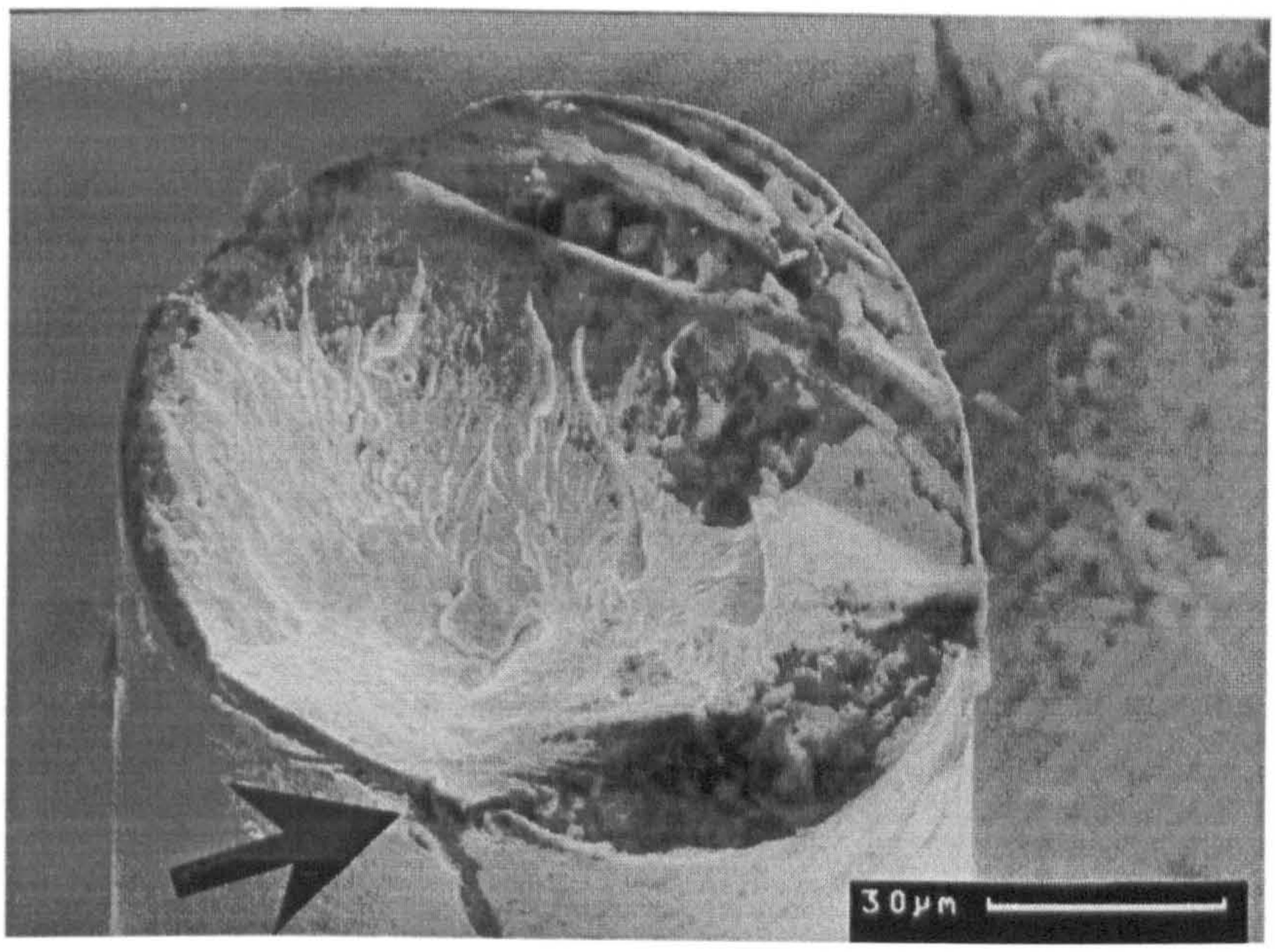

Figure 4.42. $Fe_{71.75}Cr_{6.25}Si_{10}B_{12}$ amorphous alloy wire fractured in the DP fatigue machine at 2,132 cycles under applied $\Delta\sigma_a$ = 3.34 GPa, using σ_m = 200 MPa.

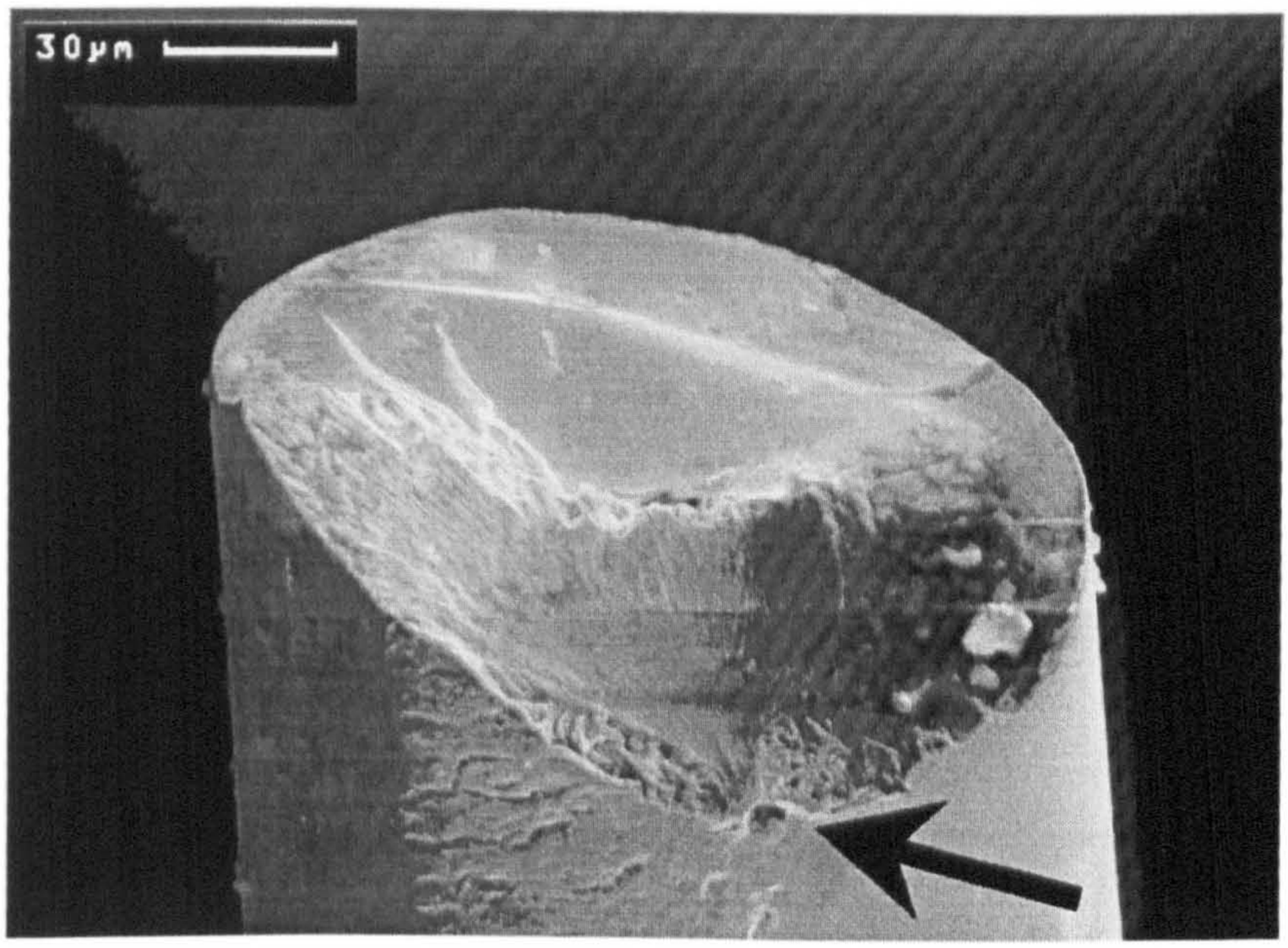

Figure 4.43. $Fe_{74.5}Cr_{3.5}Si_{10}B_{12}$ amorphous alloy wire fractured in the DP fatigue machine at 4.8 x 10^4 cycles under applied $\Delta\sigma_a$ = 1.67 GPa, using σ_m = 200 MPa. What could be a corrosion pit is shown with an arrow.

3) *15 to 50 % rough fracture*: Most of the fractures showed this type of morphology, largely for the low bend stress range (medium to high cycle), for all the glassy alloys and all the mean stresses used. For $Fe_{78}Si_{10}B_{12}$ and $Fe_{74.5}Cr_{3.5}Si_{10}B_{12}$ amorphous alloy wires, it was observed that what appeared to

be corrosion pits formed on shear events that had occurred earlier. Cracks were then nucleated at, and propagated from these possible corrosion pits when the number of cycles increased (figure 4.44). The stereopair of figure 4.45, a higher magnification view of figure 4.44, shows that the morphology at the fracture surface adjacent to the nucleation points is flat. Further afield, the morphology becomes rough as a result of ductile dimples formed during crack growth. Here, it can be seen that the pit is approximately 3 μm in diameter. Finally, the wire broke by a brittle failure mode, as is seen on figure 4.44. On the other hand, the alloys with the highest contents of chromium had a smaller ductile fracture area. Figure 4.46 shows this type of fracture. Further, the fractures for these alloys did not nucleate at pitting corrosion points, but at shear events formed during the process of cyclic bending.

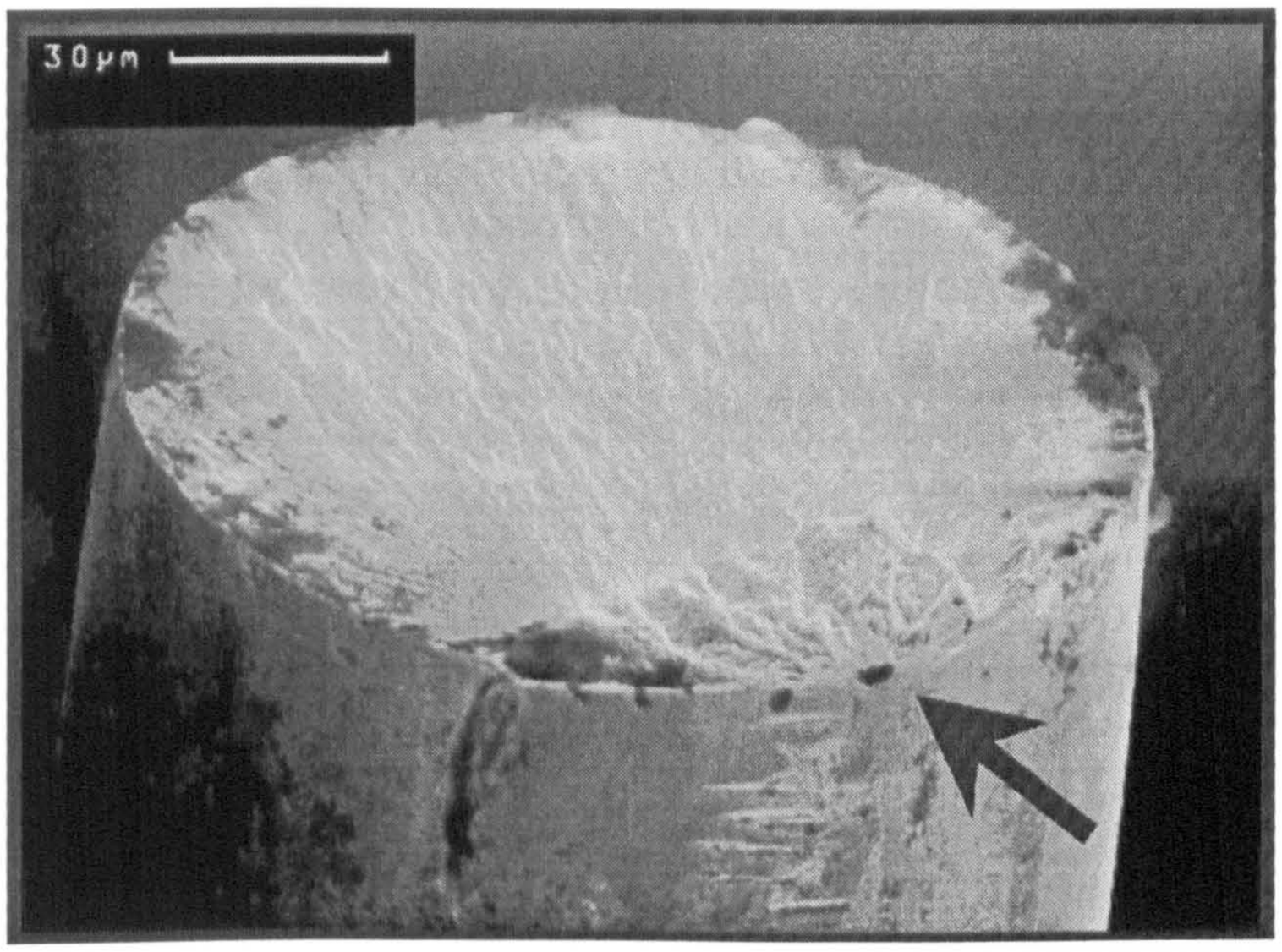

Figure 4.44. $Fe_{74.5}Cr_{3.5}Si_{10}B_{12}$ amorphous alloy wire fractured in the DP fatigue machine at 22,070 cycles under applied $\Delta\sigma_a$ = 1.42 GPa, using σ_m = 900 MPa. What appeared to be a corrosion pit is shown with an arrow.

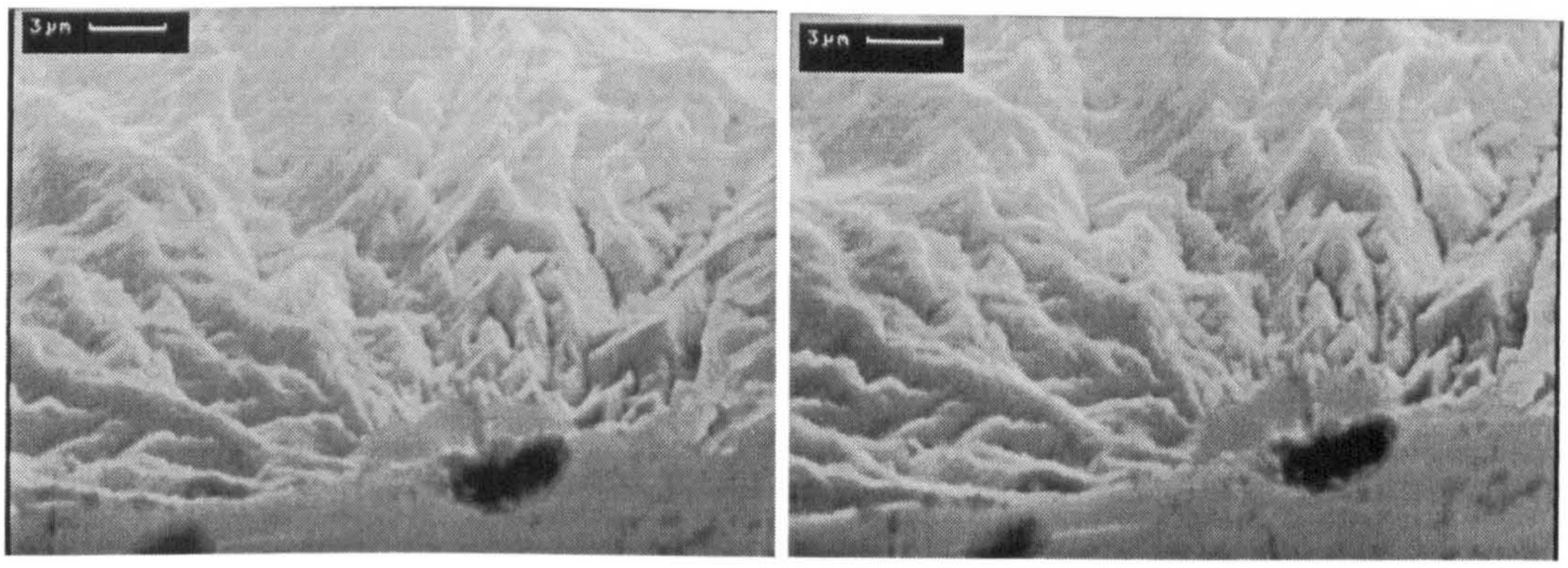

Figure 4.45. Higher magnification of figure 4.44, stereopair showing in more detail what could have been a corrosion pit.

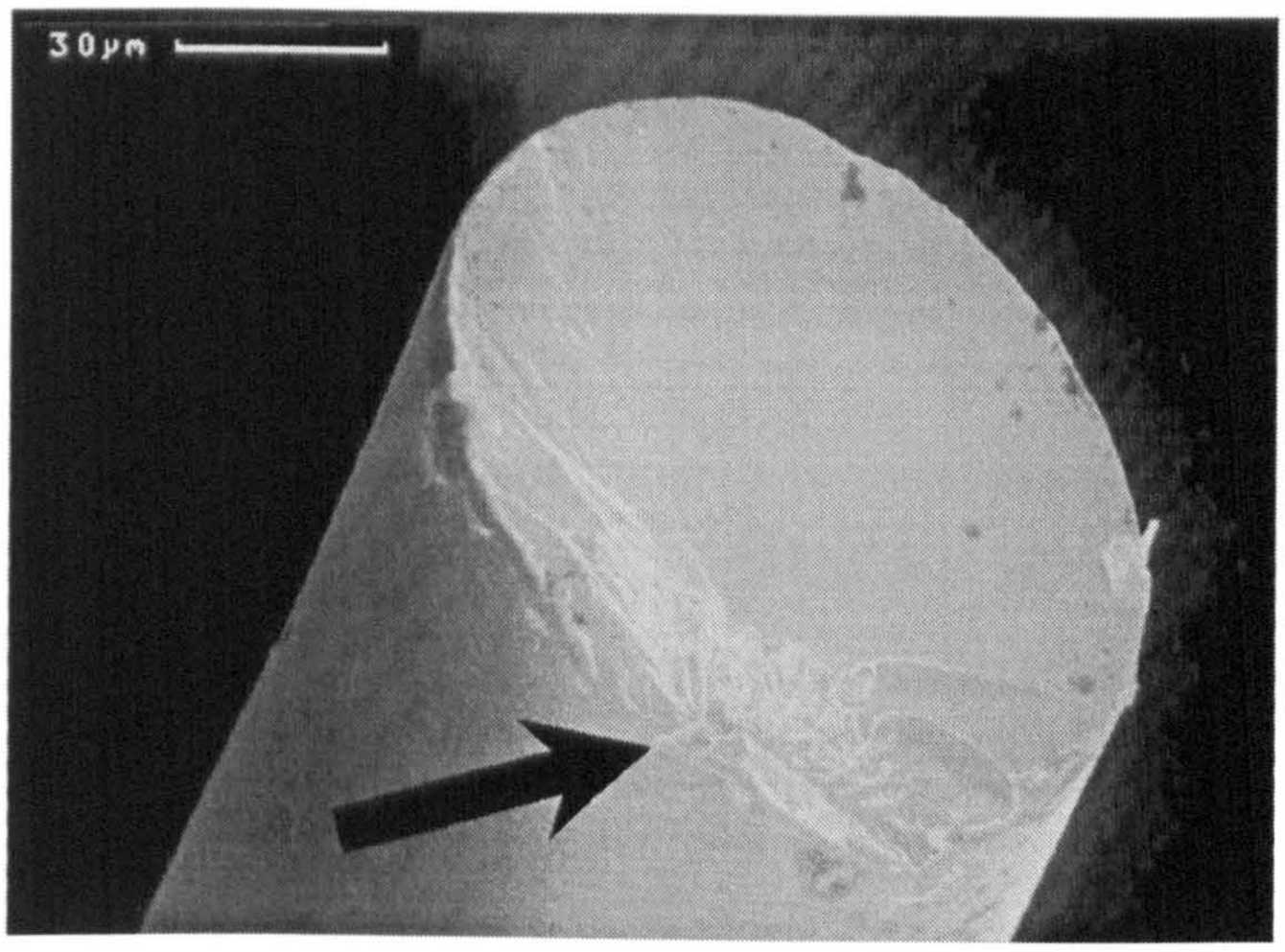

Figure 4.46. $Fe_{71.75}Cr_{6.25}Si_{10}B_{12}$ amorphous alloy wire fractured in the DP fatigue machine at 1.57 x 10^6 cycles under applied $\Delta\sigma_a$ = 1.7 GPa, using σ_m = 1550 MPa. Arrow indicates crack initiation site.

Fractography of amorphous alloy wires tested in the SP machine showed that none of the samples showed a 100 % rough fracture. In this case the percentage of rough fracture ranged between 15 and 60 % (see figure 4.38). Most of the fractures ranged between 15 and 30 % rough fracture. Some of the fractures nucleated at what could have been corrosion pits, see for example figure 4.47.

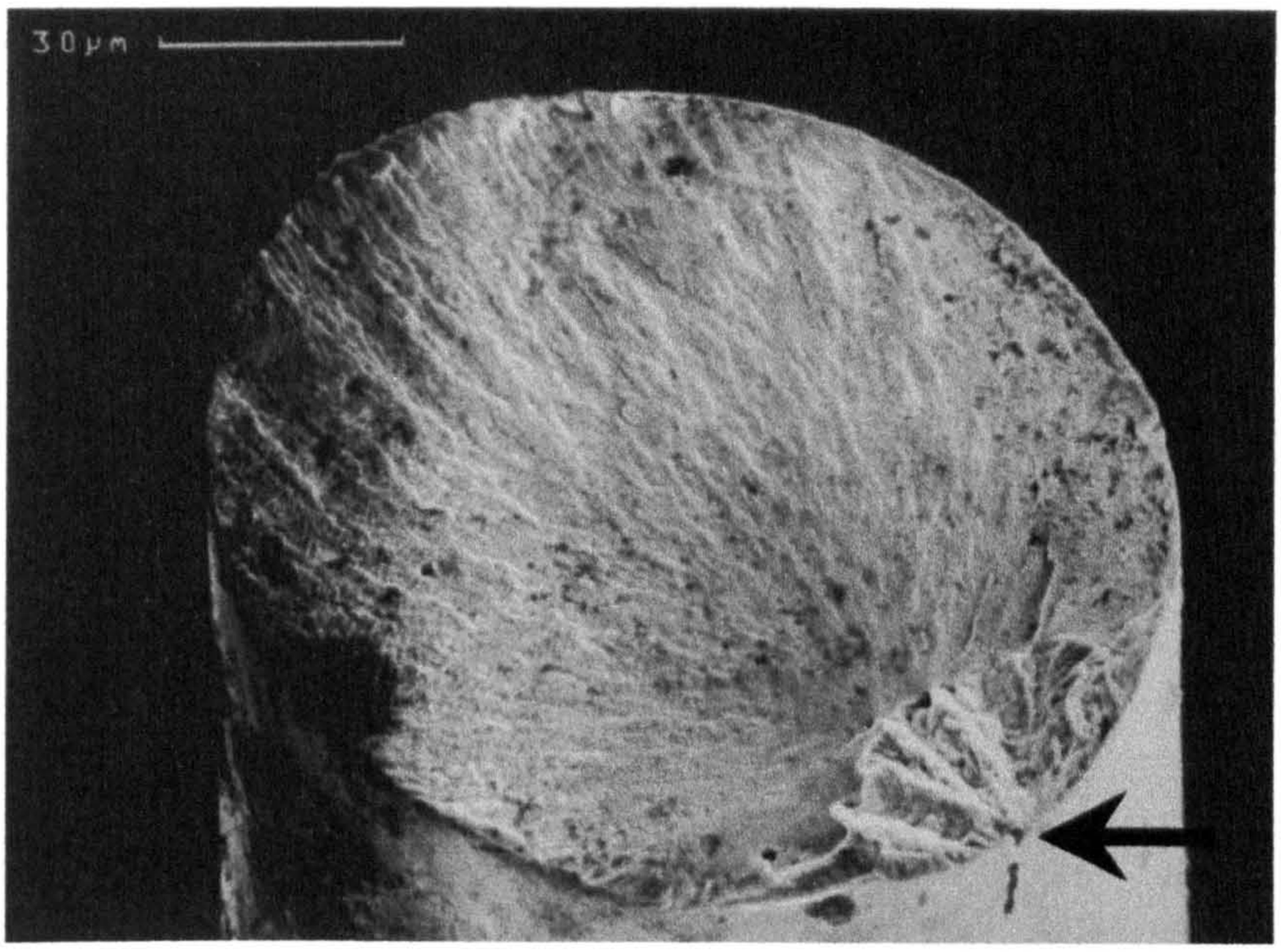

Figure 4.47. $Fe_{74.5}Cr_{3.5}Si_{10}B_{12}$ amorphous alloy wire fractured in the SP fatigue machine at 1.2 x 10^4 cycles under applied $\Delta\sigma_a$ = 400 MPa, using σ_m = 1550 MPa. Arrow indicates feature suggesting crack initiation possibly due to pitting corrosion.

Figure 4.48 shows a typical fatigue fracture for a HT steel wire, initiated at shear bands (figure 4.49) generated on both wire surfaces adjacent to both pulleys in the DP machine. The initial morphology of the fracture was relatively smooth with small peaks only about 3 µm in length. The final fracture was ductile, characteristic of crystalline wires (figure 4.50).

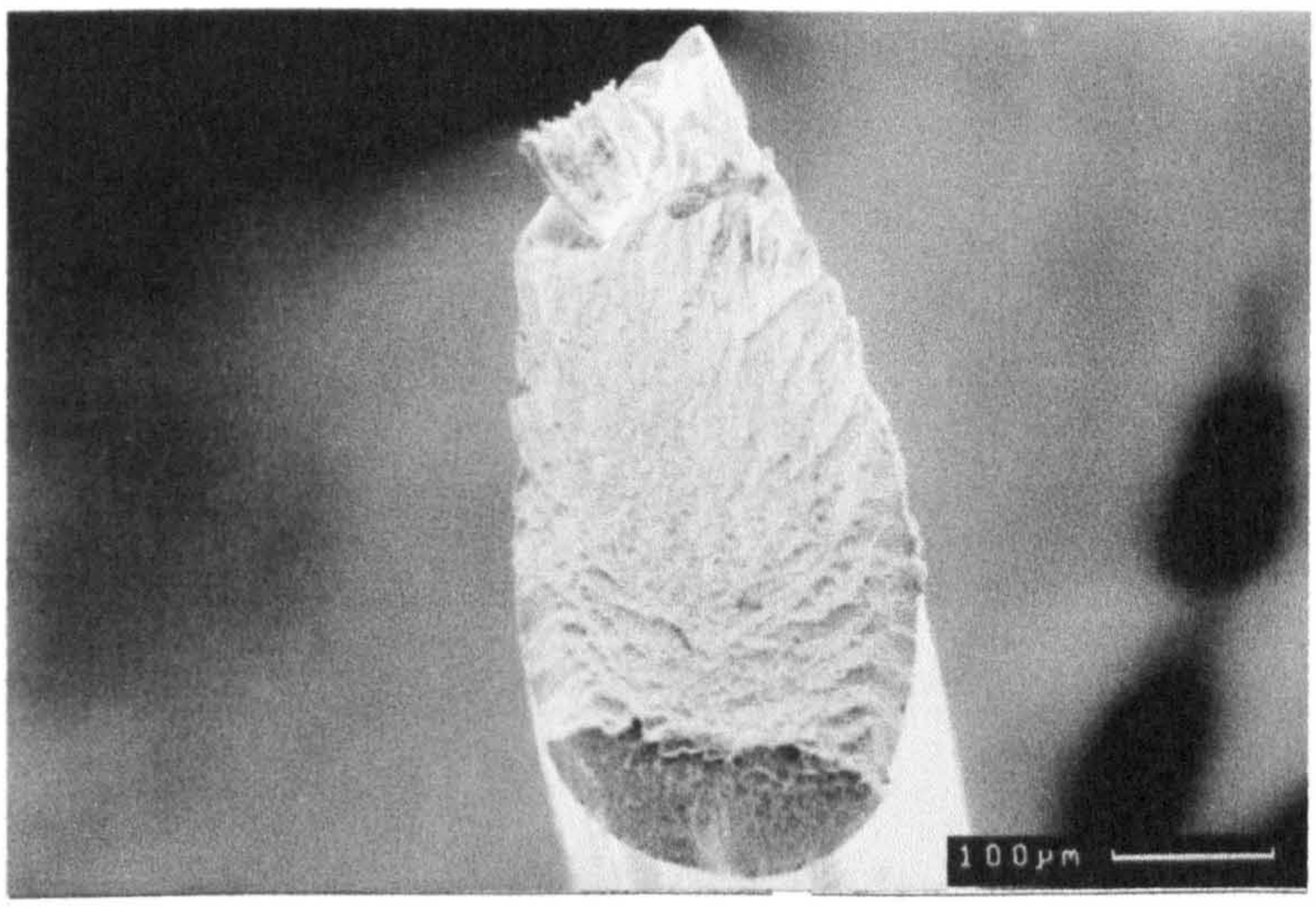

Figure 4.48. SEM photograph of a typical fatigue fracture in a HT steel wire, failed at 1,094 cycles, applying $\Delta\sigma_a$ = 6.4 GPa, using σ_m = 200 MPa.

PAGE
MISSING
IN
ORIGINAL

Chapter V: DISCUSSION

5.1 Wire casting

Although some Fe-based alloys have good glass forming ability, casting some of them in wire form proved to be difficult, and required strict and narrow limitations on several parameters; the more important will be explained separately in this section. However, when the correct parameters were established, the castability and formation of amorphous wires improved enormously, resulting in good quality wires.

5.1.1 Jet stability

In general, a liquid jet is prone to break up into droplets or to spheroidise due to the effect of the surface tension and viscosity. Thus, some consideration needs to be given to the stability of a free jet in casting amorphous wires by the rotating water bath melt spinning process since, usually, jets tend to be unstable resulting in nodes (which probably originated from perturbations in the jet). Therefore, special attention needs to be paid to the nozzle/water surface gap to ensure that jet break up in flight is not responsible for failures during wire casting and to maintaining a uniform and stable stream prior to solidification in the rotating cooling medium, water in this case. By using the Weber equation [131], the break up length for an isothermal jet in a gaseous medium can be expressed as follows:

$$L/D = \left[\sqrt{\mathrm{We}} + \frac{3\,\mathrm{We}}{\mathrm{Re}}\right] ln\left(\frac{D}{2\,\varepsilon_0}\right) \tag{5.1}$$

where L is the coherent jet length, D is the jet diameter, We and Re are the Weber and Reynolds numbers, respectively, $ln(D/2\varepsilon_0)$ is an experimental parameter relating to the perturbations in the jet, which has been determined to be approximately 12 for a wide variety of liquids and streaming conditions. The Weber and Reynolds numbers are expressed in terms of casting conditions as:

It was observed that during the casting process, the melt jet diameter decreased on leaving the nozzle outlet and became as much as 4 to 18 % smaller than the nozzle diameter. The main reason for this contraction is the removal, after leaving the nozzle, of the parabolic velocity profile, which exists within the jet within the nozzle [129].

Regarding the possible effect of acceleration due to gravity on the jet contraction, an explanation was proposed by Ohnaka *et al.* [133], as follows: the gravitional force can increase the velocity of jet, which can be expressed using the following equation:

$$V_f^{\,2} = V_j^{\,2} + 2gL \tag{5.3}$$

where V_f is the final velocity, g is the gravitational acceleration. For instance, it was calculated that V_j was of the order of 9.81 ms^{-1} (see above), and assuming a mean nozzle clearance of 4 mm, and replacing these values in equation (5.3), again gives that $V_f = 9.84$ ms^{-1}. From this calculation, it can be seen that the jet contraction may be the result of velocity relaxation, since the velocity increment remains almost unchanged in this very short distance of only 4 mm before the jet contacts the cooling water. It was proposed [129] that the amount of contraction would depend on the degree of velocity profile developed, which was directly related to the length of the orifice that might explain the variation in the contraction developed during the process of wire casting.

5.1.2 Jet incidence angle

In this work, all alloy wires showed a good section roundness, defined as the ratio of the minor to the major diameter of the wire. It is appropriate to consider the influence that the jet incidence angle may have on the degree of circularity of the wire cross section. To approach circularity, both the jet diameter and its incident angle (defined as θ in figure 2.12) should be decreased [134]; in this way, it was suggested that the jet is more likely to resist, through surface tension forces, being flattened by the dynamic pressure or drag force of the cooling water.

Ohnaka *et al.* [134] found that a smaller incidence angle was more convenient for producing a circular section, but resulted in a reduced heat transfer rate and, hence a lower cooling rate, because the attack angle of the coolant to the jet became smaller. However,

they found that it was difficult for jets with diameters < 100 μm to enter the coolant at a low incident angle, because the surface tension effect of the coolant became larger. On the other hand, when a jet of larger diameter was ejected at a larger incident angle, flow separation occurred and the cooling rate was not increased as much as was expected. Therefore, it was recommended that a smaller incidence angle be selected for a jet of larger diameter, and vice versa.

5.1.3 Superheat

The casting temperature is an important process parameter, which needs careful control during wire casting. In the present study, this parameter was controlled by empirical experience due to the difficult of measuring the melt temperature reliably; consequently the time for which the alloy was in the liquid state in the crucible prior to applying the appropriate ejection pressure, using constant R.F. induction power in the generator, was taken as a measure of the melt temperature. It was observed that if the melts were kept into the crucible for longer times than the optimal values given in table 4.I, the alloys suffered excessive superheat, which was detrimental to wire casting. This resulted in melt jet disturbance, associated with longer cooling times, which caused either short and brittle pieces of wire or, in the extreme, powder. On the other hand, shorter dwelling times were also undesirable, since these led to problems of premature melt freezing in the nozzle tip, because the R.F. heating coil did not move down with the nozzle so that the heating was effectively terminated immediately once the casting procedure was activated. Hence the alloy at low melting temperature was almost instantaneously solidified on ejecting the melt alloy, due to the close distance of the cooling water. Thus it was observed empirically that there exists an optimal dwell time in the liquid state for the molten alloy prior to casting, so as on the one hand to avoid stream disturbance during casting, and on the other hand to avoid nozzle blockage due to too low a temperature.

As commented above, when the superheat was increased the solidification was delayed. Hence, structural relaxation could take place or some crystalline phases formed, which could result in brittle wire. In addition, excessive superheat shortened the useful life of the nozzle due to distortion of the quartz, rendered the nozzle unsuitable for further wire castings.

It has been observed elsewhere [132] that the roundness of the wire section was decreased with excessive superheat. In the same study, the temperature of a $Fe_{68}Ni_{20}Si_{10}C_2$ alloy was monitored with an optical pyrometer, and it was found that the optimal casting superheat was about 120 K and gave the least variation in roundness. On the other hand, Olofinjana [129] found that a superheat in the range of 50 to 100 K was generally most suitable for Fe-Si-B based alloys. As noted in section 4.1.1 attempts to measure the superheat in the current work were unsuccessful.

5.1.4 Melt jet velocity/Rotating water velocity ratio

The jet velocity/water velocity ratio (V_j/V_w), is one of the most important parameters that must be taken care of, since the quality of the wires, i.e. the surface appearance, partially the roundness and more importantly, the continuous length of wire obtained, depends greatly on this parameter. The optimum V_j/V_w ratio has been shown to vary depending on the alloy composition. For instance, Ohnaka [133] reported that the limiting experimental range to produce long-continuous Fe-based alloy wire could be expressed as $1 < V_j/V_w < 1/\cos\theta$, where θ is the incidence angle of the jet to the water surface. Abe *et al.* [51] found that, for Pb-4.2 wt % Sb and Pb-11.1 wt % Sb hypoeutectic and eutectic alloy wires, this V_j/V_w range was between 1 and 1.2. Olofinjana [129] found a narrower range for Fe-Si-B based alloys, which was between 1.14 and 1.21. However, Ohnaka and co-workers [134] found that for various glass forming alloys, namely Pd-Si, Pd-Si-Cu, Fe-Si-B, Fe-Si-P and Co-Si-B, the velocity ratio was inverted, so that the optimum V_w/V_j, lay between 1.15 and 1.3, which is not in accord with the ratios observed by other workers. Nevertheless, all the previous studies and the present study, for which the critical V_j/V_w ratio was found to be between 1.11 and 1.33 (see table 5.I), conclude that for velocity ratios above the highest optimal value, the casting resulted in sinuous wire and eventually powder, as for the example shown in figure 4.2. Conversely, when the velocity ratio is below the lowest optimal value, discontinuous wire with short thin and necked ends and eventually powder was also obtained (see figure 4.3). Additionally, Abe *et al.* [51] found that the roundness of the cross section became approximately unity with decreasing water velocity.

Table 5.I. Melt jet and water velocity ratios.

Alloy	V_j (ms^{-1})	V_w (ms^{-1})	V_j/V_w
$Fe_{78}Si_{10}B_{12}$	9.81	7.45	1.31
$Fe_{74.5}Cr_{3.5}Si_{10}B_{12}$	9.86	8.28	1.19
$Fe_{71.75}Cr_{6.25}Si_{10}B_{12}$	9.81	7.93	1.23
$Fe_{70}Cr_8Si_{10}B_{12}$	9.76	7.91	1.23
$Fe_{77.5}Si_{7.5}B_{15}$	9.86	7.86	1.33
$Fe_{73.5}Cr_4Si_{7.5}B_{15}$	9.21	8.23	1.11
$Fe_{69.5}Cr_8Si_{7.5}B_{15}$	9.81	7.93	1.23

In addition, it is important to point out that the critical V_j/V_w ratio may also depend on other, sometimes difficult-to-measure parameters, such as superheat, melt surface tension and melt viscosity [129]. On the other hand, the roundness of the wire may depend on the dynamic pressure of the water, the diameter of the molten metal jet and the melt surface tension, and the angle of incidence of the jet to the rotating water. For instance, for Pb-Sb alloys, the cross sectional shape changed from circular to oblate as the drum velocity was increased above the optimal value. However, for iron-base alloy wires, the cross sectional shape is invariably circular. This difference is because the surface tension of Pb-Sb alloys, is roughly a factor of three smaller than typical values for molten Fe based glass forming alloys [135]. It has also been reported that the shape of the Pb-Sb alloy wire became more circular if the jet penetrated deeper into the water layer [51]. It was possible to achieve this by either lowering V_w or increasing V_j; however, as has been seen earlier, there is an optimal range for the V_j/V_w ratio.

5.1.5 Melt jet stabilisers and effect of alloy composition

The effects of the more important physical parameters on the ability to produce good quality wires have been discussed above. In this section, attention is paid in the role that

alloy composition plays in determining the wire formability, especially in the oxide film forming elements, which help to stabilise the melt jet in the coolant.

Previous studies on $Fe_{69.5}Cr_8Si_{7.5}B_{15}$ alloy wires [7] using x-ray photoelectron spectroscopy have found that the phase at the surface was mainly composed of SiO_2. Olofinjana and Davies [7] found Cr and Fe oxides in the surface; results of casting experiments indicated that Si was the most significant element on enhancing wire formation by stabilising the jet. For instance, it was found that the atomic ratios of Cr/Fe and Si/Fe in the surface film for $Fe_{69.5}Cr_8Si_{7.5}B_{15}$ were 1.2 and 3.9, respectively. It was found that Si contributed more to the oxide film than the other elements. The formation of Cr_2O_3 in appreciable quantities was also confirmed, even at 8 at% Cr. On the other hand, in an earlier study undertaken by Inoue *et al.* [53] it was found that the phase at the surface of $Fe_{70}Cr_5Si_{15}B_{10}$ wire and $Ni_{73}Cr_2Si_8B_{17}$ powder was mainly composed of SiO_2, without significant difference between the alloys. It was suggested that the formation of SiO_2 near to the surface was not the only important factor for the formation of the amorphous wire. Additional experiments [53] with other oxide forming elements, such as Al, Zr and Mg were carried out in order to study the effect of the jet stabilisation on wire castability of Ni-based alloys. The amorphous wire formation was remarkably enhanced by the addition of Al or, to a lesser extent, Zr and was attributed to a stabilised melt jet due to the formation of oxide surface films composed of Al_2O_3 and ZrO_2. This was assumed to be because Al has a greater tendency to oxidation than Si.

It has been observed that addition of Cr to alloys in the Fe-Si-B alloy system helps to improve wire formability by stabilising melt jets through promoting more rapid oxide film formation than for the basic FeSiB alloy. This can also be seen from the fact that the superheat parameter plays a less critical role for Cr-containing alloys than those without Cr.

The effect of Cr in the enhancement of wire castability was confirmed in the present study for both alloy series studied. The effect of Si in Cr-free alloys was opposite to that found in previous works, where wire formation was improved by adding this element to the alloy. For instance, wire castability and hence, wire formation in the present study was found to be better for $Fe_{77.5}Si_{7.5}B_{15}$ than for $Fe_{78}Si_{10}B_{12}$, though the latter contains more Si than the first alloy, but the B content is higher in the first alloy than in the second. The

enhancement of wire formability for the alloy with more B, can probably be explained in terms of a higher glass forming ability [8] since this parameter probably plays an important role in melt jet stabilisation, thereby controlling the wire forming process. The $Fe_{77.5}Si_{7.5}B_{15}$ composition is effectively closer to the eutectic $Fe_{75}Si_{10}B_{15}$ composition than is the $Fe_{78}Si_{10}B_{12}$ composition.

From these observations on wire casting it appears that both physical and chemical parameters are important for good quality amorphous wire production and that the control of one parameter by itself is not sufficient.

In the general case, for the increase of glass forming ability through addition of further elements to basic binary and ternary alloy systems, a number of empirical rules have been proposed, among which are [2]:

1) multicomponent alloy systems consisting of more than three elements are favourable since they lead to an increased interdiffusion requirement for the formation of crystalline phases.

2) significantly different atomic size ratios above about 12% among the main constituent elements in order to help stabilise the liquid and glassy phases. The greater the size ratio the more effectively will the smaller atoms fit into interstices between the larger atoms.

3) negative heats of mixing between their elements; the alloys used should be based on mixtures of elements for different parts of the periodic table. This fact is not independent of 2) since large atomic size differences lead in any case to large negative heats of mixing.

5.2 Ribbon casting

As was seen in section 4.2, good quality ribbons in the compositions being studied could not be cast within an atmosphere of Ar at atmospheric pressure. Casting in He was found to give noticeably better quality ribbon. An explanation will be given from previous studies done in this field.

Lieberman [136] was the first researcher to investigate the effects of different pressures (from 0 to 100 kPa) of gases of various densities (He, air and Ar), on the quality of melt spun ribbon ($Fe_{40}Ni_{40}B_{20}$) finding that the ribbon quality cast under pressure of Ar and air, improved on lowering the chamber pressure down to about 50 kPa. For ribbons cast under He pressure, the excellent quality remaining constant for all the pressures used. He explained the occurrence of serrated edges and some surface degradation in these glassy ribbons under certain conditions based on boundary layer theory. He found that good quality ribbon formability is related to a critical Reynolds number, Re^{crit}, calculated as follows:

$$\mathrm{Re} = \frac{vw}{\upsilon} \tag{5.4}$$

where v is the gas velocity (assumed to be equal to the substrate surface velocity); w is the puddle width in contact surface with the substrate (assumed to be equal to the ribbon width); $\upsilon = \eta/\rho$ is the kinematic gas viscosity, where η is the static gas viscosity and ρ is the gas density. He assumed an ideal gas behaviour, hence:

$$\rho = \frac{n\bar{M}}{V} = \frac{P\bar{M}}{\mathrm{RT}} \tag{5.5}$$

where n is the number of moles of gas, $\bar{M}$ is the gas molecular weight, V is the gas volume, P is the ambient gas pressure, R is the ideal gas constant and T is the ambient gas temperature. The Reynolds number of the gas boundary layer interacting with the melt puddle was then expressed as follows:

$$\mathrm{Re} = \left[\frac{vwP}{\mathrm{RT}}\right]\left[\frac{\bar{M}}{\eta}\right] \tag{5.6}$$

It was observed that when $\mathrm{Re}<\mathrm{Re}^{crit}$, ribbons resulted with smooth-edges, but when $\mathrm{Re}>\mathrm{Re}^{crit}$, gas turbulence occurred in the vicinity of the melt puddle, which is a mechanism of kinetic energy dissipation that was reflected in the formation of serrated edge ribbon, see figure 5.1.

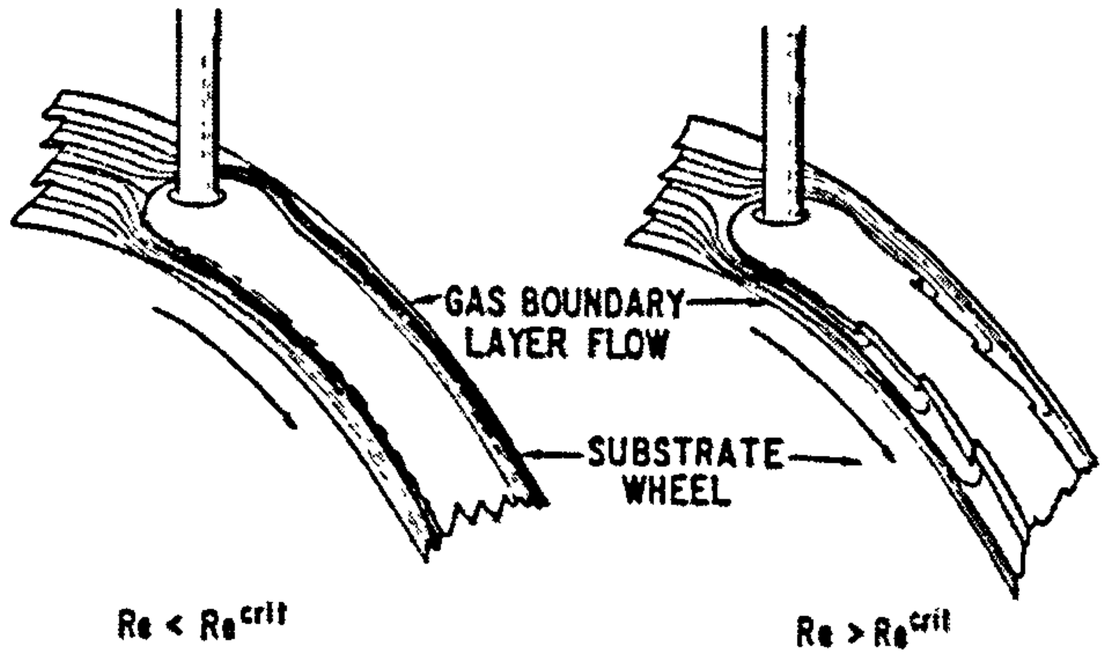

Figure 5.1. Schematic illustrations of the air boundary layer about the melt jet impingement area on the rotating substrate roll [136].

Yapp *et al.* [137] found that for nanocrystalline $Fe_{82}Nd_{11.7}B_{6.2}Zr_{0.2}$ alloy ribbons cast in argon at various environment pressures (from 0.13 Pa to 100 kPa), gas pockets formed on the roll contact surface above 50 kPa, while, for lower pressures, were absent. It was found that, with the elimination of gas pockets, the mean local grain size for crystalline ribbons was smaller and that the grains were more uniform, indicating higher and more uniform cooling rate. Similar results were found by Harland and Davies [138] for the casting of $Fe_{82}Pr_{12}B_6$ nanocrystalline ribbons under Ar pressures from 25 kPa to 100 kPa. In that study, gas pockets totally disappeared for chamber pressures of 25 kPa. Todd *et al.* [139] also studied the effects of casting $Fe_{73.5}Si_{13.5}B_9Nb_3Cu_1$ amorphous alloy ribbons, under various ambient pressures of Ar, air and He, and observed the same pattern that Lieberman found [136], regarding the influence of gas pressure on the surface quality of the ribbon. They found an increase in coercivity, H_c in ribbons cast at higher pressures or heavier gases resulting from interaction between the domain walls and the gas pocket. It was explained that the pockets between the underside of the melt puddle and the roll surface resulted from the gas being drawn under the puddle at their 'rear' end by the action of the rotating roll. These pockets of gas are expanded to form discrete bubbles during the extraction of the ribbon of liquid alloy from the puddle and its subsequent solidification. These pockets substantially retard the transfer of heat from the liquid to the roll and consequently the crystal nucleation frequency is considerably reduced locally due to the reduction in the degree of melt undercooling.

From these studies [136-139], it can be concluded that the excellent quality of ribbons obtained when casting in a He environment in the present work was because the molecular weight of He is about a factor of 10 smaller than Ar, and therefore the melt jet impingement area on the substrate roll is higher in He than in Ar, preventing, or in the extreme, avoiding the entrapment or formation of gas pockets between the melt and the roll surface, and eliminating serrated edges, giving in this way more consistent cooling rates, and hence much smoother ribbon sides and edges like those shown in figure 4.5(*b*).

5.3 Structure and thermal stability

It was shown in section 4.3 that all the alloy wires and ribbons were found to be amorphous from x-ray diffractometry. However, $Fe_{69.5}Cr_8Si_{7.5}B_{15}$ amorphous wire (115 μm diameter) could not be bent through 180° without fracturing, in contrast to the other alloys in both forms. The embrittlement of $Fe_{69.5}Cr_8Si_{7.5}B_{15}$ may occur because of the relatively high content of Cr. There is an increasing tendency for glassy alloys to become brittle at room temperature, the higher the concentration of transition metal solute(s). The effect is to increase the intrinsic ductile/brittle transition temperature T_b so that at sufficiently high concentration, T_b exceeds room temperature. This effect is also dependent on the metal:metalloid concentration.

The loss of ductility of $Fe_{69.5}Cr_8Si_{7.5}B_{15}$ alloy wire may also be suggested to have occurred during casting as a result of partial crystallisation or self-annealing during casting. It has been reported [129] that for high Cr content alloys, usually for Cr-contents ≥ 8 at% Cr, it was virtually impossible to cast ductile wires; however, in the present work, $Fe_{70}Cr_8Si_{10}B_{12}$ alloy wire proved to be ductile. The embrittlement of metallic glasses in the presence of Cr has a strong correlation with the concentration of metalloid usually carbon; it is clear that the embrittlement of $Fe_{69.5}Cr_8Si_{7.5}B_{15}$ alloy wire, may also result from the higher content of B. The embrittlement of some metallic glasses with relatively high Cr has also been attributed [129] to ultra-fine segregation by short range diffusive migration of atomic species which could occur during the casting. This phenomena has been compared to the Cr embrittling of some ferritic steels, attributed to some sort of microsegregation. It was also suggested that this effect is dependent on the imposed cooling rate, i.e. for a given concentration of metal solute and metalloid, if the section thickness was smaller and, hence

the cooling rate higher, the less likely it would be that the glass is brittle in the as-cast state. The cooling rate at lower temperatures may be especially important because if it is too low self annealing may occur leading to relaxational embrittlement.

One index of thermal stability of an amorphous alloy can be taken as the crystallisation temperature [140]. As has been seen previously, T_x (determined by DSC) was dependent on composition, mainly Cr and B. As seen in figures 4.10(*a*) and (*b*), in both alloy series for low Cr content, i.e. 0 and 3.5 at% Cr in series A, and 0 and 4 at% Cr in series B, there are two characteristic peaks, which suggests that there was a two-stage crystallisation mechanism in such alloys. With further addition of Cr, i.e. 6.25 and 8 at% Cr in series A and 8 at% in series B, the first exothermic peak gradually disappeared, suggesting now, only a single crystallisation mechanism. Koster and Herold [141] proposed that, in the case where two peaks appear, the crystallisation reaction could be expressed by a two-stage transformation:

$$A \Rightarrow MS^{I} + A^{I} \qquad (5.a)$$

$$MS^{I} + A^{I} \Rightarrow S^{II} \qquad (5.b)$$

where A and MS^{I} are the amorphous and metastable phases, respectively, A^{I} and MS^{I} are transitional amorphous and metastable crystalline phases, respectively and S^{II} the final stable crystalline phase. The almost constant heat of crystallisation in both alloy series with increasing Cr content, shown in figure 4.12, supports the suggestion of the two-stage mechanism of crystallisation for low Cr content alloys, represented by (5.*a*) and (5.*b*) reactions. Further, it is therefore suggested, in the presence of a high Cr content in the other alloys, that the first stage of crystallisation is delayed, such that, when it eventually occurred, the intermediate product MS^{I} became very unstable and was immediately transformed to the final product S^{II}. Hence, in this case, the DSC measurements would indicate the two reactions occurring as only one, i.e. thermally overlapping.

The enhancement of thermal stability was detectably higher in amorphous wires of series B, as can be seen in figure 4.11. Again, this can be explained in terms of a more densely packed atomic configuration, since the concentration of the smaller metalloid atoms in series B is slightly higher than in series A giving a more compact structure, and

therefore increasing the thermal stability. Yavari [142] compared the thermal stability of $Fe_{79.3}(SiB)_{20.7}$ and $Fe_{82}(SiB)_{18}$ ribbons and confirmed that on decreasing the metalloid content, the embrittlement temperature decreased, which indicates that the lower the metalloid content, the lower the thermal stability, which is consistent with this work, since T_x was lower for the $Fe_{78-x}Cr_xSi_{10}B_{12}$ alloy series than for the $Fe_{77.5-x}Cr_xSi_{7.5}B_{15}$ alloy wire series.

On the other hand, Donald and Davies [140], in a study of the influence of the addition of refractory metal, *X*, to $Fe_{78-x}X_xSi_{10}B_{12}$ glassy ribbons, found that T_x increased in order Cr, V, Mo, W, Ti, Nb, Ta, Zr and Hf. This effect was shown to have a trend with the weighted average of the number of conduction $s + d$ electrons per transition metal. In a similar way, although in the present study only Fe was substituted by Cr, the increase in the T_x, can be attributed to the partial bonds formed by the overlapping of *s-d* hybrid orbitals of metalloid atoms with *s-d* orbitals of the transition elements being strengthened by decreasing the *d*- electron concentration leading to a more stable structure. This interpretation was based on the numbers of bonding and antibonding electron states. Therefore, addition of transition elements that increase the number of bonding states, i.e. elements with fewer *d* electrons than Fe in Fe-based alloys lead to increased thermal stability, whilst addition of elements with more *d* electrons that increase the number of antibonding states, decrease the thermal stability.

Donald and Davies [140] also explained the increase of T_x in terms of the difference in atomic diameters between Fe and the solute metal, Cr in this case. They studied the variation of ΔT_x (defined as the difference between the measured T_x at a given e/a – the average concentration of the outer *s* and *d* electrons per atom- and the interpolated T_x at the same e/a, assuming only an electron contribution to T_x) with $(\Delta a/a)^2$ for 10 at% alloying element; $\Delta a/a$ is the fractional difference in the Goldschmidt diameter between solvent and solute metal atoms. It was found that the introduction of solute atoms larger that the host would increase the elastic strain associated with interdiffusion of the atoms, hence increasing the thermal stability, i.e., if the size of holes in the structure remained unaffected by the solute atoms, the strain associated with diffusion would be expected to scale as $(\Delta a/a)^2$. In addition, the packing density would be increased due to the admixtures of atoms of different sizes, reducing the size of available holes in the structure, increasing in this

way the thermal stability. However, this effect in the case of Cr would be small because of similar hard sphere diameters for Fe and Cr atoms.

5.4 Mechanical properties

5.4.1 Microhardness

It has been widely reported that the hardness of metallic glasses is also strongly influenced by the average concentration of the outer *s* and *d* electron per metal atom, as is the case for thermal stability [143]. This effect is more clearly seen in figure 5.2, where the hardness is plotted against *e/a*.

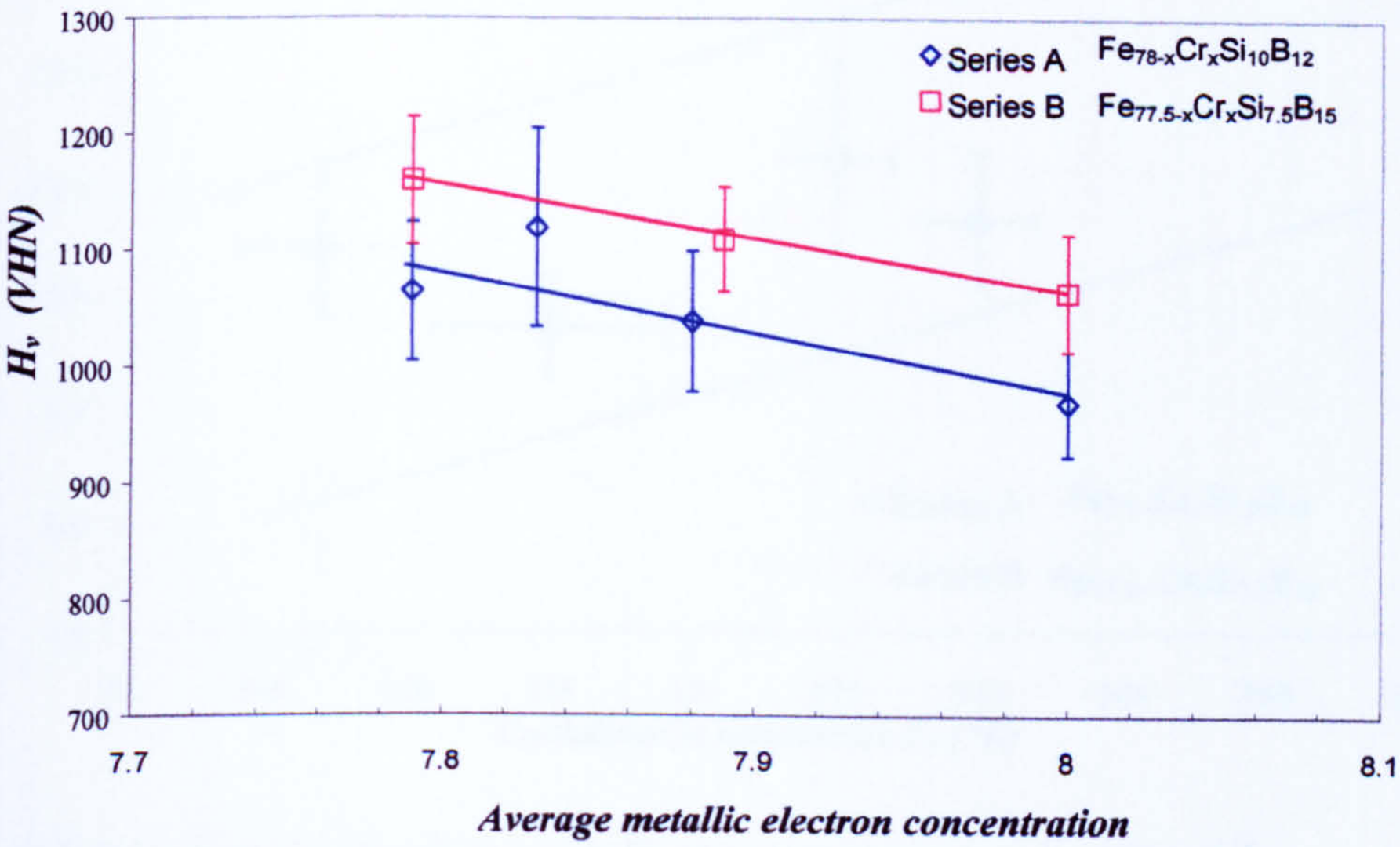

Figure 5.2. Vickers microhardness plotted against the average outer electron (*s, d*) concentration of metallic atoms (*e/a*) for both alloy wires series.

This figure shows that there is a correlation between hardness and average concentration of the outer *s,d* electrons, which is in accord with previous results [140, 143], but also that hardness varies significantly with the boron content. Masumoto [143] proposed that the major role of the outer electron of transition element in amorphous metals was to weaken the bond strength associated with metalloid atoms which seem to play the dominant role in determining the flow property of amorphous metals, instead of the increase in the cohesive energy in the case of crystalline solids. On the other hand,

Donald and Davies [140] found a broadly similar dependence of H_v versus *e/a* to that observed for T_x versus *e/a* for period 4 alloying additions. Deviations of T_x from the main period 4 dependence on *e/a* observed for solute atoms from periods 5 and 6, were not reflected to the same extent in the H_v values and, the anomalous changes in T_x for Co-containing alloys were not reflected in the hardness behaviour. They concluded that H_v versus T_x did not give a single relationship for all alloying additions, because the effect of atomic size difference, in this case, is less significant. This can be seen in figure 5.3 (data corresponding to the present work). It appears that the series B alloys follow a much better linear relationship between H_v and T_x than the series A alloys. However, the precision of the measurements did not permit a final conclusion to be drawn on this point.

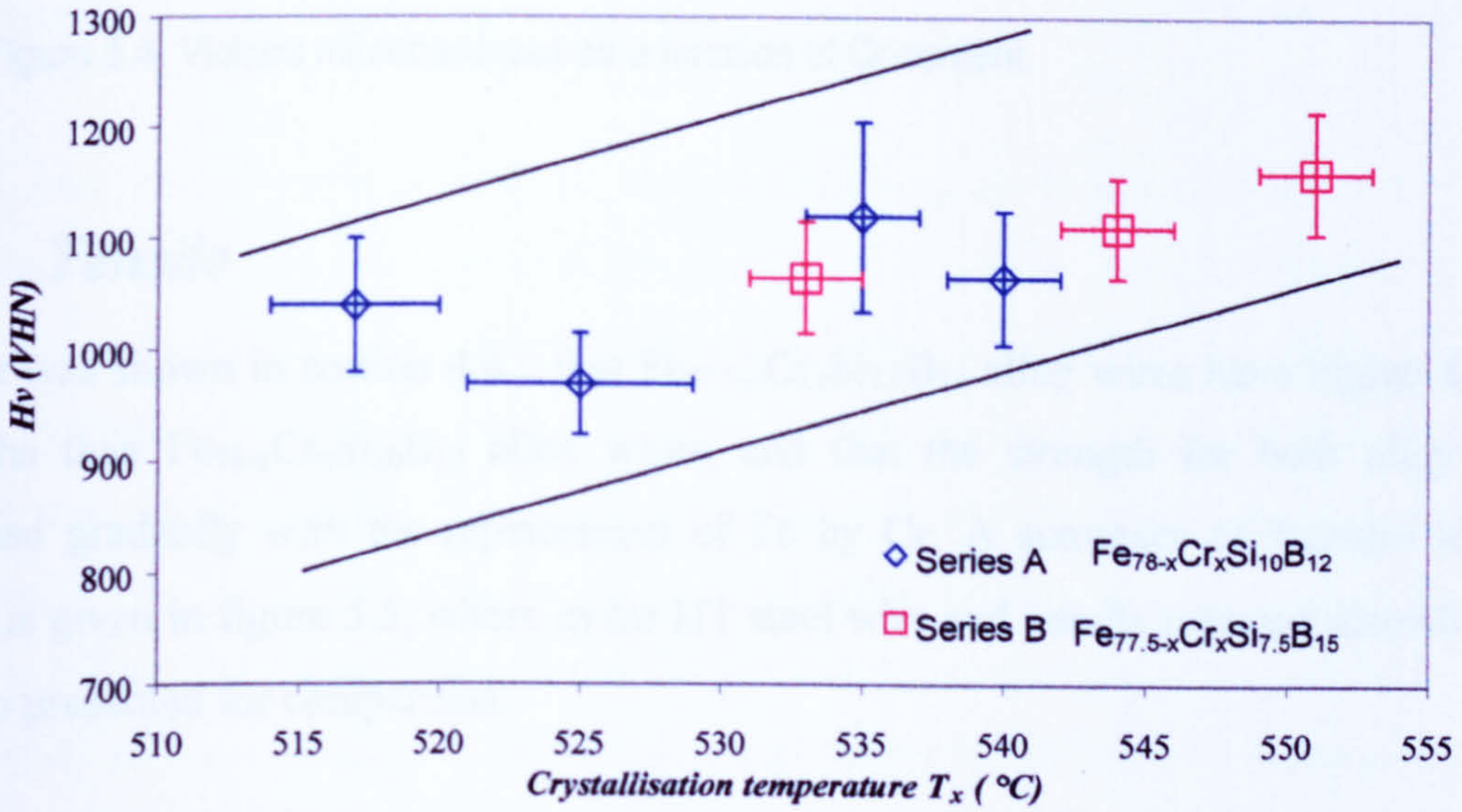

Figure 5.3. Vickers microhardness of both alloy wire series as a function of T_x.

Masumoto [143] studied the relationships between hardness and the total metalloid concentration for Fe- Co- and Ni- based alloys with various combinations of metalloids, C, P, B and Si. It was found that the effect of metalloids on hardness decreased in the order of B, Si, C and P in the Fe-based alloy glasses. The present results are compared with these findings, as can be seen in figure 5.4 where the Vickers microhardness is plotted against the Cr concentration for both alloy series. A gradual increase of H_v is seen with increasing Cr content, but with consistently higher values of H_v for series B than for series A. This effect can be attributed to the presence of a higher B content in series B, consistent with Masumoto's observations. Note the higher values of H_v for amorphous alloy wires than for

the HT steel wire. This effect is attributed to the absence of dislocations in the metallic glass structure.

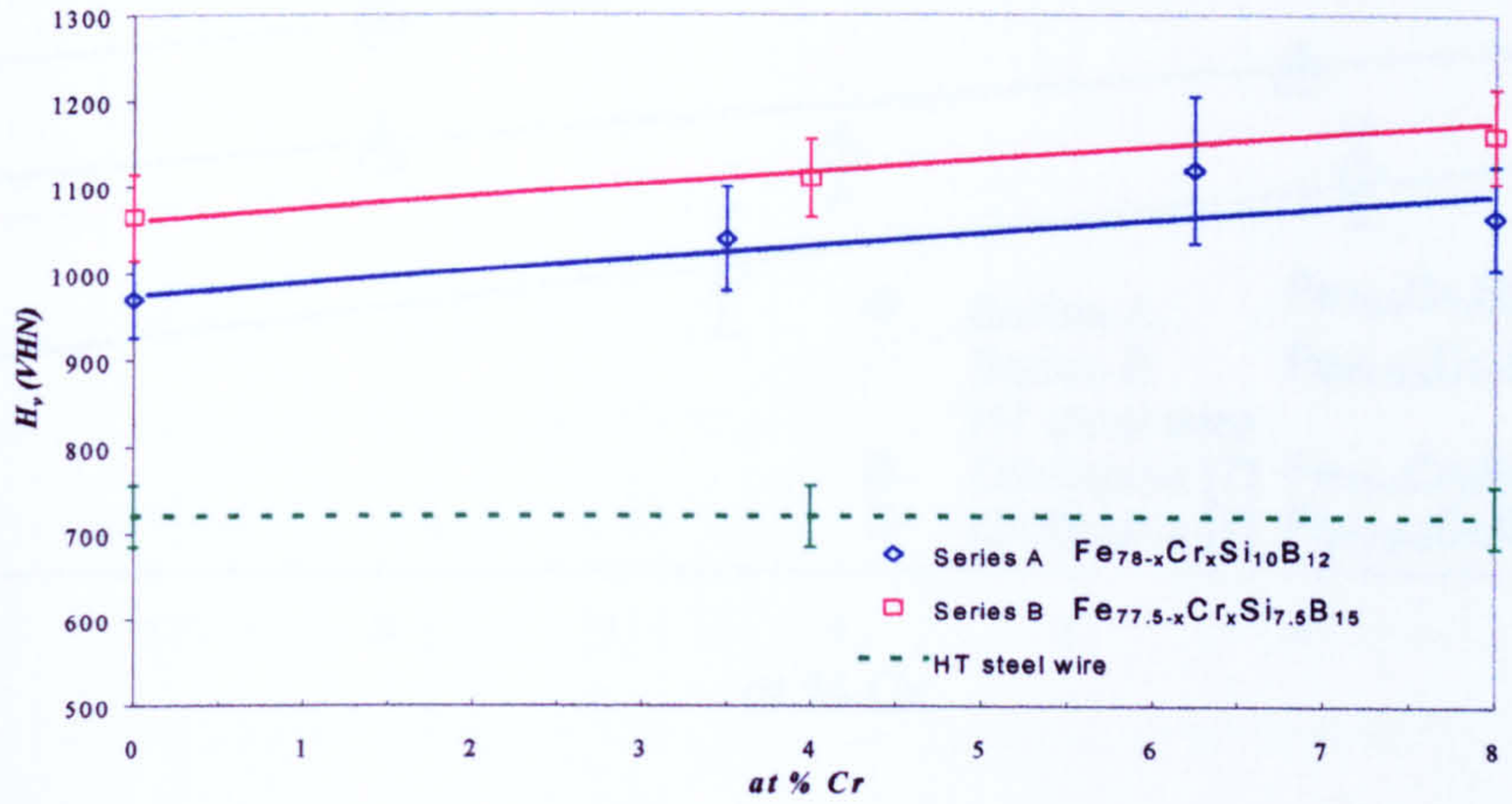

Figure 5.4. Vickers microhardness as a function of Cr content.

5.4.2 Tensile

It was shown in section 4.4.2 that $Fe_{77.5-x}Cr_xSi_{7.5}B_{15}$ alloy wires have higher fracture strengths than $Fe_{78-x}Cr_xSi_{10}B_{12}$ alloy wires, and that the strength for both alloy series increased gradually with the replacement of Fe by Cr. A summary of fracture strength results is given in figure 5.5, where σ_f for HT steel wire and results reported elsewhere [7] are also presented for comparison.

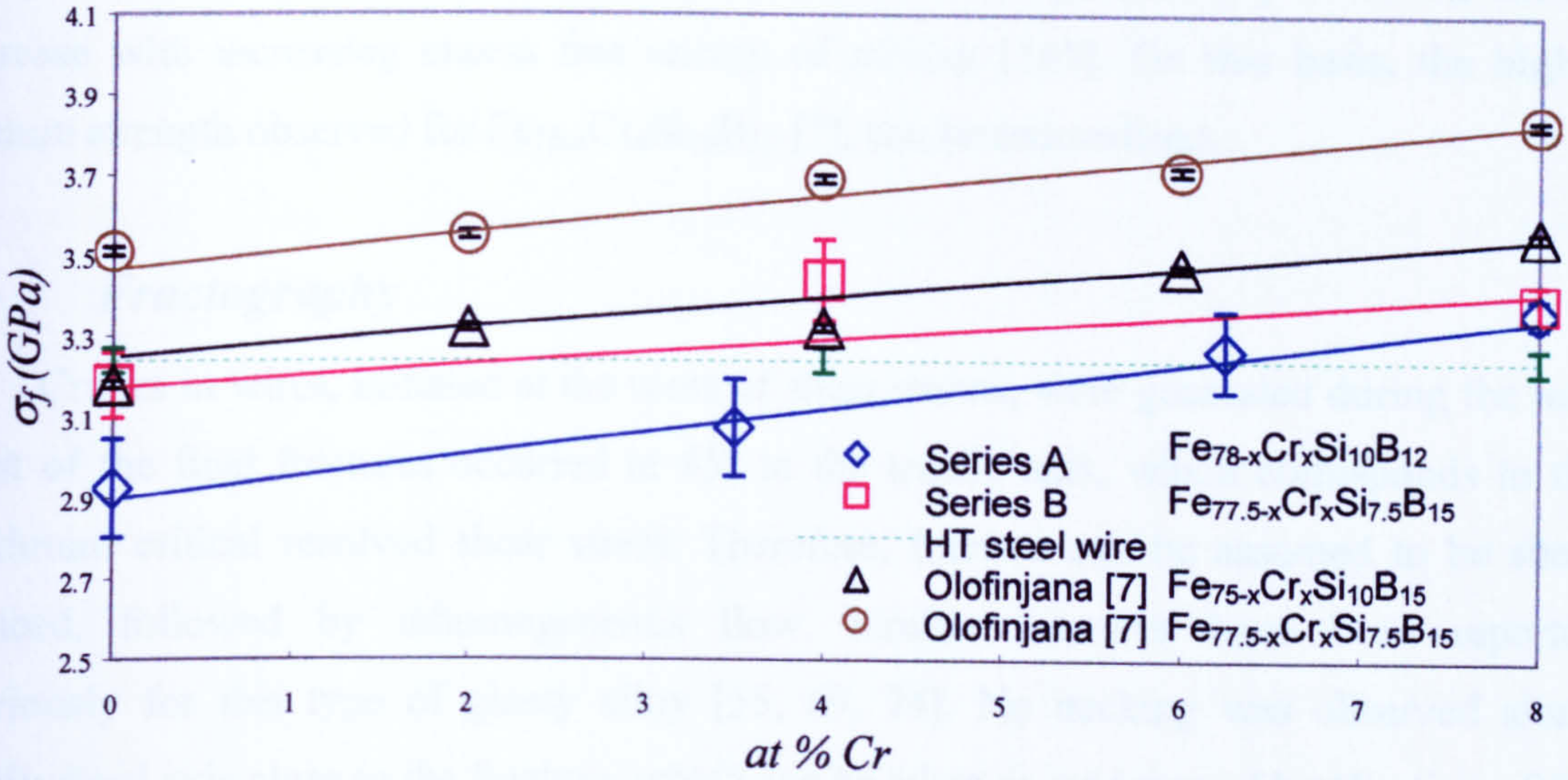

Figure 5.5. Tensile strength as a function of Cr contents.

It was pointed out in an earlier section that boron plays a more important role than Si for glass forming but also for strength, which is in some respect different from the conclusions of previous work [7]. This apparent difference regarding the effect of Si on the tensile strength may be because in the previous study, B was kept constant and the Si content was changed. In this case the concentrations of both metalloids were changed, and it is clearly seen in figure 5.5 that, even for alloy wires containing more Si and less B, the fracture strength was lower than for the alloy wires with more B and less Si. The stronger effect of B additions than Si on the mechanical properties of Fe-Si-B based glassy alloy wires has also been found in the case of the Young's modulus [144]. It was suggested that the short-range ordering tendency due to the interaction between iron and metalloid atoms is much stronger for B than for Si. On the other hand, Hagiwara *et al.* [54] found that σ_f increased by replacing Fe with relatively small amounts of a transition metal, *M*, in the order of Cr, V, Mo, W, Nb and Ta; they attributed this enhancement to an increase of the bonding force between metal and metalloid or metal and metal in $(Fe\text{-}M)_{75}Si_{10}B_{15}$ (the $Fe_{75}Si_{10}B_{15}$ ternary alloy was located around the central part of the amorphous phase-forming region, see figure 2.14 [54]). These *M* alloying elements were also found to enhance the glass forming tendency of Fe-B-Si in the same order as σ_f. This correlation between glass forming tendency and tensile strength can be explained in terms of the relation between glass forming ability, and the empirical reduced glass temperature, T_g/T_m ratio, since a strong chemical bonding nature between the solute metal and metalloids

atoms enhances T_g as well as increasing the cohesive energy [11, 38] which T_m should decrease with increasing excess free energy of mixing [145]. On this basis, the higher fracture strength observed for $Fe_{75-x}Cr_xSi_{10}B_{15}$ [7], can be rationalised.

Fractography

Cracks in wires, initiated at the roots of shear events, were generated during the test. Most of the final fractures occurred at 45° to the tensile axis, which corresponds to the maximum critical resolved shear stress. Therefore, fracture can be assumed to be shear induced, followed by inhomogeneous flow. Similar fractures have been reported previously for this type of glassy alloy [55, 69, 74]. No necking was observed along longitudinal axis close to the fracture, which can be taken as evidence of localisation of the strain on the shear surfaces. The two characteristic regions observed in the final fracture, smooth and veined, can be explained as follows: the uniform regions represent the initial displacement on the shear plane; the veined morphologies result from the existence of a "liquid-like" or softened layer formed during shear displacement, involving extensive localised plastic flow, corresponding to an instability phenomenon characteristic of ductile glassy alloys. It has been suggested [100] and supported [55] that the thin layer of softened material must result from local heating occurring under close to adiabatic conditions. Argon [86] considered the "liquid-like" layer as a supercooled liquid so that it was possible to imagine that this phase was present only in the last stage of the final rupture due to additional heating.

The development of plastic instability in the fracture of metallic glasses has been considered for glasses both in the form of ribbons (70 x 400 μm –transverse dimensions-) [100] and wires (120 μm diameter) [55]. In the latter case, the development of plastic instability was assumed to be analogous to the dendritic instability in crystal growth. In both cases, the critical wave length was found to be ~1μm, which is similar to the closest spacing of "veins" observed in the tensile fracture surfaces in the present work, see, for example, figure 4.29.

On the other hand, in the present work some features typical of brittle fracture were observed in some ribbon and wire tensile fractures. It has been proposed [74] that brittle fracture in metallic glasses is a cleavage process, which occurs when the tensile stress at a

stress concentrator, such as a microcrack, attains the theoretical fracture stress of the material, σ_{th}, before shear-induced plastic flow can blunt the crack and relieve the stress. Spaepen and Taub [74] pointed out that Steif [146], in order to explain brittle behaviour, showed that the theoretical fracture stress can be reached if the time constant and the initial viscosity of the material are large enough. Spaepen and Taub explained that Steif's model suggested that structural relaxation not only increases the viscosity but also increases the time constant for free volume redistribution, and that the differences in embrittlement kinetics between different metallic glasses, such as iron-based alloys, may be attributed to differences in the redistribution kinetics. In the case of wire samples under test, it is not known how much structural relaxation can occur during the test. However, it has been proposed [129] that thermally relaxed brittle spots may exist as casting defects.

5.4.3 Fatigue

It was observed in section 4.4.4 that in some amorphous alloy wires and HT steel wires no fatigue limit was attained. However, recent research shows that the fatigue limit in steels is a feature that arises with strictly identical fatigue cycles applied under laboratory conditions (see, for example, references [147, 148] for more details). It was also shown in section 4.4.4 that apparently the HT steel wire had a better fatigue performance than amorphous wires. It had been previously claimed that glassy alloy wires had better fatigue performance than the HT steel piano wire [9, 34], but in those cases the results were given on the basis of bend strain. In the current work the results have been obtained in terms of bend stress and, because the elastic modulus of the amorphous wires (the maximum value for the present alloys is 177 GPa) is lower than that of steel (200 GPa), the fatigue performance expressed in terms of bend stress gives a different ranking compared to the fatigue performance expressed in terms of bend strain.

Stress life approach

If *S-N* fatigue curves, such as those given in section 4.4.4, are redrawn on a log-log scale, with the true stress amplitude ($\sigma_a=\Delta\sigma_a/2$) plotted as a function of the number of cycles or load reversals to failure, a linear relation is commonly observed. The resulting expression relating σ_a, in a fully-reversed, constant amplitude fatigue test to the number of load reversals to failure, $2N_f$, is given by the Basquin equation, (see for example [149]):

$$\frac{\Delta\sigma_a}{2} = \sigma_a = \sigma_f'(2N_f)^b \tag{5.7}$$

where σ_f' is the fatigue strength coefficient (which, to a good approximation, equals the true fracture strength, σ_f, corrected for necking, in a monotonic tension test for most metals) and b is known as the fatigue strength exponent (or Basquin exponent) which, for most metals, is in the range of –0.05 to –0.12.

The Basquin relation, equation (5.7) is valid for zero mean stress. A modification of the Basquin relation (due to Morrow, again see [149]), which accounts for mean stress effects for any σ_m, is:

$$\sigma_a = (\sigma_f' - \sigma_m)(2N_f)^b \tag{5.8}$$

Thus, again, a plot of $\log(\sigma_a)$ versus $\log(2N_f)$ allows the estimation of both b and σ_f', assuming that a straight line is obtained. It can be seen, however, that straight lines can only be fitted to the data up to $N_f = 10^5$, (see for example figure 5.6). Values of the fatigue strength exponent b and σ_f', obtained from the straight line portion of figure 5.6 are given in table 5.II. The values obtained for σ_f' are in the range of the theoretical strength of these amorphous materials.

Effect of composition

It has been shown that for any constant mean stress loading, the fatigue endurance increases on adding Cr in both alloy series. These results are broadly consistent with studies carried out by Inoue *et al.* [108] and Olofinjana and Davies [7], although their results were given as functions of strain range rather than stress range and those experiments were performed at a constant minimum stress rather than constant mean stresses, as in this work.

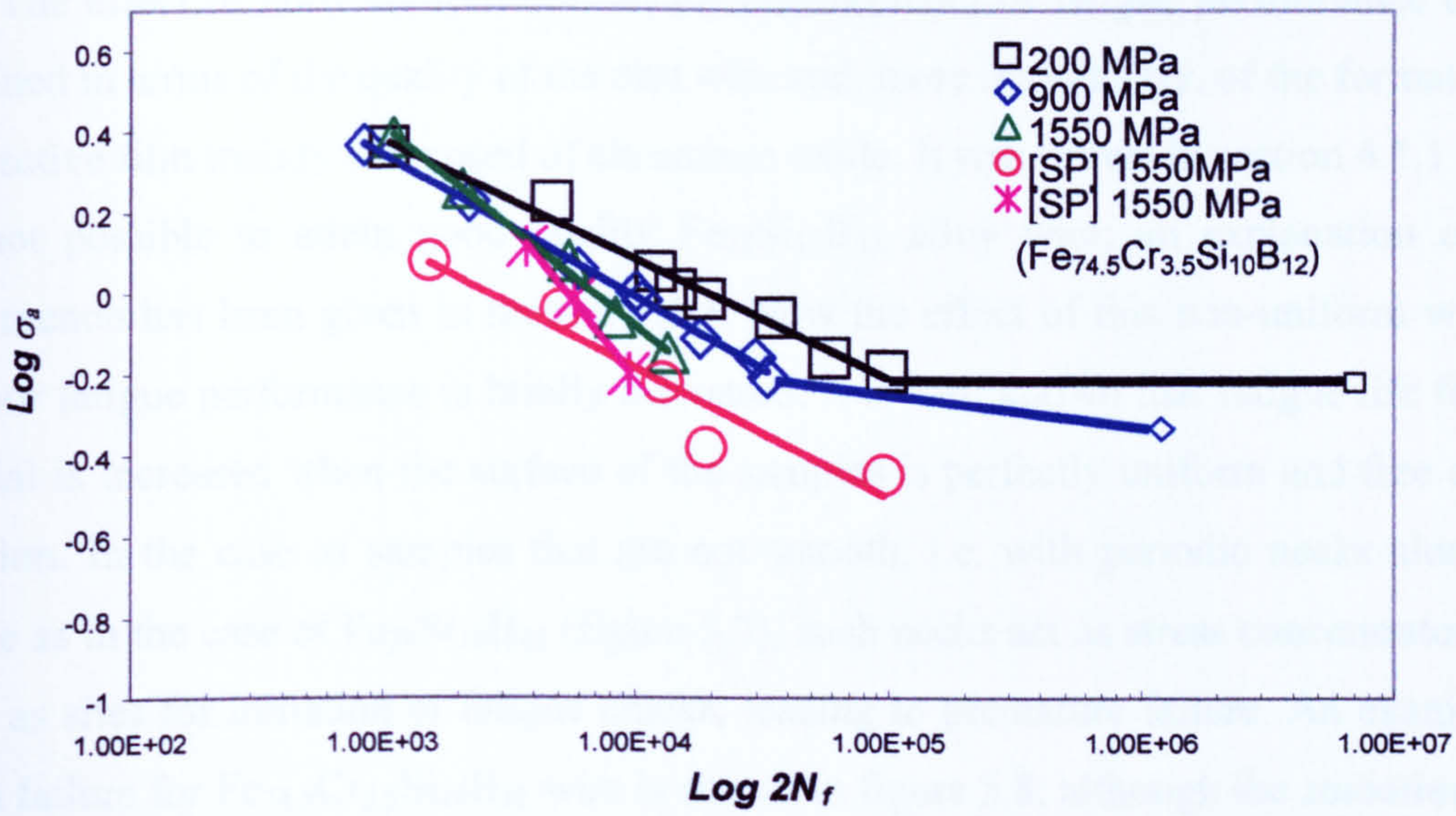

Figure 5.6. Linear relationships observed on the fatigue results for $Fe_{78}Si_{10}B_{12}$ tested at different mean stresses.

Table 5.II. Fatigue strength exponent or Basquin exponent values *b* (upper values) and fatigue strength coefficient σ_f' (lower values -GPa-) for $Fe_{78-x}Cr_xSi_{10}B_{12}$ and $Fe_{77.5-x}Cr_xSi_{7.5}B_{15}$ alloy series and HT steel wire.

Series A		0 Cr	3.5 at% Cr	6.25 at% Cr	8 at% Cr
200 MPa	*b*	-0.13	-0.14	-0.18	-0.12
	σ_f'	18.4	18.9	53.8	16.7
900 MPa	*b*	-0.15	-0.14	-0.13	-0.15
	σ_f'	26.33	24.1	20.13	34.1
1550 MPa	*b*	-0.21	-0.15	-0.09	-0.17
	σ_f'	80.5	28.6	10.46	39.4
[SP] 1550 MPa	*b*	-0.14	-0.34	-	-
	σ_f'	14	75.8		
Series B		0 Cr	4 at% Cr	8 at% Cr	HT steel wire
200 MPa	*b*	-0.1	-0.12	-0.11	-0.13
	σ_f'	12	22.8	17.26	34.38

The effect of alloy composition on the enhancement of fatigue performance can be explained in terms of the quality of the cast wire and, more importantly, of the formation of a protective film mainly composed of chromium oxide. It was shown in section 4.1.1 that it was not possible to attain good quality $Fe_{78}Si_{10}B_{12}$ alloy wire; an explanation of this phenomenon has been given in section 5.1.5. Now the effect of this non-uniform wire on the poor fatigue performance is briefly discussed. It is well known that fatigue life for any material is increased when the surface of the samples is perfectly uniform and free of any inclusion. In the case of samples that are not smooth, i.e. with periodic necks along the sample as in the case of $Fe_{78}Si_{10}B_{12}$ (figure 5.7), such necks act as stress concentrators and hence as sites for initiation of fatigue cracks, leading to premature failure. An example of such a failure for $Fe_{74.5}Cr_{3.5}Si_{10}B_{12}$ wire is shown in figure 5.8; although the smoothness of this alloy was improved by the presence of a small amount of Cr, nevertheless its morphology along the wire was not entirely uniform. This effect of premature failure due to pre-existing necks was not observed in the rest of the alloys in series A nor for any of the series B alloys, since their surface morphologies were evidently uniform along their entire gauge lengths, see for example figure 5.9.

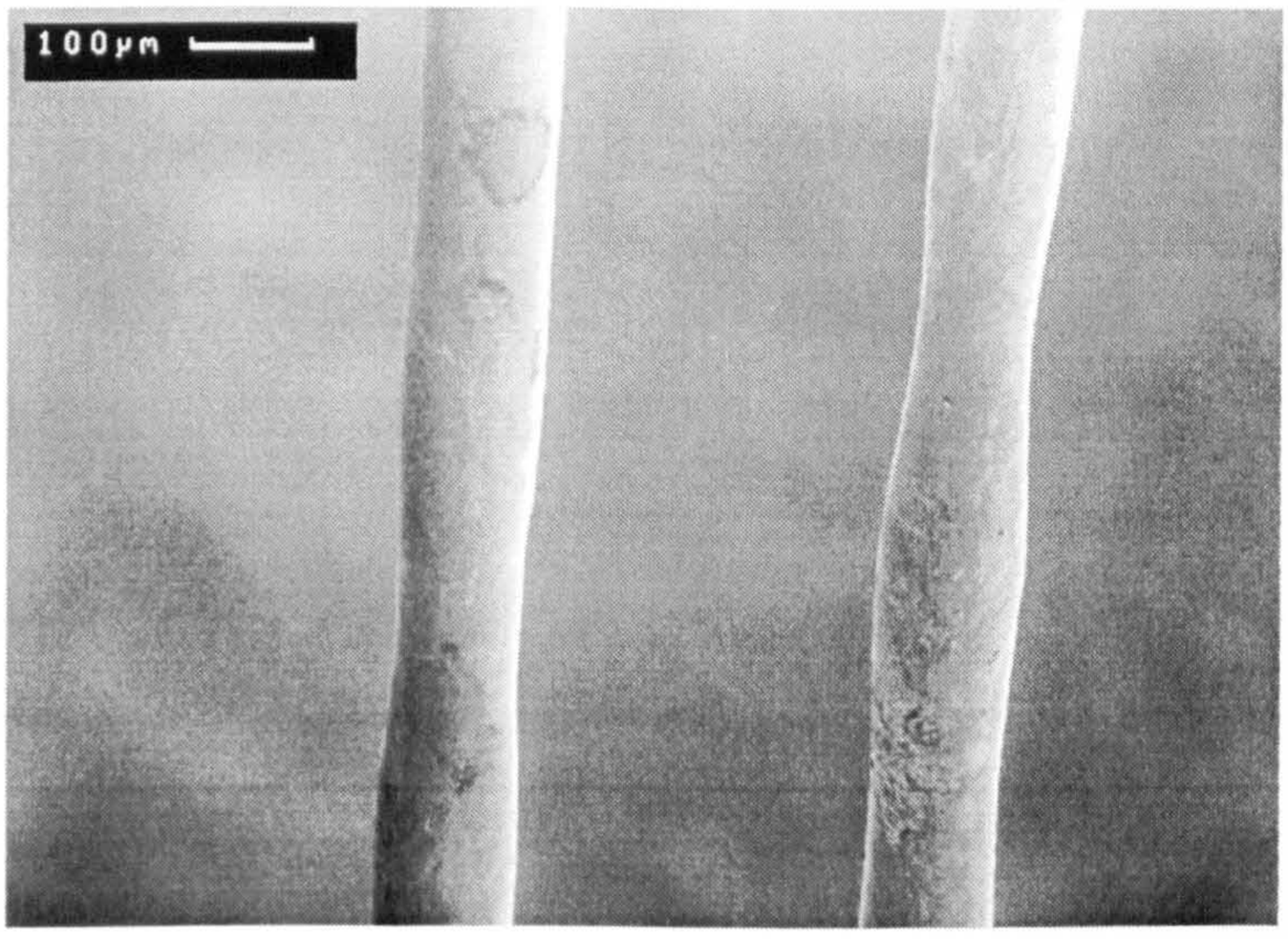

Figure 5.7. Peripheral surface of the $Fe_{78}Si_{10}B_{12}$ amorphous wire.

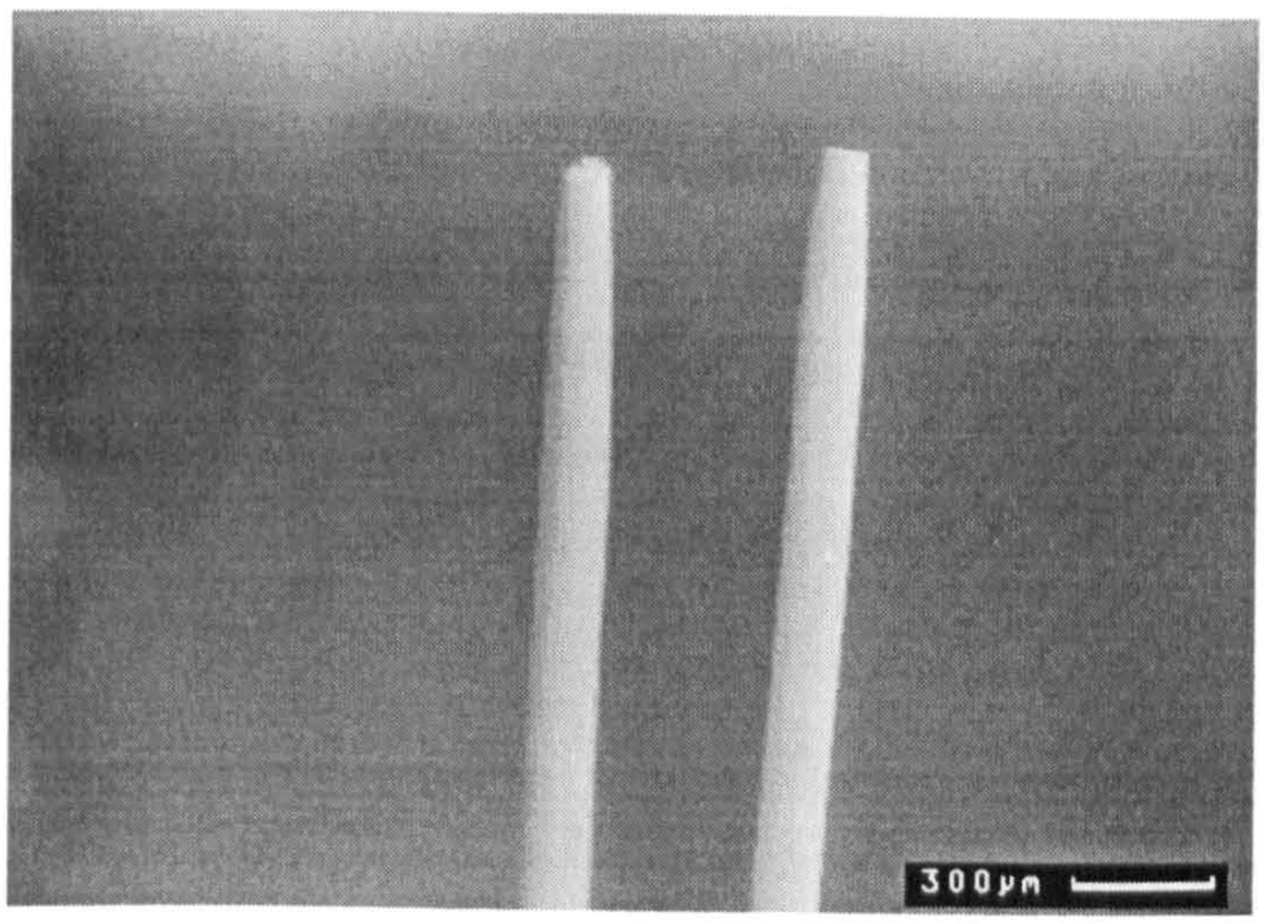

Figure 5.8. $Fe_{74.5}Cr_{3.5}Si_{10}B_{12}$ alloy wire fractured in the DP machine at the necked part of the wire, This wire fractured at 1,754 cycles, applying $\Delta\sigma_a$ = 900 MPa, using σ_m = 900 MPa.

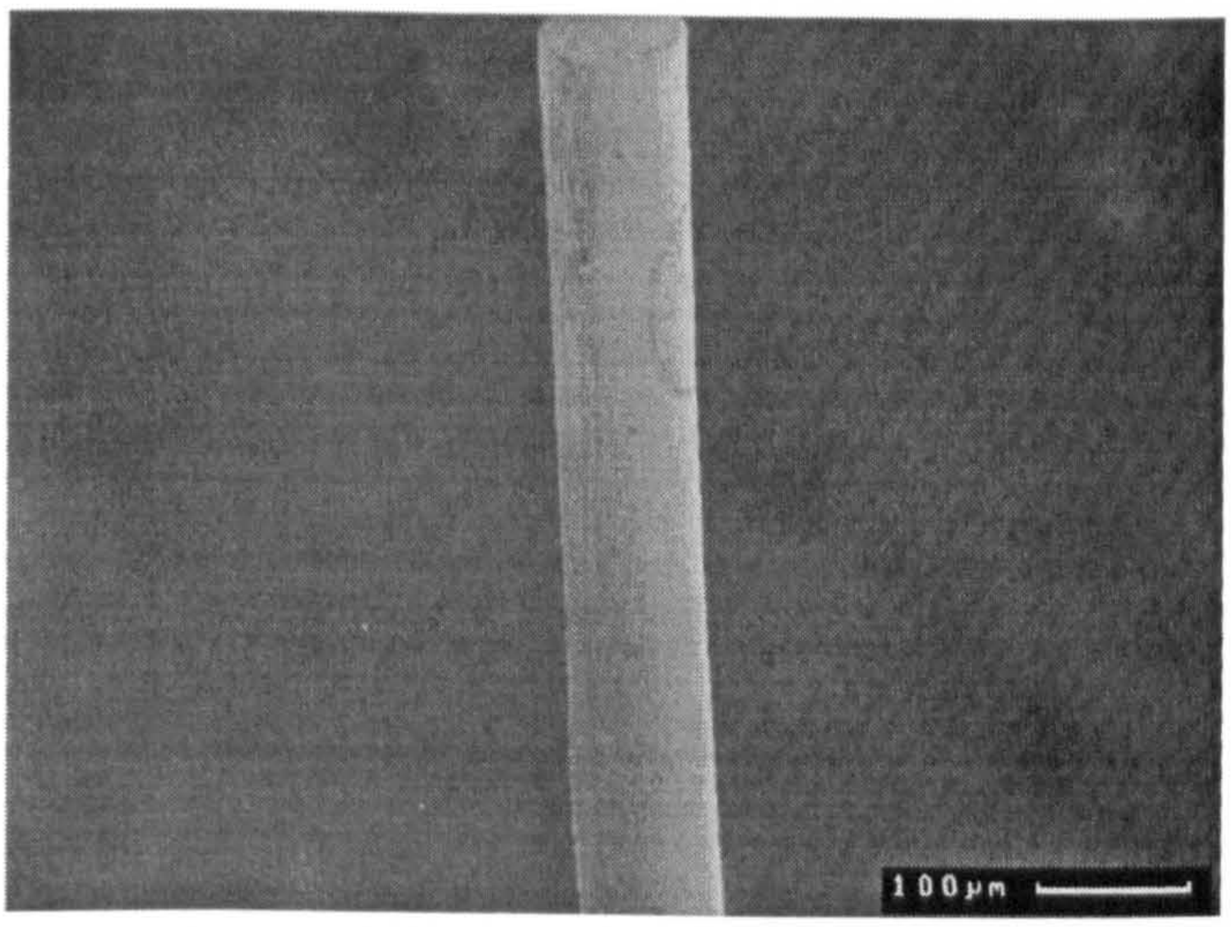

Figure 5.9. Peripheral surface of $Fe_{70}Cr_8Si_{10}B_{12}$ amorphous wire.

The improvement in fatigue endurance has been shown to increase with the substitution of Fe by Cr in both alloy series, but the increase was substantially less in series B, since the increase in the minimum measurable fatigue stress range from 0 to 8 at% Cr was ~ 94 % for series A alloys, and ~55 % for series B alloys, (samples tested in the DP machine at σ_m = 200 MPa). From these results, it is observed that the fatigue performance of these amorphous alloys showed a dependence on B content, rather than Si content, as has been observed in previous studies [7, 108] (it is important to notice that in those studies the at% of boron was kept constant and that the Si content was changed. It may be

interesting to study in future the real effect of B in these Fe-based alloys, by keeping constant the Si content for different B compositions). For instance, Inoue *et al.* [108] observed three stages of improvement due to Cr additions to Fe-Si-B series, which were described as follows: (*a*) a first stage in which no appreciable improvement was seen, (*b*) the second stage where a rapid enhancement with increasing Cr content occurred, and (*c*) the third stage where the enhancement became saturated. They concluded that the minimum chromium content required to cause significant enhancement of the fatigue limit was not constant and depended strongly on metalloid composition, particularly silicon concentration; the higher the silicon concentration the higher was the effectiveness of chromium addition. Subsequent studies made by Olofinjana and Davies [7] supported those studies, finding that the fatigue strength increased with higher silicon content. Both studies concluded that the enhancement of fatigue performance was due to the spontaneous formation of a passive thin film containing both chromium and silicon oxides on the surface of the wire, which appeared to accelerate the improvement of fatigue strength through the enhancement of corrosion resistance, thereby preventing corrosion due to ambient humidity, hence retarding, or in the extreme, avoiding crack initiation. Olofinjana and Davies [7] proved this assumption by carrying out XPS studies, they found that the peripheral film of the Cr- and Si- content rich alloys were composed mainly of hydrated chromium oxyhydroxide, $CrO_2(OH)\cdot H_2O$, and silicon dioxide. In addition, Hashimoto [150] has reported the presence of a passive film on $Fe_{70}Cr_{10}P_{13}C_7$ amorphous wire similar in form to that found on crystalline stainless steel alloys, and consisting mainly of hydrated chromium oxyhydroxide. This passive film on $Fe_{70}Cr_{10}P_{13}C_7$ amorphous alloy wires was found to be much greater in thickness than that found on crystalline stainless steel with Cr contents as high as 30 wt %. Hashimoto also reported that in Fe-B-C and Fe-Si-B alloys, the addition of Cr only slightly improved the corrosion resistance, this effect was attributed to the large amounts of borate and silicate included in the passive film.

The effect of Cr addition in enhancing the fatigue performance is seen for example in the fatigue endurance of $Fe_{73.5}Cr_4Si_{7.5}B_{15}$ and $Fe_{69.5}Cr_8Si_{7.5}B_{15}$ wires. In terms of strain range, not surprisingly the fatigue limit of the 8 at% Cr content alloy was higher than that of the 4 at% Cr (figure 4.18). However, because the fracture strength and Young's modulus of the $Fe_{73.5}Cr_4Si_{7.5}B_{15}$ wire was higher (3.44 GPa and 177 GPa, respectively) than for $Fe_{69.5}Cr_8Si_{7.5}B_{15}$ wire (3.38 and 157 GPa, respectively), the fatigue limit for the

$Fe_{73.5}Cr_4Si_{7.5}B_{15}$ wire in terms of bending stress range would be expected to be higher or at least equal to that of the $Fe_{69.5}Cr_8Si_{7.5}B_{15}$ wire, but in fact it was not, indicating that Cr has a significant effect on fatigue endurance.

It is proposed that the absence of a protective film against corrosion attack on alloys with zero or low Cr content is reflected in their relatively short fatigue lives, since they suffer attack from atmospheric humidity which leads to what could be corrosion pits on the peripheral surface of the wire (see for example figures 4.43, 4.44, 4.47 and 5.10 for series A and figure 5.11 for series B).

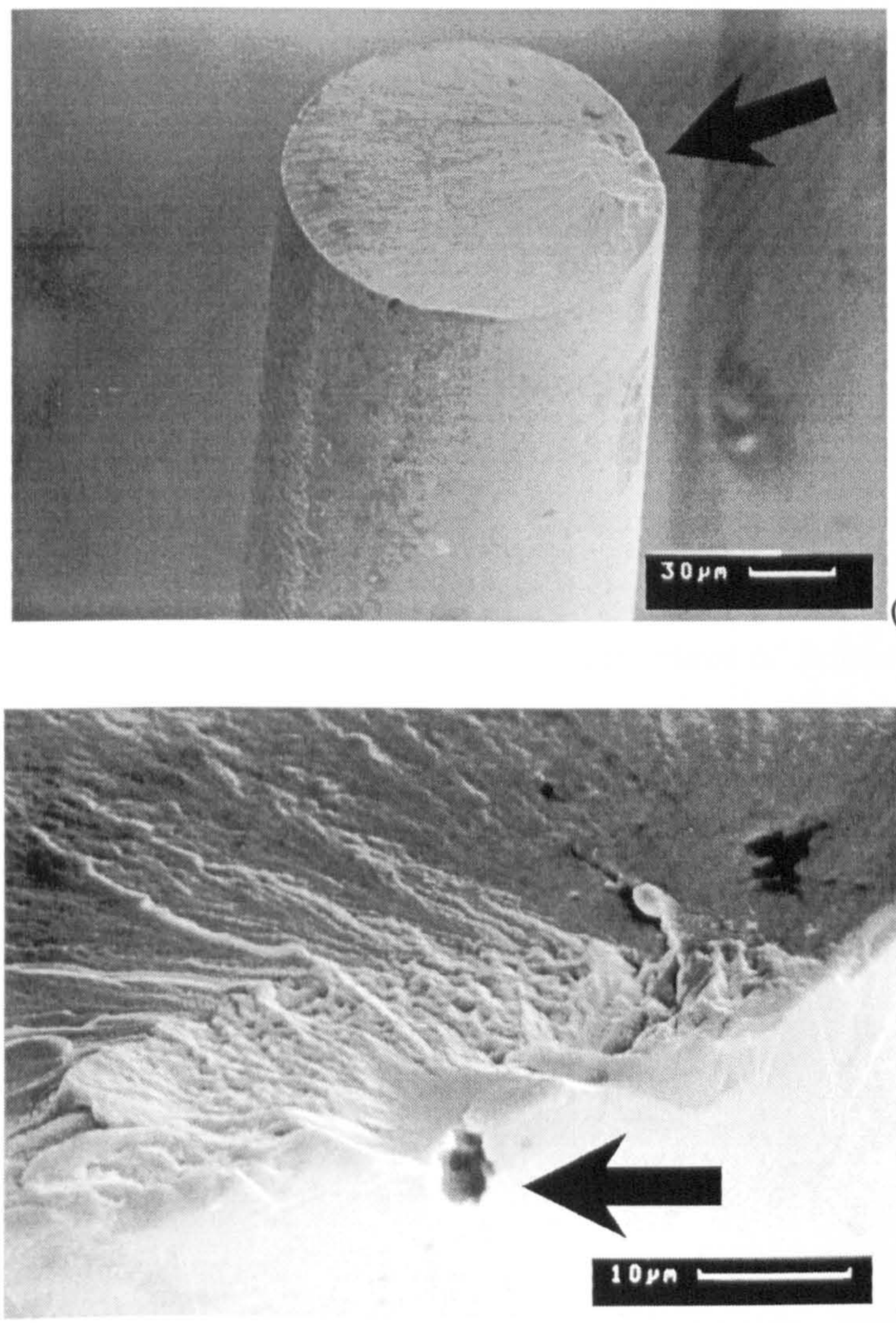

Figure 5.10. $Fe_{74.5}Cr_{3.5}Si_{10}B_{12}$ alloy wire fractured in the DP machine at ~6 x 10^5 cycles, applying $\Delta\sigma_a$ = 980 MPa, using σ_m = 1550 MPa. (*a*) general view; (*b*) higher magnification of the crack initiation site indicated by an arrow, showing what could be a corrosion pit at the fracture origin.

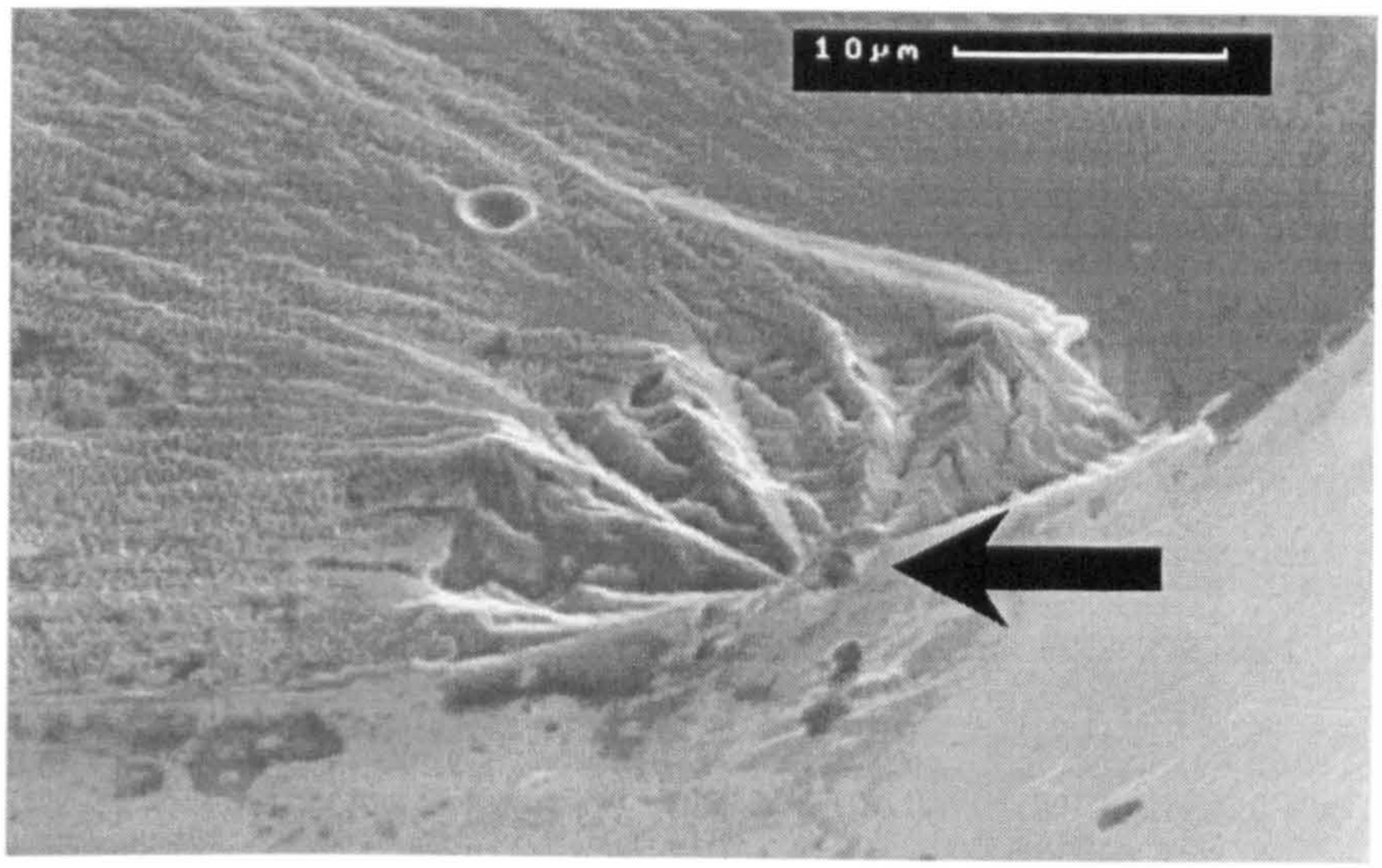

Figure 5.11. $Fe_{73.5}Cr_4Si_{7.5}B_{15}$ alloy wire fractured in the DP machine at 10,842 cycles, applying $\Delta\sigma_a$ = 2.5 GPa, using σ_m = 200 MPa. Arrow indicated feature suggesting crack initiation due to pitting corrosion.

Fractography

The fracture surface morphology for the amorphous wire samples tested on the SP machine showed similar features to those reported previously [55]; figure 5.12 shows an example of this type of fracture surface, where “mirror”, “mist” and “hackle” stages were present. This type of fracture has been discussed more broadly by Olofinjana and Davies [55]. They suggested that "mirror" represents the initial stage of fatigue crack growth; the "mist" region represents the crack growth; the "hackle" region represents the transition to high velocity crack propagation, leading to catastrophic failure. If this model is accepted then the origins of these features in the fatigue of amorphous alloys is rather different to their occurrence in silicate glasses and ceramics where all three features are associated with fast fracture.

On the other hand, the fracture surfaces of the amorphous wire samples tested on the DP machine showed three different morphological features, depending on the bending stress range but independent of the mean stress applied. Figure 5.13 summarises the morphological regimes observed on the fatigue fracture surfaces obtained in the DP machine.

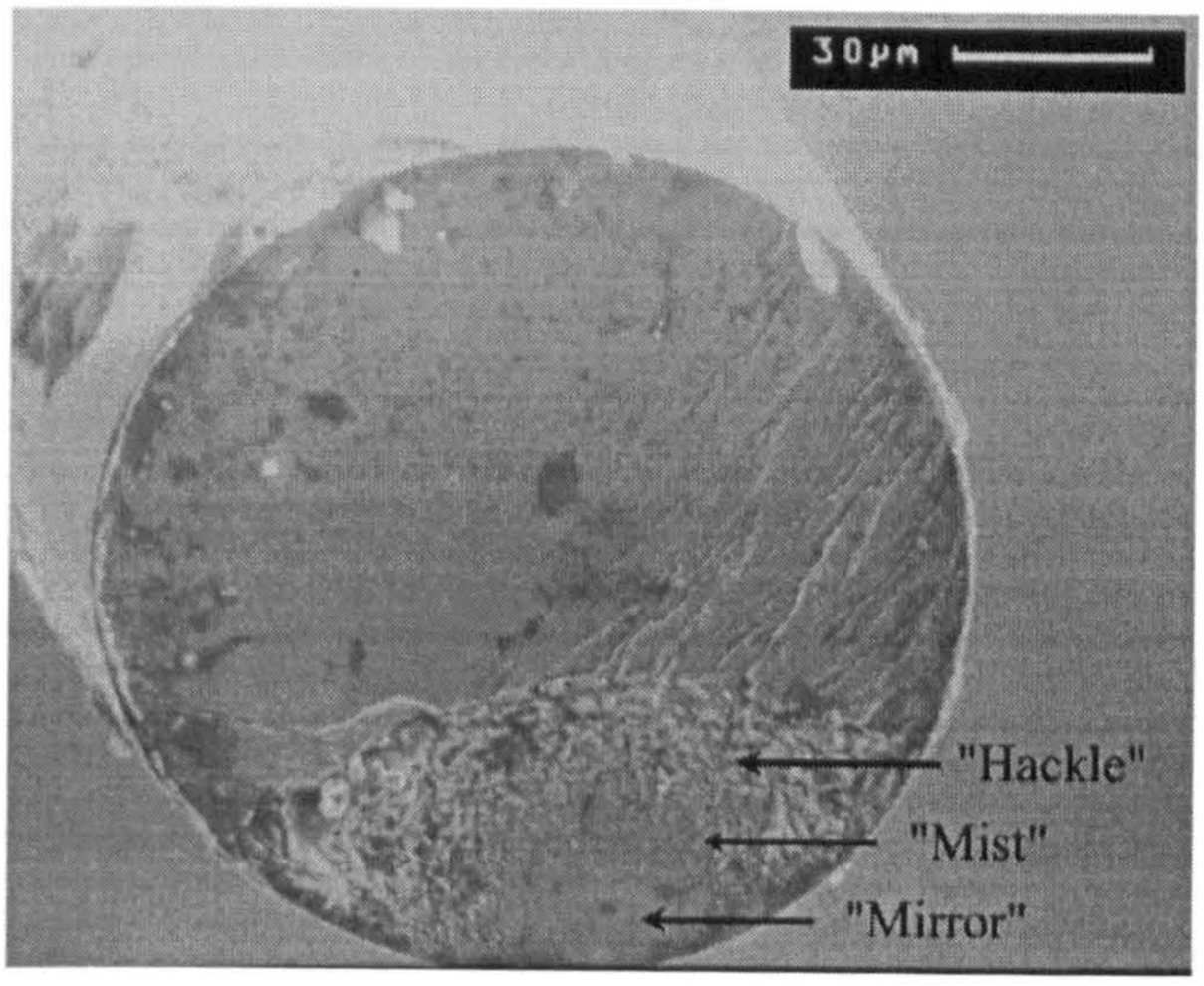

Figure 5.12. $Fe_{74.5}Cr_{3.5}Si_{10}B_{12}$ glassy wire fractured on the SP machine at ~ 1.01 x 10^6 cycles, applying $\Delta\sigma_a$ = 600 MPa, using σ_m = 1.55 GPa. "Mirror", "mist" and "hackle" stages are indicated.

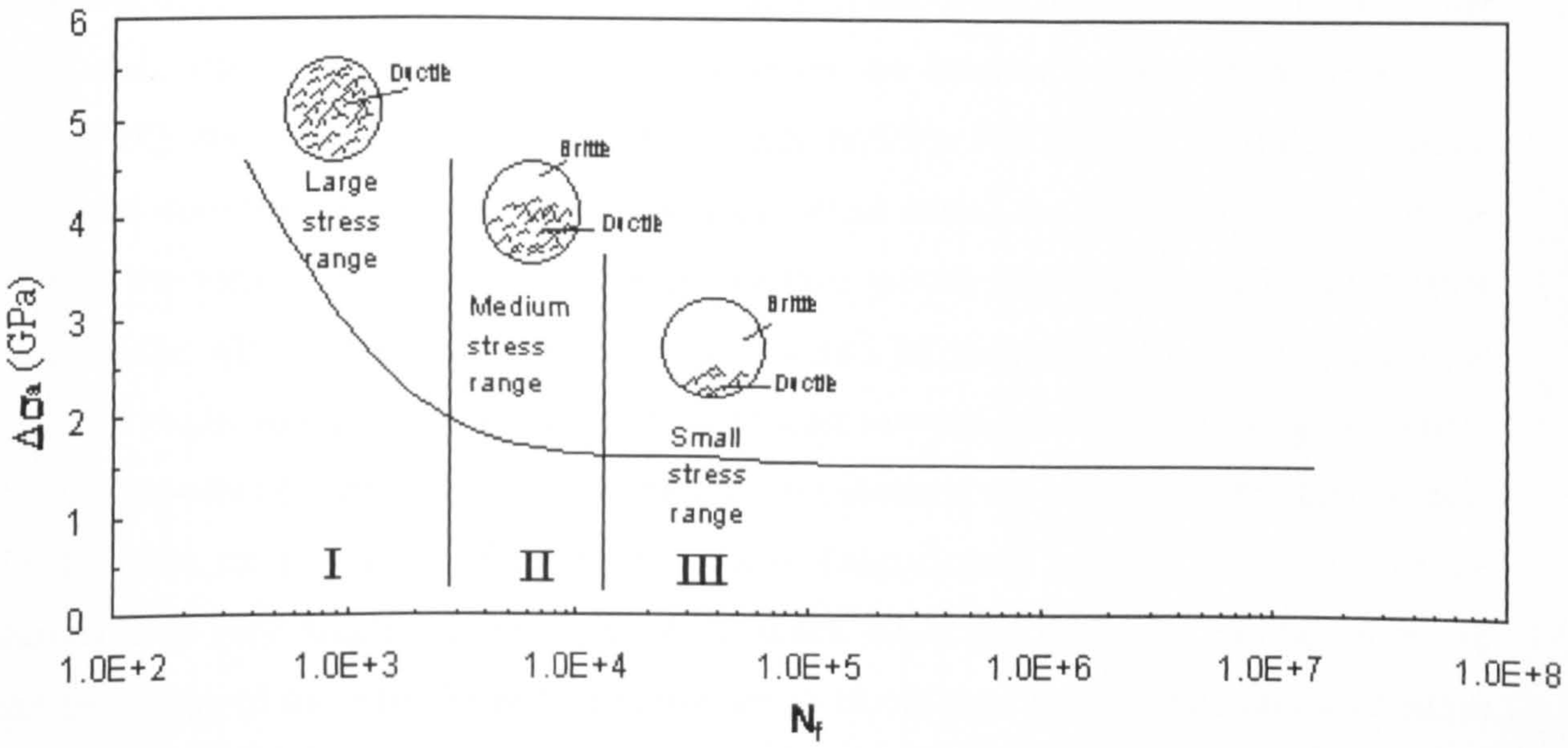

Figure 5.13. Idealised stress-cycle fatigue curve showing conceptual stress regions associated with the fracture types observed in the samples tested on the DP machine. The region III is also valid for fracture type observed in samples tested on the SP machine.

Although the DP machine can produce tension/compression loading, in practice, only the wires tested at σ_m = 200 MPa in this machine were subjected to tension/compression loading for all the stress ranges used. Under high mean stress conditions (σ_m = 900 and 1550 MPa), the wires were subjected to tension/compression stress for large stress ranges

(low cycle fatigue), but only tension/tension loading for low values of the stress range (see figure 3.12(*b*)).

Large stress range (low cycle): At high bending stresses, large numbers of shear bands were generated on the surfaces of the wires subjected to the tensile and compressive bending stress. The potential for the nucleation of cracks on these shear bands was high; the fatigue crack would be expected to initiate at the root of one or more shear steps after an incubation period. Figure 4.40 shows evidence that at least two cracks could be initiated during fracture, resulting in 100 % ductile failure (see also figures 4.39 and 4.41). It can also be seen that there is no clear evidence of a single fracture emanating from a region of cyclic crack growth. This is because two opposing regions of the wire (i.e. adjacent and away from both pulleys) experience tensile stress, whereas in tension/tension loading only one region of the wire experiences tensile stresses (which leads to cyclic crack growth and eventual failure) whereas the opposing region only experiences compressive stress. Thus, in the double pulley case, fatigue cracking can emanate from two different regions of the wire and, judging by the shear events visible on the exterior surface of the wire, may potentially start from several points within those regions. Furthermore, as a fatigue crack becomes dominant on one side of the wire the stress across the remaining section of the wire in the vicinity of a crack is increased and thus growth of a fatigue crack on the other side of the wire in the same general region would be enhanced. As a result, the final fracture might be due to the intersection of at least two fatigue cracks growing separately from each other (figure 4.40), but whose growth enhanced the stresses on the other crack. In this case, as most of the fracture was due to fatigue crack growth, the entire fracture surface was very rough. Of course, a fatigue crack might not initiate at similar points on the two sides of the wire. In this case, one crack would tend to dominate and a situation such as that shown in figure 4.42 was observed. The precise features are related to the number of shear events generated, which will depend on the stress range used.

Although in general fatigue crack initiation started on the surface of the wire, in some samples crack growth initiated at a void inside the wire (figure 5.14). Such voids have been attributed to a shrinkage phenomenon [151] during wire solidification since freezing occurs from the outer surface inwards. In this case, the crack grew outwards from this flaw. However, crack growth occurred predominantly in one direction rather than equally in all directions as might have been expected.

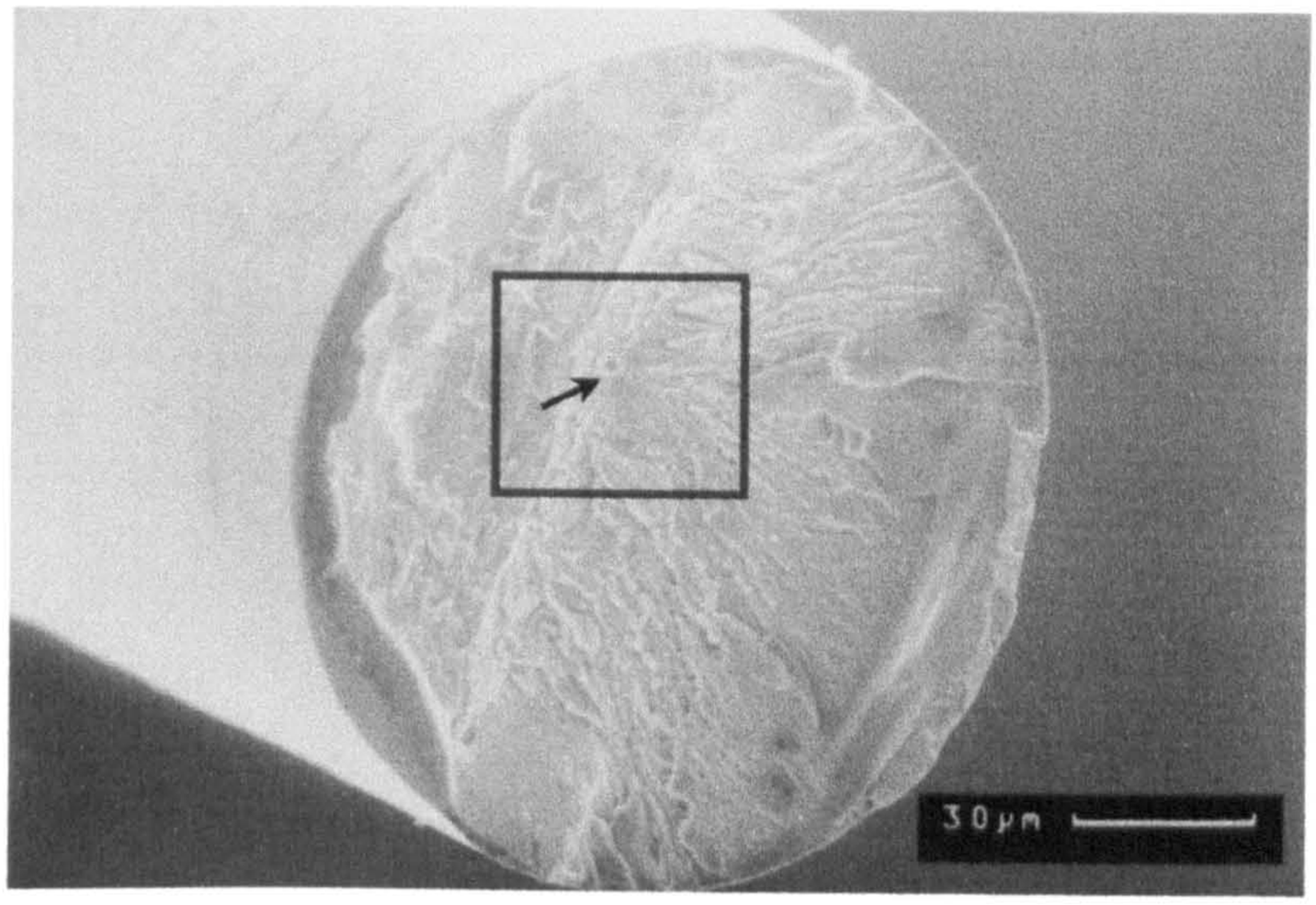

(*a*)

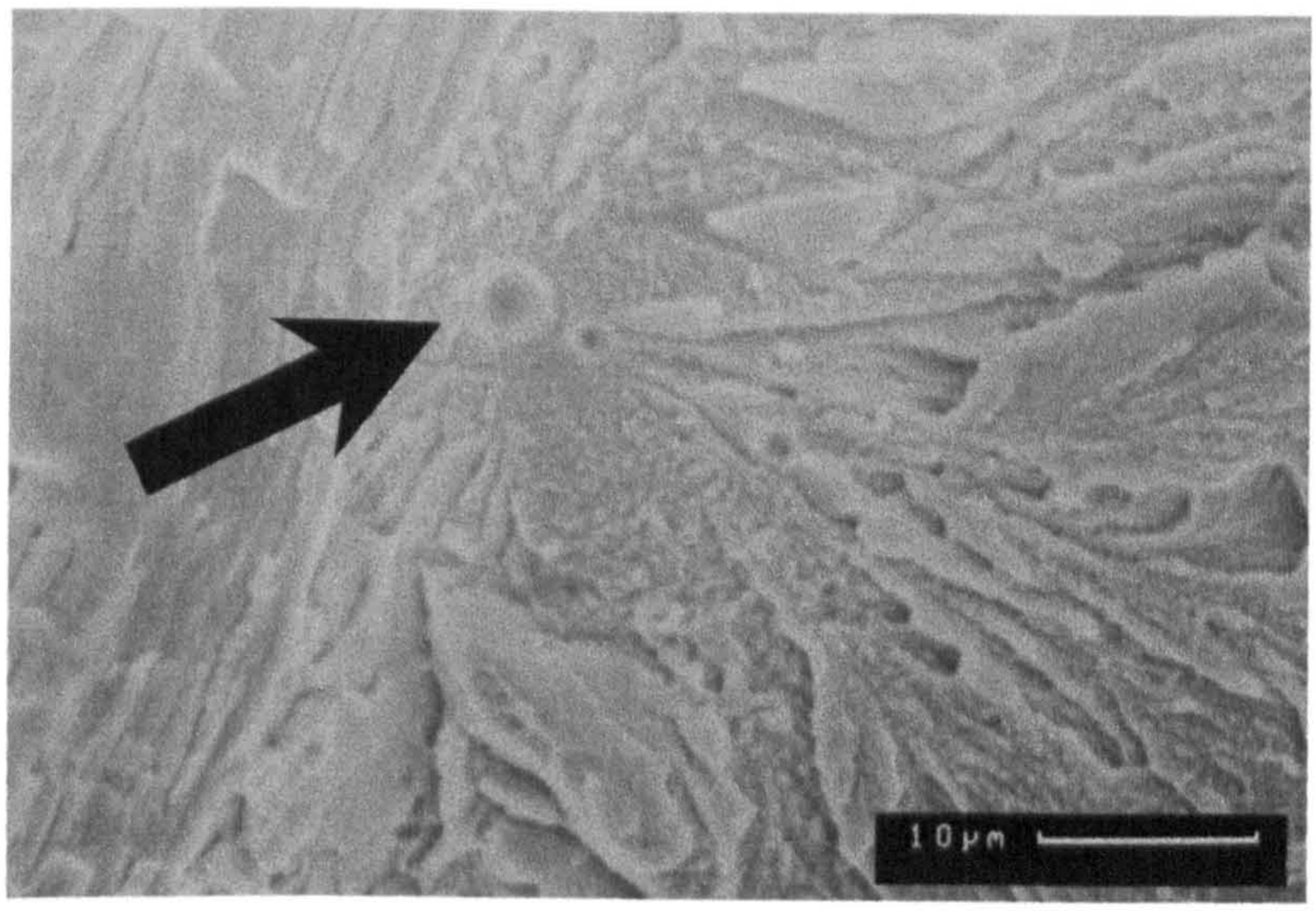

(*b*)

Figure 5.14. $Fe_{74.5}Cr_{3.5}Si_{10}B_{12}$ alloy wire fractured in the DP machine at 492 cycles, applying $\Delta\sigma_a$ = 6 GPa, using σ_m = 1550 MPa. Arrow indicates feature suggesting crack initiation at a void, (*b*) is a higher magnification of (*a*)

Medium stress range (medium cycle): In this case, the bending stress generates a few shear bands. The process of crack initiation could occur in a manner similar to that proposed by Inoue *et al.* [108], via the following stages (see figure 5.15):

a) glassy wires usually contain rather high residual stresses.

b) repetitive bending loading generates shear steps in the high tensile residual stress region on the wire surface.

c) a small corrosion pit generates at the shear event in a high surface energy state.

d) the adsorption and dissociation of moisture in air become easier near the corrosion pit, resulting in the generation and dissolution of hydrogen.

e) and f) the increases of internal stress and embrittlement sensitivity due to the dissolution of H give rise to easy initiation and propagation of a fatigue crack, leading to final fracture.

The diffusion of H down the shear band would be accelerated by the additional free volume generated by the shear event [7]. The ductile fracture, i.e. from crack initiation to the initiation of the brittle fracture extends to 50 to 80 % of the sample diameter. Figure 4.43 shows an example of this type of fracture.

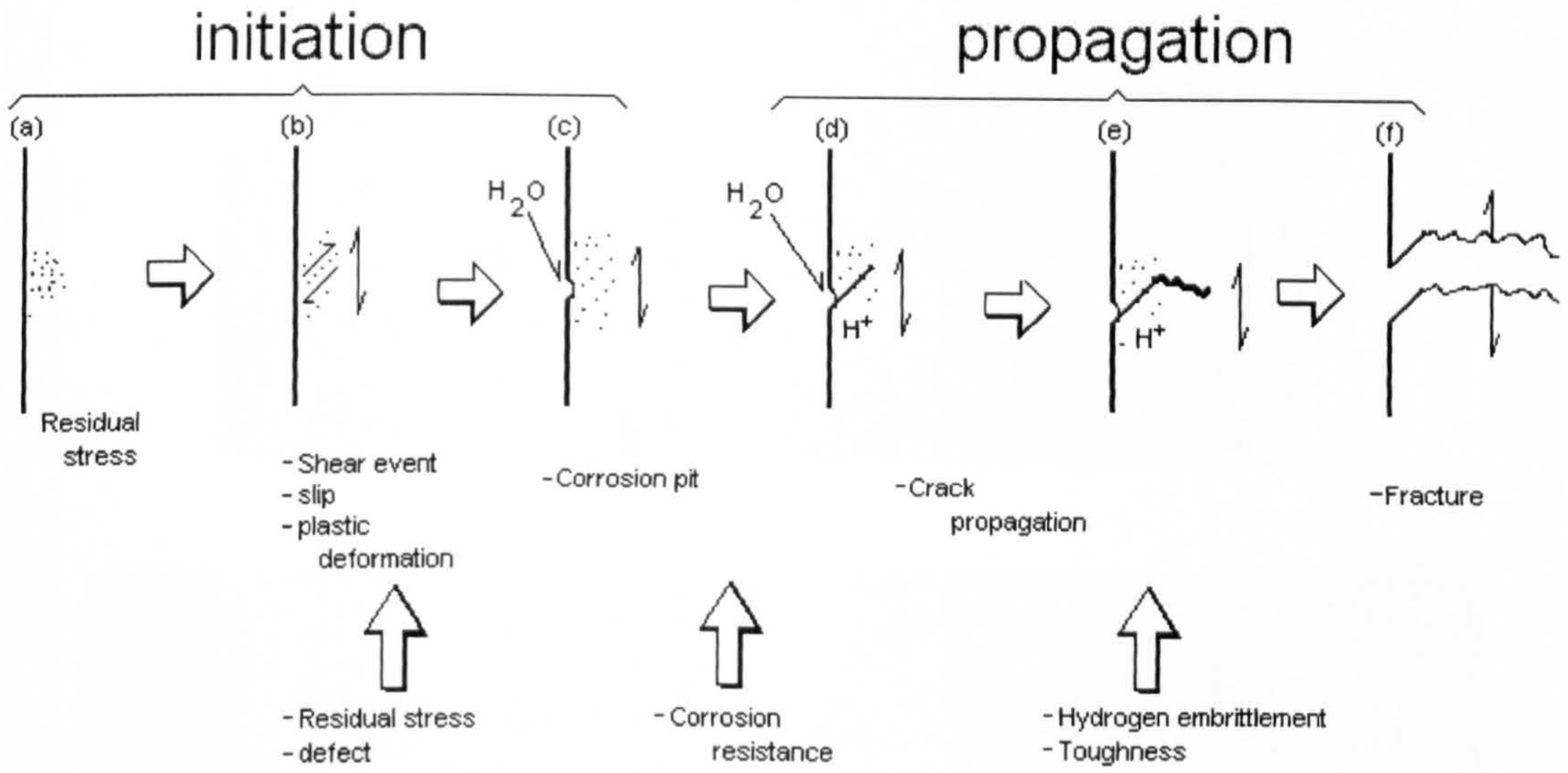

Figure 5.15. Schematic illustrations showing hypothetical processes in bending fatigue failure for and amorphous alloy wire [108].

Low stress range (high cycle): Here, the mechanism of fracture was similar to that observed in the medium stress range case. The difference is that the fraction of rough length was between 15 and 50 % of the sample diameter, see for example figure 4.44.

For samples tested at high mean stress and low stress range conditions, where the samples were subjected only to tension/tension loading, the fracture surfaces were similar

to those observed on samples tested in the SP machine. Similarly, the occurrence of pitting corrosion would only be expected for alloys with 0 and 3.5 at% Cr for series A and 0 and 4 at% for series B, because these alloys were the only ones having less than the nominal threshold concentration of Cr for corrosion protection. For the rest of the alloys, i.e $Fe_{71.75}Cr_{6.25}Si_{10}B_{12}$, $Fe_{70}Cr_8Si_{10}B_{12}$ and $Fe_{69.5}Cr_8Si_{7.5}B_{15}$, no pitting corrosion was found at any of the points of crack initiation for medium and high stress ranges. Thus, in this case, a fatigue crack was initiated at the root of a shear step after a long incubation period. The fraction of rough length from the crack initiation to fracture was approximately 15 % (figure 5.16).

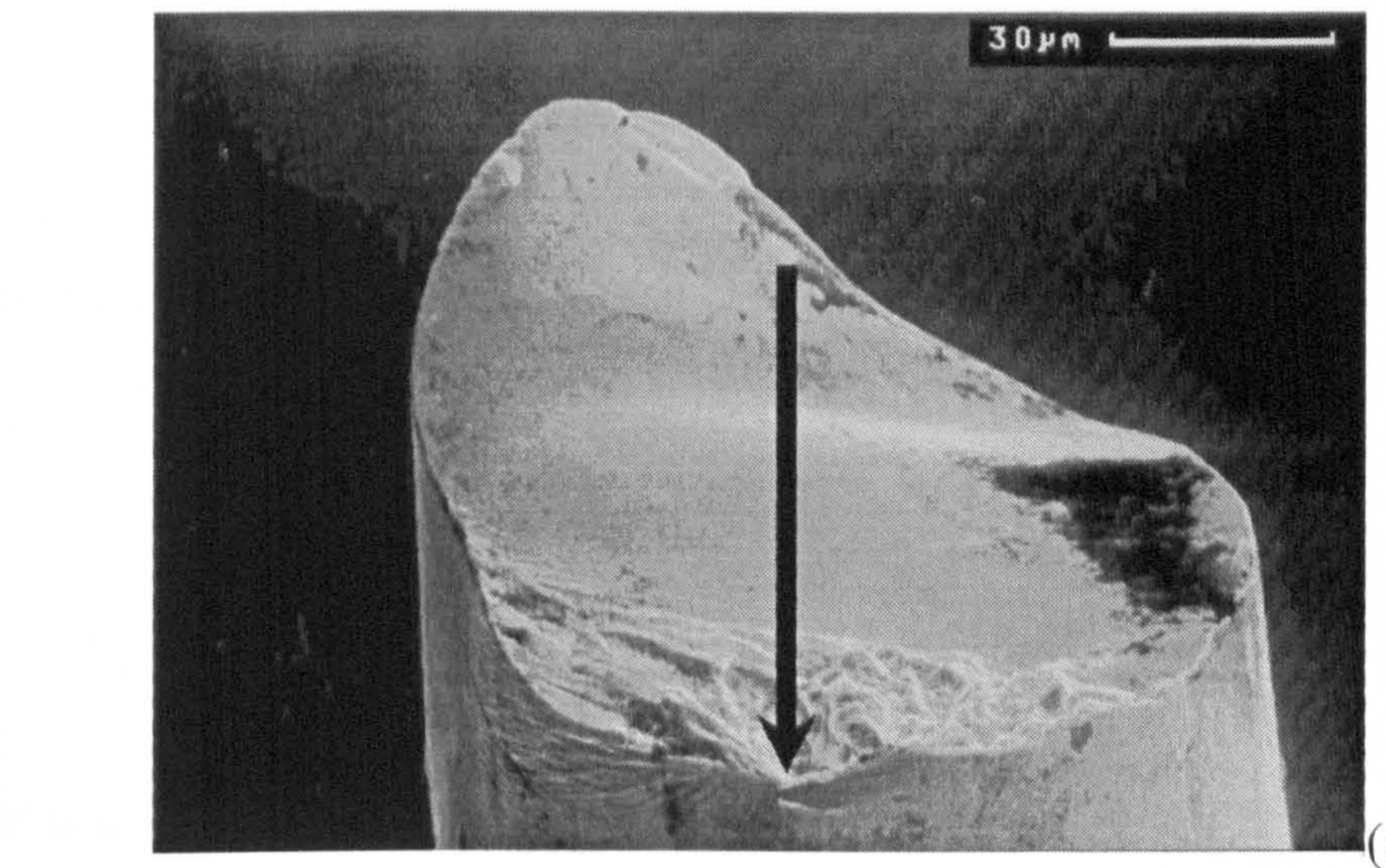

(a)

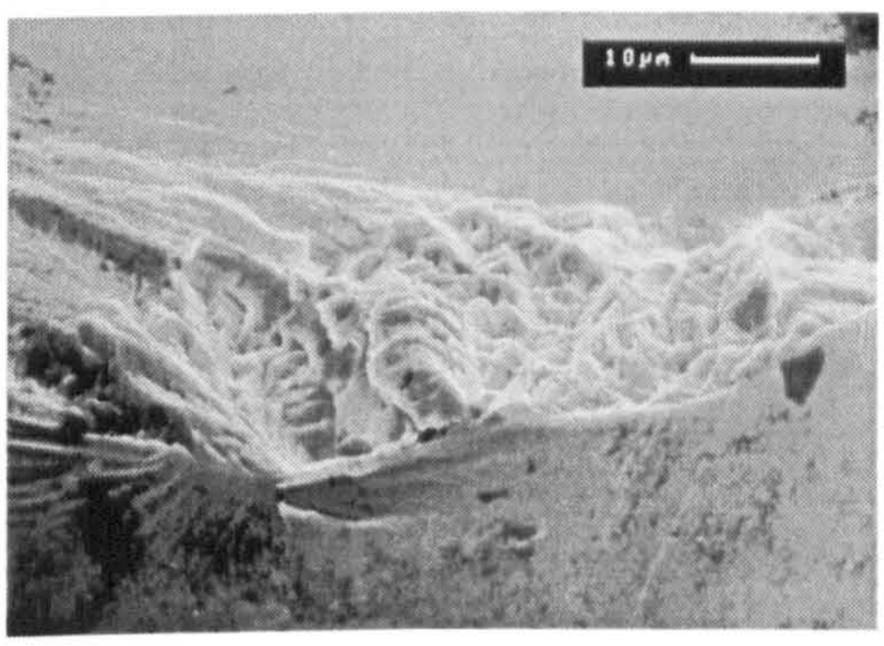

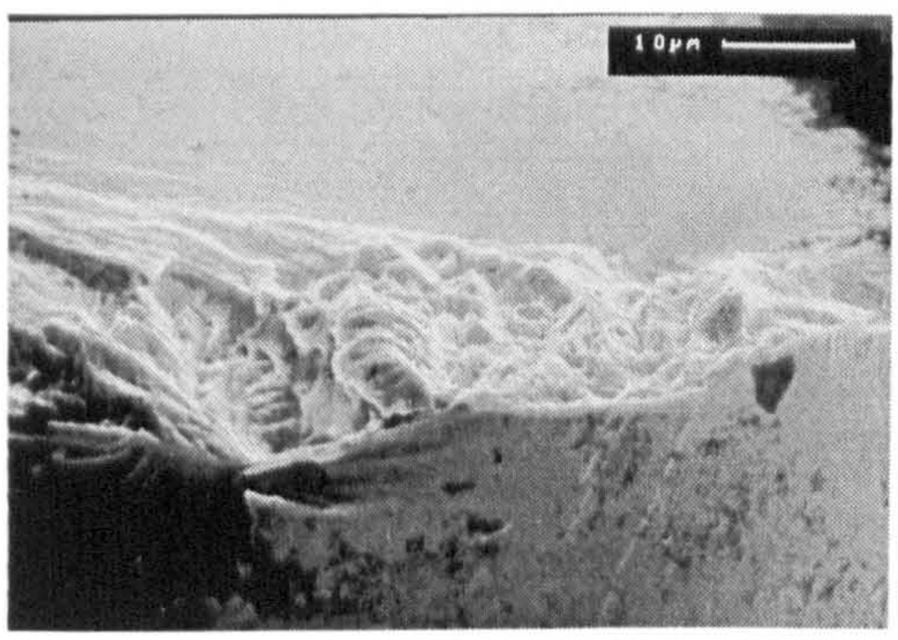

(b)

Figure 5.16. $Fe_{71.75}Cr_{6.25}Si_{10}B_{12}$ glassy wire fractured in the DP machine at 17,256 cycles applying $\Delta\sigma_a$ = 1.86 GPa, using σ_m = 200 MPa. Arrow indicates crack initiation site; (*b*) is a stereopair showing higher magnification of the point of crack initiation.

A fracture mechanics analysis of fatigue crack growth

It has been observed [70] that the fatigue crack growth behaviour of metallic glasses is similar to that of metals, in displaying three distinct regimes of growth; threshold, Paris law and fast fracture. These are shown schematically in figure 5.17(*a*). In the current samples it is possible to identify regions on the fracture surfaces that correlate with these distinct regions (see figure 5.17(*b*)).

In the present work, the temperature and environment test conditions were fixed and hence the crack growth was strongly influenced only by ΔK [152]:

$$\Delta K = K_{max} - K_{min} \tag{5.9}$$

where K_{max} and K_{min} are the maximum and minimum values, respectively, of the stress intensity factor during a fatigue stress cycle. They are related to the maximum stress, $\sigma_{max} = \sigma_m + \frac{\Delta\sigma_a}{2}$ and the minimum stress, $\sigma_{min} = \sigma_m - \frac{\Delta\sigma_a}{2}$ by:

$$K_{max} = Y\sigma_{max}\sqrt{\pi a}\ \ldots(a) \qquad K_{min} = Y\sigma_{min}\sqrt{\pi a}\ \ldots(b) \tag{5.10}$$

where Y is a factor which depends on the crack geometry, which in the present work has been interpolated from reference [153].

The load ratio, R:

$$R = \frac{\sigma_{min}}{\sigma_{max}} = \frac{K_{min}}{K_{max}} \tag{5.11}$$

can also affect fatigue results. For example if $\sigma_{min} \leq 0$, then, it can be argued that, as the crack is closed and the stress intensity factor is zero [105], $\sigma_{min} = 0$ should be used.

Table 5.III presents data for the examples analysed regarding the stress intensity factor. ΔK_{th} is defined as the stress intensity factor at the boundary between region I and II (see figures 5.17(*a*) and (*b*)). In table 5.III a line means that the boundary of this region was not clearly identifiable.

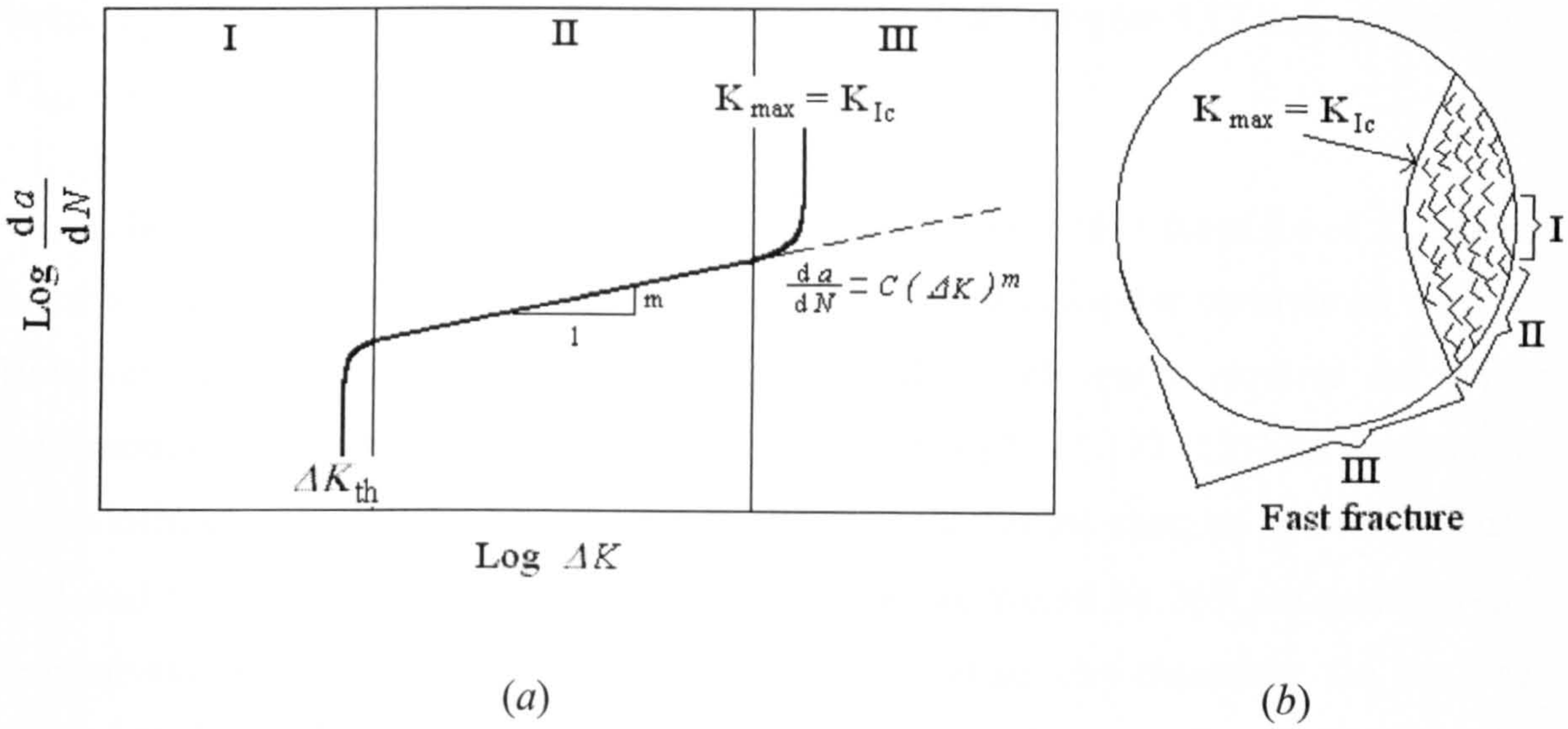

(*a*) (*b*)

Figure 5.17. (*a*) schematic of the log d*a*/d*N* versus log ΔK for fatigue crack growth in metals; (*b*) schematic illustration showing the different regions of (*a*).

Table 5.III. Stress intensity factor values, estimated for different fatigue fractures.

Alloy	σ_m **(MPa)**	$\Delta\sigma_a$ **(GPa)**	ΔK_{th} **(MPa√m)**	$K_{max} = K_{Ic}$ **(MPa√m)**	***R***	N_f	**Fig. No.**
$Fe_{74.5}Cr_{3.5}Si_{10}B_{12}$	900	1.42	3.3	10.5	0.15	$2.207x10^4$	4.44
$Fe_{70}Cr_8Si_{10}B_{12}$	1550	2.8	-	15.7	0.5	$1882x10^3$	5.18
$Fe_{71.75}Cr_{6.25}Si_{10}B_{12}$	900	1.6	6.7	9.6	0.05	$1.51x10^5$	5.19
$Fe_{70}Cr_8Si_{10}B_{12}$	200	1.57	-	5.2	-0.59	$7x10^5$	5.20
HT steel wire	200	6.4	-	27	-0.88	1,094	4.48

The fatigue growth curve shown in figure 5.17 corresponds to the region of fracture surface labelled as ductile fracture in figure 5.13. As has already been discussed, when the entire fracture surface exhibits features of ductile fracture this is due to the growth of more than one crack. In other cases a single crack becomes dominant and, when it reaches a certain size, fast fracture ensues giving the smoother region on the fracture surface. The

boundary between these 2 regions corresponds to region III in figure 5.17 and, at this stage, $K_{max} = K_{Ic}$.

The K_{max} values presented in table 5.III are much lower than those for of K_{Ic} shown in table 4.III corresponding to the fracture toughness obtained for amorphous ribbons. However, if equation 5.10(a) is used to calculate the crack length required for failure corresponding to the K_{Ic} values from table 4.III, assuming $Y = 1.173$ [153] for a maximum stress intensity factor, it can be shown that, for example, for the samples shown in figures 4.44 and 5.18, that the fatigue crack length for fracture would be 269 μm and 278 μm, respectively. These are clearly much greater than the actual wire diameters. On the other hand, additional experiments on fracture toughness carried out on $Fe_{70}Cr_8Si_{10}B_{12}$ alloy ribbon annealed at 300 °C for 30 min gave a value of 19 MPa√m. This is of a similar order of magnitude for the K_{max} values given in table 5.III. This suggests that embrittlement of the metallic glasses is occurring in the highly stressed region ahead of the crack tip. Simple bend testing of the regions of the wire near the fracture surface, which showed that good bend ductility is maintained following extended cyclic loading of the wire, indicate that this embrittlement is not a global phenomenon.

Embrittlement would therefore appear to be localised in the plane ahead of the growing crack tip. Embrittlement in annealing is associated with removal of excess cast-in free volume from within the glass structure. It is not immediately clear how free volume is removed from the material ahead of the growing fatigue crack (assuming that this is indeed the cause of embrittlement on this case). However, it is suggested that such removal of free volume may be connected in some way with the very high stresses generated immediately ahead of the crack tip and this is an area that needs further study.

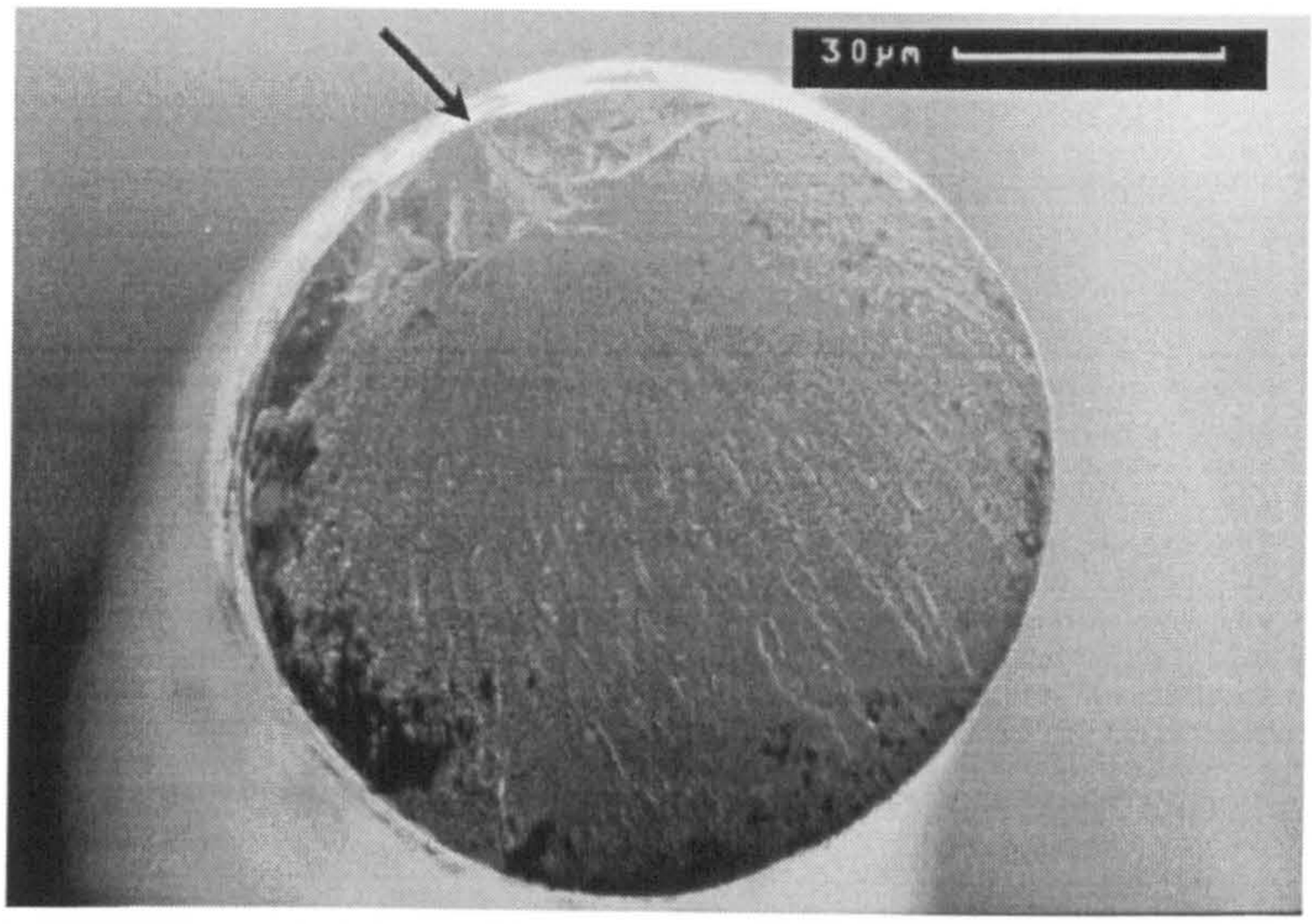

Figure 5.18. $Fe_{70}Cr_8Si_{10}B_{12}$ alloy wire fractured in the DP machine at 1,882 cycles, applying $\Delta\sigma_a$ = 2.8 GPa, using σ_m = 1550 MPa. Arrow indicates crack initiation.

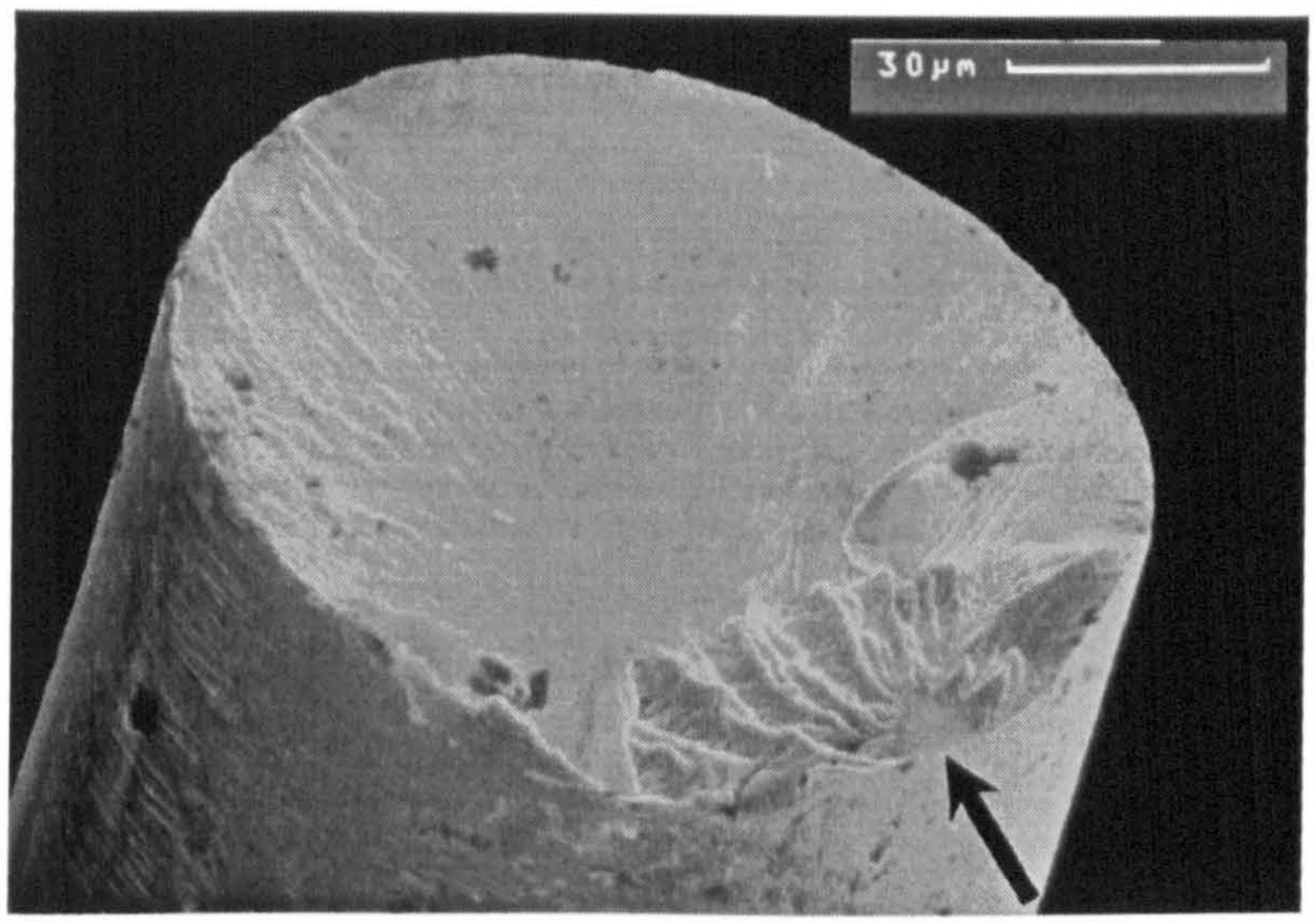

Figure 5.19. $Fe_{71.75}Cr_{6.25}Si_{10}B_{12}$ alloy wire fractured in the DP machine at 151,864 cycles, applying $\Delta\sigma_a$ = 1.6 GPa, using σ_m = 900 MPa. Arrow indicates crack initiation.

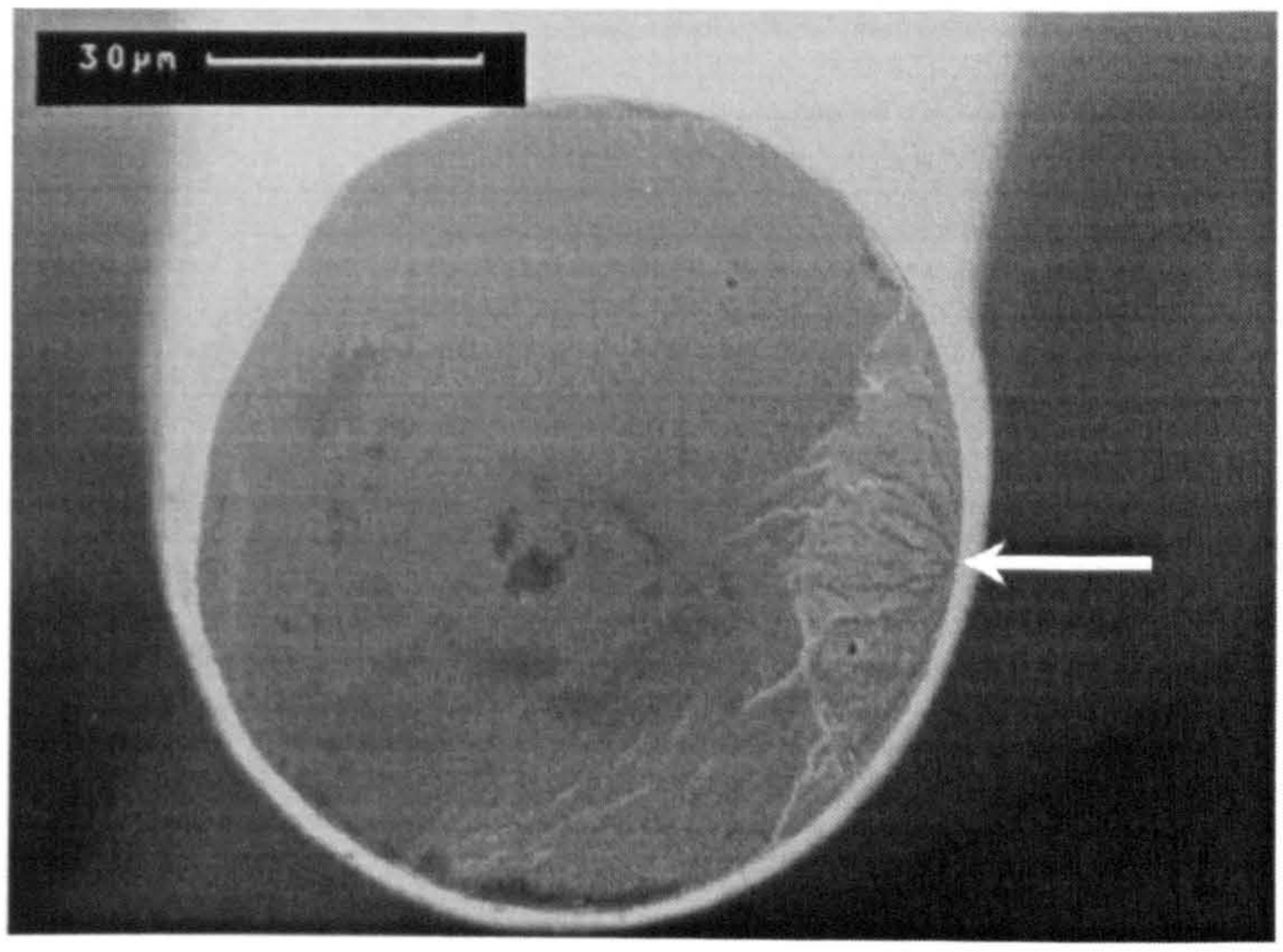

Figure 5.20. $Fe_{70}Cr_8Si_{10}B_{12}$ alloy wire fractured in the DP machine at 704,058 cycles, applying $\Delta\sigma_a$ = 1.57 GPa, using σ_m = 200 MPa. Arrow indicates crack initiation.

Chapter VI: CONCLUSIONS

1.- $Fe_{78}Si_{10}B_{12}$ alloy was found to be difficult to cast as amorphous wire with uniform cross section. The necked morphology of the wire obtained typically was reflected in relatively modest fatigue performance. The other alloys were easier to cast and the resulting wires had smoother and more uniform surfaces.

2.- All the alloy wires (diameter typically 120 μm) except for one composition, were fully ductile (i.e. underwent 180° bend) in the as-cast state. The exception was $Fe_{69.5}Cr_8Si_{7.5}B_{15}$ which fractured at a bend angle of 150°.

3.- All the ribbons (thickness typically 45 μm) cast under an argon atmosphere were brittle. However when they were cast under helium atmosphere with the same thickness, the ribbons were fully ductile.

4.- The crystallisation temperature for wires (diameter typically 120 μm), which reflects the thermal stability for both $Fe_{78-x}Cr_xSi_{10}B_{12}$ (series A) and $Fe_{77.5-x}Cr_8Si_{7.5}B_{15}$ (series B) alloys increased with increasing Cr content, but was consistently higher for series B alloys than series A alloys for all Cr concentrations. The heat of crystallisation was higher in series B alloys than series A alloys for all Cr contents but in each case was almost independent of Cr concentration.

5.- The mechanical properties of both alloy series improved with increasing Cr content, but the trend was more marked for the fatigue performance. The mechanical properties were consistently better for series B alloys than series A alloys. The fracture strength for zero and low at% Cr amorphous wires was less than that of HT steel wire, although at higher Cr levels, the fracture strength was higher for the amorphous wires. The Vickers microhardness H_v also increased with the substitution of Fe by Cr; H_v was higher for series B alloys than for series A alloys and both were higher than for HT steel wire. The fracture toughness measured on ribbons was almost constant for samples within each

alloy series and independent of composition but was higher for series B alloys than for series A alloys.

6.- Tensile fracture in both wire and ribbon forms occurred by shear deformation nucleated at the root of shear bands following inhomogeneous flow due to plastic instability. The final fracture showed the characteristic "vein pattern" due to localised viscous-like flow.

7.- A modified bend type fatigue testing machine which used two pulleys (DP machine), and which could perform compressive/tensile bend stress cycles on the very thin wire filaments, was successfully designed and developed. Compressive to tensile stresses were applied at low mean stresses (σ_m = 200 MPa) for all stress ranges tested. For higher mean stresses (σ_m = 900 and 1550 MPa), although compression/tension cycles were applied for large stress ranges, for small stress ranges it was only possible to apply tensile/tensile cycles.

8.- The fatigue performance in both amorphous alloy series improved with the replacement of Fe by Cr and again was higher for series B alloys than for series A alloys. $Fe_{69.5}Cr_8Si_{7.5}B_{15}$ amorphous alloy wire was shown to have the highest fatigue endurance. This fatigue performance enhancement due to Cr additions was more marked when the wires were tested with the SP machine than with the DP machine at a Cr content of 6.25 at% (fatigue tests with the SP machine were only performed for series A alloys).

9.- In terms of bend stress range, the fatigue endurance of HT steel wire was greater than that of amorphous wire. However in terms of bend strain range, the fatigue endurance was greater for amorphous wires than for HT steel wire, reflecting the lower elastic modulus for glassy alloys than for crystalline counterparts.

10.- No change in Vickers microhardness was observed after fatigue testing even for small bend radii in which repeated plastic deformation occurred, which suggests that no work hardening nor softening occurred during the bending fatigue process. However, the low

calculated stress intensity factors at the onset of fast fracture suggests that embrittlement is occurring ahead of the growing fatigue cracks.

11.- Fracture morphologies for samples tested in the SP machine were similar to those obtained previously, with a region of slow fatigue crack growth followed by fast fracture.

12.- Three different fracture morphologies for samples tested in the DP machine were observed, depending on the stress range and independent of the mean stress. At large stress ranges the fracture was almost 100 % ductile, which means that failure arose from the intersection of more than one fatigue crack developing on different parts of the wire (both sides see tension during tension/compression cycles). At medium stress ranges, the fraction of ductile fracture was in the range of 50 to 80 %, similar to those observed for the SP machine tests. What could be corrosion pits appeared as points of crack initiation for alloys with 0 % Cr and low Cr contents, nucleated at the roots of shear bands. For low stress ranges, the fraction of ductile fracture was in the range of 15 to 50 %, showing similar fracture features to those observed for medium stress ranges.

Chapter VII: SUGGESTIONS FOR FURTHER WORK

1.- Given that the $Fe_{77.5-x}Cr_8Si_{7.5}B_{15}$ alloy wire series showed better wire formability and better thermal and mechanical properties than $Fe_{78-x}Cr_xSi_{10}B_{12}$ alloy wires, a systematic study of the influence of B in the alloys is required, since previous studies have established that the more beneficent metalloid element on Fe-Si-B alloy wires is Si; but in the present work it seems that B has more influence than Si. It is, therefore suggested for future work to study series with a constant at% of Si and varying at% content of B.

2.- It is important to keep trying to incorporate a system which can monitor and therefore control in a systematic way the optimum wire casting temperature so that the empirical experience that has to be used for wire production can be eliminated and hence the optimum superheat can be methodically established.

3.- It is of great interest to investigate whether the amorphous wires have higher fatigue performance than HT steel wire in terms of stress range; therefore it is recommended to adapt a larger main gear to the DP machine (labelled B in figure 3.11(*a*)) so that the distance of the gauge point that is in fatigue travels a longer distance and therefore pulleys of larger diameter can be incorporated to the machine in order to generate lower stress ranges for wires having larger diameters.

4.- To study more systematically the fatigue fracture mechanics of amorphous wires tested in the DP machine at different constant mean stresses, and the effect that voids may have on fatigue crack initiation and growth in these amorphous materials.

5.- To examine in detail the behaviour of material ahead of growing fatigue cracks in these wires to assess the causes of the apparent embrittlement.

REFERENCES

1.- Luborsky, F. E., in *Amorphous Metallic Alloys*, Ed. Luborsky, F. E., Butterworths, London, (1983) 1.

2.- Ma, L. and Inoue, A., *Materials Letters,* **38**, (1999) 58.

3.- Hagiwara, M., Inoue, A. and Masumoto, T., *Sci. Rep. RITU.*, **29**, (1981) 351.

4.- Ohnaka, I., *Int. J. of Rapid Solidification*, **4**, (1984-85) 219.

5.- Hagiwara, M., Inoue, A. and Masumoto, T., *Proc. of the 5th Int. Conf. on Rapidly Quenched Metals*, Eds. Steeb, S. and Warlimont, H., Germany, vol. II, (1984) 1779.

6.- Olofinjana, O., Nurminen, J., Kern, J. H. and Davies, H. A., *Proc. of the 4th Int. Workshop on Non-Crystalline Solids*, Eds. Vázquez, M. and Hernando, A., España, (1994) 72.

7.- Olofinjana, O. and Davies, H. A., *Mater. Sci. Engng.*, **A186**, (1994) 143.

8.- Davies, H. A., *as ref.* [1], 8.

9.- Davies, H. A. and Hull, J. B., *Scripta Metall.*, **7**, (1973) 637.

10.- Vuči□, Z., Etlinger, B. and Kunstelj, D., *J. Non-crys. Solids*, **20**, (1976) 451.

11.- Davies, H. A., in *Physics and Chemistry of Glasses, Society of Glass Technology*, **17**, (1976) 156.

12.- Turnbull, D., *J. Phys. Colloque*, **35** No. 4, (1974) 1.

13.- Turnbull, D. *Contemp. Phys.*, **10**, (1969) 473.

14.- Lewis, B. G. and Davies, H. A., *Mater. Sci. Engng.*, **23**, (1976) 179.

15.- Ray, R., Hasegawa, R., Chou, C. P. and Davis, L. A., *Scripta Metall.*, **11**, (1977) 973.

16.- Donald, I. W. and Davies, H. A., *J. Mater. Sci.*, **15**, (1980) 2754.

17.- Inoue, A., Kitamura, A. and Masumoto, T., *Trans. JIM.*, **20**, (1979) 404.

18.- Chen, H. S. and Turnbull, D., *Acta Metall.*, **17**, (1969) 1021.

19.- Maitrepierre, P., *J. Appl. Phys.*, **41** No. 2, (1970) 498.

20.- Donald, I. W. and Davies, H. A., *J. mater Sci.*, **15**, (1980) 2754.

21.- Hagiwara, M., Inoue, A. and Masumoto, T., *Sci. Rep. RITU.*, **29**, (1981) 351.

22.- Klement, W., Willens, R. H. and Duwez, P., *Nature*, *Lond.*, **187**, (1960) 869.

23.- Cohen, M. H. and Turnbull, D., *Nature, Lond.*, **189**, (1961) 131.

24.- Bennett, C. H., Polk, D. E. and Turnbull, D., *Acta Metall.*, **29**, (1971) 1295.

24.- Bernal, J. D., *Nature, Lond.*, **185**, (1960) 68.

25.- Chen, H. S. and Park, B. K., *Acta Metall.*, **21**, (1973) 395.

26.- Chen, H. S., *Acta Metall.*, **22**, (1974) 1505.

27.- Nagel, S. R. and Tauc, J., *Phys. Rev. Lett.*, **35**, No. 6, (1975) 380.

28.- Davies, H. A. Aucote, J. and Hull, J. B., *Scripta Metall.*, **8**, (1974) 1179.

29.- Sarjeant, P. T. and Rustum, R., *Mater. Res. Bull.*, **3**, (1968) 265.

30.- Turnbull, D., *Contempory Physics*, **10** No. 5, (1969) 473.

31.- Uhlmann, D. R., *J. Non-crys. Solids*, **7**, (1972) 337.

32.- Johnson, W. A. and Mehl, R. F., *Trans. metall. Soc. AIME*, **135**, (1939) 416.

33.- Davies, H. A., *J. Non-crys. Solids*, **17**, (1975) 266.

34.- Vreeswijk, J. C. A., Gossink, R. G. and Stevels, J. M., *J. Non-crys. Solids*, **16**, (1974) 15.

35.- Shingu, P. H. and Ozaki, R., *Met. Trans.*, **6A**, (1975) 33.

36.- Davies, H. A. and Lewis, B. G., *Met. Trans.*, **7A**, (1976) 310.

37.- Zielinzki, P. G. and Matyja, H., *Proc. 2nd Int. Conf. Rapidly Quenched Metals, Eds. Grant, N. J. and Giessen, B. C., MIT*, section I, (1976) 237.

38.- Donald, I. W. and Davies, H. A., *J. Non-crys. Solids*, **30**, (1978) 77.

39.- Egami, T., *Mater. Sci. Engng.*, **A226-228**, (1997) 261.

40.- Zallen, R., *The physics of amorphous solids*, Wiley, New York, (1983) 170.

41.- Egami, T. and Vitek, V., in *Amorphous metals: Modelling of Structure and Properties, TMS-AIME*, Warrendale, PA, (1983) 127.

42.- Egami, T. and Srolovitz, D., *J. Phys. F.*, **12**, (1982) 2141.

43.- Egami, T., *Rep. Progr. Phys.*, **47**, (1984) 1601.

44.- Jones, H., *Rep. Progr. Phys.*, **36**, (1973) 1425.

45.- Narasimhan, M., *Allied Chemical*, U.S. Patent 4 142 571, (1979).

46.- Small, E., US Patent No. 262,625, 23rd May 1882.

47.- Leghorn, G. R., US Patent No. 3'430,680, (1969).

48.- Kavesh, S., US Patent No. 3'845,805, (1974).

49.- Masumoto, T., Ohnaka, I., Inoue, A. and Hadiwara, M., *Scripta Metall.*, **15**, (1981) 293.

50.- Liu, J., Strinning, E., Arnberg, L., Savage, S. J. and Inoue, A., *Scandinavian J. of Metallurgy*, **19** (1990) 14.

51.- Abe, Y, Miyazawa, K., Nakamura, M. and Ohashi, T., *Trans. ISIJ.*, **27** (1987) 929.

52.- Inoue, A., Masumoto, Y., Yano, N., Kawashima, A., Hashimoto, K. and Masumoto, T., *J. Mater. Sci.*, **20**, (1985) 97.

53.- Inoue, A., Furukawa, S., Hagiwara, M. and Masumoto, T., *Met. Trans.*, **18A**, (1987) 621.

54.- Hagiwara, M., Inoue, A. and Masumoto, T., *Met. Trans.*, **13A**, (1982) 373.

55.- Olofinjana, O. and Davies, H. A., *Int. J. of Rapid Solidification*, **8**, (1994) 225.

56.- Inoue, A., Hagiwara, M. and Masumoto, T., *J. Mater. Sci.*, **17**, (1982) 580.

57.- Ohnaka, I., Ichiryu, T., Yamauchi, I., Tateoka, H. and Fukusako, T., *Proceedings of an Int. Conf., San Diego, California*, (1986) 91.

58.- Hagiwara, M., Inoue, A. and Masumoto, T., *Mater. Sci. Engng.*, **54**, (1982) 197.

59.- Inoue, A. and Masumoto, T., *J. Mater. Sci.*, **19**, (1984) 3783.

60.- Inoue, A. and Masumoto, T., *J. Mater. Sci.*, **19**, (1984) 3097.

61.- Inoue, A., Tomioka, H. and Masumoto, T., *Met. Trans.*, **14A**, (1983) 2319.

62.- Inoue, A., Tomioka, H. and Masumoto, T., *Met. Trans.*, **16A**, (1985) 215.

63.- Inoue, A., Tomioka, H., Hagiwara, M. and Masumoto, T., *Trans. JIM.*, **23**, (1982) 341.

64.- Inoue, A., Yano, N. and Masumoto, T., *Trans. ISIJ.*, **25**, (1985) 1069.

65.- Inoue, A., Yano, N., Tomioka, H. and Masumoto, T., *Trans. ISIJ.*, **26**, (1986) 993.

66.- Hagiwara, M., Inoue, A. and Masumoto, T., *Sci. Rep. RITU.*, **29**, (1981) 351.

67.- Waseda, Y., Ueno, S., Hagiwara, M. and Aust, K. T., *Progress in Materials Science*, **34**, (1990) 149.

68.- Masumoto, T. and Maddin, R., *Acta Metall.*, **19**, (1971) 725.

69.- Masumoto, T. and Maddin, R., *Mater. Sci. Engng.*, **19**, (1975) 1.

70.- Alpas, A. T., Edwards, L. and Reid, C. N., *Mater. Sci Engng.*, **98**, (1988) 501.

71.- Davis, L. A., Das, S. K., Li, J. C. M. and Zedails, M. S., *Int. J. of Rapid Solidification*, **8**, (1994) 73.

72.- Davis, L. A., *Scripta Metall.*, **9**, (1975) 339.

73.- Masumoto, T. and Kimura, H., *The 1688th report of the Res. Inst. For Iron, Steel and other Metals*, (1979) 172.

74.- Spaepen, F. and Taub, A. I., *as ref.* [1], 231.

75.- Egami, T., *Proc. of 4th Int. Conf. on Rapidly Quenched Metals*, Eds. Masumoto, T. and Suzuki, K., Japan Institute of Metals, Sendai, (1982) 100.

76.- Taub, A. I. and Spaepen, F., *Scripta Metall.*, **13**, (1979), 195.

77.- Pampillo, C. A., *Scripta Metall.*, **6**, (1972) 915.

78.- Murata, T., Masumoto, T. and Sakai, M., *Proc. of the 3rd Int. Conf. on Rapidly Quenched Metals*, Ed. Cantor, B., Brighton, England, **vol II**, (1978) p. 401.

79.- Spaepen, F., *Acta Metall.*, **25**, (1977) 407.

80.- Leamy, H. J., Chen, H. S. and Wang, T. T., *Met. Trans.*, **3**, (1972) 699.

81.- Polk, D. E. and Turnbull, D., *Acta Metall.*, **20**, (1972) 493.

82.- Kobayashi, S., Maeda, K. and Takeuchi, S., *Acta Metall.*, **28**, (1980) 1641.

83.- Vitek, V., Srolovitz, D. and Egami, T., *as ref.* [75], 241.

84.- Argon, A. S. and Kuo, H. Y., *as ref.* [78], 269.

85.- Argon, A. S. and Kuo, H. Y., *Mater. Sci. Engng.*, **39**, (1979) 101.

86.- Argon, A. S., *Acta Metall.*, **27**, (1979) 47.

87.- Spaepen, F. and Turnbull, D., *Scripta Metall.*, **8**, (1974) 563.

88.- Cohen, M. H. and Turnbull, J., *Chem. Phys.*, **31**, (1959) 1164.

89.- Rice, J. R., *Fracture – an advanced treatise (Ed. Liebowitz, H.), Academic Press*, **vol. II**, (1968) 216.

90.- Bengus, V. Z., Tabachnicova, E. D., Shumilin, S. E., Golovin, Y. I., Makarov, M. V., Shibkob, A. A., Miskuf, J., Csach, K. and Ocelik, V., *Int. J. of Rapid Solidification*, **8** (1993) 21.

91.- Steif, P. S., Spaepen, F. and Hutchinon, J., W., *Acta Metall.*, **30**, (1982) 447.

92.- Kimura, H. and Masumoto, T., *as ref.* [1], 181.

93.- Bowden, P. B. and Jukes, J. A., *J. Mater. Sci.*, **7**, (1972) 52.

94.- Davis, L. A. and Kavesh, S., *J. Mater. Sci.*, **10**, (1975) 453.

95.- Takayama, S., *Mater. Sci. Engng.*, **38**, (1979) 41.

96.- Taub, A. I. and Spaepen, F., *Scripta Metall.*, **14**, (1980) 1197.

97.- Tsao, S. and Spaepen, F., *as ref.* [75] 463.

98.- Taub, A. I. and Luborsky, F. E., *Acta Metall.*, **29**, (1981) 1939.

99.- Pitts, E. and Greiller, J., *J. Fluid Met.*, **11**, (1961) 33.

100.- Spaepen, F., *Acta Metall.*, **23**, (1975) 615.

101.- Pampillo, C. A. and Reimschuessel, A. C., *J. Mater. Sci.*, **9**, (1974) 718.

102.- Eberhart, M., in *Advances in the mechanics and physics of surfaces*, Eds Latanision, R. M. and Fisher, T. E., Harwood Acad. Publ., New York, (1986) 71.

103.- Kramer, E. A., Johnson, W. L. and Cline, C., *Appl. phys. Lett.*, **35**, (1979) 815.

104.- Davis, L. A., *Scripta Metall.*, **9**, (1975), 339.

105.- Dieter, George E., *Mechanical Metallurgy*, Ed. Mc Graw Hill, U.K., (1988) 375-431.

106.- Doi, M., Sugiyama, K., Tono, T. and Imura, T., *as ref.* [75] 1349.

107.- Le, A., Kabakoff, L. T. and Martínez, N. Y., *Mat. Res. Soc. Symp. Proc. 80,* (1987) 137.

108.- Inoue, A., Hagiwara, M. and Masumoto, T., *Sci. Rep. RITU.*, **34**, (1988) 48.

109.- Ogura, T., Masumoto, T. and Fukushima, K., *Scripta Metall.*, **9**, (1975) 109.

110.- Ogura, T., Fukushima, K. and Masumoto, T., *as ref.* [109] 979.

111.- Davis, L. A., *J. Mater. Sci.*, **10**, (1975) 1557.

112.- Jost, N., Hillenbrand, H. G. and Hornbogen, E., *as ref.* [5] 1417.

113.- Hasegawa, R., in *Glassy metals: magnetic, chemical and structural properties*, Ed. CRC Press, (1983) 236.

114.- Naka, M., Hashimoto, K. and Masumoto, T., *J. Non-cryst. Solids*, **31**, (1979) 355.

115.- Naka, M., Hashimoto, K. and Masumoto, T., *Corrosion (Houston)*, **32**, (1976) 146.

116.- Hashimoto, K., Asami, K., Naka, M. and Masumoto, T., *Corrosion Science*, **19**, (1979) 857.

117.- Kulik, T., Baszkiewicz, J., Kaminski, M., Latuszkiewicz, J. and Matyja, H., *as ref.* [116] 1001.

118.- Naka, M., Hashimoto, K. and Masumoto, T., *Corrosion (Houston)*, **36**, (1980) 679.

119.- Anthony, T. R. and Cline, H. E., *J. Appl. Phys.*, **43** No. 3, (1978) 1248.

120.- Devine, T. M. and Wells, L., *Scripta Metall.*, **10**, (1976) 309.

121.- Lee, D. and Devine, T. M., *as ref.* [37] 393.

122.- Pampillo, C. A., *J. Mater. Sci.*, **10**, (1975) 1194.

123.- Kawashima, A., Hashimoto, K. and Masumoto, T., *Corrosion Science*, **16**, (1976) 935.

124.- Naguno, M. and Takahashi, T., *Mater. Sci. Engng.*, **23**, (1976) 257.

125.- Ewalds, H. L. and Wanhill, R. J. H. "Fracture mechanics", Eds. Arnols/DUM, (1989), p. 49.

126.- Donald, I. W., Whang, S. H., Davies, H. A. and Giessen, B. C., *as ref.* [75] 1377.

127.- Oliver, W. C. and Pharr, G. M., *J. Mater. Res.*, **7**, (1992) 1564.

128.- Dieter, George E., *as ref.* [105] p. 49.

129.- Olofinjana, A. O., PhD thesis, University of Sheffield, 1992.

130.- Boisfleury, F. de, PhD thesis, University of Sheffield, 1989.

131.- Weber, C.Z., *A new Math. Mech.*, **11**, (1931) 136.

132.- Liu, J., Arnberg, L., Backstrom, N. and Savage, S., *Mater. Sci. Engng.*, **98**, (1988) 21.

133.- Ohnaka, I., Fukusako, T. and Ohmichi, T., J. JIM., **45**, (1981) 751.

134.- Ohnaka, I., Fukusako, T. and Ohmichi, T., Masumoto, T., Inoue, A. and Hagiwara, M., *as ref.* [75] 31.

135.- Murry, L. E., *Interfacial Phenomena in Metals and Alloys*, Addison-Wesley, Reading, (1975) 101.

136.- Lieberman, H. H., *as ref.* [78] 34.

137.- Yapp, R., Davies, H. A., Lecabbue, F. and Watts, B. E., *Materials Letters*, **39**, (1999) 33.

138.- Harland, C. L. and Davies, H. A., *Proc. of the 15th Int. Workshop on rare-earth magnets and their applications*, Dresden, Germany, (1998) pp. 263-269.

139.- Todd, I., Davies, H. A., Gibbs, M. R. J., Lecabbue, F. and Watts, B. E., *J. of Magnetism and Magnetic Materials*, **196-197**, (1999) 196.

140.- Donald, I. W. and Davies, H. A., *Philosophical Magazine A*, **42, No. 3**, (1980) 227.

141.- Koster, U. and Herold, U., in *"Glassy Metals I"* Eds. Guntherodt, H. J. and Beck, H., Springer-Verlag, Berlin, (1981) 225.

142.- Yavari, A. R., *Mater. Sci. Engng.*, **98**, (1988) 491.

143.- Masumoto, T., *Sci. Rep. RITU.*, **26, No.4-5**, (1983) 246.

144.- Inoue, A., Chen, H. S., Krause, J. T., Masumoto, T. and Hagiwara, M., *Sci. Rep. RITU.*, **31 No.1**, (1983) 124.

145.- Castanet, R., Chastel, R. and Bergman, C., *Mater. Sci. Engng.*, **32**, (1978) 93.

146.- Steif, P. S., Thesis, Harvard University, (1982).

147.- Miller, K. J. and O'Donnell, W. J., *Fatigue and Fracture of Engineering Materials and Structures*, **22**, (1999) 545.

148.- Bathias, C., *as ref.* [147] 559.

149.- Suresh, S., Fatigue of Materials, 2nd Edition, Cambridge University Press, (1998) pp. 221-226.

150.- Hashimoto, K., *Sci. Rep. RITU.*, (1978) 233.

151.- Olofinjana, A. O. and Davies, H. A., *Scripta Metall.*, **27**, (1992) 1679.

152.- Suresh, S., *as ref.* [149] pp. 331-382.

153.- Murakami, Y., in *Stress Intensity Factors Handbook*, Pergamon Press, **2**, (1990) 659-665.